N°d'ordre NNT : 2022LYSEI055

THESE de DOCTORAT DE L'UNIVERSITE DE LYON
opérée au sein de
l'Institut National des Sciences Appliquées de Lyon

Ecole Doctorale N° ED 162
Mécanique, Energétique, Génie civil, Acoustique

Spécialité/ discipline de doctorat :
Biomécanique

Soutenue publiquement le 05/07/2022, par :
Quanshangze DU

Numerical modeling of MR elastography experiment : excitation and tissue inhomogeneity

---

Devant le jury composé de :

Jean-Luc GENNISSON	Directeur de Recherche (CNRS-INSIS)	Rapporteur
Patrick ROZYCKI	Professeur (EC Nantes)	Rapporteur
Christian GEINDREAU	Professeur (Université Grenoble Alpes)	Examinateur
Nahiène HAMILA	Professeur (ENI Brest)	Directeur de thèse
Aline BEL-BRUNON	Maître de Conférences HDR (INSA Lyon)	Co-directrice
Simon Auguste LAMBERT	Maître de Conférences HDR (Université Lyon 1)	Examinateur

Département FEDORA – INSA Lyon - Ecoles Doctorales

SIGLE	ECOLE DOCTORALE	NOM ET COORDONNEES DU RESPONSABLE
CHIMIE	**CHIMIE DE LYON** **https://www.edchimie-lyon.fr** Sec. : Renée EL MELHEM Bât. Blaise PASCAL, 3e étage secretariat@edchimie-lyon.fr	**M. Stéphane DANIELE** C2P2-CPE LYON-UMR 5265 Bâtiment F308, BP 2077 43 Boulevard du 11 novembre 1918 69616 Villeurbanne **directeur@edchimie-lyon.fr**
E.E.A.	**ÉLECTRONIQUE, ÉLECTROTECHNIQUE, AUTOMATIQUE** **https://edeea.universite-lyon.fr** Sec. : Stéphanie CAUVIN Bâtiment Direction INSA Lyon Tél : 04.72.43.71.70 secretariat.edeea@insa-lyon.fr	**M. Philippe DELACHARTRE** INSA LYON Laboratoire CREATIS Bâtiment Blaise Pascal, 7 avenue Jean Capelle 69621 Villeurbanne CEDEX Tél : 04.72.43.88.63 **philippe.delachartre@insa-lyon.fr**
E2M2	**ÉVOLUTION, ÉCOSYSTÈME, MICROBIOLOGIE, MODÉLISATION** **http://e2m2.universite-lyon.fr** Sec. : Bénédicte LANZA Bât. Atrium, UCB Lyon 1 Tél : 04.72.44.83.62 secretariat.e2m2@univ-lyon1.fr	**Mme Sandrine CHARLES** Université Claude Bernard Lyon 1 UFR Biosciences Bâtiment Mendel 43, boulevard du 11 Novembre 1918 69622 Villeurbanne CEDEX **sandrine.charles@univ-lyon1.fr**
EDISS	**INTERDISCIPLINAIRE SCIENCES-SANTÉ** **http://ediss.universite-lyon.fr** Sec. : Bénédicte LANZA Bât. Atrium, UCB Lyon 1 Tél : 04.72.44.83.62 secretariat.ediss@univ-lyon1.fr	**Mme Sylvie RICARD-BLUM** Institut de Chimie et Biochimie Moléculaires et Supramoléculaires (ICBMS) - UMR 5246 CNRS - Université Lyon 1 Bâtiment Raulin - 2ème étage Nord 43 Boulevard du 11 novembre 1918 69622 Villeurbanne Cedex Tél : +33(0)4 72 44 82 32 **sylvie.ricard-blum@univ-lyon1.fr**
INFOMATHS	**INFORMATIQUE ET MATHÉMATIQUES** **http://edinfomaths.universite-lyon.fr** Sec. : Renée EL MELHEM Bât. Blaise PASCAL, 3e étage Tél : 04.72.43.80.46 infomaths@univ-lyon1.fr	**M. Hamamache KHEDDOUCI** Université Claude Bernard Lyon 1 Bât. Nautibus 43, Boulevard du 11 novembre 1918 69 622 Villeurbanne Cedex France Tél : 04.72.44.83.69 **hamamache.kheddouci@univ-lyon1.fr**
Matériaux	**MATÉRIAUX DE LYON** **http://ed34.universite-lyon.fr** Sec. : Yann DE ORDENANA Tél : 04.72.18.62.44 yann.de-ordenana@ec-lyon.fr	**M. Stéphane BENAYOUN** Ecole Centrale de Lyon Laboratoire LTDS 36 avenue Guy de Collongue 69134 Ecully CEDEX Tél : 04.72.18.64.37 **stephane.benayoun@ec-lyon.fr**
MEGA	**MÉCANIQUE, ÉNERGÉTIQUE, GÉNIE CIVIL, ACOUSTIQUE** **http://edmega.universite-lyon.fr** Sec. : Stéphanie CAUVIN Tél : 04.72.43.71.70 Bâtiment Direction INSA Lyon mega@insa-lyon.fr	**M. Jocelyn BONJOUR** INSA Lyon Laboratoire CETHIL Bâtiment Sadi-Carnot 9, rue de la Physique 69621 Villeurbanne CEDEX **jocelyn.bonjour@insa-lyon.fr**
ScSo	**ScSo*** **https://edsciencessociales.universite-lyon.fr** Sec. : Mélina FAVETON INSA : J.Y. TOUSSAINT Tél : 04.78.69.77.79 melina.faveton@univ-lyon2.fr	**M. Christian MONTES** Université Lumière Lyon 2 86 Rue Pasteur 69365 Lyon CEDEX 07 **christian.montes@univ-lyon2.fr**

*ScSo : Histoire, Géographie, Aménagement, Urbanisme, Archéologie, Science politique, Sociologie, Anthropologie

Remerciements

Le temps s'écoule très vite tel un cheval courant à travers une fente. Pourtant, tous les moments passés au cours de ma thèse m'ont laissé des souvenirs riches et merveilleux, qui m'accompagneront tout au long de la vie. En fouillant ces images du passé, je voudrais témoigner de ma reconnaissance envers mes encadrants, mes amis et mes proches.

Je tiens avant tout à remercier mes encadrants de thèse: Aline BEL-BRUNON, Nahiène HAMILA et Simon A. LAMBERT. Aline, je garde en mémoire son écoute, son soutient et ses conseils scientifiques tout autant que sa patience et sa gentillesse lors de nos discussions. C'est grâce à elle que nous avons pu avancer et faire progresser des projets au fur et à mesure. Nahiène, j'apprécie ses connaissances et son aide professionnel dans le domaine du calcul numérique. L'expérience qu'il m'a apportée sur l'implémentation d'un solveur numérique par éléments finis de A à Z sera un trésor précieux pour mon avenir. Simon, je le remercie notamment pour ses idées ingénieuses dans l'orientation de nos recherches. Sans ses conseils, nous n'aurions pas pu voir autant de possibilités et d'opportunités. Ils sont le phare pour mon bateau, la lune pour ma nuit.

Également, je me permets de remercier mes amis présents durant la thèse. En général, j'aimerais vivement remercier tous les membres du laboratoire LaMCoS. Des activités conviviales, des équipements performants et des infrastructures solides nous permettent de dérouler nos recherches dans une ambiance agréable. En particulier, je voudrais remercier et embrasser amicalement les collègues autour de moi: Tristan DJOURACHKOVITCH, Zi Kang LOW, Tristan MAQUART, Thomas JAILIN, Alexis BONETTO, Haoming LUO, Shuai CHEN, Meng WANG, Jin HUANG, Efoé Rodrigue WALLACE, Médéric CHAUDEY, Marie GUERDER, Zhaofeng HAN, Florian MERAY, Ethel-Borel DJEUMEN NKWECHEN, Karine PETUYA, Zineb BOULAAJAJ, Alexis HINGUE, Pierre GANTIER, Julie TRICLOT, Adrien DIDIER, Ruochen ZHENG. Je retiens par cœur nos échanges académiques, nos week-ends au ski, au canoë, etc.

Je réserve une gratitude finale pour mes proches. Merci surtout à mes parents qui m'ont soutenus et qui ont consacrés tous leurs efforts pour mon éducation. L'honnêteté, la courtoisie et la fraternité sont les manières de se comporter qu'ils m'ont inculquées; la confiance, la persévérance et l'optimisme sont les caractères qu'ils m'ont transmis et appris. Grâce à eux, j'ai aujourd'hui l'énergie pour m'engager de façon affirmée dans la vie active. En plus, j'adresse mes remerciements à Daniel BRUN, mon ami qui m'a beaucoup aidé à m'intégrer en France et qui m'a appris le savoir-faire de la nature. Enfin, je dédie ma dernière reconnaissance à mon cœur pour son soutien quotidien, sa compréhension et sa compagnie.

Résumé

Le diagnostic de différentes pathologies, dont certains cancers, a longtemps été basé sur la palpation, puisqu'une tumeur est sensiblement plus rigide qu'un tissu sain. Des méthodes plus avancées et quantitatives ont été développées au cours des dernières décennies, notamment l'Elastographie par Résonance Magnétique (ERM). Cette méthode utilise l'imagerie par résonance magnétique (IRM) sur un tissu sollicité mécaniquement pour estimer les propriétés mécaniques des tissus mous. La reconstruction du module d'élasticité du tissu en ERM est souvent basée sur un modèle avec des lois de comportement simples du tissu imagé (élasticité linéaire, isotropie, homogénéité), qui pourrait être étendu à des cas plus complexes grâce à la modélisation par la Méthode des Eléments Finis (MEF) notamment. La MEF a été utilisée en ERM pour simuler la propagation des ondes mécaniques dans un tissu, pour mieux comprendre les effets de différents paramètres sur les mesures d'ERM, reconstruire la rigidité, évaluer de nouvelles méthodes d'inversion d'ERM, etc. Cependant, dans des cas inhomogènes avec interfaces complexes, la modélisation par MEF peut être particulièrement coûteuse car elle nécessite un maillage explicite de ces interfaces.

Dans ce travail, nous avons exploré, à l'aide d'un solveur EF en dynamique explicite développé dans cette thèse, le comportement d'ondes mécaniques se propageant dans un milieu linéaire, isotrope, viscoélastique et inhomogène, en vue d'une meilleure maîtrise des paramètres d'une expérimentation d'ERM. Dans le solveur a été implémentée la méthode des éléments finis étendue (XFEM); cette formulation de la MEF provient de la mécanique des fractures et a été largement utilisée au cours des deux dernières décennies pour modéliser des discontinuités comme les fissures et les inclusions.

A l'aide de l'outil numérique développé, nous avons étudié le comportement des ondes au voisinage d'une interface (oblique ou complexe), en particulier les phénomènes de réflexion et de conversion des ondes. Nous avons pu montrer que l'utilisation de la méthode XFEM réduit sensiblement les temps de calcul tout en assurant une précision équivalente, en termes de champs de déplacement et de rigidité reconstruite. Par ailleurs, nous avons abordé, par simulation, le critère d'établissement du régime stationnaire des ondes qui doit être atteint pour assurer l'enregistrement correct par IRM. Or aujourd'hui ce critère est empirique et peut influencer la qualité des données ERM. Nous avons ainsi proposé une métrique pour quantifier l'atteinte du régime stationnaire de propagation des ondes dans un tissu avec ou sans inclusion. Enfin, ces méthodes ont été mises en oeuvre sur un cas pratique d'ERM du sein. Avec les modèles du sein, nous avons évalué l'influence des paramètres expérimentaux (taille et position de l'inclusion, polarisation de l'excitation, conditions aux limites, etc.) sur l'atteinte du régime stationnaire.

MOTS CLÉS: Elastographie par résonance magnétique, méthode des éléments finis étendue, interface d'inhomogénéité, conversion des ondes, métrique de l'état stationnaire.

Abstract

The diagnosis of various pathologies, including some cancers, has long been based on palpation, since a tumor is significantly stiffer than healthy tissue. More advanced and quantitative methods have been developed over the last decades, especially the Magnetic Resonance Elastography (MRE). This method uses magnetic resonance imaging (MRI) on mechanically stressed tissue to estimate the mechanical properties of soft tissue. The reconstruction of the elasticity modulus of the tissue in MRE is often based on a model with simple behavior laws of the imaged tissue (linear elasticity, isotropy, homogeneity), which could be extended to more complex cases thanks to modeling by the Finite Element Method (FEM) in particular. FEM has been used in MRE to simulate the propagation of mechanical waves in a tissue, to better understand the effects of different parameters on MRE measurements, to reconstruct stiffness, to evaluate novel MRE inversion methods, etc. However, in inhomogeneous cases with complex interfaces, FEM modeling can be particularly costly as it requires an explicit mesh of these interfaces.

In this work, we explored, using an explicit dynamic FE solver developed in this thesis, the behavior of mechanical waves propagating in a linear, isotropic, viscoelastic and inhomogeneous medium, in order to better control the parameters of a MRE experiment. In the solver, the eXtended Finite Element Method (XFEM) has been implemented; this formulation of FEM originates from fracture mechanics and has been widely used over the last two decades to model discontinuities such as cracks and inclusions.

Using the developed numerical tool, we studied the behavior of waves in the vicinity of an interface (oblique or complex), in particular the phenomena of wave reflection and wave conversion. It has been shown that the use of the XFEM method significantly reduces the computation time while ensuring an equivalent accuracy, in terms of displacement fields and reconstructed stiffness. Furthermore, we have addressed, by simulation, the criterion of establishing the steady state of the waves which must be reached to ensure correct recording by MRI. Today, this criterion is still empirical and can influence the quality of MRE data. We have thus proposed a metric to quantify the achievement of the steady state of wave propagation in a tissue with or without inclusion. Finally, these methods were implemented on a practical case of breast MRE. Based on breast models, we evaluated the influence of experimental parameters (size and position of the inclusion, polarization of the excitation, boundary conditions, etc.) on the achievement of steady state.

KEYWORDS: Magnetic resonance elastography, extended finite element method, inhomogeneity interface, wave conversion, steady-state metric

Contents

List of Figures

List of Tables

Résumé étendu

Contexte

La palpation, qui est une action de toucher, de presser et de sentir avec les mains, est utilisée depuis longtemps dans les examens médicaux. Il s'agit d'une méthode primitive basée sur les sens tactiles et les capacités de perception de l'être humain, et sur le fait que certains tissus pathologiques présentent une plus grande rigidité que les tissus normaux environnants. Cependant, la palpation est qualitative et limitée. En effet, le diagnostic par palpation dépend largement de l'expérience du médecin et n'est applicable qu'aux organes et tissus superficiels qui peuvent être palpés à travers la peau.

Avec le développement de la technologie, de nombreuses méthodes d'imagerie médicale sont désormais disponibles pour le diagnostic médical. Les plus couramment utilisées sont les ultrasons (US) et l'imagerie par résonance magnétique (IRM). En outre, au cours des dernières décennies, une technique plus quantitative basée sur les propriétés mécaniques des tissus mous a été développée, connue sous le nom d'élastographie ou d'imagerie d'élasticité. Différente des méthodes d'imagerie médicale traditionnelles, l'élastographie vise à récupérer les valeurs spécifiques de la rigidité, conduisant à la carte de rigidité également appelée élastogramme, qui peut être plus évidente pour le diagnostic et faciliter le travail du médecin. L'élastographie basée sur l'IRM, appelée élastographie par résonance magnétique (ERM), a suscité un intérêt croissant ces dernières années. Elle est également le sujet de cette thèse de doctorat.

L'ERM a été proposée en 1995 par Muthupillai *et al.*. Comme la plupart des autres modalités élastographiques, elle se compose généralement de trois étapes consécutives. Premièrement, l'excitation mécanique, qui est généralement harmonique et de faible amplitude, est imposée pour induire une déformation des tissus. Ensuite, la technique d'imagerie IRM est appliquée pour mesurer les champs de phase ou de déplacement. Enfin, sur la base des mesures, des méthodes inverses sont utilisées pour reconstruire la rigidité des tissus (généralement le module de cisaillement). Bien que l'ERM nécessite un temps d'acquisition plus long que ses homologues, elle peut fournir des images de haute qualité en trois dimensions pour divers organes et tissus, ce qui elle rend un outil de diagnostic médical prometteur.

Dans les études d'ERM, la reconstruction de la rigidité est souvent basée sur un modèle avec des lois de comportement simples du tissu imagé (élasticité linéaire, isotropie, homogénéité), qui pourrait être étendu à des cas plus complexes grâce à la modélisation par la méthode des éléments finis (MEF). La MEF a été largement utilisée pour simuler la propagation des ondes mécaniques, ce qui peut aider à comprendre les effets de différents paramètres sur les mesures de l'ERM, à reconstruire la rigidité, à évaluer de nouvelles méthodes d'inversion de l'ERM, etc. Cependant, pour les milieux inhomogènes contenant des inclusions avec des interfaces complexes, la modélisation par MEF pourrait impliquer une tâche fastidieuse en termes de partitionnement du modèle et d'efforts de remaillage, et le maillage plus fin qui en résulte entraîne généralement des coûts de calcul importants. Dans ce contexte, une formulation de la MEF, connue sous le nom de méthode des éléments finis étendue (XFEM), est proposée dans cette thèse de doctorat comme une bonne alternative à la MEF.

XFEM a été proposée en 1999 pour modéliser la propagation des fissures en mécanique des fractures. Elle est basée sur la méthode de la partition de l'unité et étend l'espace de solution MEF classique par des fonctions d'enrichissement discontinues de sorte que certaines caractéristiques difficiles telles que la discontinuité dans la déformation ou le déplacement peuvent être reproduites avec aisance. En plus de la forte discontinuité comme le déplacement à travers la fissure, la faible discontinuité comme la déformation à travers l'interface entre deux matériaux différents peut également être modélisée par XFEM. Une autre application de XFEM consiste donc à modéliser les inhomogénéités telles que les trous et les inclusions. Grâce à une fonction level-set, l'interface de l'inhomogénéité peut être formulée mathématiquement, rendant ainsi la modélisation de l'inhomogénéité indépendante du maillage physique; les inclusions complexes peuvent être facilement intégrées dans les modèles numériques. A notre connaissance, XFEM n'a pas encore été utilisée dans les simulations d'ERM pour la modélisation des inclusions, et l'utilisation de XFEM pour modéliser les ondes mécaniques dans les milieux inhomogènes n'est pas non plus très étudiée dans la littérature.

Dans ce travail, un solveur EF fait maison, dynamique et explicite, a été développé de A à Z pour modéliser la propagation des ondes de faible amplitude dans un milieu linéaire, isotrope, inhomogène et viscoélastique, en vue d'une meilleure maîtrise des paramètres d'une expérimentation d'ERM. Les formulations XFEM ont été implémentées dans ce solveur pour l'étude de l'inhomogénéité des tissus.

Sur la base de l'outil numérique développé, nous avons tout d'abord étudié, par les modèles XFEM, MEF et analytiques, les comportements des ondes au voisinage d'une interface (oblique ou complexe), en particulier les phénomènes de réflexion et de conversion des ondes, ce qui est un sujet peu étudié dans le domaine d'ERM. Il a été montré que l'utilisation de la méthode XFEM permet de réduire sensiblement le temps de calcul tout en assurant une précision équivalente, en termes de champs de déplacement et de rigidité reconstruite. Les avantages de XFEM ont ainsi été illustrés, notamment la commodité, la précision et l'efficacité. Ensuite, nous avons abordé le critère d'établissement de l'état stationnaire des ondes dans l'ERM. En effet, l'atteinte de l'état stationnaire est importante pour assurer un enregistrement correct par IRM, alors que le jugement est aujourd'hui généralement basé sur l'expérience humaine. Une métrique a donc été proposée pour quantifier l'atteinte de l'état stationnaire de propagation des ondes dans un tissu avec ou sans inclusion. Enfin, ces méthodes ont été mises en œuvre sur un cas pratique d'ERM du sein. Sur la base de modèles de seins, nous avons évalué l'influence des paramètres expérimentaux (taille et position de l'inclusion, polarisation de l'excitation, conditions aux limites, etc.) sur l'atteinte de l'état stationnaire.

Organisation du manuscrit

Le présent manuscrit est composé de 5 différents chapitres dont les contenus sont résumés ci-dessous.

- Chapitre 1

  Dans le premier chapitre, nous nous intéressons à l'état de l'art portant sur trois disciplines : l'élastographie par résonance magnétique, la mécanique des milieux continus et la méthode des éléments finis. Dans un premier temps, les principes d'ERM sont introduits, y compris les trois étapes successives: l'excitation mécanique, l'imagerie par résonance magnétique et la reconstruction des propriétés mécaniques. Dans un deuxième temps, l'aspect mécanique est présenté. Les bases de la mécanique des milieux continus sont formulées et cela conduit à l'équation de propagation des ondes largement utilisée dans la littérature ERM. Des modèles rhéologiques sont aussi présentés pour la prise en compte de la viscoélasticité. Dans un troisième temps, la méthode des éléments finis est brièvement introduite, concernant les formulations du problème élastodynamique et la discrétisation.

- Chapitre 2

  Le deuxième chapitre présente un modèle numérique pour la propagation des ondes dans un milieu homogène et viscoélastique. Les détails de l'implémentation d'un solveur dynamique et explicite par MEF sont tout d'abord présentés, y compris les matrices critiques, les schémas d'intégration temporelle et le calcul des forces internes pour implémenter la viscoélasticité. Ensuite, pour valider le solveur fait maison, un modèle d'onde plane est proposé en deux dimensions sous l'hypothèse de déformation plane. Enfin, par une étude paramétrique, l'effet de différents paramètres sur l'atténuation des ondes est étudié.

- Chapitre 3

  Dans le troisième chapitre, tout d'abord, les bases de XFEM sont brièvement présentées, y compris la formulation et la discrétisation du problème, la méthode/fonction de level-set et la fonction d'enrichissement. Ensuite, les méthodes conventionnelles de partition d'éléments sont décrites, à la fois pour les cas bidimensionnels et tridimensionnels. Une nouvelle stratégie de partitionnement d'un élément hexaédrique 3D est également proposée. Enfin, les détails de l'implémentation numérique de XFEM sont présentés, ainsi que des exemples numériques pour démontrer les avantages de XFEM par rapport à MEF.

- Chapitre 4

  Dans le quatrième chapitre, nous présentons l'applicabilité de XFEM dans l'ERM en abordant deux problèmes de modélisation : la conversion des ondes longitudinales en ondes transversales à travers une interface plane, et un modèle d'inclusion de forme aléatoire correspondant à une application pseudo-pratique. Sont présentées avant tout les méthodes de post-traitement employées tout au long de ce chapitre, à savoir l'algorithme basé sur l'opérateur rotationnel pour l'extraction des composantes de cisaillement, et la méthode de reconstruction d'AIDE implémentée dans l'outil MREJ. Pour le premier modèle (conversion d'ondes à travers une interface plane), nous introduisons d'abord un travail théorique développé pour le problème de la réflexion et de la transmission d'ondes planes à travers une interface plane oblique entre deux matériaux viscoélastiques, et les formulations de la conversion de mode sont données. Ensuite, nous présentons le modèle numérique par XFEM/MEF et une étude paramétrique est réalisée à des fins de comparaison. Pour le deuxième modèle, à savoir celui de l'inclusion de forme aléatoire, les résultats de la rigidité reconstruite sont comparés entre les modèles XFEM et MEF pour souligner les avantages de la méthode XFEM.

- Chapitre 5

  Enfin, une métrique de l'état stationnaire est proposée pour mesurer quantitativement le régime permanent d'un milieu inhomogène ou homogène soumis à une excitation mécanique harmonique et d'amplitude faible, et des modèles numériques basés sur XFEM sont utilisés pour étudier cette métrique. Tout d'abord, la définition de la métrique de l'état stationnaire est donnée, et deux modèles carrés, conçus pour étudier cette métrique et son seuil séparant l'état stationnaire de l'état transitoire, sont étudiés. Ensuite, cette métrique est appliquée à quatre modèles de seins, basés sur différentes options techniques pour réaliser l'ERM du sein, et une étude paramétrique est réalisée pour évaluer l'influence de différentes configurations d'ERM sur l'état stationnaire.

Conclusion

En résumé, dans cette thèse, nous avons modélisé l'expérience d'ERM d'un point de vue numérique, et nous avons particulièrement abordé les questions d'inhomogénéité des tissus et d'excitation de l'ERM.

Un modèle numérique a été développé de A à Z sous forme d'un solveur dynamique et explicite par la méthode des éléments finis. Ce solveur nous a permis de modéliser la propagation d'une onde mécanique de faible amplitude dans un milieu linéaire, isotrope, localement homogène et viscoélastique. En utilisant ce solveur, nous avons étudié un modèle viscoélastique homogène avec des conditions aux limites de symétrie, et illustré la propagation d'une onde longitudinale plane et d'une onde transversale plane. La comparaison des résultats de la MEF aux résultats analytiques a confirmé la validation de notre modèle numérique. Sur la base du modèle d'ondes de cisaillement planes, une étude paramétrique a également été réalisée et l'effet de différents paramètres sur l'atténuation des ondes a été illustré ; il a été démontré que la quantité adimensionnelle de la viscosité relative était capable de décrire l'atténuation des ondes.

Pour approfondir l'étude de l'inhomogénéité des tissus dans les simulations d'ERM, la méthode XFEM a été proposée et ses formulations ont été implémentées dans le solveur. En outre, une nouvelle stratégie de partition 3D pour les éléments hexaédriques a été présentée. En comparant les résultats d'un modèle XFEM et d'un modèle MEF, que ce soit en 2D ou en 3D, nous avons pu constater la cohérence, et avons également montré les avantages de XFEM, à savoir sa commodité, sa précision et son efficacité.

Sur la base de l'implémentation de XFEM, nous avons réalisé deux études pour examiner l'applicabilité de XFEM dans l'ERM. Dans la première étude, le problème de la conversion d'une onde plane à travers une interface d'inhomogénéité oblique plane a été abordé. Un modèle XFEM et un modèle MEF ont donc été proposés pour les simulations numériques et un modèle analytique basé sur un travail précédent a également été utilisé. Par une étude paramétrique, l'effet de différents facteurs sur la conversion des ondes a été révélé. En outre, la comparaison des trois modèles a également montré la meilleure précision du modèle XFEM par rapport au modèle MEF. Dans la deuxième étude, une application pseudo-pratique a été proposée. En effet, une inclusion de forme aléatoire a été modélisée à la fois par XFEM et MEF, et une méthode de reconstruction a été appliquée pour étudier les valeurs spécifiques du module de cisaillement. Il a été démontré que les deux modèles ont produit des résultats de rigidité similaires. XFEM peut être encore plus précis que MEF en comparaison des valeurs de référence, tout en utilisant le même maillage pour différentes inclusions et en prenant moins de temps CPU. Ces résultats ont mis en évidence les avantages de XFEM par rapport à MEF. À notre connaissance, c'est la première fois que XFEM a été utilisée pour la modélisation d'inclusions dans des études d'ERM.

Enfin, une métrique a été proposée pour mesurer l'état stationnaire du modèle/phantom dans les études d'ERM. Des analyses numériques ont suggéré que la valeur 0,01 est une bonne estimation du seuil qui sépare l'état stationnaire de l'état transitoire. En utilisant cette métrique de l'état stationnaire, nous avons poursuivi l'étude des modèles de poitrine avec différentes configurations d'excitation et une étude paramétrique a été réalisée. L'effet de différents facteurs sur la stabilité du système a été illustré, tels que l'inclusion, le type d'excitateur et la fréquence d'excitation.

Introduction

Palpation, which is an action of touching, pressing and feeling by hands, has been used in medical examination for a long time. It is a primitive method based on tactile senses and perceptional abilities of human being, and on the fact that some pathological tissues present greater stiffness than surrounding normal tissues. However, palpation is qualitative and limited. Indeed, the diagnosis by palpation is largely dependent on doctor experience and is only applicable to the superficial organs and tissues that can be palpated through the skin.

With the development of technology, numerous medical imaging methods are now available for medical diagnosis. The most commonly used ones may include ultrasound (US) and magnetic resonance imaging (MRI). In addition, over the past decades, a more quantitative technique based on mechanical properties of soft tissues was developed, known as elastography or elasticity imaging (EI). Different from traditional medical imaging methods, elastography aims at recovering the specific values of stiffness, leading to the stiffness map also called elastogram, which can be more obvious for diagnosis and facilitate doctor work. The MRI-based elastography, referred to as magnetic resonance elastography (MRE), has particularly gained more and more attention in recent years. It is also the subject of this PhD thesis.

MRE was proposed in 1995 by Muthupillai *et al.*. Like most other elastographic modalities, it typically consists of three consecutive steps. Firstly, the mechanical excitation, which is generally harmonic and of small amplitude, is imposed to induce tissue deformation. Secondly, the MRI imaging technique is applied to measure the phase or displacement fields. Finally, based on the measurements, inverse methods are used to reconstruct the tissue stiffness (usually of shear modulus). Although MRE requires longer acquisition time than its counterparts, it can provide images of high quality in three-dimensions for various organs and tissues, thus making itself become a promising medical diagnostic tool.

In MRE studies, the stiffness reconstruction is often based on a model with simple behavior laws of the imaged tissue (linear elasticity, isotropy, homogeneity), which could be extended to more complex cases thanks to modeling by the finite element method (FEM). FEM has been widely used to simulate mechanical wave propagation, which can further help in understanding the effects of different parameters on MRE measurements, reconstructing stiffness, evaluating novel MRE inversion methods, etc. However, for inhomogeneous media containing inclusions with complex interfaces, modeling by FEM could imply a burdensome task in terms of model partitioning and remeshing efforts, and the resulting finer mesh usually leads to large computational costs. In this context, a formulation of FEM, known as the extended finite element method (XFEM), is proposed in this PhD thesis as a good alternative to FEM.

XFEM was proposed in 1999 for modeling crack propagation in fracture mechanics. It is based on the partition of unity method and extends the classical FEM solution space by discontinuous enrichment functions so that some challenging features such as discontinuity in strain or displacement can be reproduced with ease. In addition to the strong discontinuity like displacement across the crack, the weak discontinuity like strain across the interface between two different materials can also be modeled by XFEM. Another application of XFEM thus consists in modeling the inhomogeneities such as holes and inclusions. By a level set function, the interface of inhomogeneity can be mathematically formulated, thus making the inhomogeneity modeling independent from the physical mesh; complex inclusions can be readily integrated into numerical models. To the best of our knowledge, XFEM has not been used in MRE simulations for inclusion modeling yet, and employing XFEM to model mechanical waves in inhomogeneous media is not either much investigated in the literature.

In this work, a homemade FE solver, dynamic and explicit, was developed from scratch to model the small-amplitude wave propagation in a linear, isotropic, inhomogeneous and viscoelastic medium, for the purpose of better controlling the parameters of a MRE experiment. The XFEM formulations were implemented in this solver for the study of tissue inhomogeneity.

Based on the developed numerical tool, we first investigated, by XFEM, FEM and analytical models, the wave behaviors in the vicinity of the interface (oblique or complex), especially the phenomena of wave reflection and wave conversion, which is an issue of not many concerns in the MRE field. It has been shown that the use of the XFEM method significantly reduces the computation time while ensuring an equivalent accuracy, in terms of displacement fields and reconstructed stiffness. The advantages of XFEM have thus been illustrated, including the convenience, accuracy and efficiency. Then, we addressed the criterion of establishing steady state of waves in MRE. Indeed, reaching the steady state is important to ensure correct recording by MRI, while the judgement is today generally based on human experience. A metric was thus proposed to quantify the achievement of steady state of wave propagation in a tissue with or without inclusion. Finally, these methods were implemented on a practical case of breast MRE. Based on breast models, we evaluated the influence of experimental parameters (size and position of the inclusion, polarization of the excitation, boundary conditions, etc.) on the achievement of steady state.

This manuscript is composed of 5 chapters and structured as follows.

In the first chapter, we focus on the state of the art in three disciplines: magnetic resonance elastography, continuum mechanics and finite element method. In a first step, the principles of MRE are introduced, including the three successive steps: mechanical excitation, magnetic resonance imaging and reconstruction of mechanical properties. In a second step, the mechanical aspect is presented. The basics of continuum mechanics are formulated and this leads to the wave propagation equation widely used in the MRE literature. Rheological models are also presented to take into account the viscoelasticity. In a third step, the finite element method is briefly introduced, concerning the formulations of the elastodynamic problem and the discretization.

The second chapter presents a numerical model for wave propagation in a homogeneous, viscoelastic medium. The details of the implementation of a dynamic and explicit FE solver are first presented, including critical matrices, time integration schemes, and the calculation of internal forces to implement viscoelasticity. Then, to validate the home-made solver, a two-dimensional plane wave model is proposed under the assumption of plane deformation. Finally, by a parametric study, the effect of different parameters on the wave damping is studied.

In the third chapter, firstly, the basics of XFEM are briefly presented, including the problem formulation and discretization, the level-set method/function, and the enrichment function. Secondly, conventional methods of element partitioning are described, for both the two-dimensional and three-dimensional cases. A new strategy for partitioning a 3D hexahedral element is also proposed. Thirdly, details of the numerical implementation of XFEM are presented, along with numerical examples to demonstrate the advantages of XFEM over classical FEM.

In the fourth chapter, we present the applicability of XFEM in MRE by addressing two modeling problems: the conversion of longitudinal waves into transverse waves through a plane interface, and a random-shape inclusion model corresponding to a pseudo-practical application. First, the post-processing methods used throughout this chapter are presented, namely the algorithm based on the rotational operator for the extraction of shear components, and the AIDE reconstruction method implemented in the MREJ tool. For the first problem (wave conversion across a plane interface), we first introduce a theoretical model developed for the problem of reflection and transmission of plane waves across an oblique plane interface between two viscoelastic materials, and the mode conversion formulations are given. Next, the numerical model by XFEM/FEM is presented and a parametric study is performed for comparison. For the second problem, namely the random shape inclusion model, the reconstructed stiffness results are compared between the XFEM and FEM models to highlight the advantages of the XFEM method.

Finally, in the fifth chapter, a steady-state metric is proposed to quantitatively measure the steady state of an inhomogeneous or homogeneous medium subjected to harmonic and small-amplitude mechanical excitation, and XFEM-based numerical models are used to study this metric. First, the definition of the steady-state metric is given, and two square models, designed to study this metric and its threshold separating the steady state from the transient state, are studied. Then, this metric is applied to four breast models, based on different excitation options to perform breast MRE, and a parametric study is performed to evaluate the influence of different MRE configurations on the steady state.

At the end of this manuscript, conclusions and prospects are given.

Chapter 1

State of the art

This chapter contains three parts, the first one presenting the physical principles of magnetic resonance elastography, the second one introducing the relevant mechanical concepts and the last one elaborating the numerical method by finite element.

Contents

1.1 Magnetic Resonance Elastography

Most techniques and products were developed thanks to human observation and creativity, and were also based on our ancestors wisdom and experience. For example, the hammer is considered to be inspired by the woodpecker, the gyroscope inspired by the revolution of Earth and the camera inspired by the eye, etc [WOO 77].

In the domain of disease diagnosis, this statement holds as well. Indeed, around 50 000 years ago, human being began to evolve finer tactile senses and greater perceptional abilities, which allowed our ancestors to pay attention to the origins of pain and disease. They especially discovered the tool of “palpation”: manually pressing soft tissues and carefully feeling the reactions could provide them with rich diagnostic information [HIR 17]. This practice is still useful and can be performed as preliminary diagnosis at present. Actually, it is based on the fact that pathological changes of soft tissues such as cancer, inflammation and fibrosis are generally accompanied by altered mechanical properties. Numerous diseases thus present greater stiffness than other surrounding normal tissues.

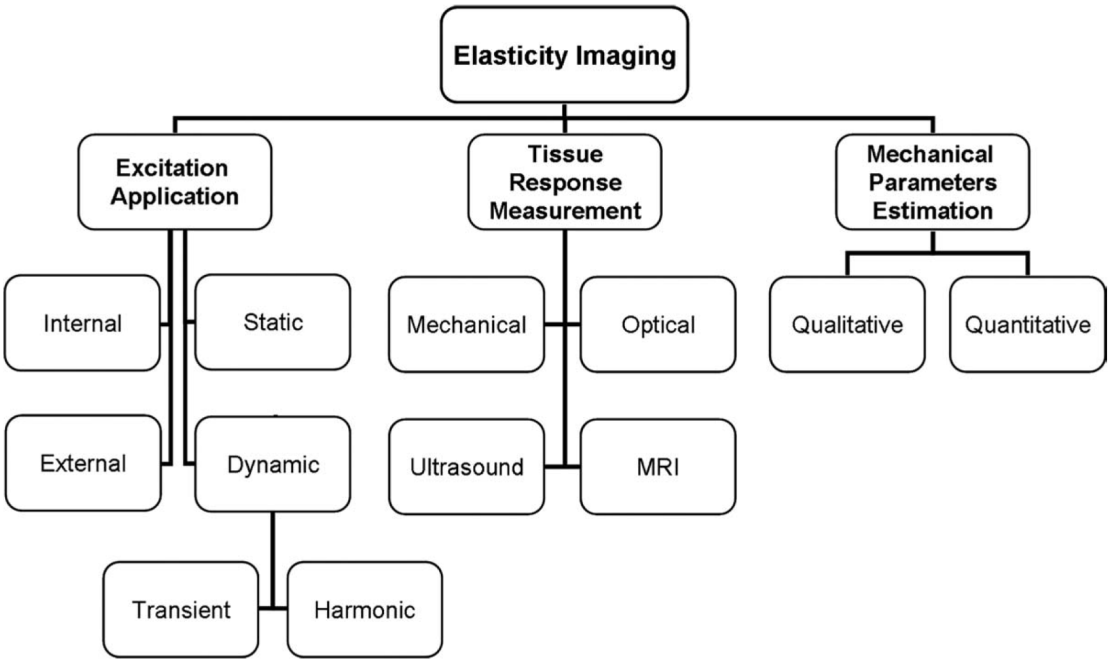

Figure 1.1: A classification of Elasticity Imaging approaches based on the three steps: (1) excitation application, (2) tissue response measurement and (3) mechanical parameters estimation. Source: [MAR 10]

However, the palpation tool is rather qualitative and subjective as it greatly depends on doctor experience. Furthermore, it is only available for certain organs and tissues that can be palpated through the skin. In this context, medical imaging has emerged as a powerful alternative to palpation and afterwards led to Elasticity Imaging (EI) or “elastography”:

deform soft tissue *in vivo* by mechanical excitation, measure the deformation information by medical imaging technique and reconstruct tissue mechanical property [MAR 10]. Likewise, the technique of elastography is based on application of a force causing tissue deformation similar to palpation pressing, and detection of the response to that force similar to palpation sensing. Differently, thanks to advanced medical imaging techniques and developed elasticity reconstruction methods, elastography can provide precise values of tissue mechanical properties, resulting in the stiffness map called “elastogram” and making itself quantitative and objective. A rough classification of EI approaches based on the three steps can be found in Fig.1.1. More details can be found in the section 1.1.1.

In terms of elastographic imaging techniques, several modalities have been developed including Magnetic Resonance Imaging (MRI), UltraSound (US) imaging, X-ray imaging, optical and acoustic signals, among others [SAR 11]. The most prominent ones are considered to be ultrasound-based and MRI-based; the latter one called Magnetic Resonance Elastography (MRE) is also the subject of this section and this thesis.

MRE was invented at the Mayo Clinic and first proposed in 1995 as a new elasticity imaging modality by Muthupillai *et al.* in a publication of SCIENCE [MUT 95]. It has received since then lots of academic attentions and become more and more popular in the last two decades, as shown in Fig.1.2. Compared to other numerous elastographic techniques, despite longer acquisition time, MRE has better capacity in providing 3D images of tissue stiffness and can be applied for various organs and tissues such as liver, muscle, lung, spleen, kidney, pancreas, uterus, thyroid, heart, brain, breast, etc [VEN 14, GLA 12].

In the following, the technical details and the state of the art of MRE will be presented, including its three main components: mechanical excitation, MRI imaging technique and inversion algorithm for recovering mechanical properties. In each part, some background knowledge and comparisons with other alternatives are first briefly introduced in order to provide readers with a global viewpoint on each step of MRE.

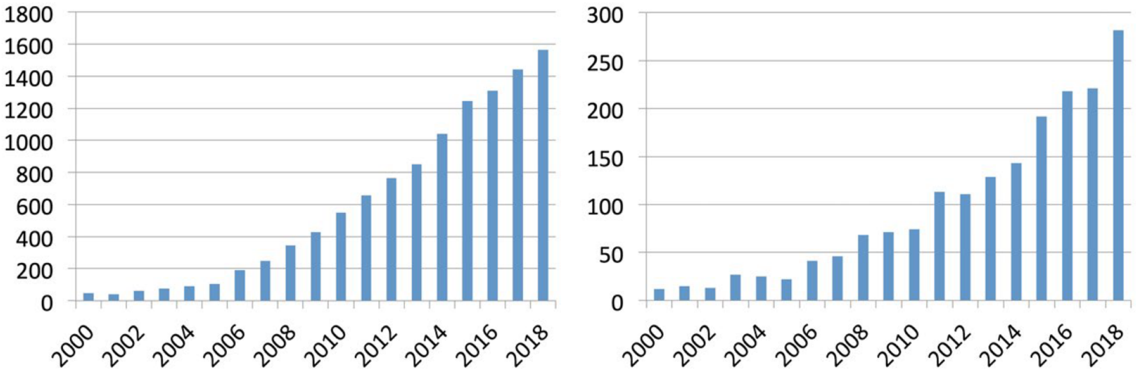

Figure 1.2: Number of publications per year returned by Web of Science searches on “elastography” (left, 13 973 total) and “magnetic resonance elastography” or “MR elastography” (right, 2 157 total). Source: [MAN 21]

1.1.1 Mechanical excitation

The first step can be done in a number of ways, depending on the excitation source and the excitation temporal characteristics. For instance, the excitation may be produced either through the internal source coming from respiration or cardiac pulsation [WIL 82, MAI 02], or through the external source from artificial actuator [XU 07, KRU 08, BOH 18]. In terms of stimulus temporal characteristics, it can also be classified as static (or quasi-static) [OPH 91] or dynamic [LER 90, MUT 95, CAT 99, GNA 21].

In static methods, tissue is slowly compressed and the displacement distribution is then measured; since the strain distribution is related to the stress distribution, the elastic moduli can be derived from the mechanical constitutive equations. However, in reality, the strain itself is often used as the estimation of stiffness, which means low strain corresponding to high stiffness and vice versa [FAT 03]. In dynamic methods, an external vibration system is used to introduce time-harmonic vibrations at one or several acoustic frequencies (usually below 200 Hz) into human body [GLA 12]; since the propagation of displacement has its own rules, the elastic moduli can be completely characterized by the wave equation.

While the above methods have been developed and have contributed a lot to the field of EI for many years, the most common form of MRE imaging is still dynamic MRE using external actuators [GLA 12].

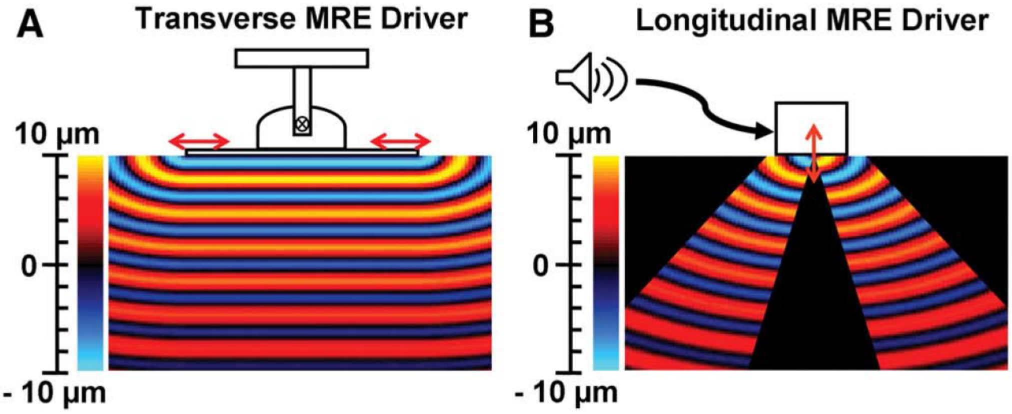

Figure 1.3: Comparison of transverse and longitudinal MRE drivers. (A) A direct shear driver applies cyclic transverse vibrations (shown as red double-headed arrows) to the surface of an object. A planar shear wave is generated within the homogeneous medium. (B) A longitudinal driver generates longitudinal vibrations (shown as the red double-headed arrow) to the surface of an object. A cone-like hemispherical shear wave field is generated in the homogeneous medium. The color bars indicate the particle shear displacement (in micrometers) along the horizontal direction. (positive motion is assumed from the left to the right). Source: [YIN 08]

As illustrated in Fig.1.3, two polarization (vibration) directions are possible for MRE dynamic actuator/driver: transverse and longitudinal. Transverse driver is characterized by shear wave (S-wave) whose polarization is perpendicular to propagation, while longitudinal driver generates pressure wave (P-wave) whose polarization is parallel to propagation. However, shear waves are much preferred in MRE as in other elasticity imaging modalities. Indeed, on the one hand, S-waves in soft tissues propagate with a relatively low velocity (1-10 m/s) in comparison with P-waves (around 1540 m/s) [GLA 12]. This means that S-waves are characterized by shorter wavelength under the same frequency, which provides more wave details considering tissue size. On the other hand, as reported by Sarvazyan *et al.* [SAR 95], bulk moduli K, related to volume change and P-wave, are approximately of the same magnitude for all soft tissues, while shear moduli G, related to shape change and S-wave, vary to a much greater extent ($G = 10^{-2} \sim 10^{-6}K$). This means that shear properties of tissues are more desirable for elasticity imaging than bulk properties as they lead to higher contrast, and thus transverse excitation is widely applied.

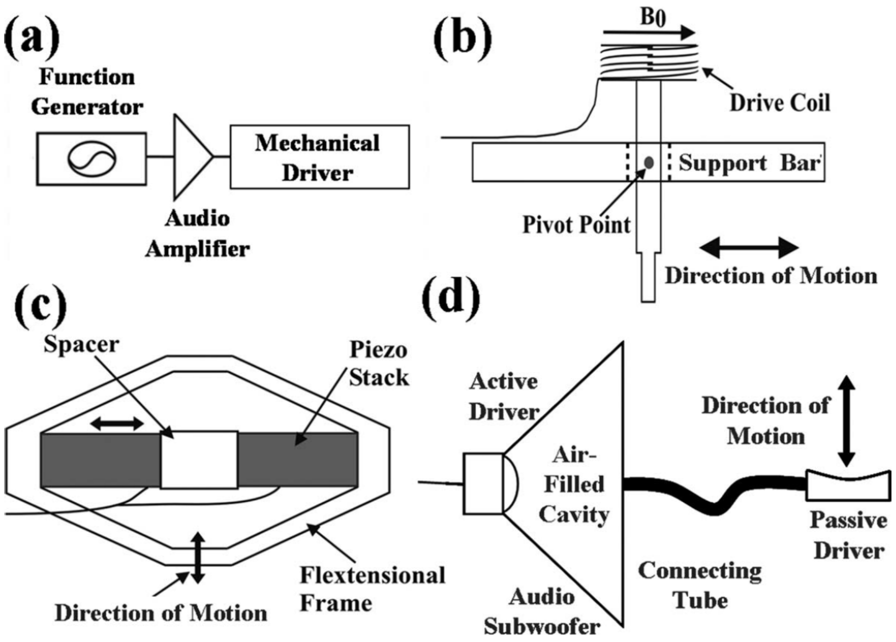

Figure 1.4: External driver systems. (a) Block diagram of the external driver setup. Examples of typical mechanical drivers include (b) electromechanical, (c) piezoelectric-stack, and (d) pressure-activated driver systems. Source: [MAR 10]

In terms of the design of external driver system, figure 1.4(a) presents its general structure by a block diagram. In fact, a signal generator triggered by and synchronized to the MR pulse sequence (which will be discussed in the next subsection) creates the electrical signal. After being amplified by an audio amplifier, the signal is fed into the mechanical driver that finally generates dynamic vibration. A few driving mechanisms have been developed over the years, among which three of the most widely used systems are schematically illustrated in Fig.1.4(b-d). Figure 1.4(b) presents an electromechanical driver based on Lorentz force and the magnetic field of the main MRI magnet. Figure 1.4(c) shows a piezoelectric stack driver system depending upon the piezoelectric property of certain materials. Finally, another commonly used system as presented in Fig.1.4(d) works also via Lorentz force. However, the force is produced by the static magnetic field from the permanent magnets of acoustic speakers. For more details, readers are recommended to refer to [TSE 09, MAR 10, GNA 21].

1.1.2 Magnetic Resonance Imaging

Once the mechanical stress has been introduced into human tissue, the next critical step consists in measuring the response (strain). There are mainly four basic measurement methods as shown in Fig.1.1: optical, mechanical, US and MRI.

Optical method is the earliest investigated method for measuring tissue response to applied stress. Figure 1.5 presents one of the early works in 1952 which used visible light (stroboscope) to measure mechanical wave propagation and to determine tissue elasticity and viscosity [VON 52]. Mechanical method uses mechanical sensors such as pressure sensors and accelerometers for the measurement [SAR 98]. In comparison with the precedent two methods, US has been used more widely for elasticity imaging. The term “elastography” was first introduced by Ophir *et al.* [OPH 91] to refer to a technique where tissue deformation response to external compression is measured by ultrasound, providing qualitative description of tissue stiffness. More US-based EI methods include such as Transient Elastography (TE) [CAT 99, SAN 03] and Supersonic Shear Imaging (SSI) [BER 04]. In terms of our subject MRI, it was implemented for assessment of cardiac motion early in 1988 [ZER 88]; later in 1995, the MRE method utilizing MRI technique was developed and formally proposed by Muthupillai *et al.* [MUT 95].

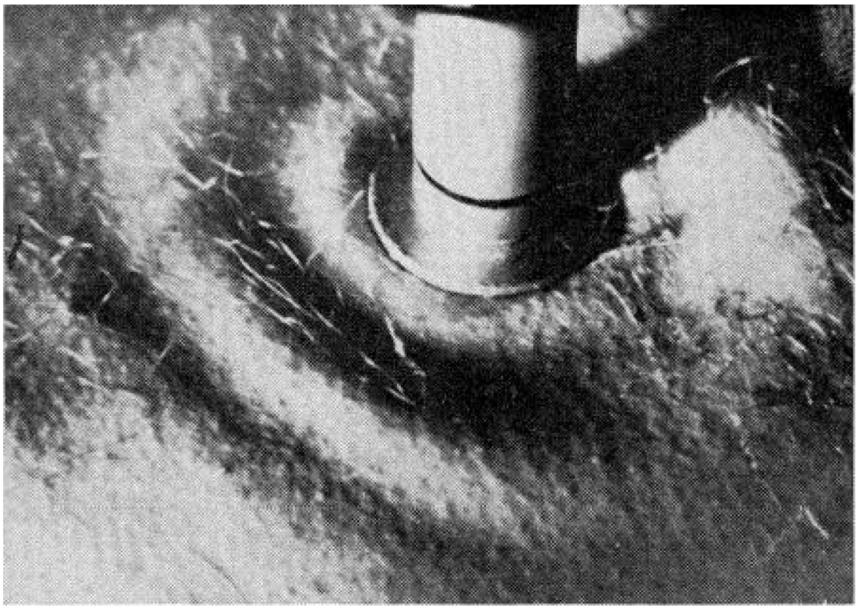

Figure 1.5: Stroboscopic picture of the wave propagation around a vibrating piston on the thigh (frequency 64 Hz, piston area 5.3 cm^2). Source: [VON 52]

Table 1.1 lists and compares several elasticity imaging methods. As can be seen, MRE is differentiated from the other methods mainly by its use of MRI instead of ultrasound technique for measurement of tissue deformation. MRI technique is characterized by the advantage of providing 3D scan data while the others are generally only capable of 2D measurement. However, MRI acquisition time is much longer and the device is more expensive, which results in the worse availability of MRI scanners than that of ultrasound scanners in clinical applications [SAR 11]. In terms of the US-based EI methods, even though they are faster and less expensive, they are also limited by the need of a suitable acoustic window for measurement and by the limited penetration in tissue.

In the following, the fundamentals of MRI technique will be briefly presented. More details can be found in references such as [VLA 03, HIR 17].

Table 1.1: Comparison of different elasticity measurement and imaging methods. Source: [SAR 11]

Method	**Excitation**		**Measurement**	**Advantages**
	Time Course	**Physical Stress**		
Elastography	Quasi-static	Mechanical	Ultrasound	Full strain and modulus images Estimate elastic nonlinearity Conventional US scanner
Mechanical Imaging	Static/Dynamic	Mechanical	Pressure	Simple, inexpensive Estimate elastic nonlinearity
MRE	Dynamic	Mechanical	MRI	3D displacement Large organ imaging
Transient Elastography	Dynamic	Mechanical	Ultrasound	Simple, inexpensive Compact package
Supersonic Shear Imaging	Dynamic	Radiation Force	Ultrasound	Full elasticity images Viscoelasticity characterization

1.1.2.1 Physical basis: Nuclear Magnetic Resonance

The physical phenomenon of Nuclear Magnetic Resonance (NMR) plays the key role in MRI technique. It was first discovered by Rabi *et al.* in 1938 [RAB 38] and Rabi was awarded the Nobel Prize in Physics in 1944 for this work. It describes the fact that the nuclei in a strong constant magnetic field can be manipulated by another dynamic magnetic field, thus producing an electromagnetic signal.

NMR roughly consists of three steps:

(1) *Application of a static magnetic field*

Since hydrogen represents about 63 % of atoms of human body, they are the most commonly used nuclei in MRI. We hence consider the hydrogen nuclei ^1H (protons) in a static magnetic field $\boldsymbol{B}_0$ typically with a strength of 1.5 or 3 T in clinical MRI applications.

In quantum mechanics, proton is one of the elementary particles which have an intrinsic property: *spin*. Spin is in fact an angular momentum $\boldsymbol{S}$ and can be described by a spin quantum number S. For proton, $S = \frac{1}{2}$ and $|\boldsymbol{S}| = \sqrt{S(S+1)}\hbar = \sqrt{\frac{3}{4}}\hbar$ where $\hbar$ is the Planck constant. Since microscopically $\boldsymbol{B}_0$ defines a quantization axis for $\boldsymbol{S}$, we can

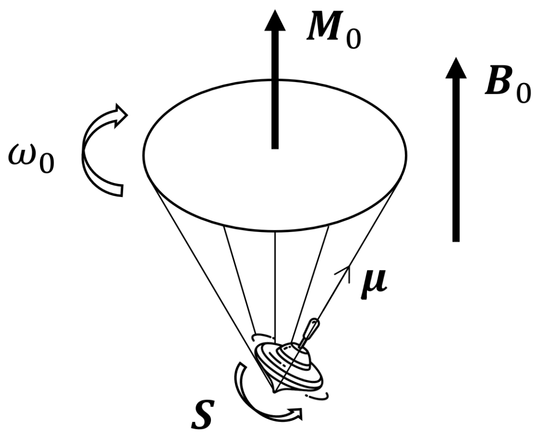

Figure 1.6: Larmor precession of proton. Proton spin is illustrated by a spinning-top. Magnetic moment $\boldsymbol{\mu}$ is caused by spin $\boldsymbol{S}$. Precession of $\boldsymbol{\mu}$ at Larmor frequency ω_0 results from the existence of static magnetic field $\boldsymbol{B}_0$. The population difference of two proton energy-states leads to a macroscopic magnetization $\boldsymbol{M}_0$ aligned with $\boldsymbol{B}_0$.

assume that $\boldsymbol{B}_0$ is aligned with the z-axis of coordinate system, namely $\boldsymbol{B}_0 = (0,0,B_0)^T$ and the projection of $\boldsymbol{S}$ onto $\boldsymbol{B}_0$ leads to $S_z = \pm\frac{1}{2}\hbar$ while the other two components S_x and S_y remain uncertain. A magnetic moment $\boldsymbol{\mu}$ is generated by proton spin and reads:

$$\boldsymbol{\mu} = \gamma_n \boldsymbol{S} \tag{1.1}$$

where γ_n is the *gyromagnetic ratio* and equal to $2\pi \cdot 42.58\ MHz/T$ for proton.

The z-component (or called longitudinal component) of $\boldsymbol{\mu}$ can thus be written as:

$$\mu_z = \pm\frac{1}{2}\gamma_n \hbar \tag{1.2}$$

while the other two components μ_x and μ_y, again, remain undetermined and form an arbitrary, transverse magnetization component in the xy-plane.

The potential energy of a magnetic moment in a magnetic field is defined as:

$$E = -\boldsymbol{B}_0 \cdot \boldsymbol{\mu} = -B_0 \mu_z \tag{1.3}$$

Combining with Eq.1.2, the precedent Eq.1.3 implies that two states are possible and the parallel alignment (↑↑) of μ_z with $\boldsymbol{B}_0$ (which means $\mu_z = +\frac{1}{2}\gamma_n \hbar$) results in lower energy-state than the antiparallel alignment (↑↓) of μ_z with $\boldsymbol{B}_0$ (which means $\mu_z = -\frac{1}{2}\gamma_n \hbar$). At human body temperature of 37 $°C$, the population of protons in parallel state slightly outnumbers that in excited antiparallel state. Given that μ_z of protons in two possible states cancel each other out and so do the transverse components μ_x and μ_y in the xy-plane, the imbalance of population hence gives rise to a small net magnetization aligned with $\boldsymbol{B}_0$:

$$\boldsymbol{M}_0 = \delta N \rho\, |\mu_z|\, \hat{\boldsymbol{z}} \tag{1.4}$$

where $\delta N = (N_{\uparrow\uparrow} - N_{\uparrow\downarrow})/N$ is the excess population of protons, ρ is the average proton density and $\hat{\boldsymbol{z}}$ is the unit vector along the z-axis.

The above generation of resultant magnetization $\boldsymbol{M}_0$ from magnetic moments can be understood and illustrated by Fig.1.6. The precession of the magnetic moment ($\boldsymbol{\mu}$) of an object (proton here) about an external magnetic field ($\boldsymbol{B}_0$) is also called *Larmor precession*. The angular frequency of the precession is called *Larmor frequency* and satisfies:

$$\omega_0 = \gamma_n B_0 \tag{1.5}$$

(2) *Application of RF pulse causing magnetization precession*

In the equilibrium state, $\boldsymbol{M}_0$ is in fact aligned with the static field $\boldsymbol{B}_0$ and doesn't precess. We define a new reference frame rotating about z-axis with Larmor frequency ω_0 and designate it by primed symbols (x'-y'-z'). It is found that if a second magnetic field $\boldsymbol{B}_1$ rotating at ω_0 in the transverse xy-plane is added, the magnetization $\boldsymbol{M}$ will flip towards $\boldsymbol{B}_1'$ in the reference system and present a spiral Larmor precession in the static laboratory system; the nuclear protons are in fact absorbing magnetic energy and described as being *in resonance*, from where the name NMR comes. Assuming $\boldsymbol{B}_1$ aligned with the x'-axis ($\boldsymbol{B}_1$ can thus be written as $\boldsymbol{B}_1' = B_1\hat{\boldsymbol{x}}'$), the time evolution of $\boldsymbol{M}$ in the rotating frame is characterized by:

$$\begin{aligned}\frac{\partial \boldsymbol{M}'}{\partial t} &= \gamma_n \boldsymbol{M}' \times \boldsymbol{B}_1' \\ &= \gamma_n B_1 (\boldsymbol{M}' \times \hat{\boldsymbol{x}}')\end{aligned} \tag{1.6}$$

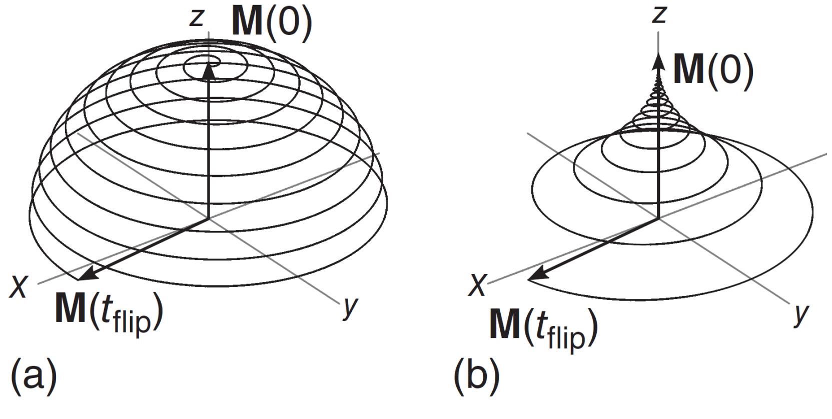

Figure 1.7: Time evolution of magnetization as seen from the laboratory frame. The black line traces the tip of $\boldsymbol{M}$(t) over time. (a) During a 90°-pulse, the longitudinal equilibrium magnetization is tipped toward the transverse plane. The combination of precession at Larmor frequency and the tipping induced by the $\boldsymbol{B}_1$ pulse causes the magnetization to spiral on a spherical shell from the z-axis toward the xy-plane. (b) After the $\boldsymbol{B}_1$ pulse, the magnetization precesses at Larmor frequency. The transverse component of $\boldsymbol{M}$ decays with time constant T_2^* , whereas the longitudinal component relaxes back toward the equilibrium value $\boldsymbol{M}(0)$ with time constant T_1. Source: [HIR 17]

This manipulation of tilting the longitudinal magnetization from its equilibrium position into the transverse plane can be illustrated by Fig.1.7. In fact, any flip angle α_f can be achieved depending on the additional field strength and duration; it is calculated as $\alpha_f(t) = \omega_F t = \gamma_n B_1 t$. The applied oscillating magnetic filed is time-varying and thus accompanied by an electric field according to Maxwell's equations. This pulsed electromagnetic field is also referred to as a *radiofrequency* (RF) pulse. The RF pulse making $\alpha_f = 90°$ is called 90°-pulse, as shown in Fig.1.7(a).

(3) *Magnetization relaxation leading to emission of NMR signals*

The induced precession of magnetization is in fact a representation of external ejection of energy. Once the RF pulse is removed, the dissipative interaction between excited spins and their environment will prevent the tipped magnetization precession and make it relax to the original equilibrium state $\boldsymbol{M}_0$, as illustrated in Fig.1.7(b).

Assuming the decomposition of total magnetization $\boldsymbol{M}(t)$ into a longitudinal component $\boldsymbol{M}_{||}(t) = M_{||}(t)\hat{\boldsymbol{z}}$ and a transverse component $\boldsymbol{M}_{\perp}(t)$:

$$\boldsymbol{M}(t) = \boldsymbol{M}_{||}(t) + \boldsymbol{M}_{\perp}(t) \tag{1.7}$$

The time evolution of the longitudinal component can be described by a differential equation proportional to the deviation from the equilibrium state:

$$\frac{\partial \boldsymbol{M}_{||}}{\partial t} = \frac{1}{T_1}(\boldsymbol{M}_0 - \boldsymbol{M}_{||}) \tag{1.8}$$

where T_1 is the time constant for longitudinal component relaxation.

For transverse component, a similar differential equation and its solution are given by:

$$\frac{\partial \boldsymbol{M}_{\perp}}{\partial t} = -\frac{1}{T_2}\boldsymbol{M}_{\perp} \tag{1.9}$$

$$\boldsymbol{M}_{\perp}(t) = \boldsymbol{M}_{\perp}(0) \cdot e^{-\frac{t}{T_2}} \tag{1.10}$$

where T_2 is the time constant for transverse component relaxation. Sometimes, the alternative T_2^* is used considering the effect of $\boldsymbol{B}_0$ inhomogeneity. Generally, the decay of transverse magnetization is always faster, i.e. $T_2^* < T_2 < T_1$. It is basically during this process that the precessing transverse magnetization induces a sinusoidal voltage in a detection coil (also referred to as *receive coil*), resulting in the NMR electromagnetic signal.

Finally, the Bloch equation is capable of combing and describing together the precession process and the relaxation effects:

$$\frac{d\boldsymbol{M}}{dt} = \gamma_n \boldsymbol{M} \times \boldsymbol{B} + \frac{1}{T_1}(M_0 - M_{||})\hat{\boldsymbol{z}} - \frac{1}{T_2}\boldsymbol{M}_{\perp} \tag{1.11}$$

with the total magnetic field $\boldsymbol{B}$.

1.1.2.2 Signal to image: spatial encoding

Although the NMR signal received in this way is helpful, for example, in providing information on chemical compounds in a sample and determining the global properties of an object, it is not yet capable of generating medical images. In this subsection, we will briefly introduce the methods for encoding spatial information in order to convert NMR signals to images.

Before the introduction, it may be crucial to understand the concept of *phase* of precession/MRI signal, frequently mentioned in MRI technique. As previously presented, the precession of transverse magnetization $\boldsymbol{M}_\perp$ induces a sinusoidal voltage signal $S(t)$ in a receive coil and can be written as:

$$S(t) = S_0 \sin((\omega_0 + \delta\omega)t) \exp\left(-\frac{t}{T_{\text{decay}}}\right) \tag{1.12}$$

with amplitude S_0, Larmor frequency ω_0, the offset $\delta\omega$ from ω_0 due to supplementary magnetic field and the relaxation time T_{decay} equal to T_2 or T_2^*. The phase of signal can be measured by isolating the desired $\delta\omega$ and expressed as:

$$\phi = \arctan\left(\frac{\text{Im}(S)}{\text{Re}(S)}\right) \tag{1.13}$$

This phase represents also the angle between $\boldsymbol{M}_\perp$ and the x'-axis of the rotating reference system, as illustrated in Fig.1.8. It can be seen that after the application of RF pulse, the magnetization vectors (represented by arrows) of all isochromats (ensemble of spins with the same precession frequency) are flipped and in phase (Fig.1.8b). Once the pulse is removed, they begin to precess about $\boldsymbol{B}_0$ at their individual frequencies $\omega_p(x,y,z)$ and dephase (being out of phase) after a certain time, causing the resultant transverse magnetization $|\boldsymbol{M}_\perp|$ to decrease (Fig.1.8c). This dephasing is natural since precession frequencies ω_p $(= \omega_0 + \delta\omega)$ are slightly different from one isochromat to another and these differences are attributed to field strength deviations resulting from B_0 inhomogeneity or other effects. Thereby, we have in general $\delta\omega \ll \omega_0$ under unaffected circumstance.

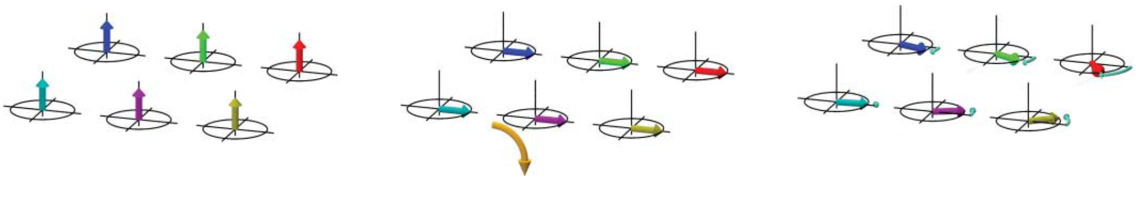

(a) **(b)** **(c)**

Figure 1.8: Illustration of precession phase, from the rotating-frame perspective. The arrows correspond to six isochromats at different positions within the imaging plane with different precession frequencies. The direction of the static magnetic field ($\boldsymbol{B}_0$) is upward. (a) Equilibrium. (b) Excitation of 90°-pulse. (c) Free precession. Source: [HIR 17]

However, the distribution of ω_p or $\delta\omega$ can be more regular and predictable by imposing additional magnetic fields. This is exactly the basis of spatial encoding of NMR signals to locate their positions of origin. It is usually composed of three steps for the aim of 3D encoding. During each step, a *gradient* magnetic field is applied and added to the original field $\boldsymbol{B}_0$. Figure 1.9 illustrates the distribution forms of the three gradient fields all parallel to z-axis and characterized by magnitude linear with one coordinate.

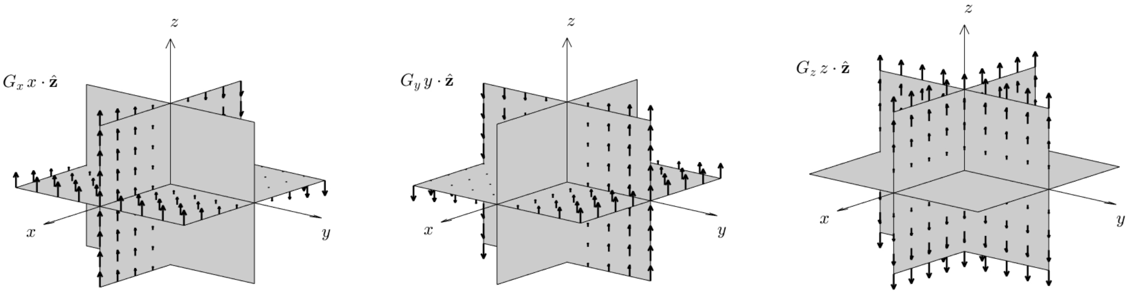

(a) field $\boldsymbol{G}_x = G_x x \cdot \hat{\mathbf{z}}$ **(b)** field $\boldsymbol{G}_y = G_y y \cdot \hat{\mathbf{z}}$ **(c)** field $\boldsymbol{G}_z = G_z z \cdot \hat{\mathbf{z}}$

Figure 1.9: Magnetic fields parallel to the z-axis with magnitude being linearly dependent on (a) x-coordinate by a gradient G_x, (b) y-coordinate by a gradient G_y, and (c) z-coordinate by a gradient G_z. Arrow designates direction and its length denotes strength.

(1) *Slice selection*

The first step is the application of a gradient filed, say $\boldsymbol{G}_z (= G_z z \cdot \hat{\mathbf{z}})$, while the RF pulse is being emitted. The magnitude of resultant field $\boldsymbol{B}$ thus becomes:

$$\boldsymbol{B}(x,y,z) = (B_0 + G_z z)\hat{\mathbf{z}} \tag{1.14}$$

And the frequencies ω_p of protons are no more uniform but dependent on positions:

$$\omega_p(x,y,z) = \gamma_n B(x,y,z) = \gamma_n (B_0 + G_z z) \tag{1.15}$$

Assuming that the frequency of RF pulse is ω_{RF}, the precedent Eq.1.15 implies that only spins at location z_0 satisfying $\omega_p(x,y,z_0) = \omega_{\mathrm{RF}}$ can flip, relax and send NMR signals. In such a way, a plane or a slice is "selected" for further imaging; this process is thus called *slice selection*.

Nevertheless, in reality, the RF pulse is usually designed to contain multiple frequencies over a range $(\omega_{\mathrm{RF}} - \delta, \omega_{\mathrm{RF}} + \delta)$ in order to excite spins within a slice in the range $(z_0 - \Delta z, z_0 + \Delta z)$ with $\Delta z = \frac{\delta}{\gamma_n G_z}$.

(2) *Phase encoding*

As illustrated in Fig.1.8(b), all magnetization vectors are in phase right after the RF excitation. The phase in plane z_0 can be hence considered as zero. The second step consists in applying a phase-encoding gradient field in the imaging plane, say $\boldsymbol{G}_y (= G_y y \cdot \hat{\mathbf{z}})$, for a limited time period T_{PE}. This causes a similar position-dependent field $\boldsymbol{B}(x,y,z) = (B_0 + G_y y)\hat{\mathbf{z}}$ and ω_p accordingly becomes $\omega_p(x,y,z) = \gamma_n (B_0 + G_y y)$. The frequency offset $\delta\omega$ $(= \gamma_n G_y y)$ will hence intervene during T_{PE} and lead to a phase offset:

$$\phi(x,y,z) = \int_0^{T_{\mathrm{PE}}} \delta\omega d\tau = \gamma_n G_y T_{\mathrm{PE}} \cdot y \qquad (1.16)$$

Equation 1.16 implies that after time T_{PE} the protons in the same row (along x-axis) perpendicular to the gradient direction (along y-axis) all keep having the same phase. This step is thereby called *phase encoding*.

(3) *Frequency encoding*

Following the previous in-plane encoding step, the next encoding step applies the gradient whose direction is perpendicular to slice selection and phase-encoding directions, i.e. $\boldsymbol{G}_x (= G_x x \cdot \hat{\boldsymbol{z}})$. This field is applied while the NMR signals are sampled by receive coil and similarly causes a position-dependent frequency offset $\delta\omega$ $(= \gamma_n G_x x)$. The phase evolution from the moment when $\boldsymbol{G}_x$ is activated can be expressed as:

$$\begin{aligned} \phi(x,y,z,t) &= \gamma_n G_y T_{\mathrm{PE}} \cdot y + \int_0^t \delta\omega d\tau \\ &= \gamma_n (G_y T_{\mathrm{PE}} \cdot y + G_x \cdot x \cdot t) \end{aligned} \qquad (1.17)$$

Recalling by Eq.1.12 and Eq.1.13 that a sinusoidal voltage signal can be measured in the receive coil due to magnetization relaxation. They can be combined to an equivalent formulation: $S(t) = S_0 \exp(i\phi)$, and the sum of all individual signals gives the actual detected signal:

$$\tilde{S}(t) = \int\int\int_{z_0-\Delta z}^{z_0+\Delta z} S_0(x,y,z) \exp(i\phi(x,y,z,t)) dz\, dy\, dx \qquad (1.18)$$

where $S_0(x,y,z)$ is the magnitude of signal from position (x,y,z).

The phases are hence coupled with NMR signals. Defining two parameters $k_y = \gamma_n G_y T_{\mathrm{PE}}$ and $k_x(t) = \gamma_n G_x \cdot t$, the signal can be expressed in frequency domain as:

$$\tilde{S}(k_x,k_y) = \int\int\int_{z_0-\Delta z}^{z_0+\Delta z} S_0(x,y,z) \exp(i(k_x x + k_y y)) dz\, dy\, dx \qquad (1.19)$$

It implies that a 2D k-space can be sampled and acquired sequentially by means of different sampling configurations of k_x and k_y. And from this k-space $\tilde{S}(k_x,k_y)$, the signal magnitude $S_0(x,y,z)$ can be recovered by applying an inverse Discrete Fourier Transform (DFT), leading to a 2D image space of signal magnitude. Equation 1.19 hereby becomes the basis of virtually all MRI experiments.

Finally, by adjusting the slice selection gradient, different slices can be measured, leading to the 3D MRI technique. As the complex data points in k-space actually correspond to spatial frequencies, this final step is called *frequency encoding* or *readout*.

1.1.2.3 Application in MRE: motion encoding

While the gradients introduced previously, $\boldsymbol{G}_x$, $\boldsymbol{G}_y$ and $\boldsymbol{G}_z$, have realized the 3D imaging functionality of MRI technique, they are not capable of encoding the tissue movement into received NMR signals, which is the basic requirement of MRE. In this subsection, the implementation of MRI into MRE by means of motion encoding gradient (MEG) magnetic fields will be briefly presented.

The phase shift ϕ has been introduced and calculated before. It can be summarized and formulated as:

$$\phi(t) = \gamma_n \int_0^t \boldsymbol{G}_r(\tau) \cdot \boldsymbol{r}(\tau) d\tau \tag{1.20}$$

where $\boldsymbol{G}_r(t)$ is the gradient field superimposed on static field $\boldsymbol{B}_0$ and $\boldsymbol{r}(t)$ is the position of nuclear spins. For complex motion, the position can be described by:

$$\boldsymbol{r}(t) = \boldsymbol{r}_0 + \boldsymbol{\xi}(\boldsymbol{r}, t) \tag{1.21}$$

where $\boldsymbol{r}_0$ is the equilibrium position and $\boldsymbol{\xi}(\boldsymbol{r}, t)$ is the vector of displacement in terms of $\boldsymbol{r}_0$. As widely applied in MRE, the time-harmonic motion underwent by nuclear spins is given by:

$$\boldsymbol{\xi}(\boldsymbol{r}, \theta) = \boldsymbol{\xi}_0 \cos(\boldsymbol{k} \cdot \boldsymbol{r} - \omega t + \theta) \tag{1.22}$$

where $\boldsymbol{k}$ is the wavenumber vector, ω is the angular frequency of harmonic excitation, θ is the initial phase shift of wave, and $\boldsymbol{\xi}_0$ is the displacement amplitude.

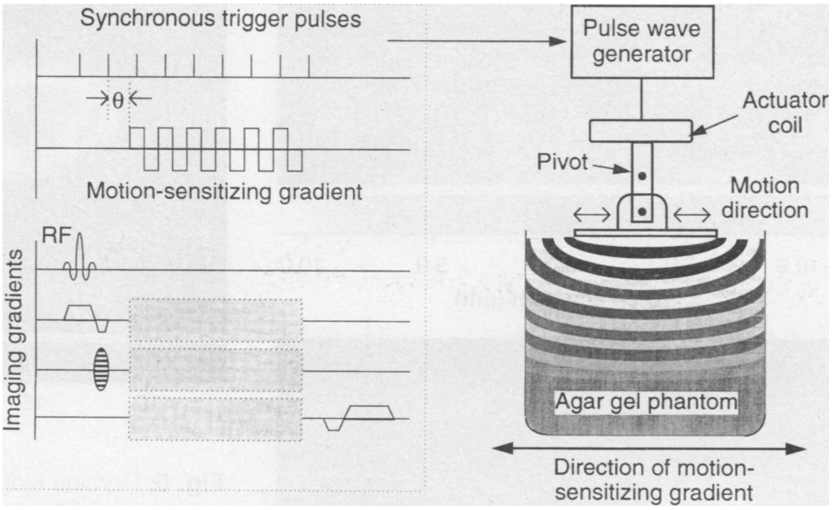

Figure 1.10: Experimental system for observing acoustic strain waves with MRI. A wave form motion encoding gradient (MEG) is incorporated into imaging sequences to sense harmonic motion. Source: [MUT 95]

In order to encode the motion information into the signal phase ϕ, several gradients can be designed following certain principles. A common choice is a trapezoid form gradient, as illustrated in Fig.1.10. Since it is characterized by equal areas between positive and negative fields and cycling property, which means $\int_0^t \boldsymbol{G}_r(\tau) d\tau = \boldsymbol{0}$, the phase offset observed in NMR signal can thus be given by [MUT 95]:

$$\begin{aligned}\phi(\boldsymbol{r},\theta) &= \gamma_n \int_0^{t=NT} \boldsymbol{G}_r(\tau)\cdot\xi_0\cos(\boldsymbol{k}\cdot\boldsymbol{r}-\omega\tau+\theta)d\tau \\ &= \frac{2\gamma_n NT(\boldsymbol{G}\cdot\xi_0)}{\pi}\sin(\boldsymbol{k}\cdot\boldsymbol{r}+\theta)\end{aligned} \tag{1.23}$$

where N is the number of gradient cycles and T is the period of harmonic excitation. This equation implies the connection between the detected phase shift ϕ and the motion amplitude ξ_0 in position $\boldsymbol{r}$ and with the wave phase θ. For a certain wave phase shift, it is the basis of MRE for converting MRI phase images to displacement images. Since the signal phase is more important and used, instead of the signal amplitude in most other MRI applications, MRE is a *phase-contrast* technique.

However, in real application, only one wave phase shift θ is not sufficient for retrieving wave phase images ϕ and further elasticity reconstruction. The MEG gradient is hence repeated by adjusting its activation time to capture multiple signal phases ϕ at different time points over one harmonic cycle, thus leading to several snapshots of wave displacements (four or eight snapshots are common).

1.1.3 Reconstruction methods

After the application of mechanical motion and the imaging of wave displacements, the last step of MRE consists in deriving tissue stiffness from the captured displacement data by solving inverse problems. Indeed, it is the underlying mechanical properties that regulate tissue motion and wave propagation; the elastography reconstruction is thus considered as an inverse problem. Typically, the reconstruction methods can be categorized into *direct* or *iterative* methods. And recently, inversion methods based on artificial neural network (ANN) has been studied as a promising alternative. As presented before in section 1.1.1, the shear modulus is more appropriate for tissue elastography than bulk modulus, thus chosen as the reconstructed target for basically all methods.

In the following, we present the three types; their respective principles, advantages, disadvantages and several example methods will be briefly introduced, leading to the start of the art of MRE reconstruction which is one of topics in this work. For more thorough details concerning an overview of different methods, see [DOY 12, HON 16, FOV 18b]; for more details about elasticity or mechanical behaviors, see section 1.2.

1.1.3.1 Direct methods

As the name suggests, direct methods are developed to retrieve stiffness by directly solving the wave equations. With the assumptions of linear (visco-)elasticity, isotropy, local homogeneity, quasi-incompressibility and small deformation, which are in fact good approximations for soft tissue in MRE, the wave equation can be converted to the Helmholtz equation for shear modulus [MAN 21]:

$$G^* = -\frac{\rho\omega^2\boldsymbol{u}}{\nabla^2\boldsymbol{u}} \tag{1.24}$$

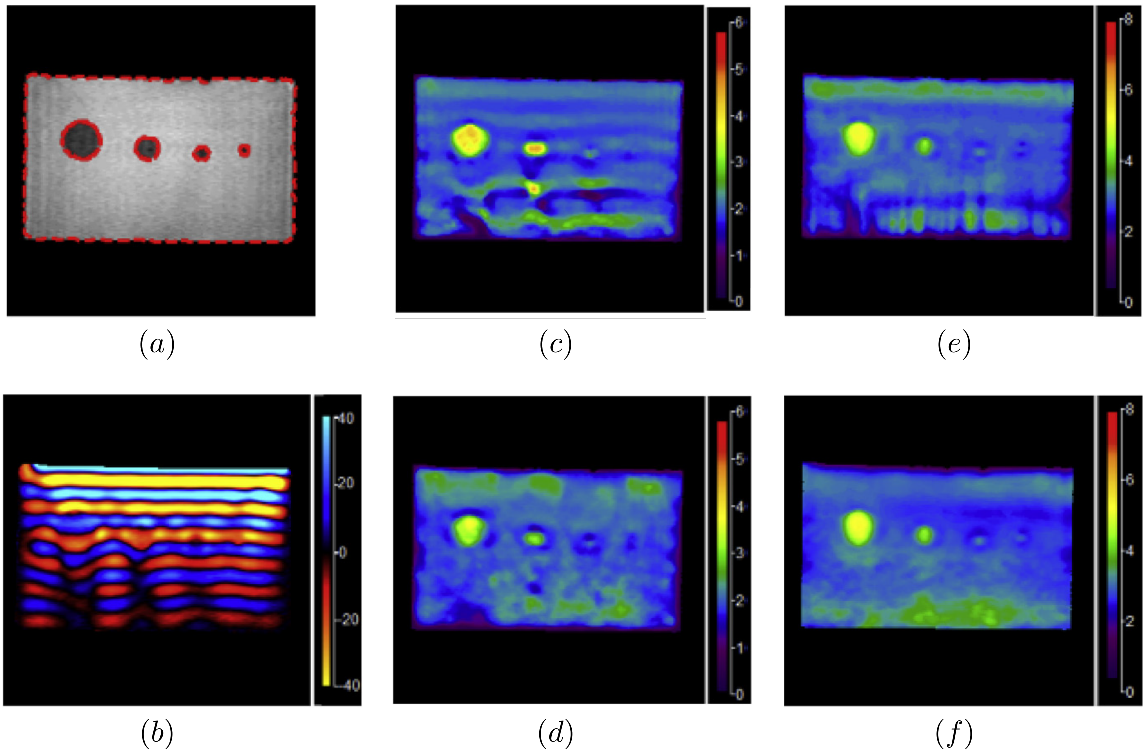
(a) (c) (e)

(b) (d) (f)

Figure 1.11: Elasticity reconstruction using MREJ tool. (a) magnitude, (b) wave, (c) AIDE, (d) AIDE with directional filtering, (e) LFE, (f) LFE with directional filtering. Source: [XIA 13]

where G^* is the complex shear modulus, ρ is the density of tissue (generally considered as 1000 kg/m^3), ω is the angular frequency of excitation, $\boldsymbol{u}$ is the complex displacement field and ∇^2 means $\nabla \cdot \nabla$ which is the divergence of the gradient, namely the Laplace operator Δ.

This equation is commonly employed in many direct methods. While being simple and direct, these methods are largely dependent on data quality since the derivatives of displacement have to be computed, as can be seen in Eq.1.24. Indeed, the measured wave displacements inherently contain noise due to the finite signal-to-noise ratio (SNR) of MR imaging, and the differentiation contributes to amplify the noise. Common methods to reduce the noise include bandpass or frequency-based filtering [MAN 03], and polynomial-fitting approaches such as applying the Savitzky-Golay filter [MAN 01].

Moreover, the wave fields usually comprise two components as aforementioned: transverse and longitudinal. The displacement caused by longitudinal waves is a confounding factor for shear modulus reconstruction and have to be removed. Although ignoring its effect was a common practice in early researches, this approach is basically no more applied nowadays due to the significant errors in reconstructed stiffness [PAR 06]. Alternatively, some filtering methods are used, such as applying a high-pass filter to remove longitudinal waves, and applying a curl-operator to the displacement fields. The latter was proposed by Sinkus *et al.* [SIN 05]. It takes advantage of the quasi-incompressible property of tissue which means the Poisson's ratio extremely close to 0.5 and the divergence-free condition on the displacements: $\nabla \cdot \boldsymbol{u} = 0$. Therefore, the displacement $\boldsymbol{u}$ in Eq.1.24 can be regarded as its curl $\nabla \times \boldsymbol{u}$.

The most frequently used direct methods may consist of Local Frequency Estimation (LFE) and Algebraic Inversion of the Differential Equation (AIDE). The former, presented by Manduca *et al.* [MAN 96, MAN 01], is based on the shear modulus-wave relation: $c_s = \sqrt{\mu/\rho}$. Local estimates of shear modulus μ can be made from local estimates of frequency computed with a bank of wavelet filters. The latter, proposed by Oliphant *et al.* [OLI 01], consists in performing inversion of a system of differential equations of mechanical motion, more or less similar to the Eq.1.24. For this Helmholtz equation, a least-square polynomial fitting is used to compute the spatial derivatives and a regularization technique is applied to prevent division by zero. These two direct methods can be accessed, for example, through MREJ which is a Java implementation of ImageJ plugin [XIA 13].

Figure 1.11 illustrates the reconstruction by the MREJ tool for a benchmark phantom. The benchmark and its dataset come from the *MRE/Wave* demo developed by Mayo Clinic, freely provided to MRE community [GRI 06]. This phantom is composed of 1.5% agar gel with four 10% bovine cylindrical inclusions whose diameters range from 5 to 25 *mm* [LI 10, MAN 03, MAH 20]. Transverse waves are generated from the top by harmonic excitation at 100 *Hz*. The FOV (field of interest) is 20 *cm* × 20 *cm* and the spatial resolution is 256 × 256. 8 snapshots are taken during each period. The reference value is 2.9 *kPa* for the background and 6.4 *kPa* for the inclusions. Both AIDE and LFE algorithms are applied, with/without directional filtering. It turns out that the background is well reconstructed, while the inclusions are generally underestimated with $3 \sim 4$ *kPa*.

1.1.3.2 Iterative methods

Different from direct methods, iterative methods are based upon iterating in force the minimization/optimization computing, which can be formulated by:

$$\min_{G^*} ||\boldsymbol{u}_c - \boldsymbol{u}_m||_X \tag{1.25}$$

where $\boldsymbol{u}_c$ is the calculated displacement, $\boldsymbol{u}_m$ is the measured displacement and $||\cdot||_X$ denotes certain norm.

Basically, an initial distribution of shear modulus is predetermined. During each iteration, the forward problem along with boundary conditions is solved for predicted displacement field $\boldsymbol{u}_c$. The updated shear modulus can then be acquired by applying certain optimization algorithms in order to minimize the error between simulated displacements and measured displacements $||\boldsymbol{u}_c - \boldsymbol{u}_m||$. This forward-optimization process is repeated till some stopping criteria are reached.

Obviously, the iterative methods are much more computationally expensive than direct methods and dependent on the forward model with boundary conditions. However,

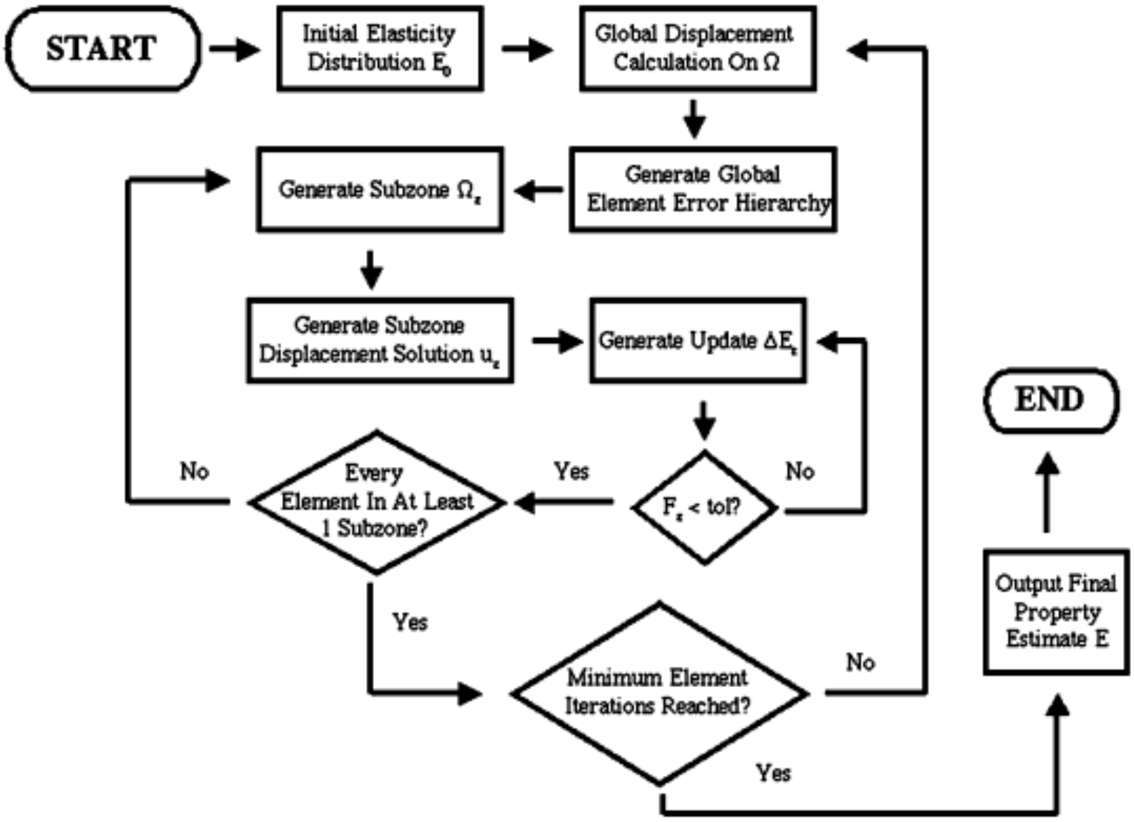

Figure 1.12: Flowchart of the two-dimensional subzone method. Source: [VAN 99]

they are less sensitive to measured data quality and have potential for producing better predictions.

The forward problem can be addressed with the help of some numerical discretization techniques such as finite difference and finite element method. For the minimization process, several approaches are generally employed such as gradient based [OBE 03, OBE 04], Gauss-Newton [KAL 96, DOY 00, MIG 03] and Levenberg-Marquardt algorithms [MAR 63, ESK 08, HON 16]. Besides, some regularization techniques, such as Tikhonov regularization [KAL 96], are widely utilized to obtain smoother results, by adding derivatives of stiffness to optimization function.

Among numerous iterative methods, the most outstanding method may be the subzone method, proposed by Van Houten *et al.* [VAN 99, VAN 01]. Like the practices just presented, this method has used finite elements for equation discretization, Gauss-Newton algorithm for optimization and Levenberg-Marquardt for regularization. It is characterized by its performing optimization in overlapping regions, or subzones constituting the global domain. Figure 1.12 presents the flowchart of the subzone inversion algorithm.

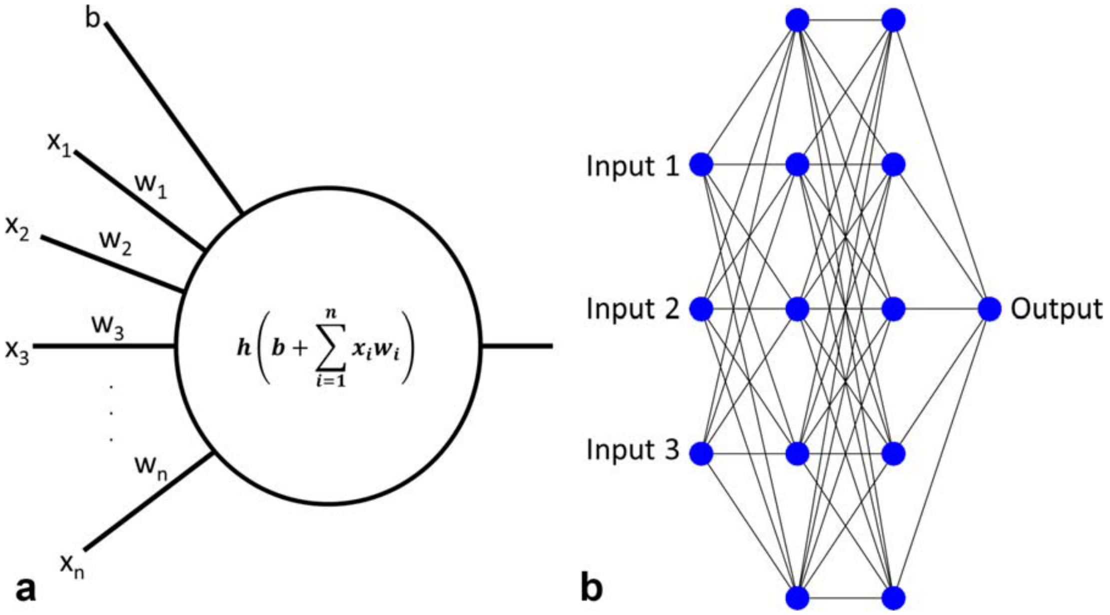

Figure 1.13: Illustration of neuron (a) and MLP model (b). Source: [MUR 18]

1.1.3.3 ANN-based methods

Both the above methods have their advantages and disadvantages: direct methods are simple and rapid, but sensitive to data quality; iterative methods are more accurate but time-consuming. Besides, they are generally based on the assumptions that materials are linear, (visco-)elastic, isotropic, locally homogeneous and quasi-incompressible, which indeed limits the MRE application. In recent years, however, with the development of artificial neural network (ANN), more advanced, ANN-based inversion methods have been studied.

To the best of our knowledge, Murphy *et al.* from Mayo Clinic were the first to develop ANN in MRE reconstruction methods [MUR 18]. The model of feedforward ANN with fully connected layers, which is also known as multilayer perceptron (MLP), was applied. An example of MLP model is shown in Fig.1.13; each layer is composed of several nodes, and each node representing a neuron connects its preceding layer to succeeding layer by a nonlinear function. In this pioneer work, 3 hidden layers of 24 neurons per layer with a tanh transfer function were used. 2D simulated data sets were generated based on 5×5 patches with 2 mm isotropic voxels, and 4 snapshots were taken during each period of 60 Hz motion. Single or multiple point-sources were randomly placed within the patches, and sinusoidal displacement without attenuation was assumed. For each sample, a homogeneous stiffness was chosen from a uniform distribution ranging from 0.1 to 10 kPa. The features fed into the MLP model were real and imaginary parts of the first harmonic of displacements of each sample. Noises were also added to test the model performance. It turned out that this new approach performed well and presented a good correlation with traditional inversion methods.

Later, Solamen *et al.* [SOL 18] employed another ANN model, known as convolu-

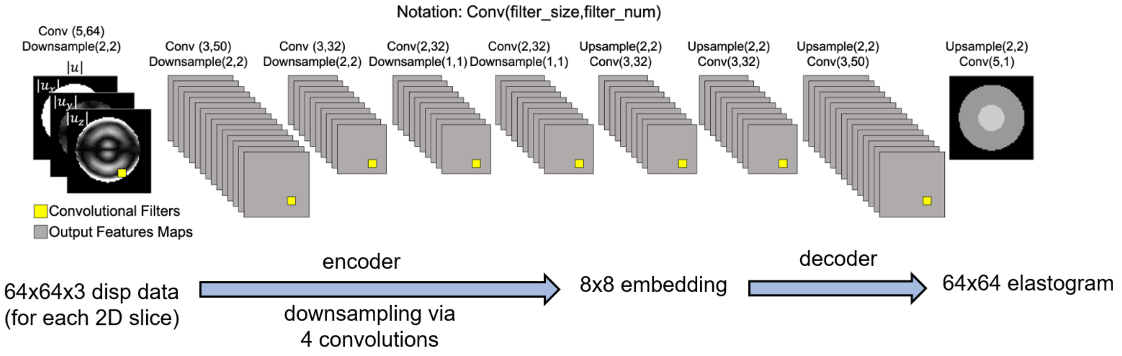

Figure 1.14: Illustration of CNN model. Source: [SOL 18]

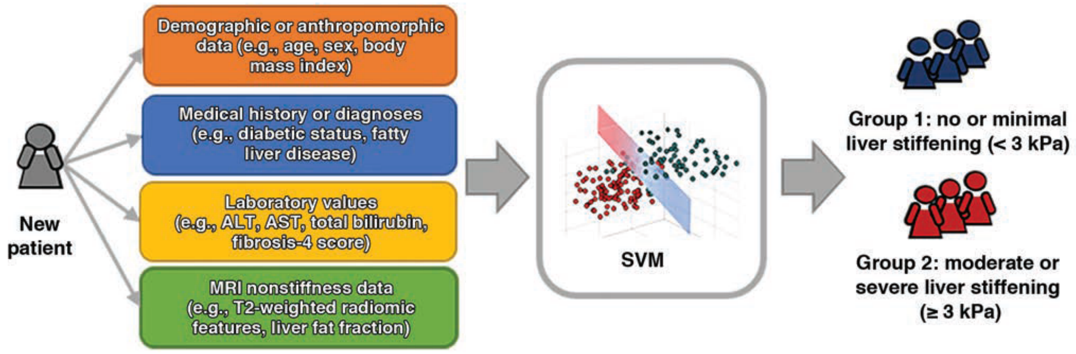

Figure 1.15: Illustration of SVM model. Source: [HE 19]

tional neural network (CNN). This model is in fact more appropriate for image processing. It manipulates image data by a convolutional kernel to automatically extract features and requires much less parameters than MLP model (since updated parameters in CNN are values of kernels, while parameters in MLP are weights and biases of neurons). In this work, as shown in Fig.1.14, 3D $64 \times 64 \times 3$ displacement data for each 2D slice were given as input to CNN model. The images were first downsampled by 4 convolutions, leading to a 8×8 embedding, then upsampled by 3 convolutions to obtain the final estimate of a 64×64 stiffness map. No pooling process was conducted.

Particularly, He *et al.* [HE 19] used a classical ANN model, known as support vector machine (SVM), to perform a 2-class classification job. Real patient records were used as features to train the model. As shown in Fig.1.15, a hyperplane is learned in SVM to partition the high-dimensional space, thus leading to 2 classes representing different states of liver stiffening.

Most recently, Murphy *et al.* [MUR 20] and Scott *et al.* [SCO 20] from Mayo Clinic published their ANN framework based on CNN model (however, the CNN structure details cannot be found). In particular, local inhomogeneity was considered in the latter work by simulating shear wave within an inhomogeneous medium based on a coupled harmonic oscillators (CHO) model. CHO allows to generate numerous synthetic samplings in a short time, while neglecting P-wave and mode conversion at interface. This was the primary limitation, as discussed in [SCO 20], and expected to be overcome by modeling full Navier equations of motion, like applying the finite element method. Indeed, this constitutes one of the prospects that we expect to address by the XFEM model introduced in this PhD thesis.

1.2 Continuum mechanics

From the previous section 1.1, it can be found that MRE is one of numerous elastography modalities which are based on mechanics theories and medical imaging techniques. Mechanical principles play a key role not only in the first step of excitation application, but also in the third step of stiffness reconstruction. Therefore, it is vital to have a deeper look at this background. In the following, we will firstly introduce some basic knowledge in the domain of continuum mechanics, especially that of linear elasticity. From these introductions, we will see how can be derived the basic equation of wave propagation that is widely used in elastography. Then, the theory of viscoelasticity will be presented, which is a general property of human tissue and also the basis of our research. For more details, several reference books are recommended such as [LAN 86, ROY 99, SAD 09] for elasticity and [LAK 98, SIM 06, CAR 07, CHR 12] for viscoelasticity.

1.2.1 From elasticity to wave propagation

This subsection mainly describes the elasticity theory in the case of linear, isotropic and homogeneous materials subject to small deformation. It briefly presents the basic concepts including strain, stress, constitutive law (Hooke's law) and equilibrium equation (Newton's law). From these bases, the widely used formulation of motion or wave propagation is obtained. Finally, the strain energy is introduced.

1.2.1.1 Strain

When external loading is applied, elastic solids will accordingly respond. The responses are usually represented as motions including rigid-body motions and extensional and shearing deformations. We are only concerned with the deformations, since the rigid-body motions contain constant displacement and rotation making no contribution to the strain field which is related to relative displacement of particles of a continuum body.

Considering the small deformation hypothesis, a two-dimensional, infinitesimal, rectangular element can be used to develop the strain-displacement relations, as illustrated in Fig.1.16. This rectangular element ($ABCD$) with dimension dx by dy deforms to a form of rhombus ($A'B'C'D'$) with certain displacements. By taking point A at location (x, y) as the reference, some displacement components and deformations can be explicitly expressed such as $u_x(x,y)$ and $u_y(x,y)$, as shown in the figure.

The *extensional* or *normal strain* in a certain direction is defined as the change in length per unit length along the same direction, and can be calculated, for example in the x-direction in Fig.1.16, by:

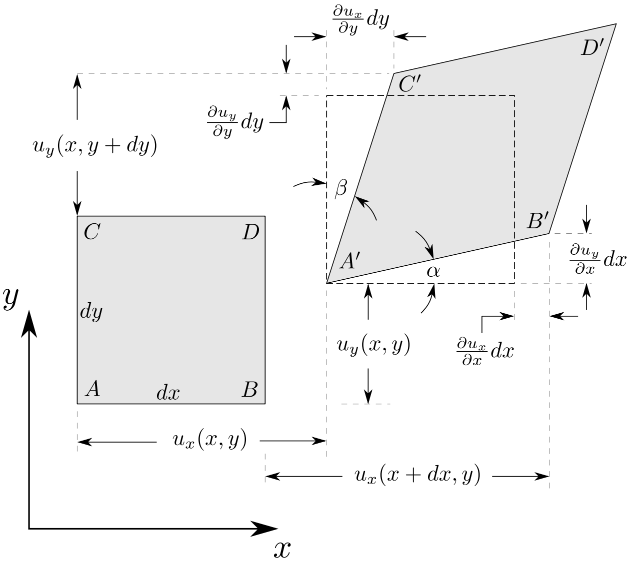

Figure 1.16: Geometric deformation of a two-dimensional, infinitesimal, rectangular element with dimension $dx \times dy$. It takes the form of a rhombus after deformation.

$$\varepsilon_x = \frac{A'B' - AB}{AB} \tag{1.26}$$

It can be observed that $AB = dx$ and $A'B' = \sqrt{(dx + \frac{\partial u_x}{\partial x}dx)^2 + (\frac{\partial u_y}{\partial x}dx)^2} \approx (1 + \frac{\partial u_x}{\partial x})dx$. Here, the square term of derivative of u_y is dropped considering the small displacement gradient. The normal strain in the x-direction hence reduces to:

$$\varepsilon_x = \frac{\partial u_x}{\partial x} \tag{1.27}$$

The other type of strain is the *shear strain* which can be defined as the change in angle between two originally orthogonal directions. For the infinitesimal element, this definition gives rise to the shear strain γ_{xy} in the xy-plane:

$$\gamma_{xy} = \alpha + \beta \tag{1.28}$$

From the geometry in Fig.1.16, we have $\tan\alpha = (\frac{\partial u_y}{\partial x}dx)/(dx + \frac{\partial u_x}{\partial x}dx) \approx \frac{\partial u_y}{\partial x}$ and $\tan\beta = (\frac{\partial u_x}{\partial y}dy)/(dy + \frac{\partial u_y}{\partial y}dy) \approx \frac{\partial u_x}{\partial y}$. Here, we neglect again some gradients by assuming that $\frac{\partial u_x}{\partial x} \ll 1$ and $\frac{\partial u_y}{\partial y} \ll 1$. For small angles, we also have $\tan\alpha \approx \alpha$ and $\tan\beta \approx \beta$. As a result, γ_{xy} becomes:

$$\gamma_{xy} = \frac{\partial u_y}{\partial x} + \frac{\partial u_x}{\partial y} \tag{1.29}$$

By simple interchanges, it can be proven that $\gamma_{xy} = \gamma_{yx}$. In similar fashion, these results can be extended to general three-dimensional case by taking yz- and xz-planes, leading to:

$$\begin{aligned} \varepsilon_x = \frac{\partial u_x}{\partial x}, \quad \varepsilon_y = \frac{\partial u_y}{\partial y}, \quad \varepsilon_z = \frac{\partial u_z}{\partial z} \\ \gamma_{xy} = \frac{\partial u_x}{\partial y} + \frac{\partial u_y}{\partial x}, \quad \gamma_{yz} = \frac{\partial u_y}{\partial z} + \frac{\partial u_z}{\partial y}, \quad \gamma_{zx} = \frac{\partial u_z}{\partial x} + \frac{\partial u_x}{\partial z} \end{aligned} \tag{1.30}$$

In fact, equations 1.30 representing the strain-displacement relations are written in the engineering strain form. However, it is usually preferred to use strain tensor $\underline{\underline{\varepsilon}}$. It is a symmetric ($\varepsilon_{ij} = \varepsilon_{ji}$) tensor of rank 2 which can be written in index notation as:

$$\varepsilon_{ij} = \frac{1}{2}(\frac{\partial u_i}{\partial x_j} + \frac{\partial u_j}{\partial x_i}) = \frac{1}{2}(u_{i,j} + u_{j,i}) \tag{1.31}$$

where $i, j = 1,2,3$ denote the components in the x, y and z directions, respectively. For example, $u_1 = u_x$, $x_1 = x$ and $x_2 = y$, $\varepsilon_{11} = \varepsilon_x$ and $\varepsilon_{12} = \frac{1}{2}\gamma_{xy} = \varepsilon_{21}$, and so forth. Besides, the $(\bullet)_{,j}$ subscript is a shorthand for the partial derivative $\partial(\bullet)/\partial x_j$.

It can also be expressed in direct tensor notation:

$$\underline{\underline{\varepsilon}} = \frac{1}{2}[\underline{\underline{\nabla \underline{u}}} + (\underline{\underline{\nabla \underline{u}}})^T] \tag{1.32}$$

where $\underline{u} = \sum_i u_i \underline{e}_i$ is the displacement tensor of rank 1, $\underline{\underline{\nabla}}$ is the nabla operator implying the second order gradient tensor. Finally in explicit form, it reads:

$$\begin{aligned} \boldsymbol{\varepsilon} &= \begin{bmatrix} \varepsilon_{11} & \varepsilon_{12} & \varepsilon_{13} \\ \varepsilon_{21} & \varepsilon_{22} & \varepsilon_{23} \\ \varepsilon_{31} & \varepsilon_{32} & \varepsilon_{33} \end{bmatrix} = \begin{bmatrix} \varepsilon_x & \frac{1}{2}\gamma_{xy} & \frac{1}{2}\gamma_{xz} \\ \frac{1}{2}\gamma_{yx} & \varepsilon_y & \frac{1}{2}\gamma_{yz} \\ \frac{1}{2}\gamma_{zx} & \frac{1}{2}\gamma_{zy} & \varepsilon_z \end{bmatrix} \\ &= \begin{bmatrix} \frac{\partial u_1}{\partial x_1} & \frac{1}{2}(\frac{\partial u_1}{\partial x_2} + \frac{\partial u_2}{\partial x_1}) & \frac{1}{2}(\frac{\partial u_1}{\partial x_3} + \frac{\partial u_3}{\partial x_1}) \\ \frac{1}{2}(\frac{\partial u_2}{\partial x_1} + \frac{\partial u_1}{\partial x_2}) & \frac{\partial u_2}{\partial x_2} & \frac{1}{2}(\frac{\partial u_2}{\partial x_3} + \frac{\partial u_3}{\partial x_2}) \\ \frac{1}{2}(\frac{\partial u_3}{\partial x_1} + \frac{\partial u_1}{\partial x_3}) & \frac{1}{2}(\frac{\partial u_3}{\partial x_2} + \frac{\partial u_2}{\partial x_3}) & \frac{\partial u_3}{\partial x_3} \end{bmatrix} \end{aligned} \tag{1.33}$$

1.2.1.2 Stress

As stated before, the strain results from the application of external loading. Indeed, the external forces are transmitted through all the structure, hence inducing internal forces that are distributed continuously within the body, according to continuum mechanics. These forces can be classified into *body forces* and *surface forces*. It is usually the latter that cause material failure and get more academic and industrial attention.

From surface forces, the concept of stress can be drawn. Consider a three-dimensional, infinitesimal cube element, as illustrated in Fig.1.17. Suppose that it is located at position $\underline{x}$, the surface has area ΔA with normal outward unit vector $\underline{n}$, and a surface force $\Delta \underline{F}$ is acting on ΔA. The *traction vector* or *stress* at point $\underline{x}$ is thus defined as:

$$\underline{T}(\underline{x}, \underline{n}) = \lim_{\Delta A \to 0} \frac{\Delta \underline{F}}{\Delta A} \tag{1.34}$$

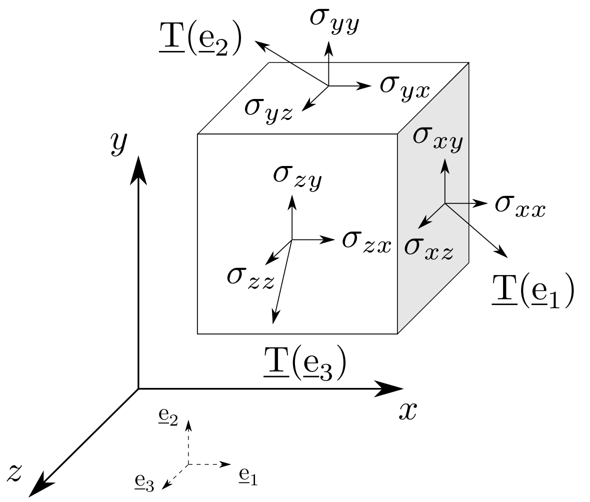

Figure 1.17: Stress components of a three-dimensional, infinitesimal cube element. $\underline{e}_i$ $(i = 1,2,3)$ denote the unit vectors along each coordinate direction and $\underline{T}(\underline{e}_i)$ $(i = 1,2,3)$ represent the traction vectors on surfaces perpendicular to $\underline{e}_i$.

and can be written, from Fig.1.17, as:

$$\begin{aligned}
\underline{T}(\underline{x},\underline{n}=\underline{e}_1) &= \sigma_{xx}\underline{e}_1 + \sigma_{xy}\underline{e}_2 + \sigma_{xz}\underline{e}_3 \\
\underline{T}(\underline{x},\underline{n}=\underline{e}_2) &= \sigma_{yx}\underline{e}_1 + \sigma_{yy}\underline{e}_2 + \sigma_{yz}\underline{e}_3 \\
\underline{T}(\underline{x},\underline{n}=\underline{e}_3) &= \sigma_{zx}\underline{e}_1 + \sigma_{zy}\underline{e}_2 + \sigma_{zz}\underline{e}_3
\end{aligned} \tag{1.35}$$

where $\underline{e}_i$ $(i = 1,2,3)$ denote the unit vectors along positive coordinate directions, and $[\sigma_{xx},\sigma_{xy},\sigma_{xz},\sigma_{yx},\sigma_{yy},\sigma_{yz},\sigma_{zx},\sigma_{zy},\sigma_{zz}]^T$ are the components of traction vectors $\underline{T}(\underline{x},\underline{n})$ on each surface. They also represent the components of stress tensor $\underline{\underline{\sigma}}$. It is a symmetric $(\sigma_{ij} = \sigma_{ji})$ tensor of rank 2 which can be written in matrix format as:

$$\boldsymbol{\sigma} = \begin{bmatrix} \sigma_{11} & \sigma_{12} & \sigma_{13} \\ \sigma_{21} & \sigma_{22} & \sigma_{23} \\ \sigma_{31} & \sigma_{32} & \sigma_{33} \end{bmatrix} = \begin{bmatrix} \sigma_{xx} & \sigma_{xy} & \sigma_{xz} \\ \sigma_{yx} & \sigma_{yy} & \sigma_{yz} \\ \sigma_{zx} & \sigma_{zy} & \sigma_{zz} \end{bmatrix} = \begin{bmatrix} \sigma_{xx} & \tau_{xy} & \tau_{xz} \\ \tau_{yx} & \sigma_{yy} & \tau_{yz} \\ \tau_{zx} & \tau_{zy} & \sigma_{zz} \end{bmatrix} \tag{1.36}$$

where the diagonal components are referred to as *normal stresses* and the others are called *shear stresses*. The latter are also denoted with τ such as $\sigma_{xy} = \tau_{xy}$.

1.2.1.3 Constitutive law

As mentioned, a material usually makes certain responses when external stimuli are imposed. *Constitutive law* consists in describing the relation between two physical quantities specific to that material, which is the one related to stimuli and the other related to responses. In continuum mechanics, the stimuli are stresses and the responses can be strain, strain rate, strain history and so forth. Their relations called *constitutive equations* characterize material mechanical properties.

The relatively simple case is the relation between stress and strain, representing the material model of *elastic solid* excluding rate or history effects. It describes the kind of material which can recover its original shape once the loading is removed. Further, the restriction in terms of linear relations leads to *linear elastic solid.* Under the assumption of small deformations, many materials can be considered as linear elastic materials which have linear stress-strain relations.

Based on the precedent introductions in 1.2.1.1 and 1.2.1.2, the components of stress and strain can be linearly related for linear elastic materials, leading to *Hooke's law*. The generic constitutive law in three-dimensions can thus be explicitly written as:

$$\begin{aligned}
\sigma_{11} &= D_{1111}\varepsilon_{11} + D_{1112}\varepsilon_{12} + D_{1113}\varepsilon_{13} + D_{1121}\varepsilon_{21} + D_{1122}\varepsilon_{22} + D_{1123}\varepsilon_{23} + D_{1131}\varepsilon_{31} + D_{1132}\varepsilon_{32} + D_{1133}\varepsilon_{33} \\
\sigma_{12} &= D_{1211}\varepsilon_{11} + D_{1212}\varepsilon_{12} + D_{1213}\varepsilon_{13} + D_{1221}\varepsilon_{21} + D_{1222}\varepsilon_{22} + D_{1223}\varepsilon_{23} + D_{1231}\varepsilon_{31} + D_{1232}\varepsilon_{32} + D_{1233}\varepsilon_{33} \\
\sigma_{13} &= D_{1311}\varepsilon_{11} + D_{1312}\varepsilon_{12} + D_{1313}\varepsilon_{13} + D_{1321}\varepsilon_{21} + D_{1322}\varepsilon_{22} + D_{1323}\varepsilon_{23} + D_{1331}\varepsilon_{31} + D_{1332}\varepsilon_{32} + D_{1333}\varepsilon_{33} \\
\sigma_{21} &= D_{2111}\varepsilon_{11} + D_{2112}\varepsilon_{12} + D_{2113}\varepsilon_{13} + D_{2121}\varepsilon_{21} + D_{2122}\varepsilon_{22} + D_{2123}\varepsilon_{23} + D_{2131}\varepsilon_{31} + D_{2132}\varepsilon_{32} + D_{2133}\varepsilon_{33} \\
\sigma_{22} &= D_{2211}\varepsilon_{11} + D_{2212}\varepsilon_{12} + D_{2213}\varepsilon_{13} + D_{2221}\varepsilon_{21} + D_{2222}\varepsilon_{22} + D_{2223}\varepsilon_{23} + D_{2231}\varepsilon_{31} + D_{2232}\varepsilon_{32} + D_{2233}\varepsilon_{33} \\
\sigma_{23} &= D_{2311}\varepsilon_{11} + D_{2312}\varepsilon_{12} + D_{2313}\varepsilon_{13} + D_{2321}\varepsilon_{21} + D_{2322}\varepsilon_{22} + D_{2323}\varepsilon_{23} + D_{2331}\varepsilon_{31} + D_{2332}\varepsilon_{32} + D_{2333}\varepsilon_{33} \\
\sigma_{31} &= D_{3111}\varepsilon_{11} + D_{3112}\varepsilon_{12} + D_{3113}\varepsilon_{13} + D_{3121}\varepsilon_{21} + D_{3122}\varepsilon_{22} + D_{3123}\varepsilon_{23} + D_{3131}\varepsilon_{31} + D_{3132}\varepsilon_{32} + D_{3133}\varepsilon_{33} \\
\sigma_{32} &= D_{3211}\varepsilon_{11} + D_{3212}\varepsilon_{12} + D_{3213}\varepsilon_{13} + D_{3221}\varepsilon_{21} + D_{3222}\varepsilon_{22} + D_{3223}\varepsilon_{23} + D_{3231}\varepsilon_{31} + D_{3232}\varepsilon_{32} + D_{3233}\varepsilon_{33} \\
\sigma_{33} &= D_{3311}\varepsilon_{11} + D_{3312}\varepsilon_{12} + D_{3313}\varepsilon_{13} + D_{3321}\varepsilon_{21} + D_{3322}\varepsilon_{22} + D_{3323}\varepsilon_{23} + D_{3331}\varepsilon_{31} + D_{3332}\varepsilon_{32} + D_{3333}\varepsilon_{33}
\end{aligned} \tag{1.37}$$

It can be expressed more concisely by tensors in index notation as:

$$\sigma_{ij} = D_{ijkl}\varepsilon_{kl} \tag{1.38}$$

where $i, j, k, l = 1, 2, 3$ and D_{ijkl} implies the *elasticity tensor* $\underline{\underline{\underline{\underline{D}}}}$ of rank 4. Commonly, this tensor has $3 \times 3 \times 3 \times 3 = 81$ elements. Due to the symmetry of stress and strain tensors, it is characterized by $D_{ijkl} = D_{jikl}$ and $D_{ijkl} = D_{ijlk}$, and thus the number can be reduced to 36. As presented later in 1.2.1.6, the strain energy leads to another symmetric property $D_{ijkl} = D_{klij}$, which means further reduction to 21 independent components. As a result, the elasticity tensor can be regarded as D_{ij} $(i, j = 1, ..., 6)$ which is a symmetric $(D_{ij} = D_{ji})$ tensor of rank 2, whose 21 independent elements are also called *elastic moduli*. Accordingly, the second-order tensors of stress and strain are usually reduced to vectors noted in Voigt notation as $\boldsymbol{\sigma} = [\sigma_{11}, \sigma_{22}, \sigma_{33}, \sigma_{12}, \sigma_{23}, \sigma_{31}]^T$ and $\boldsymbol{\varepsilon} = [\varepsilon_{11}, \varepsilon_{22}, \varepsilon_{33}, 2\varepsilon_{12}, 2\varepsilon_{23}, 2\varepsilon_{31}]^T$, respectively. The constitutive law hence reduces to:

$$\begin{Bmatrix} \sigma_{11} \\ \sigma_{22} \\ \sigma_{33} \\ \sigma_{12} \\ \sigma_{23} \\ \sigma_{31} \end{Bmatrix} = \begin{bmatrix} D_{11} & D_{12} & D_{13} & D_{14} & D_{15} & D_{16} \\ D_{21} & D_{22} & D_{23} & D_{24} & D_{25} & D_{26} \\ D_{31} & D_{32} & D_{33} & D_{34} & D_{35} & D_{36} \\ D_{41} & D_{42} & D_{43} & D_{44} & D_{45} & D_{46} \\ D_{51} & D_{52} & D_{53} & D_{54} & D_{55} & D_{56} \\ D_{61} & D_{62} & D_{63} & D_{64} & D_{65} & D_{66} \end{bmatrix} \begin{Bmatrix} \varepsilon_{11} \\ \varepsilon_{22} \\ \varepsilon_{33} \\ 2\varepsilon_{12} \\ 2\varepsilon_{23} \\ 2\varepsilon_{31} \end{Bmatrix} \tag{1.39}$$

where the factors of 2 before shear strains are due to the symmetry of strain tensor.

Till now, we have assumed materials being elastic and linear in terms of stress-strain relations. There exist another two important material properties which can be assumed to further simplify the formulation Eq.1.39, namely *homogeneity* and *isotropy*. On one hand, homogeneous materials are characterized by constant elastic moduli not varying in space. This assumption doesn't effect the expression (1.39) but dramatically simplifies the problems since only 21 constants are required to determine material mechanical behaviours through the space within the continuum body. On the other hand, isotropic materials are characterized by the same elastic properties in all spatial directions. This assumption is greatly helpful in reducing the independent components from 21 to 2 constants. The constitutive law (also called the *generalized Hooke's law*) for linear, (homogeneous,) isotropic elastic materials can finally be written in index notation as:

$$\sigma_{ij} = \lambda \varepsilon_{kk} \delta_{ij} + 2\mu \varepsilon_{ij} \tag{1.40}$$

where λ and μ are called Lamé constants, Einstein summation convention is used for ε_{kk} (namely $\varepsilon_{kk} = \varepsilon_{11} + \varepsilon_{22} + \varepsilon_{33}$) and δ_{ij} is the Kronecker delta (equal to 1 if $i = j$ and 0 otherwise). Usually, μ is also denoted by G and referred to as *shear modulus*.

In direct tensor notation, it can also be expressed as:

$$\underline{\underline{\sigma}} = \lambda \,\mathrm{tr}(\underline{\underline{\varepsilon}}) \underline{\underline{I}} + 2\mu \underline{\underline{\varepsilon}} \tag{1.41}$$

where $\mathrm{tr}(\bullet)$ denotes the trace of a matrix (defined as the sum of diagonal elements) and $\underline{\underline{I}}$ is the second-rank identity tensor.

And in explicit matrix form, it is written as:

$$\begin{Bmatrix} \sigma_{11} \\ \sigma_{22} \\ \sigma_{33} \\ \sigma_{12} \\ \sigma_{23} \\ \sigma_{31} \end{Bmatrix} = \begin{bmatrix} \lambda + 2\mu & \lambda & \lambda & 0 & 0 & 0 \\ \lambda & \lambda + 2\mu & \lambda & 0 & 0 & 0 \\ \lambda & \lambda & \lambda + 2\mu & 0 & 0 & 0 \\ 0 & 0 & 0 & \mu & 0 & 0 \\ 0 & 0 & 0 & 0 & \mu & 0 \\ 0 & 0 & 0 & 0 & 0 & \mu \end{bmatrix} \begin{Bmatrix} \varepsilon_{11} \\ \varepsilon_{22} \\ \varepsilon_{33} \\ 2\varepsilon_{12} \\ 2\varepsilon_{23} \\ 2\varepsilon_{31} \end{Bmatrix} \tag{1.42}$$

However, another pair of constants (E, ν) is more common in practice than the pair (λ, μ). E is called *Young's modulus* or *modulus of elasticity*, and ν is the *Poisson's ratio*. These two parameters are widely used in tension or compression experiments. E measures the tensile or compressive stiffness of materials, while ν measures the ratio of transverse strain to axial strain. The two pairs are related by:

$$\lambda = \frac{E\nu}{(1+\nu)(1-2\nu)}; \qquad \mu = \frac{E}{2(1+\nu)} \tag{1.43}$$

In two-dimensional problems, two assumptions are commonly used to simplify the constitutive equations: *plane stress* and *plane strain*. Plane stress, as the name suggests, refers to the case where stresses only exist in a two-dimensional plane and are equal to zero across the plane. It is a valid approximation for the thin structures whose third dimension is far less than the other two in-plane dimensions, like thin plates. Suppose the in-plane dimensions being denoted by x and y (or 1 and 2), and the other one being denoted by z (or 3). We thus have the zero stresses $\sigma_{13} = \sigma_{31} = \sigma_{23} = \sigma_{32} = \sigma_{33} = 0$. The Hooke's law for plane stress can reduce to:

$$\begin{Bmatrix} \sigma_{11} \\ \sigma_{22} \\ \sigma_{12} \end{Bmatrix} = \frac{E}{1-\nu^2} \begin{bmatrix} 1 & \nu & 0 \\ \nu & 1 & 0 \\ 0 & 0 & \frac{1-\nu}{2} \end{bmatrix} \begin{Bmatrix} \varepsilon_{11} \\ \varepsilon_{22} \\ 2\varepsilon_{12} \end{Bmatrix} \tag{1.44}$$

On the other hand, plane strain refers to the opposite case where the structure length is much greater than the two in-plane dimensions, like long rods. Therefore, when external forces are applied in the direction orthogonal to its length, the structure can be considered as being under plane strain state. Using the same subscript notations as before, we can nullify the strains associated with length: $\varepsilon_{13} = \varepsilon_{31} = \varepsilon_{23} = \varepsilon_{32} = \varepsilon_{33} = 0$. The Hooke's law for plane strain can reduce to:

$$\begin{Bmatrix} \sigma_{11} \\ \sigma_{22} \\ \sigma_{12} \end{Bmatrix} = \frac{E}{(1+\nu)(1-2\nu)} \begin{bmatrix} 1-\nu & \nu & 0 \\ \nu & 1-\nu & 0 \\ 0 & 0 & \frac{1-2\nu}{2} \end{bmatrix} \begin{Bmatrix} \varepsilon_{11} \\ \varepsilon_{22} \\ 2\varepsilon_{12} \end{Bmatrix} \tag{1.45}$$

Moreover, plane strain can also be applied to the axisymmetric structure, like a cylinder. In this case, a 2D section revolves around an axis to form the solid. The angular "length" of revolution (= 360° in cylindrical coordinate reference) can be regarded as much greater than the section dimensions. It conforms to plane strain hypothesis and can thus be analysed using its 2D section and Eq.1.45.

Finally, note that $\varepsilon_{33} = -\frac{\nu}{E}(\sigma_{11} + \sigma_{22})$ is non-zero for plane stress and $\sigma_{33} = \lambda(\varepsilon_{11} + \varepsilon_{22})$ is non-zero for plane strain. They are usually removed from the analysis in order to reduce the law to 2D case, but can be determined by boundary conditions.

1.2.1.4 Equilibrium equation

In section 1.2.1.2, we have given the definition and expression of stress. However, the explicit relations between stresses and external forces are not yet clearly derived. To this end, we have to utilize the concept of *equilibrium state*.

For the body in static equilibrium, all the applied forces sum up to zero. Besides, any part/subdomain of the body is also in equilibrium and follows this rule. We could thus consider a closed subdomain with volume V and surface S, having a density of surface tractions $\underline{T}$ and body forces $\underline{F}$. This concept can be written in index notation as:

$$\iint_S T_i \, \mathrm{d}S + \iiint_V F_i \, \mathrm{d}V = 0 \tag{1.46}$$

For traction in arbitrary direction with unit vector $\underline{n}$, define n_i as the projection of $\underline{n}$ onto coordinate x_i ($i = 1,2,3$). The traction can be related to stresses by $T_i = \sigma_{ij} n_j$ with Einstein notation. Moreover, the divergence theorem (Gauss's theorem) can convert the surface integral of a vector to the volume integral of its divergence, leading to $\iint_S \sigma_{ij} n_j \mathrm{d}S = \iiint_V \sigma_{ij,j} \mathrm{d}V$. Equation 1.46 can then be reformulated as:

$$\iiint_V (\sigma_{ij,j} + F_i)\mathrm{d}V = 0 \tag{1.47}$$

Since the region V is arbitrary and the tensors are continuous within the continuum body, then according to the localization theorem, the integrand is null. The equilibrium equations for static case can thus be derived and written as follows:

$$\sigma_{ij,j} + F_i = 0 \tag{1.48}$$

For the body in dynamic equilibrium, like the case of elastic wave propagation, we have to further consider and incorporate the law of motion. Newton's second law of motion states that the rate of change of momentum of an object over time is equal to the force acting on it. More commonly, for an object with constant mass, this law can also be reformulated in terms of object acceleration:

$$\underline{F} = \frac{\mathrm{d}\underline{p}}{\mathrm{d}t} = \frac{\mathrm{d}(\mathrm{m}\underline{v})}{\mathrm{d}t} = \mathrm{m}\frac{\mathrm{d}\underline{v}}{\mathrm{d}t} = \mathrm{m}\underline{a} \tag{1.49}$$

where $\underline{F}$ is the resultant force, $\underline{p}$ is the momentum, m is the mass, $\underline{v}$ is the velocity and $\underline{a}$ is the acceleration. This law can be rewritten in integral form as $\underline{F} = \iiint_V \rho\partial_{tt}\underline{u}\mathrm{d}V$ where ρ is the mass density, ∂_{tt} indicates $\partial^2/\partial t^2$ and $\underline{u}$ is the displacement vector. Combining it with Eq.1.47 and re-using the localization theorem, we finally get the equilibrium equations for dynamic case written in index notation as:

$$\sigma_{ij,j} + F_i = \rho\partial_{tt}u_i \tag{1.50}$$

For the study of elastic waves, equation 1.50 is one of the basic field equations. It can also be formulated in tensor format as:

$$\underline{\nabla} \cdot \underline{\underline{\sigma}} + \underline{F} = \rho\underline{\ddot{u}} \tag{1.51}$$

where $(\ddot{\bullet})$ represents the second derivative with respect to time.

1.2.1.5 Motion equation

Till now, we have developed the basic field equations for linear isotropic elasticity, including the strain-displacement relation (1.32), the constitutive law (1.41) and the equilibrium equation (1.51). This leads to a system of 15 relations involving 15 unknowns, namely 3 displacements u_i, 6 strains ε_{ij} and 6 stresses σ_{ij}. It is thus possible to solve these unknowns for a three-dimensional problem where the two material constants (say λ and μ) and force density F_i are given a priori. However, further simplification by combining these field equations is usually required. Based on different types of boundary conditions, two different formulations can be obtained, one in terms of displacements and the other in terms of stresses [SAD 09]. In MRE, we generally prescribe certain displacements/strains other than forces/stresses on the boundary, leading to the *displacement formulation*.

For this case, the strains and stresses should be eliminated from the basic field equations, leaving the displacements as the only unknowns to be solved. To this end, we first substitute the strains in constitutive law (1.40) with displacements, using the definition of strain-displacement (1.31):

$$\begin{aligned}\sigma_{ij} &= \lambda\delta_{ij}\varepsilon_{kk} + 2\mu\varepsilon_{ij} \\ &= \lambda\delta_{ij}u_{k,k} + \mu(u_{i,j} + u_{j,i})\end{aligned} \tag{1.52}$$

Considering the summation notation, the differentials sum up to:

$$\sigma_{ij,j} = \lambda u_{k,ki} + \mu(u_{i,jj} + u_{j,ij}) \tag{1.53}$$

Note that $\sigma_{ji,j} = \sigma_{ij,j}$. We can thus remove the stress terms in equilibrium law (1.50):

$$\lambda u_{k,ki} + \mu(u_{i,jj} + u_{j,ij}) + F_i = \rho\partial_{tt}u_i \tag{1.54}$$

It can be reorganized into the more popular form:

$$(\lambda + \mu)u_{j,ij} + \mu u_{i,jj} + F_i = \rho\partial_{tt}u_i \tag{1.55}$$

It can also be written in tensor form as:

$$(\lambda + \mu)\underline{\nabla}(\underline{\nabla}\cdot\underline{u}) + \mu\underline{\nabla}^2\underline{u} + \underline{F} = \rho\partial_{tt}\underline{u} \tag{1.56}$$

This is the equilibrium equations in terms of displacements and also referred to as *Navier-Cauchy equations*. In the domain of elastic waves, like in MRE, we usually suppose that the displacements are time harmonic, leading to:

$$\underline{u}(\underline{r},\mathrm{t}) = \underline{u}_0\exp[i(\omega\mathrm{t} - \underline{k}\cdot\underline{r})] \tag{1.57}$$

where $\underline{u}_0$ is the amplitude vector, i is the imaginary unit, ω is the angular frequency, $\underline{k}$ is the vector of wavenumber and $\underline{r}$ is the vector of coordinates.

With this assumption applied and body forces neglected, we finally obtain the governing equation of elastic waves with small amplitude and harmonic motion, propagating in a linear, isotropic, (visco-)elastic medium:

$$(\lambda + \mu)\underline{\nabla}(\underline{\nabla}\cdot\underline{u}) + \mu\underline{\nabla}^2\underline{u} + \rho\omega^2\underline{u} = 0 \tag{1.58}$$

which is written in index form as:

$$(\lambda + \mu)u_{j,ij} + \mu u_{i,jj} + \rho\omega^2 u_i = 0 \tag{1.59}$$

1.2.1.6 Strain energy

In elasticity, strain energy is a kind of potential energy stored inside the elastic body resulting from the work done by surface or body forces. Due to this storage, idealized elastic solid can completely recover its original shape when loading is removed. Infinitesimally, it is related to the stress and strain, leading to the strain energy per unit volume, or *strain energy density*, written in index notation as:

$$U = \frac{1}{2}\sigma_{ij}\varepsilon_{ij} \tag{1.60}$$

with summation convention applied. And in tensor notation it reads:

$$U = \frac{1}{2}\underline{\underline{\sigma}} : \underline{\underline{\varepsilon}} \tag{1.61}$$

where : denotes the double dot product of two tensors of rank 2, namely the Hadamard product or element-wise product of two matrices of the same dimensions.

In reality, both stress and strain can be decomposed into two parts: *volumetric* and *deviatoric* part. The former is related to the volume change while the latter is associated with the shape change. Taking the example of strain tensor, we have:

$$\underline{\underline{\varepsilon}} = \underline{\underline{\varepsilon}}^{vol} + \underline{\underline{\varepsilon}}^{dev} \tag{1.62}$$

where

$$\underline{\underline{\varepsilon}}^{vol} = \frac{\mathrm{tr}(\underline{\underline{\varepsilon}})}{3}\underline{\underline{I}} \tag{1.63}$$

Substituting into the constitutive equation in tensor form (Eq.1.41) leads to:

$$\begin{aligned}\underline{\underline{\sigma}} &= \lambda\,\mathrm{tr}(\underline{\underline{\varepsilon}})\underline{\underline{I}} + 2\mu\underline{\underline{\varepsilon}} \\ &= 3\lambda\underline{\underline{\varepsilon}}^{vol} + 2\mu(\underline{\underline{\varepsilon}}^{vol} + \underline{\underline{\varepsilon}}^{dev}) \\ &= (3\lambda + 2\mu)\underline{\underline{\varepsilon}}^{vol} + 2\mu\underline{\underline{\varepsilon}}^{dev}\end{aligned} \tag{1.64}$$

Combining this result with Eq.1.61 and considering $\underline{\underline{\bullet}}^{vol} : \underline{\underline{\bullet}}^{dev} = 0$, we obtain:

$$\begin{aligned}U &= \frac{1}{2}((3\lambda + 2\mu)\underline{\underline{\varepsilon}}^{vol} + 2\mu\underline{\underline{\varepsilon}}^{dev}) : (\underline{\underline{\varepsilon}}^{vol} + \underline{\underline{\varepsilon}}^{dev}) \\ &= \frac{3\lambda + 2\mu}{2}\underline{\underline{\varepsilon}}^{vol} : \underline{\underline{\varepsilon}}^{vol} + \mu\underline{\underline{\varepsilon}}^{dev} : \underline{\underline{\varepsilon}}^{dev}\end{aligned} \tag{1.65}$$

where the first term on the right side represents *volumetric energy* U^{vol} and the second represents *deviatoric energy* U^{dev}.

Finally, the strain energy can also be regarded as a bridge between stress and strain, due to general stress-strain relations:

$$\sigma_{ij} = \frac{\partial U}{\partial \varepsilon_{ij}} \tag{1.66}$$

The symmetry relations can thus be derived:

$$\frac{\partial \sigma_{ij}}{\partial \varepsilon_{kl}} = \frac{\partial \sigma_{kl}}{\partial \varepsilon_{ij}} \tag{1.67}$$

Recalling the constitutive equation $\sigma_{ij} = D_{ijkl}\varepsilon_{kl}$, this leads to the symmetry relation for elasticity tensor as used in section 1.2.1.3:

$$D_{ijkl} = D_{klij} \tag{1.68}$$

1.2.2 Viscoelasticity

Unlike lossless elastic solids, viscoelastic materials with vibrations applied would not continue to indefinitely vibrate due to the energy dissipation. The viscous effect makes the strain response to applied stress not-instantaneous, leading to the time-dependent behaviors. All the strains arising in different time increments would sum up and the material is hence said to have memory [CAR 07].

Several rheological models are available for describing the viscoelasticity of materials like soft tissues, and their different frequency-dependent characteristics have been investigated by MRE researchers [HIR 17, KLA 07, YAS 13]. The two simplest models with only two parameters, i.e. the Voigt and Maxwell model, may not represent well the tissue behaviors in MRE frequency range [MAN 21, HIR 17, ROY 11]. Other complex models, such as the standard linear solid (SLS) model and the generalized Maxwell model, can have better performance in fitting MRE experimental measurements at multiple frequencies [KLA 07, YAS 13]. Currently, there is no agreement regarding the choice of model, but models with least parameters and good performance are preferred [YAS 13]. For the sake of simplicity and being representative, we have chosen to employ in this work the Maxwell form of SLS model, as will be presented.

In this subsection, we would focus on linear viscoelasticity in which the stress is linearly related to the strain history. We first introduce some widely used mechanical models for describing viscoelastic behaviors, including the Maxwell model, the Kelvin-Voigt model and the SLS model (or the Zener model). The linear constitutive relations and model properties are presented. Then, the dynamic modulus of each model will be derived, which is necessary for quantification of viscoelastic materials.

1.2.2.1 Basic models and their constitutive equations

As the name suggests, viscoelasticity is composed of viscosity and elasticity. While the elasticity is typically applied for elastic solids and physically modeled by a spring, the viscosity is for viscous liquids and modeled by a dashpot. The former is characterized by the elastic modulus or the Young's modulus, denoted as E or k with the unit Pascal (Pa), and the latter is usually described by the metric of *dynamic viscosity*, denoted as η or μ with the unit Pascal·second ($Pa \cdot s$). Following conventions in solid mechanics, we take herein the notations of E and η for describing linear elasticity and linear viscosity, respectively.

The Hooke's law leads to the constitutive equation for spring component:

$$\sigma = E\varepsilon \tag{1.69}$$

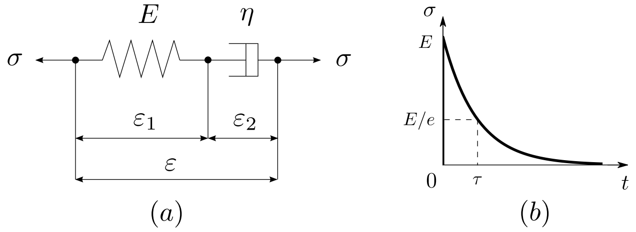

Figure 1.18: Maxwell model (a) for viscoelastic materials and its relaxation function (b) and creep function (c).

and the Newton's law gives rise to the stress-strain rate relation for dashpot component:

$$\sigma = \eta \frac{\partial \varepsilon}{\partial t} \tag{1.70}$$

which is in fact the constitutive equation for one-dimensional, linear, viscous flow.

Different linear viscoelastic models can be acquired by combining these two types of components in different manners, which thus exhibit both viscous and elastic characteristics when undergoing external loading. Among them, the two simplest models are the Maxwell model and the Kelvin-Voigt model, which also constitute the elements of other more complex models. In addition, two time-dependent functions, the *relaxation function* $G(t)$ and the *creep function* $J(t)$, can be derived from convolution integrals and are usually used to characterize the model properties. The former measures the stress response after imposing a constant unit strain, i.e. $\varepsilon = H(t)$ where $H(t)$ is the *Heaviside function* (equal to 1 if $t > 0$ and 0 otherwise). And the latter describes the resulting strain due to an instantaneously applied constant unit stress, namely $\sigma = H(t)$. They can be embodied, respectively, in the response formulations of stress and strain [SIM 06]:

$$\sigma(t) = \int_{-\infty}^{t} G(t-s)\dot{\varepsilon}(s)ds \tag{1.71}$$

$$\varepsilon(t) = \int_{-\infty}^{t} J(t-s)\dot{\sigma}(s)ds \tag{1.72}$$

(1) *Maxwell model*

The combination of two components in series leads to the Maxwell model a illustrated in Fig.1.18(a). A stress σ is applied to the model and produces a total strain ε comprising one strain ε_1 for the spring E and the other one ε_2 for the dashpot η, written as:

$$\varepsilon = \varepsilon_1 + \varepsilon_2 \tag{1.73}$$

Given that the two components undergo the same stress σ, the constitutive equation of Maxwell element can thus be obtained by combining Eqs.1.69 to 1.73:

$$\sigma + \frac{\eta}{E}\frac{\partial \sigma}{\partial t} = \eta \frac{\partial \varepsilon}{\partial t} \tag{1.74}$$

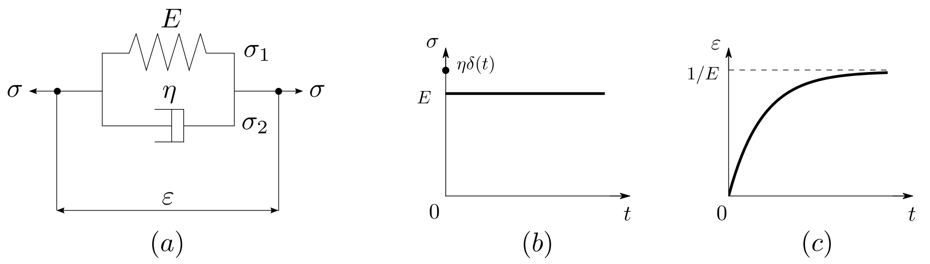

Figure 1.19: Kelvin-Voigt model (a) for viscoelastic materials and its relaxation function (b) and creep function (c).

The relaxation and creep functions of Maxwell model are:

$$G(t) = E\exp(-t/\tau)H(t) \tag{1.75}$$

$$J(t) = \frac{1}{E}(1+\frac{t}{\tau})H(t) \tag{1.76}$$

where $\tau = \eta/E$ is the relaxation time. The two functions are roughly illustrated in Fig.1.18(b) and (c), respectively. As can be seen, the relaxation function doesn't have an asymptotical residual stress as in the case of real solids. However, the creep function is almost linear and rather representative of creep behaviors of viscous fluids instead of real solids. The Maxwell model is thus more appropriate for representing viscoelastic fluids.

(2) *Kelvin-Voigt model*

The other simple model is the Kelvin-Voigt model, which consists of the two components in parallel, as depicted in Fig.1.19(a). The total stress σ is composed of an elastic stress σ_1 for the spring E and a viscous stress σ_2 for the dashpot η, leading to:

$$\sigma = \sigma_1 + \sigma_2 \tag{1.77}$$

Considering that the two components have the same strain ε, we could derive the constitutive equation of Kelvin-Voigt element from Eq.1.77 in combination with Eqs.1.69 and 1.70:

$$\sigma = E\varepsilon + \eta\frac{\partial\varepsilon}{\partial t} \tag{1.78}$$

The relaxation and creep functions are:

$$G(t) = EH(t) + \eta\delta(t) \tag{1.79}$$

$$J(t) = \frac{1}{E}[1-\exp(-t/\tau)]H(t) \tag{1.80}$$

with $\delta(t)$ being the Dirac delta function. The two functions are also depicted in Fig.1.19(b) and (c), respectively. As shown, the relaxation function is almost constant, which is rather the case of pure elastic solids. In terms of the creep function, it doesn't

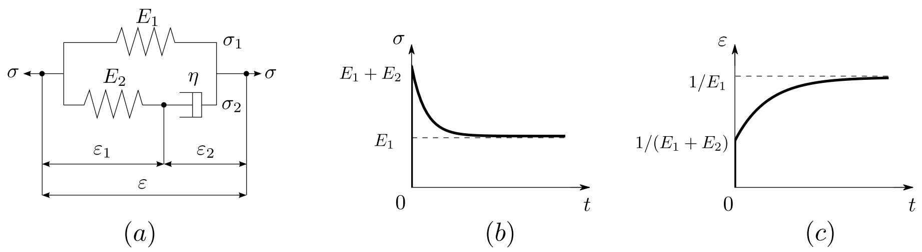

Figure 1.20: Maxwell representation of standard linear solid (SLS) model (a) for viscoelastic materials and its relaxation function (b) and creep function (c).

present an initial instantaneous strain, which is not the case of real solids, and tends to the strain of $1/E$ at infinite time. The Kelvin-Voigt model is commonly used for describing anelastic effects.

(3) *Standard linear solid model*

As introduced above, the two simplest models both have their own limitations in describing viscoelastic behaviors, which is that the Maxwell model is not good at representing creep process and the Kelvin-Voigt model cannot describe the relaxation behaviors.

To this end, the standard linear solid (SLS) model, also known as the Zener model, was developed as a remedy. It is the simplest model which can predict both relaxation and creep phenomena. Two representations exist and are discussed in the following.

The Maxwell representation of SLS model, as shown in Fig.1.20(a), is composed of a spring E_1 and a Maxwell element (E_2 plus η) in parallel. The following relationships:

$$\begin{aligned} \sigma &= \sigma_1 + \sigma_2 \\ \sigma_1 &= E_1 \varepsilon \\ \sigma_2 + \frac{\eta}{E_2}\frac{\partial \sigma_2}{\partial t} &= \eta \frac{\partial \varepsilon}{\partial t} \end{aligned} \tag{1.81}$$

can lead to the constitutive equation of Maxwell representation of SLS model:

$$\sigma + \frac{\eta}{E_2}\frac{\partial \sigma}{\partial t} = E_1 \varepsilon + \frac{\eta(E_1+E_2)}{E_2}\frac{\partial \varepsilon}{\partial t} \tag{1.82}$$

The relaxation and creep functions are [SIM 06]:

$$G(t) = [E_1 + E_2 \exp(-t/\tau_1)]H(t) \tag{1.83}$$

$$J(t) = \frac{1}{E_1}\left[1 - \frac{E_2}{E_1+E_2}\exp(-t/\tau_2)\right]H(t) \tag{1.84}$$

where $\tau_1 = \eta/E_2$ is the relaxation time constant and $\tau_2 = \eta(E_1+E_2)/(E_1E_2)$ is the creep time constant. These two functions are presented in Fig.1.20(b) and (c), respectively. It can be observed that both the relaxation and creep behaviors are well modeled for viscoelastic solids. For this form of SLS model, E_1+E_2 is also called initial modulus

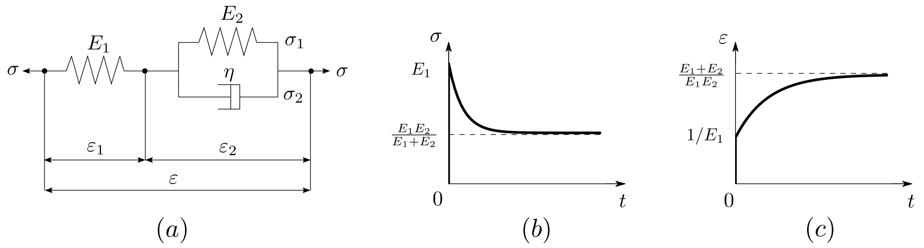

Figure 1.21: Kelvin-Voigt representation of standard linear solid (SLS) model (a) for viscoelastic materials and its relaxation function (b) and creep function (c).

denoted by E_0, and E_1 is called relaxed modulus and sometimes denoted by E_∞ meaning modulus at infinite time [SIM 06].

The Kelvin-Voigt representation of SLS model, as depicted in Fig.1.21(a), is comprised of a spring E_1 and a Kelvin-Voigt element (E_2 plus η) in series. The following relations:

$$\begin{gathered} \varepsilon = \varepsilon_1 + \varepsilon_2 \\ \sigma = E_1\varepsilon_1 \\ \sigma = E_2\varepsilon_2 + \eta\frac{\partial \varepsilon_2}{\partial t} \end{gathered} \tag{1.85}$$

give rise to the constitutive equation of Kelvin-Voigt representation of SLS model:

$$\sigma + \frac{\eta}{E_1+E_2}\frac{\partial \sigma}{\partial t} = \frac{E_1E_2}{E_1+E_2}\varepsilon + \frac{\eta E_1}{E_1+E_2}\frac{\partial \varepsilon}{\partial t} \tag{1.86}$$

The relaxation and creep functions are [CAR 07]:

$$G(t) = M_R\left[1-\left(1-\frac{\tau_\varepsilon}{\tau_\sigma}\right)\exp(-t/\tau_\sigma)\right]H(t) \tag{1.87}$$

$$J(t) = \frac{1}{M_R}\left[1-\left(1-\frac{\tau_\sigma}{\tau_\varepsilon}\right)\exp(-t/\tau_\varepsilon)\right]H(t) \tag{1.88}$$

where $M_R = E_1E_2/(E_1+E_2)$ is the relaxed modulus, $\tau_\sigma = \eta/(E_1+E_2)$ and $\tau_\varepsilon = \eta/E_2$ are the relaxation times. The two functions are illustrated in Fig.1.21(b) and (c), respectively. As can be seen, this form of SLS model is similar to the previous one in terms of the capability in describing viscoelastic behaviors. However, it is characterized by an initial modulus of E_1 and a relaxed modulus of $E_1E_2/(E_1+E_2)$.

For convenience, the Maxwell representation of SLS model was chosen and used in this work. The detailed implementation will be discussed in Chapter 2. For more general models such as generalized Maxwell model and generalized SLS model, see, for example, [SIM 06, CAR 07, HAO 19].

1.2.2.2 Dynamic modulus

The dynamic modulus is useful in characterizing the stress-strain relations of viscoelastic materials under harmonic excitation. It can be derived from the constitutive equations of precedent basic model by applying the Fourier transform. Before performing the derivations, we recall some bases of Fourier transform. For a function $f(t)$ in time domain, its Fourier transform $\hat{f}(\omega)$ in frequency domain can be defined, among others, as:

$$\hat{f}(\omega) = \frac{1}{\sqrt{2\pi}} \int_{-\infty}^{\infty} f(t) e^{-i\omega t} dt \tag{1.89}$$

where the time is extended to $-\infty$ and ω is angular frequency. Especially, the Fourier transform of the derivative $\frac{d^n f(t)}{dt^n}$ can be proven to be $(i\omega)^n \hat{f}(\omega)$. With this result, we could derive with ease the dynamic modulus of different models.

(1) *Maxwell model*

Applying the Fourier transform to the Eq.1.74 of the Maxwell model yields:

$$\begin{aligned} & \hat{\sigma} + i\tau\omega\hat{\sigma} = i\eta\omega\hat{\varepsilon} \\ \Rightarrow \qquad & \hat{\sigma} = \frac{i\eta\omega}{1+i\tau\omega}\hat{\varepsilon} \\ & \quad = \frac{\eta\tau\omega^2 + i\eta\omega}{1+\tau^2\omega^2}\hat{\varepsilon} \\ & \quad = E^*(\omega)\,\hat{\varepsilon} \end{aligned} \tag{1.90}$$

where $\hat{\sigma}$ and $\hat{\varepsilon}$ is the Fourier transform of stress σ and strain ε, respectively, and $E^*(\omega)$ is the dynamic elastic modulus. As can be seen, the dynamic modulus is usually complex, written as $E^* = E' + iE''$. The real part E' represents the storage modulus related to energy storage, and the imaginary part E'' represents the loss modulus related to energy loss.

(2) *Kelvin-Voigt model*

Similarly, the Fourier transform of Eq.1.78 leads to the dynamic modulus of Kelvin-Voigt model:

$$E^*(\omega) = E + i\eta\omega \tag{1.91}$$

(3) *Standard linear solid model*

For the Maxwell representation of SLS model, we could derive from the Eq.1.82 its dynamic modulus E^* with the storage modulus and the loss modulus being, respectively:

$$E'(\omega) = E_1 + \frac{\tau^2\omega^2}{1+\tau^2\omega^2}E_2 \tag{1.92}$$

$$E''(\omega) = \frac{\tau\omega}{1+\tau^2\omega^2}E_2 \tag{1.93}$$

where $\tau = \eta/E_2$. These two formulas are to be employed in the following chapters.

For the Kelvin-Voigt representation of SLS model, its dynamic modulus from the Eq.1.86 is calculated as:

$$\begin{aligned} E^*(\omega) &= \frac{E_1E_2(E_1+E_2) + E_1\eta^2\omega^2}{(E_1+E_2)^2 + \eta^2\omega^2} + i\frac{E_1^2\eta\omega}{(E_1+E_2)^2+\eta^2\omega^2} \\ &= M_R\left(\frac{1+i\omega\tau_\varepsilon}{1+i\omega\tau_\sigma}\right) \end{aligned} \tag{1.94}$$

1.3 Finite Element Method

In the precedent section of continuum mechanics, we have introduced the basic formulations in elasticity and viscoelasticity. For a problem subject to, for example, the equilibrium equation Eq.1.51 or the governing equation of elastic waves Eq.1.58, analytical solutions of these partial differential equations are not easy to find, due to the complicated geometries of studied object, various boundary conditions, etc. In this case, the powerful tool of numerical methods has been applied to provide robust solutions.

Among them, the Finite Element Method (FEM) is the most widely used numerical method in MRE studies. It has gained popularity with its performance in modeling wave propagation in tissue-like materials with complex geometries, pre-deformation, inhomogeneities and different boundary conditions, etc. For example, in early literature, Azar *et al.* [AZA 00, AZA 01] studied the FEM models in elastography for predicting breast deformations. Chen *et al.* [CHE 05, CHE 06] examined, by a finite element model, the effects of boundary conditions, geometry, pre-tension and frequency on MRE measurements. Bilasse *et al.* [BIL 18] developed a 2D finite element model for simulating the shear waves in inhomogeneous soft tissues, with low computational cost. And recently, McGarry *et al.* [MCG 20] proposed an inhomogeneous, nearly incompressible, transverse isotropic (NITI) finite element model for 3D simulations of brain in MRE.

As mentioned in section 1.1.3 of reconstruction methods, FEM has also been used in elastography to reproduce the stiffness maps by solving an inverse problem. Indeed, it can be performed in a direct way or a iterative way, as reported and compared in [HON 16]. Honarvar *et al.* [HON 17] further compared the FEM-based inversion algorithms with some popular direct methods used in MRE.

In this section, we present a general introduction of the principles and basic formulations of FEM theory, and some other formulations of FEM. Considering our mechanics background, only the forward displacement-based problems are discussed here. For the sake of clarity, the detailed numerical implementation of the FEM formulations/matrices won't be presented in this chapter but in Chapters 2 and 3. For more information, or applications in other fields like heat conduction, we recommend the reference books [ZIE 00, ZIE 05, HUG 12].

1.3.1 Problem formulation and discretization

In this subsection, we briefly introduce the FEM formulations by considering a problem of elastodynamics which is based on linear elasticity in dynamic cases. Small deformation is assumed. The Bubnov-Galerkin procedure is used for obtaining approximations of a discrete system. For the other common procedure using variational functionals, see [ZIE 05].

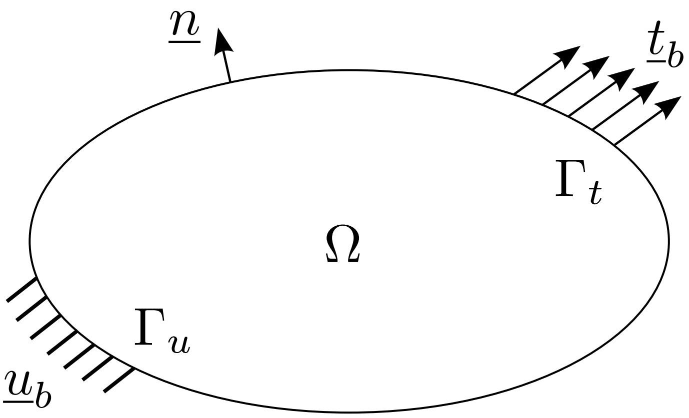

Figure 1.22: A solid body with boundaries subjected to displacements and loads.

1.3.1.1 Motivation and strong formulation

Consider a solid body within a bounded domain Ω, as illustrated in Fig.1.22. The boundary Γ is comprised of Γ_u and Γ_t such that $\Gamma = \Gamma_u \cup \Gamma_t$ and $\Gamma_u \cap \Gamma_t = \emptyset$. Prescribed boundary displacements $\underline{u}_b$ are imposed on Γ_u, leading to the essential or Dirichlet type boundary condition. And prescribed boundary tractions $\underline{t}_b$ are imposed on Γ_t, leading to the natural or Neumann type boundary condition. Considering the equilibrium equation Eq.1.51, this elastodynamics problem can be formulated by the governing equations as:

$$\begin{aligned} \underline{\nabla} \cdot \underline{\underline{\sigma}} + \underline{b} &= \rho \underline{\ddot{u}} \quad \text{in } \Omega \\ \underline{u} &= \underline{u}_b \quad \text{on } \Gamma_u \\ \underline{\underline{\sigma}} \cdot \underline{n} &= \underline{t}_b \quad \text{on } \Gamma_t \end{aligned} \tag{1.95}$$

where $\underline{\underline{\sigma}}$ is Cauchy stress tensor, $\underline{b}$ is body force vector, ρ is mass density, $\underline{u}$ is displacement vector, $\underline{n}$ is unit outward normal vector to Γ and $(\dot{\bullet})$ denotes partial differentiation with respect to time.

Indeed, the first equation in the above corresponds to the main differential equations to be solved and the other two equations are restrictions represented as boundary conditions. Without loss of generality, we denote them by the equation set, respectively, as:

$$\begin{aligned} \boldsymbol{\mathcal{A}}(\underline{u}) &= [A_1(\underline{u}), A_2(\underline{u}), \ldots]^T = \mathbf{0} \quad \text{in } \Omega \\ \boldsymbol{\mathcal{B}}(\underline{u}) &= [B_1(\underline{u}), B_2(\underline{u}), \ldots]^T = \mathbf{0} \quad \text{on } \Gamma \end{aligned} \tag{1.96}$$

1.3.1.2 Weak formulation

The system of Eq.1.96 is typically known as the strong formulation due to the differential equations. However, the integral form is more practical which can be stated as:

$$\begin{aligned} \int_\Omega \boldsymbol{v}^T \boldsymbol{\mathcal{A}}(\underline{u}) d\Omega &= \int_\Omega [v_1 A_1(\underline{u}) + v_2 A_2(\underline{u}) + \ldots] d\Omega = 0 \\ \int_\Gamma \hat{\boldsymbol{v}}^T \boldsymbol{\mathcal{B}}(\underline{u}) d\Gamma &= \int_\Gamma [\hat{v}_1 B_1(\underline{u}) + \hat{v}_2 B_2(\underline{u}) + \ldots] d\Gamma = 0 \end{aligned} \tag{1.97}$$

where $\boldsymbol{v} = [v_1, v_2, ...]^T$ and $\hat{\boldsymbol{v}} = [\hat{v}_1, \hat{v}_2, ...]^T$ are a set of arbitrary functions. It can be proved that if the integral form Eq.1.97 is satisfied for all $\boldsymbol{v}$ and $\hat{\boldsymbol{v}}$, then the differential form Eq.1.96 must be satisfied. Indeed, equation 1.97 can be further reduced to:

$$\int_\Omega \boldsymbol{v}^T \boldsymbol{\mathcal{A}}(\underline{u}) d\Omega + \int_\Gamma \hat{\boldsymbol{v}}^T \boldsymbol{\mathcal{B}}(\underline{u}) d\Gamma = 0 \tag{1.98}$$

and we have the conclusion that the satisfaction of Eq.1.98 for all $\boldsymbol{v}$ and $\hat{\boldsymbol{v}}$ is equivalent to the satisfaction of the differential equations and boundary conditions in Eq.1.96.

More generally, equation 1.98 can be converted to another form by performing integration by part (or Green's theorem), expressed as:

$$\int_\Omega \boldsymbol{\mathcal{C}}(\boldsymbol{v})^T \boldsymbol{\mathcal{D}}(\underline{u}) d\Omega + \int_\Gamma \boldsymbol{\mathcal{E}}(\hat{\boldsymbol{v}})^T \boldsymbol{\mathcal{F}}(\underline{u}) d\Gamma = 0 \tag{1.99}$$

where $\boldsymbol{\mathcal{C}}$, $\boldsymbol{\mathcal{D}}$, $\boldsymbol{\mathcal{E}}$, $\boldsymbol{\mathcal{F}}$ are operators containing lower order derivatives than those in $\boldsymbol{\mathcal{A}}$ and $\boldsymbol{\mathcal{B}}$. This integral form allows us to choose the approximations of $\underline{u}$ with lower order of continuity, and is hence called the weak formulation.

Back to the instance of system in Eq.1.95, we can write the statement (1.98) as:

$$-\int_\Omega \boldsymbol{v}^T (\nabla \cdot \boldsymbol{\sigma} + \boldsymbol{b} - \rho \ddot{\boldsymbol{u}}) d\Omega + \int_{\Gamma_t} \hat{\boldsymbol{v}}^T (\boldsymbol{\sigma} \cdot \boldsymbol{n} - \boldsymbol{t}_b) d\Gamma = 0 \tag{1.100}$$

presuming that the essential boundary condition $\underline{u} - \underline{u}_b = \underline{0}$ is automatically satisfied by the choice of function $\underline{u}$ on Γ_u.

We set the test function $\hat{\boldsymbol{v}} = \boldsymbol{v}$ on the boundary Γ and denote it as $\delta\boldsymbol{u} = [\delta u_1, \delta u_2, \delta u_3]^T$ in three-dimensional case, also known as the virtual displacement. The first component of Eq.1.100 reads:

$$-\int_\Omega \delta u_1 (\frac{\partial \sigma_{11}}{\partial x_1} + \frac{\partial \sigma_{12}}{\partial x_2} + \frac{\partial \sigma_{13}}{\partial x_3} + b_1 - \rho \ddot{u}_1) d\Omega + \int_{\Gamma_t} \delta u_1 (\sigma_{11} n_1 + \sigma_{12} n_2 + \sigma_{13} n_3 - t_{b1}) d\Gamma \tag{1.101}$$

Considering the Green's formula, we have:

$$\begin{aligned} \int_\Omega \delta u_1 \frac{\partial \sigma_{11}}{\partial x_1} d\Omega &= -\int_\Omega \frac{\partial \delta u_1}{\partial x_1} \sigma_{11} d\Omega + \int_\Gamma \delta u_1 \sigma_{11} n_1 d\Gamma \\ \int_\Omega \delta u_1 \frac{\partial \sigma_{12}}{\partial x_2} d\Omega &= -\int_\Omega \frac{\partial \delta u_1}{\partial x_2} \sigma_{12} d\Omega + \int_\Gamma \delta u_1 \sigma_{12} n_2 d\Gamma \\ \int_\Omega \delta u_1 \frac{\partial \sigma_{13}}{\partial x_3} d\Omega &= -\int_\Omega \frac{\partial \delta u_1}{\partial x_3} \sigma_{13} d\Omega + \int_\Gamma \delta u_1 \sigma_{13} n_3 d\Gamma \end{aligned} \tag{1.102}$$

Combining Eq.1.102 with the term of 1.101 leads to:

$$\begin{aligned} \int_\Omega (\frac{\partial \delta u_1}{\partial x_1} \sigma_{11} + \frac{\partial \delta u_1}{\partial x_2} \sigma_{12} + \frac{\partial \delta u_1}{\partial x_3} \sigma_{13}) d\Omega + \int_\Omega \delta u_1 \rho \ddot{u}_1 d\Omega - \int_\Omega \delta u_1 b_1 d\Omega \\ - \int_{\Gamma - \Gamma_t} \delta u_1 (\sigma_{11} n_1 + \sigma_{12} n_2 + \sigma_{13} n_3) d\Gamma - \int_{\Gamma_t} \delta u_1 t_{b1} d\Gamma \end{aligned} \tag{1.103}$$

where the set subtraction $\Gamma - \Gamma_t$ is equal to Γ_u given that $\Gamma = \Gamma_u \cup \Gamma_t$. Indeed, since the choice of $\underline{u}$ is restricted so as that $\underline{u} - \underline{u}_b = \underline{0}$ is satisfied on Γ_u, we can omit the fourth integral term of the above 1.103 by restricting that $\delta\underline{u} = \underline{0}$ on Γ_u.

Performing similar procedures over the other two components of Eq.1.100 and combining the results lead to:

$$\begin{aligned}&\int_\Omega \left[\frac{\partial\delta u_1}{\partial x_1}\sigma_{11}+\frac{\partial\delta u_2}{\partial x_2}\sigma_{22}+\frac{\partial\delta u_3}{\partial x_3}\sigma_{33}+\left(\frac{\partial\delta u_1}{\partial x_2}+\frac{\partial\delta u_2}{\partial x_1}\right)\sigma_{12}+\left(\frac{\partial\delta u_2}{\partial x_3}+\frac{\partial\delta u_3}{\partial x_2}\right)\sigma_{23}+\left(\frac{\partial\delta u_1}{\partial x_3}+\frac{\partial\delta u_3}{\partial x_1}\right)\sigma_{13}\right]d\Omega\\ &+\int_\Omega \rho\left(\delta u_1\ddot{u}_1+\delta u_2\ddot{u}_2+\delta u_3\ddot{u}_3\right)d\Omega-\int_\Omega\left(\delta u_1 b_1+\delta u_2 b_2+\delta u_3 b_3\right)d\Omega-\int_{\Gamma_t}\left(\delta u_1 t_{b1}+\delta u_2 t_{b2}+\delta u_3 t_{b3}\right)d\Gamma=0\end{aligned} \tag{1.104}$$

By investigating the first term of the above equation, we could introduce a virtual strain defined and written in Voigt notation as:

$$\delta\boldsymbol{\varepsilon} = [\frac{\partial\delta u_1}{\partial x_1} \quad \frac{\partial\delta u_2}{\partial x_2} \quad \frac{\partial\delta u_3}{\partial x_3} \quad \frac{\partial\delta u_1}{\partial x_2}+\frac{\partial\delta u_2}{\partial x_1} \quad \frac{\partial\delta u_2}{\partial x_3}+\frac{\partial\delta u_3}{\partial x_2} \quad \frac{\partial\delta u_1}{\partial x_3}+\frac{\partial\delta u_3}{\partial x_1}]^T \tag{1.105}$$

The Eq.1.104 can thus be written in index form using summation convention as:

$$\int_\Omega \delta\varepsilon_{ij}\sigma_{ij}d\Omega + \int_\Omega \delta u_i\ \rho\ddot{u}_i d\Omega - \int_\Omega \delta u_i b_i d\Omega - \int_{\Gamma_t} \delta u_i t_{bi} d\Gamma = 0 \tag{1.106}$$

or in tensor form as:

$$\int_\Omega \delta\boldsymbol{\varepsilon}^T\boldsymbol{\sigma}d\Omega + \int_\Omega \delta\boldsymbol{u}^T\rho\ddot{\boldsymbol{u}}d\Omega - \int_\Omega \delta\boldsymbol{u}^T\boldsymbol{b}d\Omega - \int_{\Gamma_t} \delta\boldsymbol{u}^T\boldsymbol{t}_b d\Gamma = 0 \tag{1.107}$$

where $\boldsymbol{\sigma}$ denotes the stress tensor in Voigt notation, for example, $\boldsymbol{\sigma} = [\sigma_{11},\sigma_{22},\sigma_{33},\sigma_{12},\sigma_{23},\sigma_{31}]^T$ in three-dimensional case.

The form of Eq.1.106 or Eq.1.107, corresponding to the statement (1.99), is the weak formulation of the considered elastodynamics problem equivalent to Eq.1.95.

1.3.1.3 Discretization

Taking the integral weak form of Eq.1.98 for example. A common practice for the approximation of the unknown $\underline{u}(\underline{x},t)$ is using piecewise functions times a column vector:

$$\boldsymbol{u}(\underline{x},t) \approx \sum_{i=1}^{n}\boldsymbol{N}_i(\underline{x})\tilde{\boldsymbol{u}}_i(t) = [\boldsymbol{N}_1(\underline{x}),\boldsymbol{N}_2(\underline{x}),\ldots]\begin{Bmatrix}\tilde{\boldsymbol{u}}_1(t)\\ \tilde{\boldsymbol{u}}_2(t)\\ \vdots\end{Bmatrix} = \boldsymbol{N}(\underline{x})\tilde{\boldsymbol{u}}(t) \tag{1.108}$$

where $\boldsymbol{N}_i(\underline{x}) = N_i(\underline{x})\boldsymbol{I}$ is a matrix of *shape function* in terms of independent variables of coordinates $\underline{x}$, $\underline{\tilde{u}}_i(t)$ denotes a vector of nodal displacement parameters dependent on time, and n indicates the total number of nodes of interest. This implies that a spatial mesh by finite elements composed of nodes are required for the approximation.

However, to allow an approximation to be made, we generally prescribe, instead of choosing arbitrarily, the test functions $\boldsymbol{v}$ and $\hat{\boldsymbol{v}}$ being a set of functions:

$$\boldsymbol{v} = \sum_{j=1}^{n} \boldsymbol{w}_j \delta\tilde{\boldsymbol{u}}_j; \quad \hat{\boldsymbol{v}} = \sum_{j=1}^{n} \hat{\boldsymbol{w}}_j \delta\tilde{\boldsymbol{u}}_j \tag{1.109}$$

with $\delta\tilde{\boldsymbol{u}}_j$ being arbitrary functions.

The statement (1.98) thus changes to:

$$\sum_{j}^{n} \delta\tilde{\boldsymbol{u}}_j^T \left[\int_{\Omega} \boldsymbol{w}_j \boldsymbol{\mathcal{A}}(\boldsymbol{N}\tilde{\boldsymbol{u}}) d\Omega + \int_{\Gamma} \hat{\boldsymbol{w}}_j \boldsymbol{\mathcal{B}}(\boldsymbol{N}\tilde{\boldsymbol{u}}) d\Gamma \right] = 0 \tag{1.110}$$

As $\delta\tilde{\boldsymbol{u}}_j$ are arbitrary, we can obtain the following set of equations for solving the parameter $\underline{\tilde{u}}$:

$$\int_{\Omega} \boldsymbol{w}_j \boldsymbol{\mathcal{A}}(\boldsymbol{N}\tilde{\boldsymbol{u}}) d\Omega + \int_{\Gamma} \hat{\boldsymbol{w}}_j \boldsymbol{\mathcal{B}}(\boldsymbol{N}\tilde{\boldsymbol{u}}) d\Gamma = \boldsymbol{0}; \quad j = 1, 2, ..., n \tag{1.111}$$

Indeed, $\boldsymbol{\mathcal{A}}(\boldsymbol{N}\tilde{\boldsymbol{u}})$ and $\boldsymbol{\mathcal{B}}(\boldsymbol{N}\tilde{\boldsymbol{u}})$ in the above equation can be regarded as representing the residual or error after applying the approximation of $\underline{u}$; $\boldsymbol{w}_j$ and $\hat{\boldsymbol{w}}_j$ are the weights for the residual. Such a method for solving the approximation is thus called the *method of weighted residual*. In general, the weights can be determined using different strategies. The most common choice in FEM is the *Galerkin method* where we take the shape functions and prescribe $\boldsymbol{w}_j = \boldsymbol{N}_j$.

Back to our elastodynamics problem of Eq.1.107, the virtual displacements $\delta\underline{u}$ can thus be considered as the shape functions times arbitrary parameters, $\delta\boldsymbol{u} = \sum_j \boldsymbol{N}_j \delta\tilde{\boldsymbol{u}}_j = \boldsymbol{N}\delta\tilde{\boldsymbol{u}}$. The virtual strain can also be computed as $\delta\boldsymbol{\varepsilon} = \boldsymbol{S}\delta\boldsymbol{u} = \boldsymbol{S}\boldsymbol{N}\delta\tilde{\boldsymbol{u}} = \boldsymbol{B}\delta\tilde{\boldsymbol{u}}$ where $\boldsymbol{S}$ is the strain differential operator and $\boldsymbol{B}$ denotes the strain-displacement matrix. Based on the approximation by $\boldsymbol{u} = \boldsymbol{N}\tilde{\boldsymbol{u}}$, the weak formulation Eq.1.107 can finally be discretized as:

$$\delta\tilde{\boldsymbol{u}}^T \left(\int_{\Omega} \boldsymbol{B}^T \boldsymbol{\sigma} d\Omega + \int_{\Omega} \rho \boldsymbol{N}^T \boldsymbol{N} \ddot{\tilde{\boldsymbol{u}}} d\Omega - \int_{\Omega} \boldsymbol{N}^T \boldsymbol{b} d\Omega - \int_{\Gamma_t} \boldsymbol{N}^T \boldsymbol{t}_b d\Gamma \right) = 0 \tag{1.112}$$

Noting that the functions $\delta\tilde{\boldsymbol{u}}$ are arbitrary, we can obtain the discrete system which is the basis and widely used for numerical implementation of FEM:

$$\boldsymbol{M}\ddot{\tilde{\boldsymbol{u}}} + \boldsymbol{f}^{int} = \boldsymbol{f}^{ext} \tag{1.113}$$

where $\boldsymbol{M}$ is termed the *mass matrix*, $\boldsymbol{f}^{int}$ denotes the *internal force vector* resulting from the internal stress and $\boldsymbol{f}^{ext}$ indicates the *external force vector* due to body force and applied tractions. From Eq.1.112, it is obvious that:

$$\begin{aligned} \boldsymbol{M} &= \int_{\Omega} \rho \boldsymbol{N}^T \boldsymbol{N} d\Omega \\ \boldsymbol{f}^{int} &= \int_{\Omega} \boldsymbol{B}^T \boldsymbol{\sigma} d\Omega \\ \boldsymbol{f}^{ext} &= \int_{\Omega} \boldsymbol{N}^T \boldsymbol{b} d\Omega + \int_{\Gamma_t} \boldsymbol{N}^T \boldsymbol{t}_b d\Gamma \end{aligned} \tag{1.114}$$

In the case of linear elasticity, the stress-strain relation can be concluded from Eq.1.42 and expressed as:

$$\boldsymbol{\sigma} = \boldsymbol{D}\boldsymbol{\varepsilon} \tag{1.115}$$

where $\boldsymbol{D}$ is the stress-strain matrix containing elastic moduli. Similar to the virtual strain, a displacement method can be used to obtain the strains from the nodal displacements:

$$\boldsymbol{\varepsilon} = \boldsymbol{B}\tilde{\boldsymbol{u}} \tag{1.116}$$

and the internal force vector thus becomes:

$$\boldsymbol{f}^{int} = \left(\int_{\Omega} \boldsymbol{B}^T \boldsymbol{D}\boldsymbol{B} d\Omega\right) \tilde{\boldsymbol{u}} = \boldsymbol{K}\tilde{\boldsymbol{u}} \tag{1.117}$$

where $\boldsymbol{K}$ is known as the *stiffness matrix*. In addition, for the convergence of elastic media problem, we usually apply a damping term $\boldsymbol{C}\dot{\tilde{\boldsymbol{u}}}$ to the left side of Eq.1.113 and the *damping matrix* $\boldsymbol{C}$ can be regulated as $\boldsymbol{C} = \alpha_M \boldsymbol{M} + \alpha_K \boldsymbol{K}$ where α_M and α_K are damping coefficients to be adjusted.

In other cases such as viscoelasticity, the internal force vector is basically computed directly from the original form in Eq.1.114. Furthermore, all the integrals are generally approximated by Gaussian quadrature rules, such as Gauss-Legendre quadrature of classical FEM and Gauss-Lobatto quadrature of spectral element method, etc.

The above introduction is mainly dedicated to spatial discretization by means of piecewise polynomials, i.e. the shape functions or basis functions. In terms of the temporal discretization and time integration strategies, and more details concerning the numerical implementation of the above matrices and the case of viscoelasticity, we will have a further discussion in Chapter 2 within the framework of wave propagation of MRE.

1.3.2 Other methods

In addition to classic FEM formulation, some other methods have also emerged and play important roles in numerical analysis with different characteristics.

The Finite Difference Method (FDM) is a numerical method for solving differential equations based on the discretization using finite difference. It can be derived from the Taylor's theorem and applied for both spatial and temporal domain. Take a time-dependent function $f(t)$ as an example. Define Δt as the time step after temporal discretization. At time $t = t_0$, the approximation of the first-order derivative by considering a forward difference can be written as:

$$f'(t_0) = \frac{f(t_0 + \Delta t) - f(t_0)}{\Delta t} \tag{1.118}$$

and the approximation of the second-order derivative by a central difference reads:

$$f''(t_0) = \frac{f(t_0 + \Delta t) - 2f(t_0) + f(t_0 - \Delta t)}{(\Delta t)^2} \tag{1.119}$$

Such discretization based on regular mesh or grids converts the differential equations into a system of linear equations which can be solved by linear algebra techniques. This makes FDM much easier to implement than FEM, but less flexible and less adaptable to curved boundary than FEM. In practice, we usually combine these two methods, as studied by Frehner *et al.* [FRE 08] in terms of elastic waves. For example, in this work, we use FEM based methods for spatial domain discretization and FDM for time integration.

The Spectral Element Method (SEM) is another formulation similar to FEM. It was first proposed by Patera in 1984 for the domain of fluid dynamics [PAT 84]. The principles are basically the same as those of FEM, except that SEM applies high order piecewise polynomials as basis functions. In general, very high degree Lagrange polynomials are used for the basis. The Lagrangian interpolation points within an element are distributed non-uniformly over the Gauss-Lobatto-Legendre (GLL) points. The same points are also used for the quadrature, naturally leading to the mass lumping which reduces the complexity of mass matrix. SEM has better performance than FEM in accuracy and convergence rate, due to the polynomials of high degree. However, FEM is always more flexible in modeling complex geometries. Some works based on SEM for modeling wave propagation can be found, for example, in [HEN 10, XU 17].

The eXtended Finite Element Method (XFEM) is the numerical technique first introduced by Moës *et al.* in 1999 for the domain of fracture mechanics [MOË 99] and based on FEM and the partition of unity method [MEL 96]. In XFEM, the key idea is to enrich the elements in the vicinity of interface by additional degrees of freedom, leading to the interface location being independent of mesh. XFEM is hence featured by the great advantage of being remeshing-free. Besides, with respect to FEM, it is more rapid and has the same, even better accuracy. It can be formulated in terms of displacement as:

$$\begin{aligned} \boldsymbol{u}^{XFEM} &= \boldsymbol{u}^{FEM} + \boldsymbol{u}^{enr} \\ \text{with } \boldsymbol{u}^{FEM} &= \sum_{i \in I} \boldsymbol{N}_i \boldsymbol{u}_i \\ \boldsymbol{u}^{enr} &= \sum_{j \in J} \boldsymbol{N}_j F \boldsymbol{a}_j \end{aligned} \tag{1.120}$$

where $\boldsymbol{N}_i$, $\boldsymbol{N}_j$ are shape functions, $\boldsymbol{u}_i$ is FEM classical degree of freedom, $\boldsymbol{a}_j$ is enriched degree of freedom, F is the enrichment function, I and J are the sets of regular and enriched nodes, respectively. $\boldsymbol{u}^{enr}$, represented as enriched displacement, is only applied for elements around interface and equals zero otherwise. In addition to strong discontinuity like the displacements in cracks, this method also allows the modeling of weak discontinuity like the strains across interface of inhomogeneities, such as holes and inclusions [SUK 01]. To the best of our knowledge, XFEM has not been used in MRE studies for modeling the inclusions yet. Therefore, we have implemented this method in our work and expect to introduce its power to the MRE community, which will be presented in Chapter 3.

1.4 Novelty of this work

As presented in the precedent section, an elastodynamics problem can be converted from the analytical differential formulations into a discrete system and thus be solved by numerical methods, especially like FEM. The power of FEM makes it popular not only in academic researches but also in industrial processes. This is the same case for MRE studies where FEM plays a key role in modeling wave propagation, analysing different factors and even reconstructing mechanical parameters. This PhD project had an initial objective for the third one, namely developing a new numerical model/method to improve the MRE reconstruction of viscoelastic properties, while taking into account the behavior law of different tissue components. To this end, we first developed a homemade Fortran solver based on FEM formulations and then implemented XFEM. The three main points that we aim to address in this thesis are:

1. the development of a numerical model based on FEM for accurately simulating small-amplitude mechanical wave propagation in a linear, locally homogeneous, isotropic and viscoelastic medium;

2. the implementation of XFEM formulations into our developed FEM-based solver for modeling inhomogeneous materials;

3. the investigation, by means of the implemented numerical tool, of the plane wave behaviors across a plane interface between two viscoelastic media, and of a proposed metric for measuring the steady state in MRE.

The first point will be addressed in Chapter 2. Details concerning numerical implementation of FEM formulations are introduced. Using the developed solver, we simulate the propagation of plane wave. The numerical model is validated by comparison with the analytical model. A parametric study is performed to reveal the effect of different parameters on wave damping.

The second point will be addressed in Chapter 3. The principles of XFEM are introduced and the element partitions are illustrated. Based on the FEM implementation, XFEM model is integrated and some numerical examples are given. Indeed, to our knowledge, XFEM is not known to MRE community. Through this chapter, we would like to introduce to the community the power of XFEM: readily and efficiently modeling the inhomogeneity whatever the scale is. A multi-scale simulation tool can thus be expected.

The third point will be addressed in Chapter 4 and 5.

The inhomogeneity interface is not much studied in MRE and the mode conversion across interface is usually neglected. Thus, in Chapter 4, the implemented XFEM model is first applied to model the wave conversion across a plane interface between viscoelastic materials. The results are compared with those by FEM model and analytical model in a parametric study; the effect of different parameters on wave conversion are illustrated. Then, a random-shape inclusion is modeled in a pseudo-practical MRE application; the advantages of XFEM over FEM are further demonstrated.

In MRE, while reaching steady state is generally required for models under study, a quantitative measurement of the steady-state property is not available. Thus, in Chapter 5, a metric is proposed to measure the steady state of MRE displacement fields. Its threshold is investigated based on homogeneous and inhomogeneous models, using the numerical implementation. The metric is also applied to MRE breast models and a parametric study is performed; the effect of different experimental parameters on the system steady state is illustrated.

We end this thesis with conclusions and perspectives. In particular, the use of XFEM model is expected to promote the MRE reconstruction method based on CNN model as discussed in section 1.1.3.3.

Chapter 2

Viscoelastic waves modeling

In this chapter, we present the FEM implementation of a numerical model for waves propagation in a homogeneous viscoelastic medium. A plane wave model is proposed for numerical validation. Using the developed tool, a parametric study based on the plane shear wave model is performed to investigate the effect of different parameters on the wave damping.

Contents

2.1 Introduction

As presented in Chapter 1, FEM is a numerical method which converts differential equations describing a specific problem into a discrete system that is numerically solved to provide approximate solutions. It has the advantages of handling complex geometries and boundary conditions. FEM has gained great popularity among different domains, including the MRE community in which this method is used to model wave propagation within human tissues. In early literature, Azar *et al.* [AZA 00, AZA 01] developed the FEM models in elastography for predicting breast deformations. Chen *et al.* [CHE 05, CHE 06] examined, by a finite element model, the effects of boundary conditions, geometry, pretension and frequency on MRE measurements. Bilasse *et al.* [BIL 18] developed a 2D finite element model for simulating shear waves in inhomogeneous soft tissues, with low computational cost. Recently, McGarry *et al.* [MCG 20] proposed an inhomogeneous, nearly incompressible, transverse isotropic (NITI) finite element model for 3D simulations of wave propagation in the brain, for MRE purposes.

The objective of this chapter is to introduce a FEM-based numerical model for propagation of time-harmonic waves with small amplitude in a linear, homogeneous, isotropic and viscoelastic medium. A homemade explicit solver written in Fortran was implemented from scratch. This model is based on elastodynamics, described by the constitutive equation Eq.1.51, and the discrete system of Eq.1.113 is used for FEM implementation. As can be seen later in Chapter 3, this homogeneous model is the basis of further implementation of XFEM for an inhomogeneous model.

In this chapter, we firstly present the FEM implementation details, including the numerical quadrature of matrices in Eq.1.114, the explicit time integration schemes and the computation of internal forces for implementing viscoelasticity. Secondly, to validate our FEM implementation, a plane wave model is proposed in two-dimensions under the plane strain hypothesis. Finally, the effect of different parameters on wave damping is investigated via a parametric study.

2.2 FEM implementation of viscoelastic materials

In this section, the details of our FEM solver are presented. Firstly, the basic components such as the shape functions and mass matrix, etc. are analysed, and we will see how to implement them numerically. Secondly, several time integration schemes are introduced. In particular, an explicit scheme for reducing spurious oscillations in wave propagation simulation is detailed and implemented in our solver. Finally, the numerical implementation of viscoelasticity, especially the SLS model as described in Chapter 1, is presented based on two different algorithms.

It should be noted that some matrices in subsection 2.2.1 are mainly considered in the purely elastic case, i.e. the stress-strain $\boldsymbol{D}$, stiffness $\boldsymbol{K}$ and damping $\boldsymbol{C}$. Since the body force is not considered in our solver and the surface force can be applied directly through nodes, implementation details for $\underline{f}^{ext}$ are not presented. For convenience, we

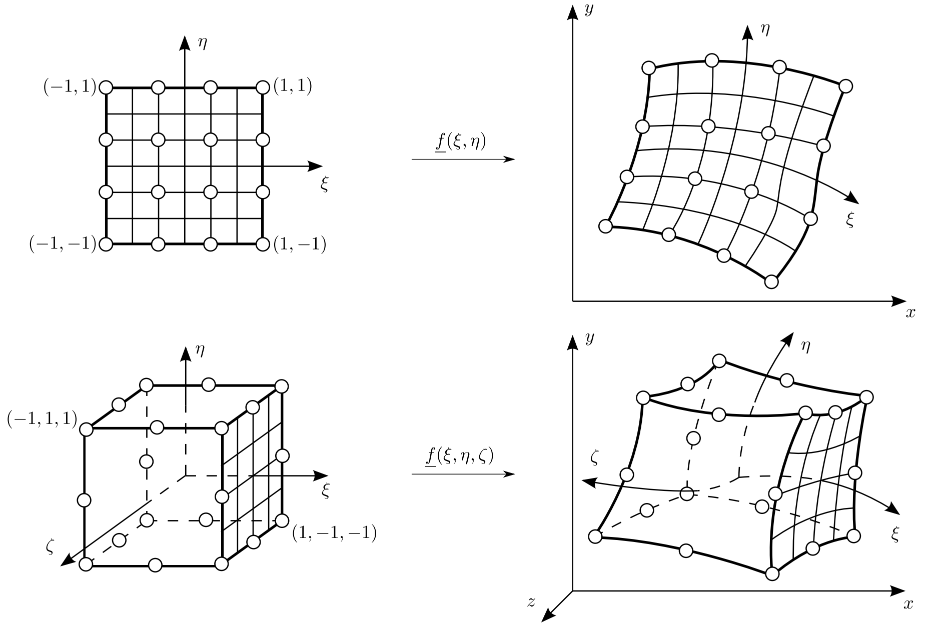

Figure 2.1: Mapping from local parametric coordinates into global Cartesian coordinates.

herein let the coordinates and displacements be, (x,y) and (u,v) in 2D case, (r,θ,z) and (u_r,u_θ,u_z) in 2D axisymmetric case, (x,y,z) and (u,v,w) in 3D case, respectively. In 2D axisymmetric case, the three coordinates are defined in a cylindrical coordinate system, with r denoting the axial distance from the z-axis, θ denoting the azimuth angle and z indicating the axial coordinate. Furthermore, we define that the nodal displacement vector $\underline{\tilde{u}}$ is written, for example in 3D case, in the order $[u_1,v_1,w_1,u_2,v_2,w_2,...]^T$ instead of $[u_1,u_2,...,v_1,v_2,...,w_1,w_2,...]^T$, where the subscript indicates node number.

2.2.1 Matrices implementation

2.2.1.1 Basis: parametric coordinates

In academic problems, elements such as regular quadrangle and hexahedron would be able to discretize the geometry under study. However, more complex geometries require irregular elements. A "mapping" is then typically applied from regular elements into irregular elements. This is a common practice in FEM programs.

Mapping can be illustrated by an example of 2D and 3D cases in Fig.2.1. In 2D, a square element is chosen as the "parent" element with local coordinates ξ (xi) and η (eta) both within the domain $[-1,1]$. Similarly in 3D, a cube element is chosen with local coordinates ξ, η and ζ (zeta) all within the domain $[-1,1]$. A one-to-one correspondence between the local coordinates and the global Cartesian coordinates can be established by the mapping functions. For example in 3D we have $\underline{f}(\xi,\eta,\zeta)$ acting as:

$$\begin{aligned} x &= f_x(\xi,\eta,\zeta) \\ y &= f_y(\xi,\eta,\zeta) \\ z &= f_z(\xi,\eta,\zeta) \end{aligned} \tag{2.1}$$

We call such normalized coordinates and regular elements as parametric coordinates and parametric elements, respectively. As shown later, this choice of coordinates is convenient for numerical integration.

2.2.1.2 Shape function *N*

A key idea of FEM is the approximation of the unknown by an expansion, as stated in Eq.1.108. Taking the first component as an example, we have the approximation:

$$u(\underline{x},t) = \sum_{a=1}^{n} N_a(\underline{x})\tilde{u}_a(t) \tag{2.2}$$

where n is the number of nodes of interest, N_a is the shape function or basis function of node a, and $\tilde{u}_a$ denotes the first component of displacement of node a.

On the other hand, the shape function in terms of local coordinates can be used to define the shape of distorted element in a similar way, corresponding to the mapping in Eq.2.1. Taking the first component as an example, we have the interpolation:

$$x(\underline{\xi}) = \sum_{a=1}^{n'} N'_a(\underline{\xi})x_a \tag{2.3}$$

where $\boldsymbol{\xi} = [\xi,\eta,\zeta]^T$ is the local coordinates vector, n' is the number of points of interest, N'_a is the shape function in terms of local coordinates, and x_a indicates the x coordinate of point a. If $n = n'$ and the same points are used for the unknown approximation and the geometry definition, we would have the same functions, i.e. $N = N'$. Such elements are called *isoparametric* and are widely used in FEM and also employed in our solver. In what follows, the two types of shape functions are no more differentiated.

As a rigid body movement does not cause strain, shape functions verify:

$$\sum_{a=1}^{n} N_a(\underline{x}) = 1 \tag{2.4}$$

at any point $\underline{x}$ of the domain. This property is called *partition of unity*. In addition, each shape function verifies:

$$N_a(\underline{x}_b) = \delta_{ab} = \begin{cases} 1, & a = b \\ 0, & a \neq b \end{cases} \tag{2.5}$$

indicating that the shape function equals 1 at the “host” node but equals 0 at the other nodes.

With the isoparametric coordinates, the most common choice of shape functions satisfying the above requirements is the *Lagrange polynomials* written in ξ coordinate as:

$$L_k^{n_1}(\xi) = \prod_{\substack{i=0 \\ i\neq k}}^{n_1} \frac{\xi-\xi_i}{\xi_k-\xi_i} = \frac{(\xi-\xi_0)(\xi-\xi_1)\cdots(\xi-\xi_{k-1})(\xi-\xi_{k+1})\cdots(\xi-\xi_{n_1})}{(\xi_k-\xi_0)(\xi_k-\xi_1)\cdots(\xi_k-\xi_{k-1})(\xi_k-\xi_{k+1})\cdots(\xi_k-\xi_{n_1})} \tag{2.6}$$

The shape function is obtained by the product of polynomials in each coordinate. For example, in three-dimensions, it gives:

$$N_a(\underline{\xi}) = L_i^{n_1}(\xi)\,L_j^{n_2}(\eta)\,L_k^{n_3}(\zeta) \tag{2.7}$$

where n_1, n_2, n_3 are the node numbers in ξ, η, ζ coordinates, respectively, and i, j, k indicate the position of node a in ξ, η, ζ coordinates, respectively. Taking a linear quadrilateral element with four nodes as an example, we could write:

$$N_a(\underline{\xi}) = \frac{1}{4}(1+\xi_a\xi)(1+\eta_a\eta) \tag{2.8}$$

where ξ_a and η_a are the local coordinates of node a ($a = 1,2,3,4$).

Sometimes, as can be seen in section 2.2.1.3, we need to compute the derivatives of shape functions with respect to global Cartesian coordinates. To this end, a transformation can be carried out using usual rules of partial differentiation and formulated as:

$$\begin{Bmatrix} \frac{\partial N_a}{\partial \xi} \\ \frac{\partial N_a}{\partial \eta} \\ \frac{\partial N_a}{\partial \zeta} \end{Bmatrix} = \begin{bmatrix} \frac{\partial x}{\partial \xi} & \frac{\partial y}{\partial \xi} & \frac{\partial z}{\partial \xi} \\ \frac{\partial x}{\partial \eta} & \frac{\partial y}{\partial \eta} & \frac{\partial z}{\partial \eta} \\ \frac{\partial x}{\partial \zeta} & \frac{\partial y}{\partial \zeta} & \frac{\partial z}{\partial \zeta} \end{bmatrix} \begin{Bmatrix} \frac{\partial N_a}{\partial x} \\ \frac{\partial N_a}{\partial y} \\ \frac{\partial N_a}{\partial z} \end{Bmatrix} = \boldsymbol{J} \begin{Bmatrix} \frac{\partial N_a}{\partial x} \\ \frac{\partial N_a}{\partial y} \\ \frac{\partial N_a}{\partial z} \end{Bmatrix} \tag{2.9}$$

where $\boldsymbol{J}$ is referred to as the *Jacobian matrix*. Indeed, the left side of the above equation can be easily determined by the shape functions in terms of local coordinates as given in Eq.2.7, and $\boldsymbol{J}$ can also be calculated by the mappings as given in Eq.2.3. The derivatives of interest can thus be computed by inverting the system as:

$$\begin{Bmatrix} \frac{\partial N_a}{\partial x} \\ \frac{\partial N_a}{\partial y} \\ \frac{\partial N_a}{\partial z} \end{Bmatrix} = \boldsymbol{J}^{-1} \begin{Bmatrix} \frac{\partial N_a}{\partial \xi} \\ \frac{\partial N_a}{\partial \eta} \\ \frac{\partial N_a}{\partial \zeta} \end{Bmatrix} = \begin{bmatrix} \sum_a \frac{\partial N_a}{\partial \xi} x_a & \sum_a \frac{\partial N_a}{\partial \xi} y_a & \sum_a \frac{\partial N_a}{\partial \xi} z_a \\ \sum_a \frac{\partial N_a}{\partial \eta} x_a & \sum_a \frac{\partial N_a}{\partial \eta} y_a & \sum_a \frac{\partial N_a}{\partial \eta} z_a \\ \sum_a \frac{\partial N_a}{\partial \zeta} x_a & \sum_a \frac{\partial N_a}{\partial \zeta} y_a & \sum_a \frac{\partial N_a}{\partial \zeta} z_a \end{bmatrix}^{-1} \begin{Bmatrix} \frac{\partial N_a}{\partial \xi} \\ \frac{\partial N_a}{\partial \eta} \\ \frac{\partial N_a}{\partial \zeta} \end{Bmatrix} \tag{2.10}$$

Finally, for the approximation Eq.1.108 stating that $\boldsymbol{u} = \boldsymbol{N}\tilde{\boldsymbol{u}}$, we could write a matrix of shape functions $\boldsymbol{N} = [\boldsymbol{N}_1, \boldsymbol{N}_2, \ldots]$ where each component $\boldsymbol{N}_a$ reads, in three-dimensional case for example:

$$\boldsymbol{N}_a = \begin{bmatrix} N_a & 0 & 0 \\ 0 & N_a & 0 \\ 0 & 0 & N_a \end{bmatrix} \tag{2.11}$$

2.2.1.3 Strain-displacement $\boldsymbol{B}$

The strain-displacement matrix $\boldsymbol{B}$, as the name suggests, relates the element strain tensor $\underline{\underline{\varepsilon}}$ to the nodal displacement tensor $\underline{\tilde{u}}$ by the Eq.1.116 stating that $\boldsymbol{\varepsilon} = \boldsymbol{B}\tilde{\boldsymbol{u}}$.

To derive this matrix, we could start with the strain definition, for example the explicit form in three-dimensions of Eq.1.33. It can be rewritten as $\boldsymbol{\varepsilon} = \boldsymbol{S}\boldsymbol{u}$ where $\underline{\underline{\varepsilon}}$ is the strain tensor in Voigt notation, $\boldsymbol{S}$ denotes the strain differential operator and $\underline{u}$ is the displacement tensor. Obviously, we have:

$$\boldsymbol{\varepsilon} = \left\{ \begin{matrix} \varepsilon_{xx} \\ \varepsilon_{yy} \\ \varepsilon_{zz} \\ 2\varepsilon_{xy} \\ 2\varepsilon_{yz} \\ 2\varepsilon_{zx} \end{matrix} \right\} = \left\{ \begin{matrix} \frac{\partial u}{\partial x} \\ \frac{\partial v}{\partial y} \\ \frac{\partial w}{\partial z} \\ \frac{\partial u}{\partial y} + \frac{\partial v}{\partial x} \\ \frac{\partial v}{\partial z} + \frac{\partial w}{\partial y} \\ \frac{\partial u}{\partial z} + \frac{\partial w}{\partial x} \end{matrix} \right\} = \begin{bmatrix} \frac{\partial}{\partial x} & 0 & 0 \\ 0 & \frac{\partial}{\partial y} & 0 \\ 0 & 0 & \frac{\partial}{\partial z} \\ \frac{\partial}{\partial y} & \frac{\partial}{\partial x} & 0 \\ 0 & \frac{\partial}{\partial z} & \frac{\partial}{\partial x} \\ \frac{\partial}{\partial z} & 0 & \frac{\partial}{\partial x} \end{bmatrix} \left\{ \begin{matrix} u \\ v \\ w \end{matrix} \right\} = \boldsymbol{S}\boldsymbol{u} \tag{2.12}$$

Considering the approximation by Eq.1.108, the strain tensor can be further developed as $\boldsymbol{\varepsilon} = \boldsymbol{S}\boldsymbol{u} = \boldsymbol{S}\boldsymbol{N}\tilde{\boldsymbol{u}} = \boldsymbol{B}\tilde{\boldsymbol{u}}$. From the definition of the matrix of shape functions and its component in Eq.2.11, we have the matrix $\boldsymbol{B} = [\boldsymbol{B}_1, \boldsymbol{B}_2, \ldots]$ where each component $\boldsymbol{B}_a$ reads:

$$\boldsymbol{B}_a = \begin{bmatrix} \frac{\partial N_a}{\partial x} & 0 & 0 \\ 0 & \frac{\partial N_a}{\partial y} & 0 \\ 0 & 0 & \frac{\partial N_a}{\partial z} \\ \frac{\partial N_a}{\partial y} & \frac{\partial N_a}{\partial x} & 0 \\ 0 & \frac{\partial N_a}{\partial z} & \frac{\partial N_a}{\partial y} \\ \frac{\partial N_a}{\partial z} & 0 & \frac{\partial N_a}{\partial x} \end{bmatrix} \tag{2.13}$$

The elements of matrix $\boldsymbol{B}$ can be calculated by the inversion of the Jacobian matrix and the derivatives of shape functions with respect to the local coordinates, as presented in the previous subsection.

In particular, the strain tensor in cylindrical coordinates reads:

$$\boldsymbol{\varepsilon} = \left\{ \begin{matrix} \varepsilon_{rr} \\ \varepsilon_{\theta\theta} \\ \varepsilon_{zz} \\ 2\varepsilon_{r\theta} \\ 2\varepsilon_{\theta z} \\ 2\varepsilon_{zr} \end{matrix} \right\} = \left\{ \begin{matrix} \frac{\partial u_r}{\partial r} \\ \frac{1}{r}\frac{\partial u_\theta}{\partial \theta} + \frac{u_r}{r} \\ \frac{\partial u_z}{\partial z} \\ \frac{1}{r}\frac{\partial u_r}{\partial \theta} + \frac{\partial u_\theta}{\partial r} - \frac{u_\theta}{r} \\ \frac{\partial u_\theta}{\partial z} + \frac{1}{r}\frac{\partial u_z}{\partial \theta} \\ \frac{\partial u_r}{\partial z} + \frac{\partial u_z}{\partial r} \end{matrix} \right\} \tag{2.14}$$

For the 2D axisymmetric case, we have $u_\theta = 0$ and $\frac{\partial}{\partial\theta} = 0$, reducing the strain tensor to:

$$\boldsymbol{\varepsilon} = \begin{Bmatrix} \varepsilon_{rr} \\ \varepsilon_{\theta\theta} \\ \varepsilon_{zz} \\ 2\varepsilon_{zr} \end{Bmatrix} = \begin{Bmatrix} \frac{\partial u_r}{\partial r} \\ \frac{u_r}{r} \\ \frac{\partial u_z}{\partial z} \\ \frac{\partial u_r}{\partial z} + \frac{\partial u_z}{\partial r} \end{Bmatrix} = \begin{bmatrix} \frac{\partial}{\partial r} & 0 \\ \frac{1}{r} & 0 \\ 0 & \frac{\partial}{\partial z} \\ \frac{\partial}{\partial z} & \frac{\partial}{\partial r} \end{bmatrix} \begin{Bmatrix} u_r \\ u_z \end{Bmatrix} \tag{2.15}$$

Similarly, the matrix $\boldsymbol{B}$ components can be developed as:

$$\boldsymbol{B}_a = \begin{bmatrix} \frac{\partial N_a}{\partial r} & 0 \\ \frac{N_a}{r} & 0 \\ 0 & \frac{\partial N_a}{\partial z} \\ \frac{\partial N_a}{\partial z} & \frac{\partial N_a}{\partial r} \end{bmatrix} \tag{2.16}$$

2.2.1.4 Stress-strain $\boldsymbol{D}$

The stress-strain matrix $\boldsymbol{D}$, describing the constitutive law, connects the stress tensor $\underline{\underline{\sigma}}$ to the strain tensor $\underline{\underline{\varepsilon}}$ as $\boldsymbol{\sigma} = \boldsymbol{D}\boldsymbol{\varepsilon}$. It is mostly applied in linear elasticity where the relation between stress and strain can be expressed explicitly by a matrix. For example, in three-dimensions, we can derive from Eq.1.42:

$$\boldsymbol{D} = \begin{bmatrix} \lambda+2\mu & \lambda & \lambda & 0 & 0 & 0 \\ \lambda & \lambda+2\mu & \lambda & 0 & 0 & 0 \\ \lambda & \lambda & \lambda+2\mu & 0 & 0 & 0 \\ 0 & 0 & 0 & \mu & 0 & 0 \\ 0 & 0 & 0 & 0 & \mu & 0 \\ 0 & 0 & 0 & 0 & 0 & \mu \end{bmatrix} \tag{2.17}$$

and in two-dimensions and plane strain, including axisymmetry, deriving from Eq.1.45 by adding the $\sigma_{zz} - \varepsilon_{zz}$ term, we have:

$$\boldsymbol{D} = \begin{bmatrix} \lambda+2\mu & \lambda & \lambda & 0 \\ \lambda & \lambda+2\mu & \lambda & 0 \\ \lambda & \lambda & \lambda+2\mu & 0 \\ 0 & 0 & 0 & \mu \end{bmatrix} \tag{2.18}$$

2.2.1.5 Mass $\boldsymbol{M}$

As presented in section 1.3.1.3, several integrals should be calculated for the matrices in FEM, such as the mass matrix $\boldsymbol{M} = \int_\Omega \rho \boldsymbol{N}^T \boldsymbol{N} d\Omega$ in Eq.1.114. First of all, considering isoparametric coordinates, a transformation of the integral domain can be carried out with the help of the Jacobian matrix determinant J. For that purpose, the differential $d\Omega$ needs to be explicit. Indeed, we have $d\Omega = dxdydz$ for 3D, $d\Omega = tdxdy$ with t the thickness for

2D plane stress, $d\Omega = dx\,dy$ for 2D plane strain and $d\Omega = 2\pi r\,dr\,dz$ for 2D axisymmetry. For example, a volume integral in three-dimensions is developed for the element as:

$$\boldsymbol{M}^e = \int_{\Omega^e} \rho \boldsymbol{N}^T \boldsymbol{N} dx\,dy\,dz = \int_{-1}^{1}\int_{-1}^{1}\int_{-1}^{1} \rho \boldsymbol{N}^T \boldsymbol{N} J(\xi,\eta,\zeta) d\xi\, d\eta\, d\zeta \tag{2.19}$$

where $\boldsymbol{M}^e$ is the element mass matrix, Ω^e the element domain and $J(\xi,\eta,\zeta) = \det \boldsymbol{J}$. Element matrices are then assembled into the system matrix as $\boldsymbol{M} = \sum_e \boldsymbol{M}^e$. Similar transformation process can also be performed for 1D and 2D cases.

While the limits of integral are simple, the integrand functions are generally too complicated. The numerical integration, also termed *quadrature*, has to be used. This method approximates the definite integral of a function by means of weighted sum of function values at certain points within the integral domain. The most widely used quadrature rule in FEM would be the Gauss-Legendre quadrature. In one-dimension, for a function $f(\xi)$, it is stated as:

$$\int_{-1}^{1} f(\xi) d\xi \approx \sum_{i=1}^{n} f(\xi_i) w_i \tag{2.20}$$

where w_i are the weighting coefficients and ξ_i the sampling points. With the weights and positions listed in Tab.2.1, the Gaussian quadrature of n points allows to accurately calculate the integral only if the function $f(\xi)$ can be approximated by a polynomial of degree $2n-1$ or less in the range $[-1,1]$.

Table 2.1: Points positions and weights of Gaussian quadrature.

Points number n	Positions ξ_i	Weights w_i
1	0	2
2	$\pm\frac{1}{\sqrt{3}}$	1
3	0	$\frac{8}{9}$
	$\pm\sqrt{\frac{3}{5}}$	$\frac{5}{9}$

In multidimensional cases, the quadrature can also be applied one coordinate after another. The above transformed integral in Eq.2.19 becomes:

$$\boldsymbol{M}^e = \sum_{k=1}^{n_3}\sum_{j=1}^{n_2}\sum_{i=1}^{n_1} \rho \boldsymbol{N}_{ijk}^T \boldsymbol{N}_{ijk} J_{ijk}\, w_i w_j w_k \tag{2.21}$$

where n_1, n_2, n_3 denote the sampling points numbers in ξ, η, ζ coordinates, respectively, and the subscript $_{ijk}$ indicates the point (ξ_i, η_j, ζ_k). We usually take the same number of points in each direction, and the above multi-summation is often reduced to a single one over $m = n_1 \times n_2 \times n_3$ unique points. Written in block matrix corresponding to row partition a and column partition b, the element mass matrix finally becomes:

$$\boldsymbol{M}_{ab}^e = \sum_{l=1}^{m} \rho \boldsymbol{N}_a(\xi_l,\eta_l,\zeta_l) \boldsymbol{N}_b(\xi_l,\eta_l,\zeta_l) J(\xi_l,\eta_l,\zeta_l) W_l \tag{2.22}$$

with W_l the product of all weights w_i and $\boldsymbol{N}_a, \boldsymbol{N}_b$ given by Eq.2.11. This matrix is known as *consistent mass matrix*. However, in numerical practice, the mass is often physically lumped/distributed at the nodes, leading to a diagonal mass matrix, known as *lumped mass matrix*, which dramatically reduces the cost of matrix inversion. For example, a simple practice for mass lumping is the row-sum technique, for each row, summing all the elements to the diagonal one. This technique can indeed provide almost identical results, even more accurate in some cases, and is hence employed in our solver.

2.2.1.6 Stiffness $\boldsymbol{K}$

The stiffness matrix $\boldsymbol{K}$ is derived from the calculation of internal forces in linear elasticity problems, as presented in Eq.1.117. It is hence mainly used in linear elasticity for calculating the internal force. In other cases such as viscoelasticity, the internal forces are typically computed directly from the original form in Eq.1.114, which will be further discussed in section 2.2.3 in terms of the detailed implementation.

Let us recall that in linear elasticity, we have:

$$\boldsymbol{K} = \int_{\Omega} \boldsymbol{B}^T \boldsymbol{D} \boldsymbol{B} d\Omega \tag{2.23}$$

Similarly to the development of the mass matrix, we could consider the three-dimensional case and perform the transformation of integral domain for the element as follows:

$$\boldsymbol{K}^e = \int_{\Omega^e} \boldsymbol{B}^T \boldsymbol{D} \boldsymbol{B} dx\,dy\,dz = \int_{-1}^{1}\int_{-1}^{1}\int_{-1}^{1} \boldsymbol{B}^T \boldsymbol{D} \boldsymbol{B} J(\xi,\eta,\zeta) d\xi d\eta d\zeta \tag{2.24}$$

where $\boldsymbol{K}^e$ denotes the element stiffness matrix.

Applying the Gaussian quadrature converts the integration to practical summation, which can be written by block matrix as:

$$\boldsymbol{K}^e_{ab} = \sum_{l=1}^{m} \boldsymbol{B}_a^T(\xi_l,\eta_l,\zeta_l) \boldsymbol{D} \boldsymbol{B}_b(\xi_l,\eta_l,\zeta_l) J(\xi_l,\eta_l,\zeta_l) W_l \tag{2.25}$$

where $\boldsymbol{B}_a$ and $\boldsymbol{B}_b$ can be calculated by Eq.2.13, and the constitutive matrix $\boldsymbol{D}$ is defined in Eq.2.17.

For the stiffness matrix, reduced integration is sometimes used along with the full Gaussian integration, leading to the *selective reduced integration* (SRI). For example, in quasi-incompressibility (Poisson's ratio $\nu \to 0.5$), volume locking can occur. To avoid it, SRI is usually applied in which the shear contribution to stiffness (deviatoric part) is exactly integrated whereas the "pressure" contribution (volumetric part) is roughly evaluated by reduced integration [GRI 95].

Element matrices are then assembled to build the global stiffness matrix without any lumping technique, which can be noted as $\boldsymbol{K} = \sum_e \boldsymbol{K}^e$.

2.2.1.7 Damping $\boldsymbol{C}$

Often, in linear elasticity, we could consider a damping term in the discrete system to improve stability and numerical convergence. The discrete system of Eq.1.113 can thus be written as:

$$\boldsymbol{M}\ddot{\tilde{\boldsymbol{u}}}+\boldsymbol{C}\dot{\tilde{\boldsymbol{u}}}+\boldsymbol{K}\tilde{\boldsymbol{u}}=\boldsymbol{f}^{ext} \tag{2.26}$$

where $\boldsymbol{C}$ is termed damping matrix. Indeed, $\boldsymbol{C}$ can be formulated by the block element matrix as:

$$\boldsymbol{C}^e_{ab}=\int_{\Omega^e}\boldsymbol{N}_a^T\boldsymbol{\mu}\boldsymbol{N}_b d\Omega \tag{2.27}$$

where the matrix $\boldsymbol{\mu}$ is a set of viscosity parameters. Since the viscous matrix $\boldsymbol{\mu}$ is usually unknown, the damping matrix $\boldsymbol{C}$ is often assumed to be a linear combination of mass and stiffness matrix, written as:

$$\boldsymbol{C}=\alpha_M\boldsymbol{M}+\alpha_K\boldsymbol{K} \tag{2.28}$$

where the coefficients α_M and α_K can be determined experimentally in structural dynamics studies, or numerically in simulations by manual adjustment.

2.2.2 Time integration schemes

In the first chapter, we have seen how a semi-discrete system (Eq.1.113) with respect to space can be derived, and in the previous section, we have described in detail the numerical implementation of the matrices coming from the spatial discretization. However, the target problems are dynamic, time-dependent, as depicted, for example, by the elastodynamics governing equations in Eq.1.95. Thus, the discretization in time/frequency domain has to be considered to solve the FEM discretized equilibrium equations.

In fact, the dynamic problems can be divided into structural dynamic (for structures) and wave propagation (for solids) ones; two distinct schemes have been developed respectively [BAT 06]. Mode analysis by superposition in frequency domain is generally dedicated to the structure problems, and direct time integration schemes in time domain are widely used for solving wave propagation problems. The latter one, which is of great interest for us, includes the implicit and explicit methods, both requiring the time discretization by time steps Δt. In implicit methods, the solution at time $t+\Delta t$ is obtained using the discrete system at time $t+\Delta t$. In explicit methods, the solution at time $t+\Delta t$ is however based on the equations at time t. Implicit schemes have the advantages of being unconditionally stable, while the explicit ones are conditionally stable (requiring a sufficiently small time step). However, compared to explicit schemes, implicit schemes require more computational efforts per time step [NOH 13, MIR 15]. Therefore, explicit methods are more commonly used in wave propagation problems. They were employed in our solver and will be detailed here.

2.2.2.1 Central difference method and time step

In FEM, the central difference (CD) method has been the most popular explicit method for time integration. Indeed, it can be derived from the Newmark integration scheme which is stated as [BAT 06]:

$$\begin{aligned}
\tilde{\boldsymbol{u}}_{t+\Delta t} &= \tilde{\boldsymbol{u}}_t + \Delta t\,\dot{\tilde{\boldsymbol{u}}}_t + \Delta t^2 \left[\left(\frac{1}{2} - \beta\right)\ddot{\tilde{\boldsymbol{u}}}_t + \beta\ddot{\tilde{\boldsymbol{u}}}_{t+\Delta t}\right] \\
\dot{\tilde{\boldsymbol{u}}}_{t+\Delta t} &= \dot{\tilde{\boldsymbol{u}}}_t + \Delta t\left[(1-\gamma)\,\ddot{\tilde{\boldsymbol{u}}}_t + \gamma\ddot{\tilde{\boldsymbol{u}}}_{t+\Delta t}\right]
\end{aligned} \tag{2.29}$$

where β and γ are the parameters to be determined for obtaining stability and accuracy, and the subscripts indicate the time (for example, $\tilde{\boldsymbol{u}}_{t+\Delta t}$ implies the nodal displacements at time $t+\Delta t$). The Newmark scheme can lead to several methods, implicit or explicit, by setting different values of β and γ. For example, the classical implicit constant-average-acceleration method can be obtained when $\beta = \frac{1}{4}$ and $\gamma = \frac{1}{2}$. In the case of $\beta = 0$ and $\gamma = \frac{1}{2}$, we have the CD method which, considering the semi-discretized equation of motion Eq.2.26 at time $t+\Delta t$, can be summarized by the following algorithm:

$$\begin{aligned}
\tilde{\boldsymbol{u}}_{t+\Delta t} &= \tilde{\boldsymbol{u}}_t + \Delta t\,\dot{\tilde{\boldsymbol{u}}}_t + \frac{1}{2}\Delta t^2\,\ddot{\tilde{\boldsymbol{u}}}_t \\
\ddot{\tilde{\boldsymbol{u}}}_{t+\Delta t} &= \left(\boldsymbol{M} + \frac{1}{2}\Delta t\boldsymbol{C}\right)^{-1}\left[\boldsymbol{f}^{ext}_{t+\Delta t} - \boldsymbol{C}\left(\dot{\tilde{\boldsymbol{u}}}_t + \frac{1}{2}\Delta t\,\ddot{\tilde{\boldsymbol{u}}}_t\right) - \boldsymbol{K}\tilde{\boldsymbol{u}}_{t+\Delta t}\right] \\
\dot{\tilde{\boldsymbol{u}}}_{t+\Delta t} &= \dot{\tilde{\boldsymbol{u}}}_t + \frac{1}{2}\Delta t\,\left[\ddot{\tilde{\boldsymbol{u}}}_t + \ddot{\tilde{\boldsymbol{u}}}_{t+\Delta t}\right]
\end{aligned} \tag{2.30}$$

As mentioned, the explicit methods are conditionally stable, implying that the time step used for time integration should be carefully chosen and smaller than the so-called *critical time step* Δt_{cr} to ensure the simulations stability, and given by [HUG 12]:

$$\Delta t_{cr} = \frac{2}{\omega^G_{max}} \tag{2.31}$$

where ω^G_{max} denotes the maximum eigenfrequency of the global system. As investigating the whole finite element assembly is often too expensive, we usually choose instead the smallest element and consider its maximum eigenfrequency as the global one [ASK 15].

To solve the eigenfrequency problem, we could consider the free-vibration equilibrium equations without damping term:

$$\boldsymbol{M}\ddot{\tilde{\boldsymbol{u}}} + \boldsymbol{K}\tilde{\boldsymbol{u}} = \boldsymbol{0} \tag{2.32}$$

By assuming the solution to be of the form:

$$\tilde{\boldsymbol{u}} = \boldsymbol{\phi}\sin\omega(t-t_0) \tag{2.33}$$

we could obtain the generalized eigenvalue problem [BAT 06]:

$$(-\omega^2\boldsymbol{M} + \boldsymbol{K})\boldsymbol{\phi} = \boldsymbol{0} \tag{2.34}$$

from which the eigenfrequencies ω_i and the corresponding eigenvectors $\boldsymbol{\phi}_i$ $(i = 1, 2, \ldots, n)$ can be computed. Sorting the n eigenfrequencies leads to the maximum one as required.

In practice, it is easier to use another metric as an approximation, which is known as the *Courant-Friedrichs-Lewy* (CFL) condition:

$$\Delta t_{cr} = \frac{L_e}{c_P} \tag{2.35}$$

where L_e is the characteristic length of the smallest element and c_P is the longitudinal wave speed of the material. For more discussions about stability and time steps, see the literature, for example, [LIN 02, ASK 15].

Finally, a safety factor $\gamma_s \in (0,1)$ is usually employed such that $\Delta t = \gamma_s \Delta t_{cr}$.

2.2.2.2 Some other explicit methods for reducing spurious oscillations

When solving dynamic problems of wave propagation using standard FEM, numerical noises referred to as *spurious oscillations* usually occur due to the spatial and time discretizations, especially for waves high frequency modes. These errors can alter the displacement fields, and thus the stiffness estimation results in MRE. The classical CD scheme is not spurious dissipative and thus no longer appropriate in wave propagation simulations [WU 05]. Many other explicit time integration schemes introducing numerical dissipation to reduce noise have been developed, such as the Newmark method, the bulk viscosity method (BVM), the Tchamwa-Wielgosz (TW) scheme and the Chung Lee (CL) algorithm [FUN 03, MAH 13]. For instance, the BVM is an explicit method based on CD scheme, used in some commercial software codes including LS-Dyna and Abaqus [MAH 13]. It was initially developed in fluid mechanics for the calculation of hydrodynamics shocks [VON 50]. A pressure q called *artificial viscosity* is applied in this method for damping spurious oscillations in dynamics computations, which can be expressed as [JOH 01]:

$$q = \begin{cases} C_L \rho c_d L_e |\dot{\varepsilon}_{vol}| + C_Q \rho L_e^2 \dot{\varepsilon}_{vol}^2 & \text{for } \dot{\varepsilon}_{vol} < 0 \\ 0 & \text{for } \dot{\varepsilon}_{vol} \geq 0 \end{cases} \tag{2.36}$$

where C_L and C_Q are the linear and quadratic damping coefficients, respectively, ρ is the material density, c_d is the dilatational wave speed, L_e denotes the element characteristic length, and $\dot{\varepsilon}_{vol}$ is the volumetric strain rate. For instance, the two coefficients are set in Abaqus by default as $C_L = 0.06$ and $C_Q = 1.2$ [SIM 14].

Some dissipative explicit methods are only first-order accurate and the others are second-order accurate but not satisfyingly accurate. Recently, Noh and Bathe (NB) developed another explicit scheme which is second-order accurate, characterized by a better accuracy and a greater critical time step [NOH 13]. Later, Mirbagheri *et al.* proposed a modified version of NB method presenting even better stability and accuracy [MIR 15]. Considering the advantages of explicit scheme in terms of low computational cost and stability in wave propagation problems, we chose to implement in our solver the modified NB method which is briefly presented now.

In the frame of FEM equations of Eq.2.26, the modified NB scheme to solve these equations proceeds as:

1. Firstly, initialize the following parameters with a predefined time step Δt:
    (a) $p = 0.54$
    (b) $q_1 = \frac{1-2p}{2p(1-p)}$; $q_2 = 0.5 - pq_1$; $q_0 = -q_1 - q_2 + 0.5$
    (c) $a_0 = q_0(1-p)\Delta t$; $a_1 = (0.5 + q_1)(1-p)\Delta t$; $a_2 = q_2(1-p)\Delta t$
2. Then, for each time step:
    (a) First sub-step:
        i. $\tilde{\boldsymbol{u}}_{t+p\Delta t} = \tilde{\boldsymbol{u}}_t + (p\Delta t)\dot{\tilde{\boldsymbol{u}}}_t + \frac{\eta}{2}(p\Delta t)^2\ddot{\tilde{\boldsymbol{u}}}_t$
        ii. $\boldsymbol{f}^{ext}_{t+p\Delta t} = (1-p)\boldsymbol{f}^{ext}_t + p\boldsymbol{f}^{ext}_{t+\Delta t}$
        iii. $\ddot{\tilde{\boldsymbol{u}}}_{t+p\Delta t} = \boldsymbol{M}^{-1}[\boldsymbol{f}^{ext}_{t+p\Delta t} - \boldsymbol{C}(\dot{\tilde{\boldsymbol{u}}}_t + (p\Delta t)\ddot{\tilde{\boldsymbol{u}}}_t) - \boldsymbol{K}\tilde{\boldsymbol{u}}_{t+p\Delta t}]$
        iv. $\dot{\tilde{\boldsymbol{u}}}_{t+p\Delta t} = \dot{\tilde{\boldsymbol{u}}}_t + \frac{1}{2}(p\Delta t)[\ddot{\tilde{\boldsymbol{u}}}_t + \ddot{\tilde{\boldsymbol{u}}}_{t+p\Delta t}]$
    (b) Second sub-step:
        i. $\tilde{\boldsymbol{u}}_{t+\Delta t} = \tilde{\boldsymbol{u}}_{t+p\Delta t} + [(1-p)\Delta t]\dot{\tilde{\boldsymbol{u}}}_{t+p\Delta t} + \frac{\eta}{2}[(1-p)\Delta t]^2\ddot{\tilde{\boldsymbol{u}}}_{t+p\Delta t}$
        ii. $\ddot{\tilde{\boldsymbol{u}}}_{t+\Delta t} = \boldsymbol{M}^{-1}[\boldsymbol{f}^{ext}_{t+\Delta t} - \boldsymbol{C}(\dot{\tilde{\boldsymbol{u}}}_{t+p\Delta t} + [(1-p)\Delta t]\ddot{\tilde{\boldsymbol{u}}}_{t+p\Delta t}) - \boldsymbol{K}\tilde{\boldsymbol{u}}_{t+\Delta t}]$
        iii. $\dot{\tilde{\boldsymbol{u}}}_{t+\Delta t} = \dot{\tilde{\boldsymbol{u}}}_{t+p\Delta t} + a_0\ddot{\tilde{\boldsymbol{u}}}_t + a_1\ddot{\tilde{\boldsymbol{u}}}_{t+p\Delta t} + a_2\ddot{\tilde{\boldsymbol{u}}}_{t+\Delta t}$

In fact, this scheme becomes the NB method when the parameter η is set to 1 and the NB method reduces to the CD method when p equals 1. Finally, as suggested in [MIR 15], $\eta = 1.1$ is a good compromise between accuracy and stability, and thus applied in our solver.

2.2.3 Internal force in viscoelasticity

As described before, the internal force in the semi-discrete system Eq.1.113 can be calculated by means of a stiffness matrix as derived in Eq.1.117. This practice is commonly applied in the case of linear elasticity. However, in the case of linear viscoelasticity, since the constitutive law becomes time-dependent, it is more practical to calculate directly the internal force by a numerical recursive formula. A consistent linearization can be further performed to obtain a viscoelastic tangent modulus which, therefore, is not constant and requires updating at each time step.

We introduce in this subsection two algorithms to implement viscoelasticity. Both are unconditionally stable and second-order accurate. One was presented by Simo & Hughes in their book about computational inelasticity [SIM 06]. Rather basic mathematical formulations were employed for explanation and demonstration. The other one was described in the article of Kaliske & Rothert [KAL 97] where formulations were given explicitly, suited not only for the case of small strain but also for the case of finite deformation. Both algorithms were developed from the simplest one-dimensional case to the fully three-dimensional case, and based on the generalized Maxwell model of viscoelasticity which is composed of a single spring E_∞ and N Maxwell elements (E_i, η_i) in parallel

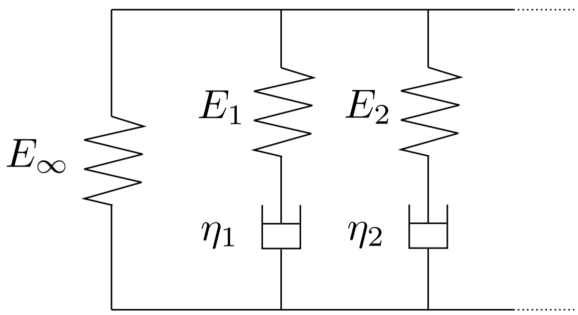

Figure 2.2: Generalized Maxwell-element

as illustrated in Fig.2.2. The small deformation hypothesis is considered here and in our solver.

Before introducing the two algorithms, we would like to review the formulation of internal force (originally introduced in Eq.1.114) by considering the isoparametric coordinates and the numerical integration as employed in section 2.2.1 for numerically integrating the matrices. In a similar way, the internal force vector $\underline{f}_e^{int}$ associated with element Ω_e at time t can be developed as:

$$\begin{aligned} \boldsymbol{f}_e^{int}(t) &= \int_{\Omega_e} \boldsymbol{B}_e^T \boldsymbol{\sigma}(t) dx\,dy\,dz \\ &= \int_{-1}^{1}\int_{-1}^{1}\int_{-1}^{1} \boldsymbol{B}_e^T \boldsymbol{\sigma}(t) J(\xi,\eta,\zeta) d\xi d\eta d\zeta \\ &\approx \sum_{i=1}^{n_{Gauss}} \boldsymbol{B}_e^T(\underline{x}_i)\boldsymbol{\sigma}_i(t) w_i J_i \end{aligned} \tag{2.37}$$

The strain-displacement matrix $\boldsymbol{B}_e$ depends on the mesh and can be determined for each Gauss point x_i of each element Ω_e in the preprocessing. Therefore, the evaluation of $\underline{f}_e^{int}(t)$ only depends on the stress $\underline{\underline{\sigma}}_i$ at the quadrature point $\underline{x}_i \in \Omega_e$. As can be seen later, the stress history can be associated to the strain history $\underline{\underline{\varepsilon}}_i$ assumed to be given at the quadrature points, and the evaluation of internal force is thus dependent on the calculation of strain history. For the sake of simplicity, the subscripts are omitted in the following algorithms, while all variables are still evaluated at quadrature points.

In addition, we also would like to describe the generalized Maxwell model in one-dimension. Define σ_i and the internal variable α_i as the viscous stress and strain, respectively, of each dashpot η_i. From the relations of $\sigma = E_\infty\varepsilon + \sum\sigma_i$ and $\sigma_i = E_i(\varepsilon - \alpha_i)$, we can derive:

$$\sigma = E_0\varepsilon - \sum_{i=1}^{N} E_i\alpha_i \tag{2.38}$$

and from $\sigma_i = \eta_i\dot{\alpha}_i = E_i(\varepsilon - \alpha_i)$, we have:

$$\dot{\alpha}_i + \frac{1}{\tau_i}\alpha_i = \frac{1}{\tau_i}\varepsilon \tag{2.39}$$

where the initial modulus E_0 and the relaxation time τ_i of each dashpot are given as:

$$\begin{aligned} E_0 &= E_\infty + \sum_{i=1}^{N} E_i \\ \tau_i &= \eta_i / E_i \end{aligned} \tag{2.40}$$

Alternatively, the stress response can also be formulated in a convolution integral representation by removing the internal variables α_i, leading to:

$$\sigma(t) = \int_0^t G(t-s) \frac{d\varepsilon(s)}{ds} ds \tag{2.41}$$

where the relaxation function, similar to the derivation of Eq.1.83, is written as:

$$G(t) = E_\infty + \sum_{i=1}^{N} E_i \exp\left(-\frac{t}{\tau_i}\right) \tag{2.42}$$

Indeed, one major difference between the following two algorithms consists in the considered stress formulation. The development of Simo's algorithm takes into account the expression in Eq.2.38, while Kaliske's algorithm starts from the integral representation of Eq.2.41.

2.2.3.1 Simo's algorithm

The algorithm of Simo & Hughes is based on an initial elastic stored-energy function associated to the initial elastic modulus E_0, which was also described in an early work of Simo [SIM 87]. As presented in section 1.2.1.6, the stress is obtained by deriving the strain energy. The initial elastic stress tensor $\underline{\underline{\sigma}}_0$, which can be decomposed into volumetric part and deviatoric part as in Eq.1.64, is written in the isotropic case as:

$$\begin{aligned} \underline{\underline{\sigma}}_0(t) &= \underline{\underline{\sigma}}_0^{vol}(t) + \underline{\underline{\sigma}}_0^{dev}(t) \\ &= (3\lambda_0 + 2\mu_0)\underline{\underline{\varepsilon}}^{vol}(t) + 2\mu_0 \underline{\underline{\varepsilon}}^{dev}(t) \end{aligned} \tag{2.43}$$

where $\lambda_0 = \frac{E_0 \nu}{(1+\nu)(1-2\nu)}$, $\mu_0 = \frac{E_0}{2(1+\nu)}$, $\underline{\underline{\varepsilon}}^{vol} = \frac{tr(\underline{\underline{\varepsilon}})}{3} \underline{\underline{I}}$ and $\underline{\underline{\varepsilon}}^{dev} = \underline{\underline{\varepsilon}} - \underline{\underline{\varepsilon}}^{vol}$.

For a 3D generalized Maxwell model, the "constitutive equation" Eq.2.38 becomes:

$$\underline{\underline{\sigma}}(t) = \underline{\underline{\sigma}}_0(t) - \sum_{i=1}^{N} \underline{\underline{q}}_i(t) \tag{2.44}$$

where $\underline{\underline{q}}_i$ is an internal stress variable described by the linear rate equation:

$$\dot{\underline{\underline{q}}}_i + \frac{1}{\tau_i} \underline{\underline{q}}_i = \frac{\gamma_i}{\tau_i} \underline{\underline{\sigma}}_0^{dev} \tag{2.45}$$

Solving this linear differential equation leads to the closed-form solution represented by a convolution:

$$\underline{\underline{q}}_i = \frac{\gamma_i}{\tau_i}\int_0^t \exp\left(-\frac{t-s}{\tau_i}\right)\underline{\underline{\sigma}}_0^{dev}(s)ds \tag{2.46}$$

The stress tensor can thus be written using convolution as:

$$\underline{\underline{\sigma}}(t) = \underline{\underline{\sigma}}_0^{vol}(t) + \int_0^t g(t-s)\frac{d\underline{\underline{\sigma}}_0^{dev}(s)}{ds}ds \tag{2.47}$$

where the normalized relaxation function $g(t)$ is defined as:

$$g(t) = \gamma_\infty + \sum_{i=1}^{N}\gamma_i \exp\left(-\frac{t}{\tau_i}\right) \tag{2.48}$$

And the above dimensionless moduli are defined as:

$$\begin{aligned}\gamma_\infty &= E_\infty/E_0\\ \gamma_i &= E_i/E_0\end{aligned} \tag{2.49}$$

Next, for numerical implementation purpose, we need to transform the convolution integral of Eq.2.47 into a recursive formula within the interval $[t_n, t_{n+1}]$. To this end, we define a set of N internal variables $\underline{\underline{h}}_i(t)$ corresponding to N pairs (E_i, η_i), expressed as:

$$\underline{\underline{h}}_i(t) = \int_0^t \exp\left(-\frac{t-s}{\tau_i}\right)\frac{d}{ds}\underline{\underline{\sigma}}_0^{dev}(s)ds \tag{2.50}$$

leading to:

$$\underline{\underline{\sigma}}(t) = \underline{\underline{\sigma}}_0^{vol}(t) + \gamma_\infty\underline{\underline{\sigma}}_0^{dev}(t) + \sum_{i=1}^{N}\gamma_i\underline{\underline{h}}_i(t) \tag{2.51}$$

The key idea of this recurrence algorithm is thus to calculate the variables at time $t_{n+1} = t_n + \Delta t$ based on the variables history at time t_n. Since the terms of $\underline{\underline{\sigma}}_0^{vol}(t_{n+1})$ and $\underline{\underline{\sigma}}_0^{dev}(t_{n+1})$ can be easily updated from the strain tensor $\underline{\underline{\varepsilon}}(t_{n+1})$, as can be found through Eq.2.43, we only need to develop the internal variables $\underline{\underline{h}}_i(t_{n+1})$. Using the additivity of domain for definite integral, $\underline{\underline{h}}_i$ can be expressed as:

$$\begin{aligned}\underline{\underline{h}}_i(t_{n+1}) &= \int_0^{t_{n+1}} \exp\left(-\frac{t_{n+1}-s}{\tau_i}\right)\frac{d}{ds}\underline{\underline{\sigma}}_0^{dev}(s)ds\\ &= \int_0^{t_n} \exp\left(-\frac{\Delta t}{\tau_i}\right)\exp\left(-\frac{t_n-s}{\tau_i}\right)\frac{d}{ds}\underline{\underline{\sigma}}_0^{dev}(s)ds\\ &\quad + \int_{t_n}^{t_{n+1}} \exp\left(-\frac{t_{n+1}-s}{\tau_i}\right)\frac{d}{ds}\underline{\underline{\sigma}}_0^{dev}(s)ds\\ &= \exp\left(-\frac{\Delta t}{\tau_i}\right)\underline{\underline{h}}_i(t_n) + \int_{t_n}^{t_{n+1}} \exp\left(-\frac{t_{n+1}-s}{\tau_i}\right)\frac{d}{ds}\underline{\underline{\sigma}}_0^{dev}(s)ds\end{aligned} \tag{2.52}$$

Using the midpoint rule, the last integral can be approximated as follows:

$$\begin{aligned}\int_{t_n}^{t_{n+1}} \exp\left(-\frac{t_{n+1}-s}{\tau_i}\right) \frac{d}{ds}\underline{\underline{\sigma}}_0^{dev}(s)ds \\ &\approx \exp\left(-\frac{t_n+\Delta t-s}{\tau_i}\right) \frac{d}{ds}\underline{\underline{\sigma}}_0^{dev}(s)\bigg|_{s=\frac{t_n+t_{n+1}}{2}} \Delta t \\ &= \exp\left(-\frac{\Delta t}{2\tau_i}\right) \frac{d}{ds}\underline{\underline{\sigma}}_0^{dev}\left(\frac{t_n+t_{n+1}}{2}\right)\Delta t \\ &= \exp\left(-\frac{\Delta t}{2\tau_i}\right)\left[\underline{\underline{\sigma}}_0^{dev}(t_{n+1})-\underline{\underline{\sigma}}_0^{dev}(t_n)\right]\end{aligned} \tag{2.53}$$

Finally, the variable $\underline{\underline{h}}_i$ can be updated as:

$$\underline{\underline{h}}_i(t_{n+1}) = \exp\left(-\frac{\Delta t}{\tau_i}\right)\underline{\underline{h}}_i(t_n) + \exp\left(-\frac{\Delta t}{2\tau_i}\right)\left[\underline{\underline{\sigma}}_0^{dev}(t_{n+1})-\underline{\underline{\sigma}}_0^{dev}(t_n)\right] \tag{2.54}$$

2.2.3.2 Kaliske's algorithm

In the work of Kaliske & Rothert [KAL 97], two types of formulations were developed for linear viscoelasticity. One considers total viscoelasticity and the other considers partial viscoelasticity by performing volumetric and deviatoric split of stress as presented in Simo's algorithm.

(a) *Total viscoelasticity*

As pointed out previously, this algorithm starts from the integral representation of stress response in Eq.2.41. In one-dimension, it can be developed by splitting the integral into an elastic part and a viscoelastic part as:

$$\begin{aligned}\sigma(t) &= \int_0^t E_\infty \frac{d\varepsilon(s)}{ds}ds + \int_0^t \sum_{i=1}^N E_i \exp\left(-\frac{t-s}{\tau_i}\right)\frac{d\varepsilon(s)}{ds}ds \\ &= E_\infty \varepsilon(t) + \int_0^t \sum_{i=1}^N E_i \exp\left(-\frac{t-s}{\tau_i}\right)\frac{d\varepsilon(s)}{ds}ds \\ &= \sigma_\infty(t) + \sum_{i=1}^N \hat{h}_i(t)\end{aligned} \tag{2.55}$$

where $\sigma_\infty(t)$ is the elastic stress contribution from the modulus E_∞ and $\hat{h}_i(t)$ is the internal stress variable similar to $h_i(t)$ defined by Eq.2.50.

New dimensionless moduli are introduced:

$$\hat{\gamma}_i = E_i/E_\infty \tag{2.56}$$

Substituting the strain by $\varepsilon(t) = \sigma_\infty(t)/E_\infty$, we can rewrite $\hat{h}_i(t)$ as:

$$\hat{h}_i(t) = \int_0^t \hat{\gamma}_i \exp\left(-\frac{t-s}{\tau_i}\right)\frac{d\sigma_\infty(s)}{ds}ds \tag{2.57}$$

Extending the Eq.2.55 and Eq.2.57 to three-dimensional case, we could obtain:

$$\underline{\underline{\sigma}}(t) = \underline{\underline{\sigma}}_{\infty}(t) + \sum_{i=1}^{N} \underline{\underline{\hat{h}}}_i(t) \tag{2.58}$$

The elastic contribution is calculated by $\boldsymbol{\sigma}_\infty(t) = \boldsymbol{D}_\infty \boldsymbol{\varepsilon}(t)$ where $\boldsymbol{D}_\infty$ is the constitutive matrix associated to the modulus E_∞, and $\underline{\underline{\hat{h}}}_i(t)$ is defined as:

$$\underline{\underline{\hat{h}}}_i(t) = \int_0^t \hat{\gamma}_i \exp\left(-\frac{t-s}{\tau_i}\right) \frac{d\underline{\underline{\sigma}}_{\infty}(s)}{ds} ds \tag{2.59}$$

To develop a recursive scheme, we focus again on the time interval $[t_n, t_{n+1}]$ with a time step Δt. The elastic part can be updated by $\boldsymbol{\sigma}_\infty(t_{n+1}) = \boldsymbol{D}_\infty \boldsymbol{\varepsilon}(t_{n+1})$. As in Eq.2.52, we can develop Eq.2.59 at time t_{n+1} into:

$$\underline{\underline{\hat{h}}}_i(t_{n+1}) = \exp\left(-\frac{\Delta t}{\tau_i}\right) \underline{\underline{\hat{h}}}_i(t_n) + \hat{\gamma}_i \int_{t_n}^{t_{n+1}} \exp\left(-\frac{t_{n+1}-s}{\tau_i}\right) \frac{d\underline{\underline{\sigma}}_{\infty}(s)}{ds} ds \tag{2.60}$$

The last integral term in the above Eq.2.60 can be evaluated in a different manner than Eq.2.53. Assuming that $\frac{d\underline{\underline{\sigma}}_{\infty}(s)}{ds}$ is constant over the interval $[t_n, t_{n+1}]$, we have:

$$\begin{aligned}
&\int_{t_n}^{t_{n+1}} \exp\left(-\frac{t_{n+1}-s}{\tau_i}\right) \frac{d\underline{\underline{\sigma}}_{\infty}(s)}{ds} ds \\
&\qquad \approx \left.\frac{d\underline{\underline{\sigma}}_{\infty}(s)}{ds}\right|_{s=\frac{t_n+t_{n+1}}{2}} \int_{t_n}^{t_{n+1}} \exp\left(-\frac{t_{n+1}-s}{\tau_i}\right) ds \\
&\qquad = \frac{\underline{\underline{\sigma}}_{\infty}(t_{n+1}) - \underline{\underline{\sigma}}_{\infty}(t_n)}{\Delta t} \tau_i \exp\left(-\frac{t_{n+1}-s}{\tau_i}\right)\Bigg|_{s=t_n}^{s=t_{n+1}} \\
&\qquad = \frac{1-\exp\left(-\frac{\Delta t}{\tau_i}\right)}{\frac{\Delta t}{\tau_i}} \left[\underline{\underline{\sigma}}_{\infty}(t_{n+1}) - \underline{\underline{\sigma}}_{\infty}(t_n)\right]
\end{aligned} \tag{2.61}$$

Finally, the internal stress variables can be calculated as:

$$\underline{\underline{\hat{h}}}_i(t_{n+1}) = \exp\left(-\frac{\Delta t}{\tau_i}\right) \underline{\underline{\hat{h}}}_i(t_n) + \hat{\gamma}_i \frac{1-\exp\left(-\frac{\Delta t}{\tau_i}\right)}{\frac{\Delta t}{\tau_i}} \left[\underline{\underline{\sigma}}_{\infty}(t_{n+1}) - \underline{\underline{\sigma}}_{\infty}(t_n)\right] \tag{2.62}$$

It is to be noticed that $\hat{\gamma}_i$ is here a scalar quantity, corresponding to the material isotropy.

(b) *Partial viscoelasticity*

In reality, the viscoelastic behaviors are mainly associated with the isochoric/deviatoric part of the deformation, and the volumetric part is often regarded as being purely elastic. Therefore, the second recursive scheme for updating the stress tensor consists in separating stress as:

$$\underline{\underline{\sigma}}(t_{n+1}) = \underline{\underline{\sigma}}^{vol}(t_{n+1}) + \underline{\underline{\sigma}}^{dev}(t_{n+1}) \tag{2.63}$$

where $\underline{\underline{\sigma}}^{vol}(t_{n+1})$ is indeed the elastic hydrostatic pressure $\underline{\underline{\sigma}}_0^{vol}(t_{n+1})$, and $\underline{\underline{\sigma}}^{dev}(t_{n+1})$ the viscoelastic deviatoric part of stress expressed as:

$$\underline{\underline{\sigma}}^{dev}(t_{n+1}) = \underline{\underline{\sigma}}^{dev}_{\infty}(t_{n+1}) + \sum_{i=1}^{N} \underline{\underline{\tilde{h}}}_i(t_{n+1}) \tag{2.64}$$

where $\underline{\underline{\sigma}}^{dev}_{\infty}(t_{n+1}) = 2\mu_{\infty}\underline{\underline{\varepsilon}}(t_{n+1})$ with $\mu_{\infty} = \frac{E_{\infty}}{2(1+\nu)}$, and $\underline{\underline{\tilde{h}}}_i(t_{n+1})$ is the history variable similar to $\underline{\underline{\hat{h}}}_i(t_{n+1})$ considering only the deviatoric stress part:

$$\underline{\underline{\tilde{h}}}_i(t_{n+1}) = \exp\left(-\frac{\Delta t}{\tau_i}\right)\underline{\underline{\tilde{h}}}_i(t_n) + \hat{\gamma}_i \frac{1-\exp\left(-\frac{\Delta t}{\tau_i}\right)}{\frac{\Delta t}{\tau_i}} \left[\underline{\underline{\sigma}}^{dev}_{\infty}(t_{n+1}) - \underline{\underline{\sigma}}^{dev}_{\infty}(t_n)\right] \tag{2.65}$$

Globally, the stress-splitting formulation of Kaliske in Eq.2.63 is quite similar to the formulation of Simo in Eq.2.51. The differences mainly lie in the way to consider and formulate the deviatoric contribution in terms of the dimensionless moduli (γ_i or $\hat{\gamma}_i$) and the deviatoric stress (in $\underline{\underline{h}}_i$ or $\underline{\underline{\tilde{h}}}_i$). The two strategies for evaluating the integrals as in Eq.2.53 and Eq.2.61 are in fact both second-order accurate and hence should not be regarded as their difference.

2.3 Simulations of linear viscoelastic plane wave

Now that the numerical implementation of viscoelasticity is stated, we apply it to two 2D cases of plane wave propagation, i.e. pressure wave (P-wave) and shear wave (S-wave). In each case, the three recursive schemes presented above, namely Simo's scheme, Kaliske's total scheme and Kaliske's partial scheme are tested. Results are compared with the analytical model in terms of the wavelength.

2.3.1 Model description

To validate the numerical implementation of viscoelasticity, one simple method is to investigate the wavelength of simulated waves based on a plane wave model. The most intuitive way to obtain plane wave may be designing a model of large dimensions and just focusing on the central zone which is not affected by reflections. However, plane wave can be simulated in a more efficient manner by applying specific boundary conditions (BC), such as periodic BC (PBC) and symmetry BC (SBC). The latter one, more convenient for implementation, consists in imposing constraints in the direction orthogonal to the wave polarization [VAN 17]. As illustrated in Fig.2.3, a two-dimensional model in plane strain is proposed, with SBC to generate a plane wave. Specifically, the displacements of top and bottom edges are constrained along the y-axis ($u_y = 0$) for the case of plane P-wave and along the x-axis ($u_x = 0$) for the case of plane S-wave. The left edge is embedded and the right edge is actuated by a prescribed displacement. The model is characterized by length L and height H.

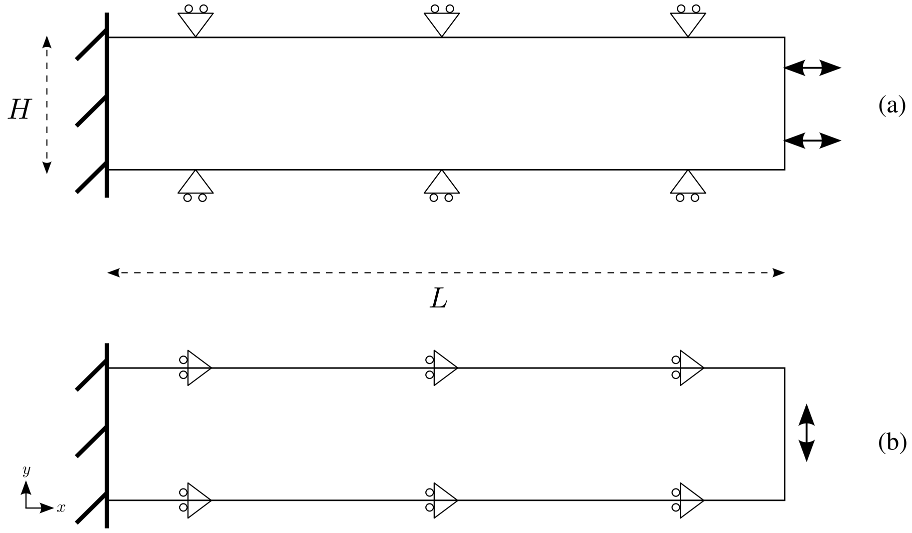

Figure 2.3: Plane wave model with symmetry boundary conditions (SBC). (a) The case of plane P-wave; (b) The case of plane S-wave.

In terms of the analytical wavelength of plane wave, it can be derived from the decomposition of the wave equation (Eq.1.58). Indeed, it is based on the Helmholtz theorem stating that any sufficiently smooth vector field can be decomposed into an irrotational (curl-free) vector field and a solenoidal (divergence-free) vector field. For the displacement field $\underline{u}$, the curl-free part represents the compressional/longitudinal component $\underline{u}_P$ and the divergence-free part represents the shear/transverse component $\underline{u}_S$. Using this decomposition, the wave equation can be separated into two equations describing the propagation of P-wave and S-wave, leading to the respective wave velocities c_P and c_S [SIN 05, PAR 10]:

$$\begin{aligned} \rho\partial_t^2\underline{u}_P &= (\lambda+2\mu)\underline{\nabla}^2\underline{u}_P & &\Rightarrow c_P = \sqrt{\frac{\lambda+2\mu}{\rho}} \\ \rho\partial_t^2\underline{u}_S &= \mu\underline{\nabla}^2\underline{u}_S & &\Rightarrow c_S = \sqrt{\frac{\mu}{\rho}} \end{aligned} \tag{2.66}$$

Then, the analytical wavelength is calculated by $l = c/f$ where f is the wave frequency.

In particular, for viscoelastic materials, the above velocities are usually estimated with the norm of complex modulus, leading to:

$$c_P^I = \sqrt{|\lambda^* + 2\mu^*|/\rho} \qquad c_S^I = \sqrt{|\mu^*|/\rho} \tag{2.67}$$

where $|\lambda^*| = \frac{|E^*|\nu}{(1+\nu)(1-2\nu)}$ and $|\mu^*| = \frac{|E^*|}{2(1+\nu)}$. Another formulation has also been proposed in [OLI 01, CHR 12]:

$$c^{II} = \sqrt{\frac{2|G_3^*|^2}{\rho(G_3' + |G_3^*|)}} \tag{2.68}$$

where $G_3^* = G_3' + iG_3''$ is a complex modulus, $G_3^* = \lambda^* + 2\mu^*$ for P-wave and $G_3^* = \mu^*$ for S-wave. Equation 2.68 reduces to Eq.2.66 in the case of pure elasticity, i.e. $G_3'' = 0$. In fact, these two formulations (Eq.2.67 and Eq.2.68) can give similar analytical results, as presented later. To respect the fact that P-wave is mainly dominated by the volumetric deformation associated to pure elasticity, a formulation for P-wave modified from Eq.2.67 is proposed, based on the initial modulus E_0 instead of $|E^*|$:

$$c_P^{III} = \sqrt{(\lambda^\circ + 2\mu^\circ)/\rho} \tag{2.69}$$

where $\lambda^\circ = \frac{E_0 \nu}{(1+\nu)(1-2\nu)}$ and $\mu^\circ = \frac{E_0}{2(1+\nu)}$. For the Maxwell form of SLS model (see section 1.2.2) used in this work, the initial modulus E_0 is calculated as $E_0 = E_1 + E_2$.

Soft tissues are characterized by their quasi-incompressibility, corresponding to Poisson's ratio ν tending to 0.5. Indeed, the P-wave in soft tissues usually propagates at $c_P \approx 1540\ m/s$, corresponding to $\nu \approx 0.4999999$ [SIN 05]. However, as presented before, explicit time integration schemes are usually used for solving wave propagation problems. This implies a numerical limit since the closer to 0.5 the Poisson's ratio, the smaller the time step and the more expensive the computational cost. Therefore, as a compromise, ν is set to 0.49 in this work.

The parameters of the model in Fig.2.3 are summarized in Tab.2.2. Two cases of P-wave and S-wave are studied with different model lengths, due to highly different wavelengths. However, all the other material (E_1, E_2, η, ρ, ν) and excitation (f, u_0) parameters are identical. The harmonic excitation follows the equation:

$$u_{x/y} = u_0 \sin(2\pi f t) \tag{2.70}$$

where u_x is for the P-wave case and u_y for the S-wave case. Quadrilateral elements (QUAD4) are used to mesh the solid, with an element size of 1 *mm* for the P-wave model and 0.5 *mm* for the S-wave model, ensuring more than 20 elements per wavelength.

Table 2.2: Simulations parameters for the plane wave model of Fig.2.3.

Case	L (mm)	H (mm)	E_1 (kPa)	E_2 (kPa)	η $(Pa \cdot s)$	ρ (kg/m^3)	ν	f (Hz)	u_0 (μm)	l^I (mm)	l^{II} (mm)	l^{III} (mm)
P-wave	300	20	3.47	7	8.8	1000	0.49	100	50	109.75	113.34	133.86
S-wave	100	20	3.47	7	8.8	1000	0.49	100	50	15.37	15.87	-

[*] L and H, model sizes; E_1, E_2 and η, parameters of SLS model; ρ, density; ν, Poisson's ratio; f, frequency; u_0, amplitude; l^I, l^{II} and l^{III}, wavelength corresponding to velocity c^I, c^{II} and c^{III}, respectively.

The simulations of both the P-wave case and the S-wave case last for two periods, namely 0.2 *s*, with a time step of $1.29 \times 10^{-5}\ s$ for numerical stability.

2.3.2 Results and discussion

Figure 2.4 and Fig. 2.5 present the simulation results for the case of P-wave and S-wave, respectively. In each figure, the displacement field within the model and the displacement distribution along a horizontal central line are shown for the simulation by Simo's scheme, Kaliske's total scheme and Kaliske's partial scheme. The waves propagate from right to left and they are all presented at the last moment of simulation, i.e. 0.2 s. The wavelength measurements are summarized in Tab.2.3.

Table 2.3: Wavelength measurements of simulations by the validation model in Fig.2.3.

Case	Simo's scheme	Kaliske's total scheme	Kaliske's partial scheme
P-wave	133.13	115.10	133.13
S-wave	15.85	15.85	15.85

* unit: *mm*.

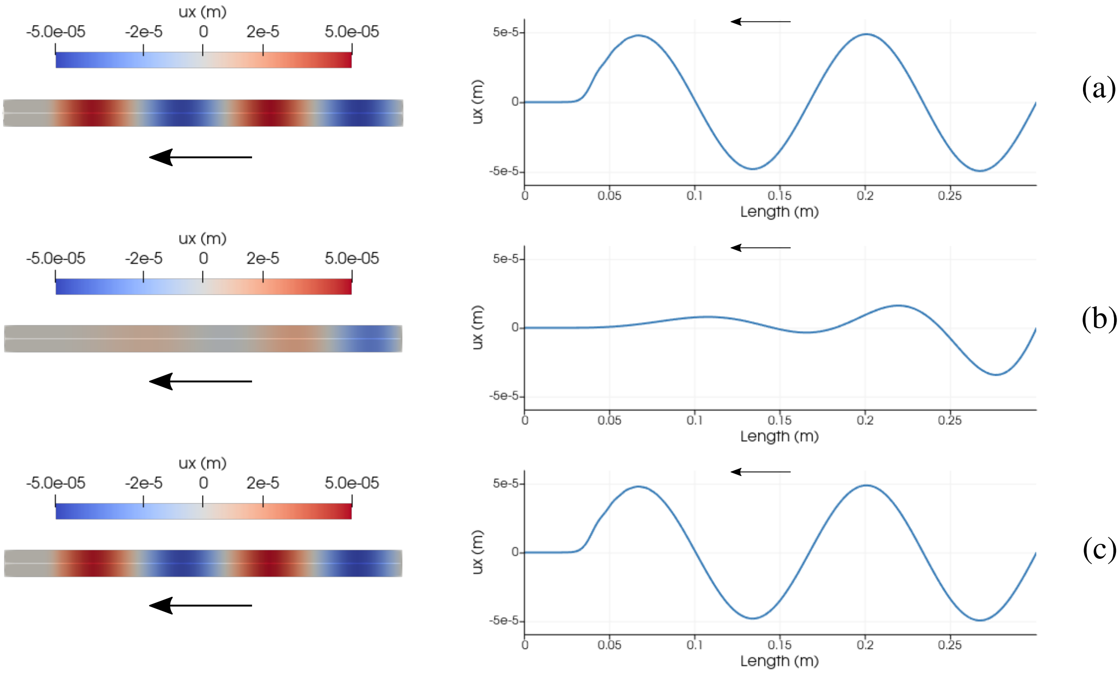

Figure 2.4: Simulated plane P-wave. (a) Simo's scheme; (b) Kaliske's total scheme; (c) Kaliske's partial scheme.

In terms of viscoelasticity scheme, it can be found that all the three tested schemes have the same performance in the case of plane S-wave. However, in the case of plane P-wave where viscosity is of much less importance, only Simo's scheme and the Kaliske's partial scheme perform well due to the split of volumetric and deviatoric deformation; Kaliske's total scheme leads to an important attenuation which is not realistic.

In terms of the wavelength, the measurements from simulated S-wave correspond better to the analytical results given by the velocity c^{II} than those given by c^{I}, revealing the accuracy of Eq.2.68 for estimating wavelength of plane S-wave. However, for plane P-wave, the estimates by the formulae of either c^{I} or c^{II} match the unrealistic results by

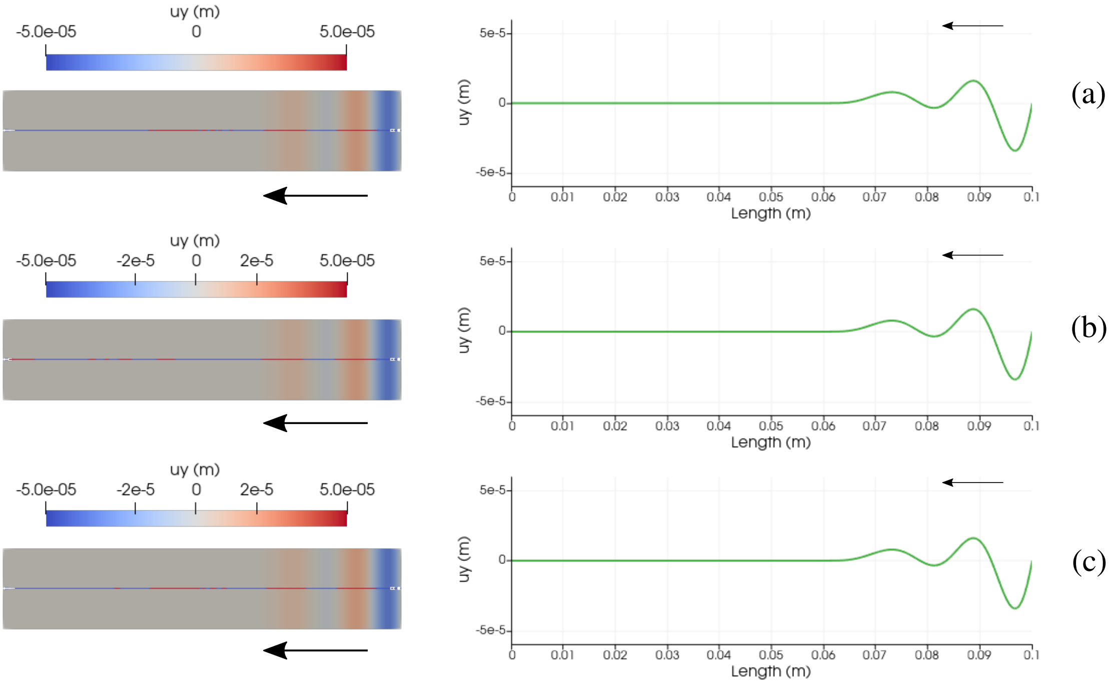

Figure 2.5: Simulated plane S-wave. (a) Simo's scheme; (b) Kaliske's total scheme; (c) Kaliske's partial scheme.

Kaliske's total scheme; the formulation of c_P^{III} gives instead rather similar predictions to the results by Simo's scheme and Kaliske's partial scheme.

Overall, these simulations are successfully compared to the analytical models and validate the numerical implementation of viscoelasticity. In particular, Simo's scheme and Kaliske's partial scheme have almost the same performance and can give rise to reliable simulated results. In the following, Simo's scheme is used due to its wider applicability (E_1 can be equal to zero).

2.4 Parametric study of plane shear wave model

In this section, a parametric study is presented using the implemented FEM tool. The objective is to investigate the effect of material and excitation parameters on wave damping, based on the plane shear wave model shown in Fig.2.3(b). To this end, in a preliminary analysis, damping estimation by a dimensionless quantity resulting from the complex modulus is first presented; configurations of each parameter are accordingly determined. Based on the simulations, another dimensionless quantity resulting from wave-related variables is analysed, compared and correlated with the modulus-based quantity. The relation between the two damping quantity is illustrated.

Default parameters are summarized in Tab.2.4. Based on the wavelength estimation, quadrilateral element size was chosen as 1 *mm*. Five periods were simulated and ten snapshots were sampled during each period. By default, the displayed displacements correspond to u_y, along the polarization direction, of the horizontal middle line ($y = 10$ *mm*) of the last snapshot of the last period.

2.4.1 Preliminary analysis

In a parametric study, it is important to appropriately select the values of each investigated parameter. The appropriateness may be related to the variability of input and also of output. For example, the values of input are expected to be different from one to another as much as possible, and the same for the output results (if varying).

To investigate the effect of parameters on wave damping and well determine the parameters values range, a preliminary study is necessary. For plane shear wave propagating in viscoelastic materials, a simple way of estimating the wave damping can be focusing on the *relative viscosity* which is the ratio of loss modulus to storage modulus, such as E''/E' for the complex elastic modulus E^*, or G''/G' for the complex shear modulus G^*. It is a dimensionless quantity and may provide quick estimation of wave damping for selecting the parameters values. Based on the default parameters in Tab.2.4 and the dynamic moduli given by Eq.1.92 and Eq.1.93, analytical relationships between E''/E' and different parameters can be obtained, as plotted in Fig.2.6. The relative viscosity E''/E' is monotonic with respect to material parameters E_1 and E_2, while it presents a peak with respect to the dynamic viscosity η and the frequency f. Based on these graphs, we chose four values per parameter for the parametric study, illustrated by the circle marks in Fig.2.6.

In the following, the numerically obtained waves are plotted along the horizontal middle line, and post-processed to extract the wavelength l_s and damping α. For wavelength, the five last (from the right side of plot) crests and troughs were determined by gradient change. The distance of each crest-trough pair was measured and averaging the distances could lead to an estimate of half-wavelength, thus of the wavelength by a factor of 2. For damping, a conventional exponential formulation is applied to fit the spatial displacements, expressed as:

$$u_y(x) = u_0 \exp[\alpha(x - x_0)] \tag{2.71}$$

where u_0 is the amplitude at the location of x_0; for example, in the default case, they can be $u_0 = 50$ *µm* and $x_0 = 0.2$ *m*. The coefficient α hence represents the spatial shear wave damping rate.

Since the indicator E''/E' is dimensionless, the product of l_s and α is further calculated to produce comparable dimensionless measurements. Finally, the correlation between E''/E' and αl_s is performed to find out whether the two dimensionless quantities are related and to investigate the feasibility of using relative viscosity for describing wave damping property.

2.4.2 Effect of E_1

First of all, the effect of the SLS model parameter E_1 is investigated. Four values of 10 *kPa*, 15 *kPa*, 20 *kPa* and 25 *kPa* are chosen and all other parameters take their default

Table 2.4: Default parameters of the plane shear wave model in the parametric study.

Case	L (mm)	H (mm)	E_1 (kPa)	E_2 (kPa)	η $(Pa \cdot s)$	ρ (kg/m^3)	ν	f (Hz)	u_0 (μm)
S-wave	200	20	15	20	31.83	1000	0.49	100	50

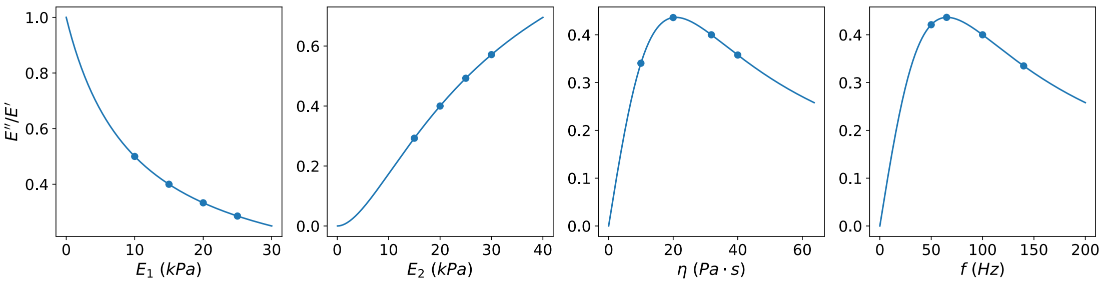

Figure 2.6: Preliminary study of relative viscosity E''/E' in terms of different parameters. Circle marks represent the configurations selected for the parametric study.

values, leading to the relative viscosity E''/E' of 0.5, 0.4, 0.33 and 0.29, respectively.

The displacements u_y along the horizontal middle line are presented in Fig.2.7; the exponential envelope curves are also plotted in dotted lines using the corresponding color. In particular, as can be seen, a residual wave is propagating ahead with quite distinct amplitude, probably resulting from the numerical implementation. The wavelength l_s is measured to 27.86 mm, 30.35 mm, 32.84 mm and 34.83 mm, respectively, and hence presents a increasing tendency as expected. The damping α is also fitted using the formulation Eq.2.71, leading to the values of $54.5/m$, $40.59/m$, $31.45/m$ and $25.17/m$, respectively. Therefore, the dimensionless quantity αl_s is calculated to 1.52, 1.23, 1.03 and 0.88, respectively.

2.4.3 Effect of E_2

Then, we present the effect the second parameter E_2 of SLS model whose values are set to 15 kPa, 20 kPa, 25 kPa or 30 kPa. The corresponding viscosity E''/E' is 0.29, 0.4, 0.49 and 0.57, respectively.

The results are shown in Fig.2.8. The wavelength increases slightly with E_2, measured to 29.35 mm, 30.35 mm, 30.85 mm and 30.85 mm, respectively, while the coefficient α presents a considerable growing tendency with the estimates of $30.63/m$, $40.59/m$, $48.94/m$ and $55.68/m$, respectively. These lead to the product of αl_s as 0.9, 1.23, 1.51 and 1.72, respectively.

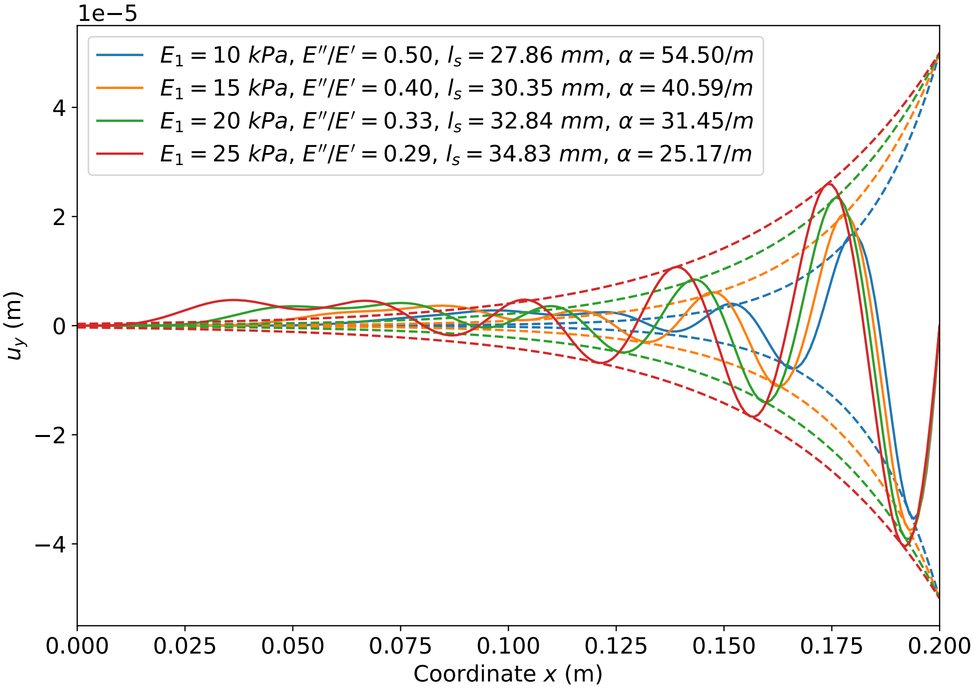

Figure 2.7: Effect of E_1. Waves are plotted spatially along the horizontal middle line, and their exponential envelope curves are traced in dotted lines with corresponding color.

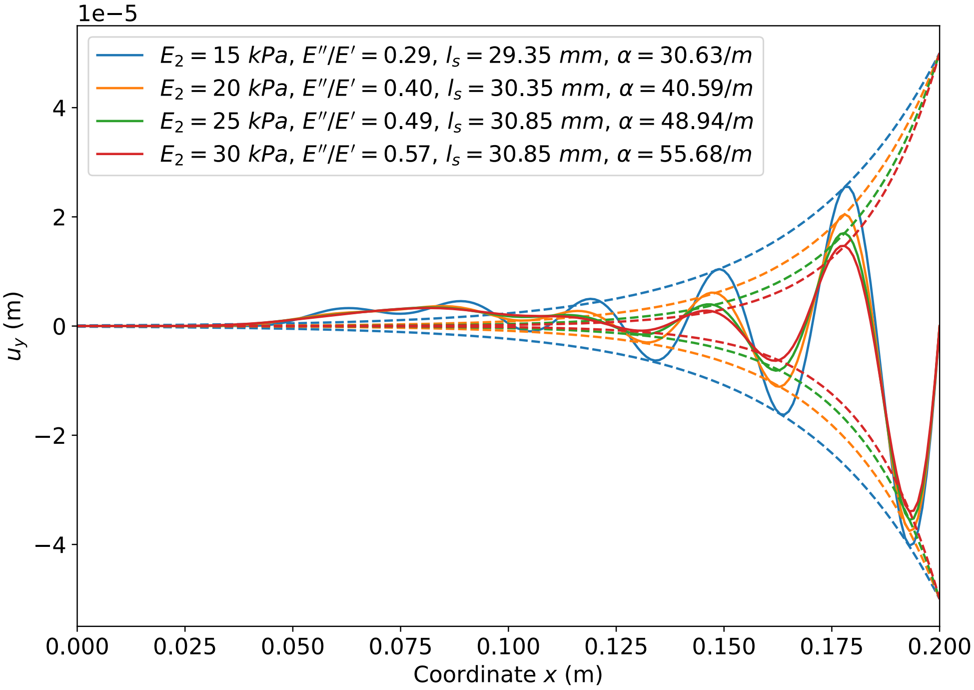

Figure 2.8: Effect of E_2. Waves are plotted spatially along the horizontal middle line, and their exponential envelope curves are traced in dotted lines with corresponding color.

2.4.4 Effect of η

The third study consists in investigating the effect of the parameter η of SLS model. Like the other investigations, four different values of η are selected, namely 10 $Pa \cdot s$, 20 $Pa \cdot s$, 31.83 $Pa \cdot s$ and 40 $Pa \cdot s$. The relative viscosity E''/E' is hence calculated to be 0.34, 0.44, 0.4 and 0.36, respectively. Indeed, the second choice of $\eta = 20$ $Pa \cdot s$ corresponds to the maximum value of E''/E' in the $E''/E' - \eta$ curve as presented in Fig.2.6.

The waves are illustrated in Fig.2.9. A small increase in wavelength can be observed, with the specific measurements of 24.38 mm, 27.86 mm, 30.35 mm and 31.34 mm, respectively. However, the damping α presents the same increasing-decreasing tendency as the viscosity E''/E', with fitted values being $42.9/m$, $48.32/m$, $40.59/m$ and $35.06/m$, respectively. The dimensionless product αl_s is hence given as 1.05, 1.35, 1.23 and 1.1, respectively.

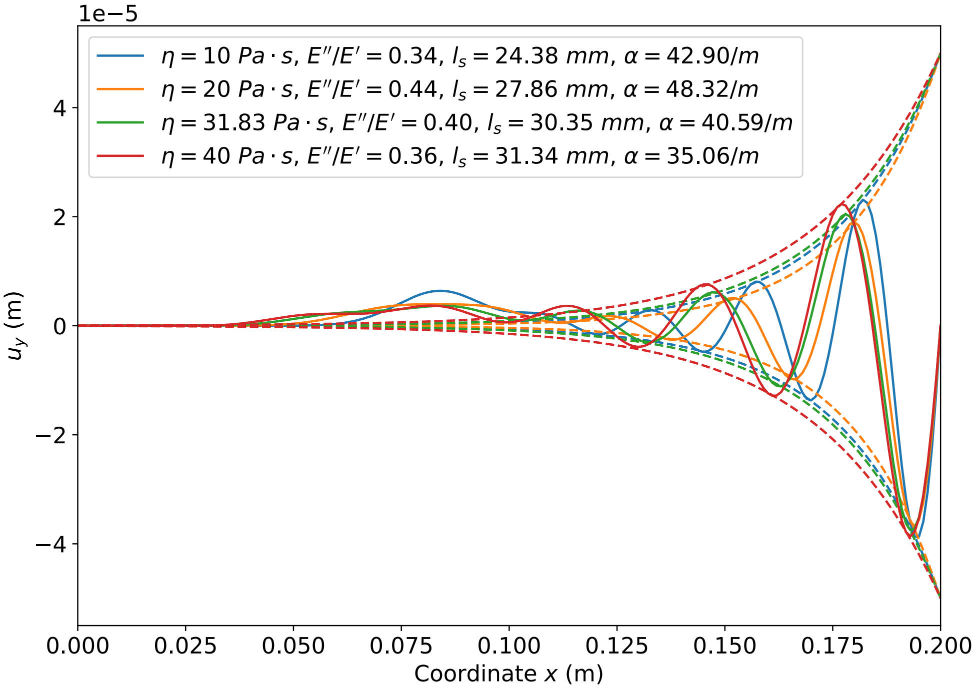

Figure 2.9: Effect of η. Waves are plotted spatially along the horizontal middle line, and their exponential envelope curves are traced in dotted lines with corresponding color.

2.4.5 Effect of frequency

Then, we focus on the effect of source excitation. The frequency is here investigated with four distinct frequencies of 50 Hz, 65 Hz, 100 Hz and 140 Hz. They correspond to the dimensionless viscosity E''/E' of 0.42, 0.44, 0.4 and 0.33, respectively. In particular, the choice of 65 Hz represents the peak of $E''/E' - f$ curve as shown in Fig.2.6.

The results of the displacements u_y are plotted in Fig.2.10. As expected, the wavelength l_s obviously decreases with the frequency f. Concretely, it is measured to be 54.23 mm, 43.28 mm, 30.35 mm and 22.89 mm, respectively. However, the damping α is not like that of the precedent study of effect of η which presents the same increasing-decreasing tendency as E''/E'. A monotonic growing tendency is observed here, with estimates of $23.96/m$, $31.11/m$, $40.59/m$ and $45.26/m$, respectively. Accordingly, the product αl_s is found to be 1.3, 1.35, 1.23 and 1.03, respectively.

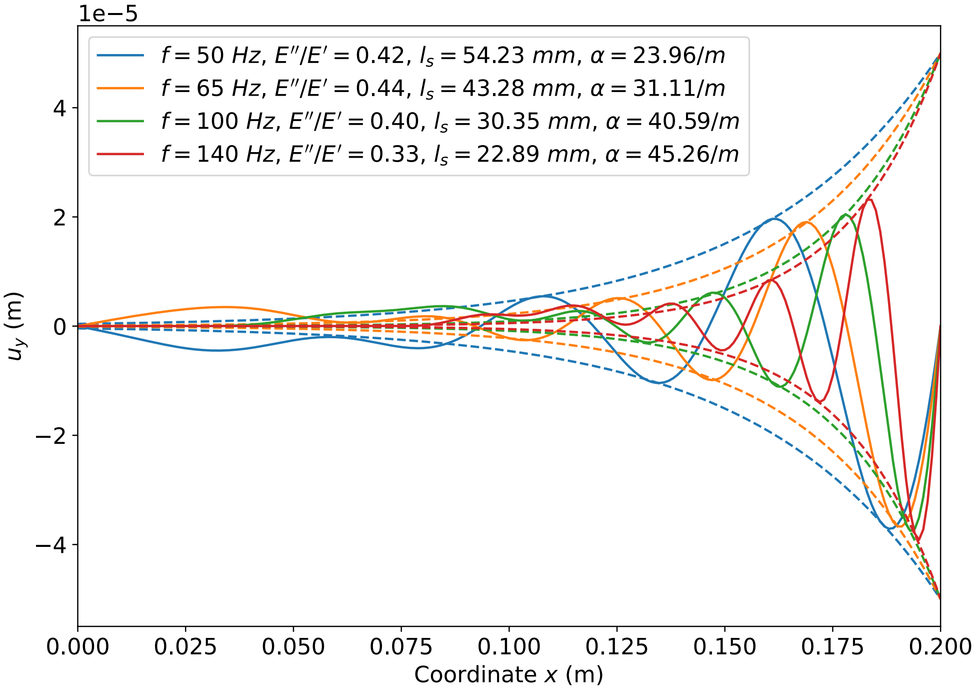

Figure 2.10: Effect of f. Waves are plotted spatially along the horizontal middle line, and their exponential envelope curves are traced in dotted lines with corresponding color.

2.4.6 Effect of amplitude

Finally, different amplitudes of excitation are investigated with the values of 50 μm, 100 μm, 150 μm and 200 μm. Since the amplitude u_0 is not concerned in the calculation of Eq.2.71, the relative viscosity is kept constant as 0.4.

As shown in Fig.2.11, the four waves present four different amplitudes but the same wavelength that is measured to be 30.35 mm. In addition, the same damping α is observed, with the estimate to be $40.59/m$ for all the four configurations. The product αl_s is thus a constant being 1.23.

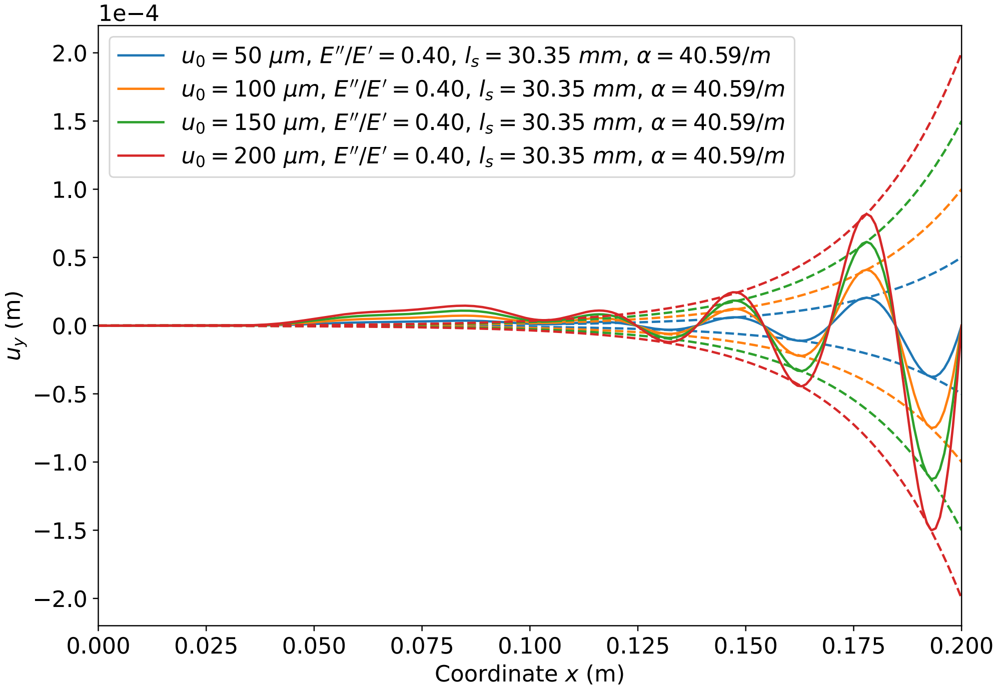

Figure 2.11: Effect of u_0. Waves are plotted spatially along the horizontal middle line, and their exponential envelope curves are traced in dotted lines with corresponding color.

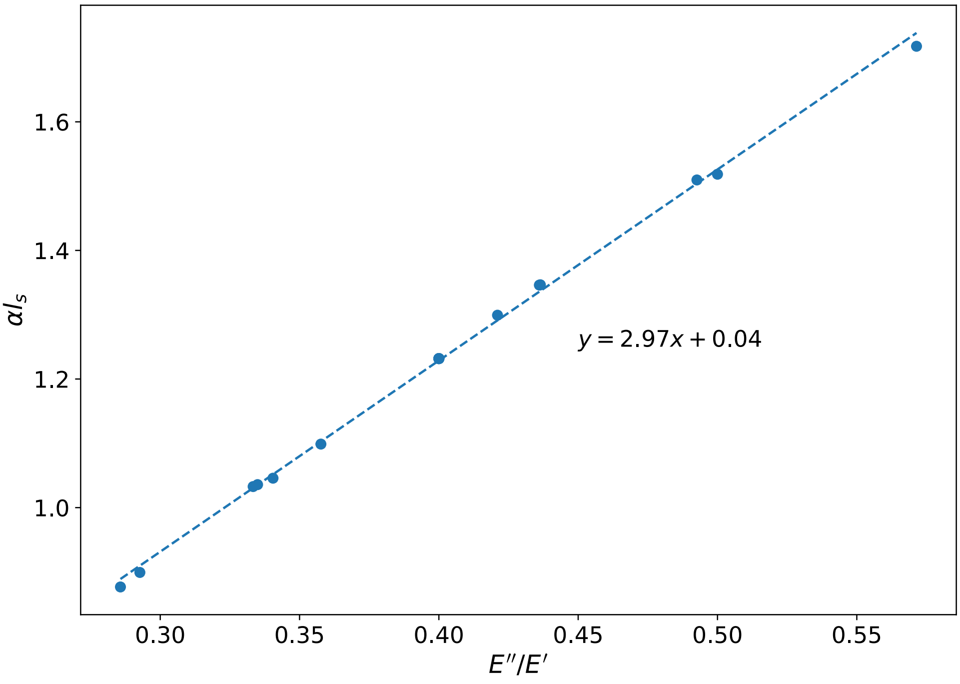

Figure 2.12: Correlation analysis between αl_s and E''/E'.

2.4.7 Discussion

In this section, the effect of different parameters on the propagation of plane shear wave, especially the wave damping, is numerically studied, including the three parameters of SLS viscoelastic model, frequency and amplitude of source excitation. Indeed, it can be demonstrated that all the simulated wavelengths match well the analytical ones given by Eq.2.68. The damping coefficients α are also well fitted as illustrated by the envelope curves in the figures.

As shown in the previous investigations of different parameters, neither the wavelength l_s nor the coefficient α can reveal alone the damping property of plane shear wave. No agreement in tendency with the ratio E''/E' can be observed. However, the product αl_s, dimensionless like E''/E', succeeds in presenting the same damping tendency as E''/E', namely the increasing one for E_1 and E_2, and increasing-decreasing one for η and f. Finally, a correlation analysis between the two dimensionless quantities is conducted, leading to the linear relation as illustrated in Fig.2.12. This linear relationship shows that, we could estimate the wave damping by the relative viscosity without getting into the details of wave patterns, or reversely, we could infer the ratio E''/E' or G''/G' given wave information.

2.5 Conclusion

In this chapter, we presented how to model the wave propagation in a linear, isotropic, homogeneous, viscoelastic medium. A homemade finite element solver was implemented and introduced with the formulations including explicit matrices, time integration schemes and internal force. The implementation was then tested by simulations based on a plane wave model. Comparisons with analytical models in terms of the wavelength validated our FE solver. Finally, using the plane shear wave model, a parametric study was performed to investigate the effect of different parameters on the wave damping.

Three schemes in terms of the numerical implementation of viscoelastic model were presented, namely Simo's scheme, Kaliske's total scheme and Kaliske's partial scheme. As validated by simulations, Kaliske's total scheme is sometimes not realistic as it does not consider the split of volumetric and deviatoric strain. In contrast, Simo's scheme and Kaliske's partial scheme produce similar results close to the analytical ground truth. However, Simo's scheme is more applicable since it allows the parameter E_1 to be zero, thus preferred and applied in this work.

In the case of plane shear wave, the relative viscosity defined by the ratio of loss modulus to storage modulus was found to be linear with another dimensionless quantity which is the product of wavelength and coefficient of exponential damping formulation. It is thus believed that the relative viscosity can reveal the damping property of wave propagation. This linearity is worth being further studied.

Chapter 3

eXtended Finite Element Method

In this chapter, the bases of the extended finite element method (XFEM) and the details of its numerical implementation are introduced. Numerical examples are presented. In addition, conventional methods of element partition are illustrated for both 2D and 3D cases, and a strategy for partitioning hexahedral element is proposed.

Contents

3.1 Introduction

The objective of this chapter is to present a formulation of FEM, known as the eXtended Finite Element Method (XFEM) to be implemented into our FEM Fortran solver. XFEM is indeed particularly adapted to model inhomogeneous media, as will be presented later in Chapters 4 and 5. Here in this chapter, not only the existing formulations of XFEM are presented, but also a new strategy for partitioning the hexahedral element.

XFEM approach is based on the partition of unity method [MEL 96]. The key idea is to enrich the displacement approximation of standard FEM by discontinuous functions. It originally intended to solve crack growth problems in the domain of fracture mechanics [BEL 99, MOË 99, DOL 00], and is still widely used and studied for this purpose. Compared to classical FEM, this formulation has the key advantage of being remeshing free, especially useful for dynamic problems like the crack propagation.

In crack modeling, the focus is on the discontinuous displacement across the crack interface. However, in addition to the strong discontinuity of displacement, the weak discontinuity like strain across the interface between two different materials can also be modeled by XFEM. Another application of XFEM thus consists in modeling the inhomogeneities such as holes and inclusions as reported in [SUK 01, JUN 13]. By a level set function, the interface of inhomogeneity can be mathematically formulated, thus making the inhomogeneity modeling independent from the physical mesh; complex inclusions can be readily integrated into numerical models.

To the best of our knowledge, XFEM is not yet used in MRE simulations for inclusion modeling, and employing XFEM to model mechanical waves in inhomogeneous media is not either much investigated in the literature [LIU 13, JUN 13]. This explains why we chose to implement and apply XFEM in the framework of this PhD thesis. Indeed, XFEM has been incorporated into either commercial software like Abaqus [GIN 09] and Comsol [JAF 21], or custom-developed codes [SUK 03, NIS 08], but mainly applied to fracture problems. For inclusion modeling by XFEM, there is still a lack of available commercial tools. The numerical implementation complexity might explain why XFEM is still unknown to the MRE community. The details of applying XFEM in MRE will be presented in the next chapter.

The outline of this chapter is as follows. Firstly in section 3.2, the XFEM bases are briefly introduced, including the problem formulation and discretization, the level set method/function and the enrichment function. Secondly in section 3.3, the conventionally used methods of element partition are described, for both the two-dimensional and the three-dimensional cases. A new strategy of partitioning a 3D hexahedral element is also proposed here. Thirdly in section 3.4, the details of XFEM numerical implementation are presented, along with numerical 2D and 3D examples to demonstrate the advantages of XFEM over FEM. Finally, a conclusion is given in section 3.5.

3.2 XFEM bases

In this section, we mainly introduce the XFEM bases in the framework of modeling the interface between different materials; the strong discontinuity of displacement across a crack is not considered. In addition, the governing equations are based on linear elastodynamics as addressed in section 1.3.1, instead of elastostatics commonly formulated in XFEM articles. This is because in MRE, we are mainly interested in dynamic problems of mechanical wave propagation. Nevertheless, it needs to be emphasized that the principles and basic functions are typically the same for the two types of problem.

3.2.1 Problem formulation and discretization

As in section 1.3.1, a linear elastic solid within a domain Ω is considered. However, in addition to the external boundaries Γ_u and Γ_t, two internal boundaries Γ_h and Γ_I are also taken into account, as illustrated in Fig.3.1, leading to the boundary Γ satisfying $\Gamma = \Gamma_u \cup \Gamma_t \cup \Gamma_h \cup \Gamma_I$, $\Gamma_u \cap (\Gamma_h \text{ or } \Gamma_I) = \emptyset$ and $\Gamma_t \cap (\Gamma_h \text{ or } \Gamma_I) = \emptyset$. Γ_h represents the traction-free boundary of an internal hole and Γ_I a material interface along which traction continuity holds. The governing equations and boundary conditions of the elastodynamics problem can be given as:

$$\begin{aligned}
\underline{\nabla} \cdot \underline{\underline{\sigma}} + \underline{b} &= \rho \underline{\ddot{u}} && \text{in } \Omega \\
\underline{u} &= \underline{u}_b && \text{on } \Gamma_u \\
\underline{\underline{\sigma}} \cdot \underline{n} &= \underline{t}_b && \text{on } \Gamma_t \\
\underline{\underline{\sigma}} \cdot \underline{n} &= \underline{0} && \text{on } \Gamma_h \\
[\![\underline{\underline{\sigma}} \cdot \underline{n}]\!] &= \underline{0} && \text{on } \Gamma_I
\end{aligned} \tag{3.1}$$

where $\underline{\underline{\sigma}}$ is Cauchy stress tensor, $\underline{b}$ the body force vector, ρ the mass density, $\underline{u}$ the displacement vector, $\underline{n}$ the unit outward normal vector to Γ and $(\dot{\bullet})$ denotes partial differentiation with respect to time. $\underline{u}_b$ and $\underline{t}_b$ are the prescribed displacement and traction imposed on Γ_u and Γ_t, respectively. $[\![\bullet]\!] := \bullet^+ - \bullet^-$ is a notation representing a jump of quantity $\bullet$.

Using the same procedures as in section 1.3.1, the strong formulation of Eq.3.1 can be further reduced. For the sake of concision and clarity, we define here two vector spaces of functions. Define $H^1(\Omega)$ as the Sobolev space of functions with square-integrable first derivatives in Ω, and $H_0^1(\Omega) \subseteq H^1(\Omega)$ as the (sub)space of functions in $H^1(\Omega)$ that vanish on the essential boundary Γ_u. Let $\underline{u} \in H^1(\Omega)$ be the trial function of displacement, and $\delta\underline{u} \in H_0^1(\Omega)$ be the test function. Using the integral form with the multiplication of test function $\delta\underline{u}$ and after integration by part, equation 3.1 becomes the weak formulation:

$$\int_\Omega \delta\boldsymbol{\varepsilon}^T \boldsymbol{\sigma} d\Omega + \int_\Omega \delta\boldsymbol{u}^T \rho \ddot{\boldsymbol{u}} d\Omega = \int_\Omega \delta\boldsymbol{u}^T \boldsymbol{b} d\Omega + \int_{\Gamma_t} \delta\boldsymbol{u}^T \boldsymbol{t}_b d\Gamma, \qquad \forall \delta\boldsymbol{u} \in H_0^1(\Omega) \tag{3.2}$$

To approximate the displacement field in the numerical simulations, the above formulation has to be further discretized into a discrete system, as done in section 1.3.1.3. The

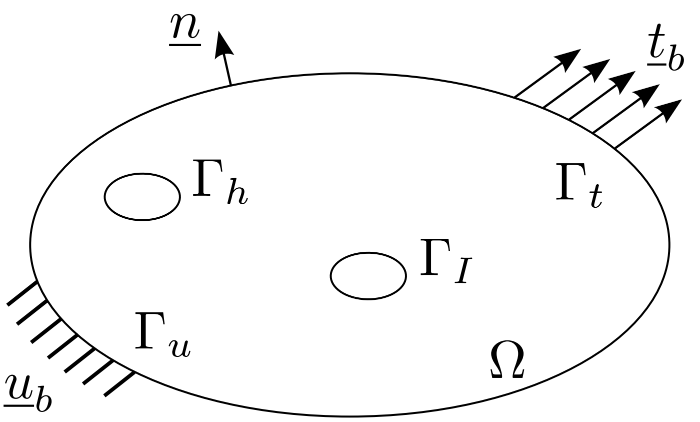

Figure 3.1: A solid body with internal boundaries.

spatial mesh by finite elements is thus required, accordingly leading to the shape functions defined on element node. We can define two subspaces $H^{1h} \subseteq H^1$ and $H_0^{1h} \subseteq H_0^1$ which are finite dimensional spaces composed of shape functions. Let $\underline{u}^h \in H^{1h}$ and $\delta\underline{u}^h \in H_0^{1h}$ be the approximations by finite element of the trial and test function, $\underline{u}$ and $\delta\underline{u}$, respectively. The discrete system in weak form can be derived from Eq.3.2, and stated as: finding $\underline{u}^h \in H^{1h}(\Omega)$ such that

$$\int_\Omega (\delta\boldsymbol{\varepsilon}^h)^T \boldsymbol{\sigma} d\Omega + \int_\Omega (\delta\boldsymbol{u}^h)^T \rho \ddot{\boldsymbol{u}}^h d\Omega = \int_\Omega (\delta\boldsymbol{u}^h)^T \boldsymbol{b} d\Omega + \int_{\Gamma_t} (\delta\boldsymbol{u}^h)^T \boldsymbol{t}_b d\Gamma, \qquad \forall \delta\boldsymbol{u}^h \in H_0^{1h}(\Omega) \tag{3.3}$$

Based on the partition of unity method and using the standard Bubnov-Galerkin procedure, the approximation of displacement $\underline{u}^h$ can be represented as linear combinations of shape functions:

$$\boldsymbol{u}^h(\underline{x},t) = \sum_{i\in I} \boldsymbol{N}_i(\underline{x}) \tilde{\boldsymbol{u}}_i(t) + \sum_{j\in J} \boldsymbol{N}_j^*(\underline{x}) \tilde{\boldsymbol{a}}_j(t) F(\underline{x}) \tag{3.4}$$

Indeed, this discretized approximation of displacement consists of a standard FEM approximation, which is the first term on the right, and an enriched XFEM approximation, which is the second term on the right. $\underline{x}$ is the coordinate vector and t is the time. $\boldsymbol{N}_i(\underline{x})$ and $\boldsymbol{N}_j^*(\underline{x})$ denote the shape functions at location $\underline{x}$ of node i and j, respectively. They are not necessarily the same, but in general it is assumed and applied that $\boldsymbol{N}(\underline{x}) = \boldsymbol{N}^*(\underline{x})$. $\tilde{\boldsymbol{u}}_i(t)$ and $\tilde{\boldsymbol{a}}_j(t)$ are, both at moment t, the standard nodal displacement of node i and the enriched nodal displacement of node j, respectively. I is the set of all element nodes, while $J \subseteq I$ indicates the set of nodes to be enriched for the discontinuity. Finally, $F(\underline{x})$ is the enrichment function that incorporates discontinuity of the boundaries Γ_h or Γ_I. The key issue in XFEM is the selection of the enriched nodes, i.e. the set J, and the determination of the appropriate enrichment function based on the discontinuity; these points will be discussed in the following subsections.

Finally, using Eq.3.4 to replace the trial and test functions in Eq.3.3 leads to the discrete system used for numerical implementation, written in compact form as:

$$\boldsymbol{M}\ddot{\boldsymbol{d}} + \boldsymbol{f}^{int} = \boldsymbol{f}^{ext} \tag{3.5}$$

or

$$\begin{bmatrix} \boldsymbol{M}^{uu} & \boldsymbol{M}^{ua} \\ \boldsymbol{M}^{au} & \boldsymbol{M}^{aa} \end{bmatrix} \begin{Bmatrix} \ddot{\boldsymbol{u}} \\ \ddot{\boldsymbol{a}} \end{Bmatrix} + \begin{Bmatrix} \boldsymbol{f}_u^{int} \\ \boldsymbol{f}_a^{int} \end{Bmatrix} = \begin{Bmatrix} \boldsymbol{f}_u^{ext} \\ \boldsymbol{f}_a^{ext} \end{Bmatrix} \tag{3.6}$$

$\boldsymbol{M}$ is the mass matrix; its submatrices $\boldsymbol{M}^{uu}$, $\boldsymbol{M}^{ua}$ (or $\boldsymbol{M}^{au}$) and $\boldsymbol{M}^{aa}$ represent the mass associated to the classical FEM degrees of freedom, the coupling of standard and enriched degrees of freedom, and the enriched XFEM degrees of freedom, respectively. $\boldsymbol{d} = [\tilde{\boldsymbol{u}}\ \tilde{\boldsymbol{a}}]^T$ is the solution vector of the nodal displacement approximation. $\underline{f}^{int}$ and $\underline{f}^{ext}$ denote the internal and external forces, respectively; the components $\underline{f}_u^{int}$ (or $\underline{f}_u^{ext}$) and $\underline{f}_a^{int}$ (or $\underline{f}_a^{ext}$) are time-dependent internal (or external) forces for the classical and enriched displacement approximation, $\underline{\tilde{u}}$ and $\underline{\tilde{a}}$, respectively. For an element e, they are defined as:

$$\boldsymbol{M}_e^{pq} = \int_{\Omega_e} \rho (\boldsymbol{N}^p)^T \boldsymbol{N}^q d\Omega \tag{3.7}$$

$$\boldsymbol{f}_p^{int} = \int_{\Omega_e} \left(\frac{\partial \boldsymbol{N}^p}{\partial \boldsymbol{x}} \right)^T \boldsymbol{\sigma} d\Omega \tag{3.8}$$

$$\boldsymbol{f}_p^{ext} = \int_{\Omega_e} (\boldsymbol{N}^p)^T \boldsymbol{b} d\Omega + \int_{\Gamma_t} (\boldsymbol{N}^p)^T \boldsymbol{t}_b d\Gamma \tag{3.9}$$

where $p, q = u, a$. For more details concerning the above tensors and the numerical implementation, see section 3.4.

3.2.2 Level set method and function

To model arbitrary inhomogeneities such as voids and inclusions, XFEM was coupled to the level set method [SUK 01]. In the framework of this PhD thesis, it is thus necessary to give a brief introduction of the level set method, in particular the level set function, as a support for the use of XFEM in MRE for inclusion modeling.

The level set method was first proposed by Osher and Sethian [OSH 88]. It is a numerical approach to track the interface evolution. In this method, the key idea is to model the moving interface by the zero level set of the function with a higher dimension. We first give some instances to illustrate the concept of zero level set. Define $\Gamma \subset \mathbb{R}^n$ as a static interface and $\phi(\underline{x}) : \mathbb{R}^n \to \mathbb{R}$ as a level set function. For example, in one-dimension where $n = 1$, Γ can represent a point partitioning a line, as shown in Fig.3.2(b), and in two-dimensions where $n = 2$, Γ can represent a curve partitioning a plane, as illustrated in Fig.3.2(d). They are respectively formulated by:

$$\begin{aligned} \Gamma &= \left\{ \boldsymbol{x} = (x) \in \mathbb{R}^1 \,|\, \phi(\boldsymbol{x}) = \phi(x) = x^2 - 1 = 0 \right\} \\ \Gamma &= \left\{ \boldsymbol{x} = (x, y) \in \mathbb{R}^2 \,|\, \phi(\boldsymbol{x}) = \phi(x, y) = x^2 + y^2 - 1 = 0 \right\} \end{aligned} \tag{3.10}$$

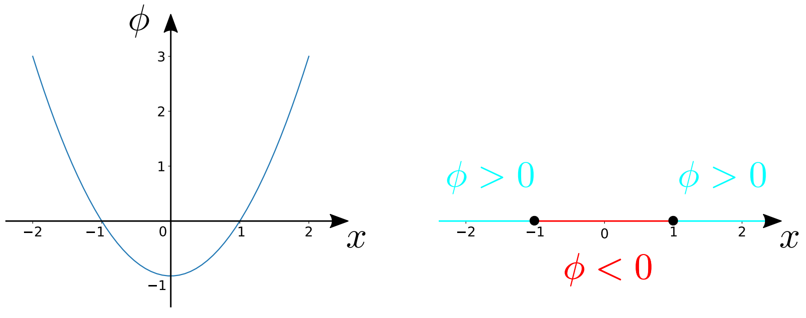

(a) $\phi(x)$

(b) $\Gamma \subset \mathbb{R}^1$

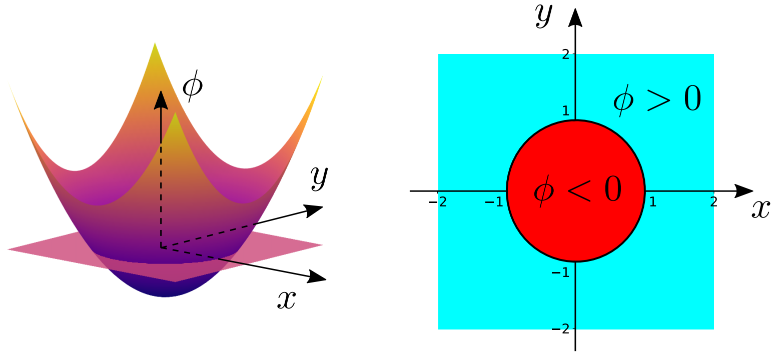

(c) $\phi(x,y)$

(d) $\Gamma \subset \mathbb{R}^2$

Figure 3.2: Illustration of zero level set in one-dimension (a,b) and two-dimensions (c,d).

In the level set method, the higher dimensional level set function is time-dependent $\phi(\underline{x},t) : \mathbb{R}^n \times \mathbb{R} \to \mathbb{R}$, leading to its zero level set, i.e. a moving interface, represented as:

$$\Gamma(t) = \{\underline{x} \in \mathbb{R}^n \,|\, \phi(\underline{x},t) = 0\} \tag{3.11}$$

The interface evolution is then subject to a partial differential equation, also a Hamilton-Jacobi equation, formulated as:

$$\begin{aligned} &\frac{\partial \phi}{\partial t} + v|\nabla \phi| = 0 \\ &\phi(\underline{x},0) = \phi_0(\underline{x}) \end{aligned} \tag{3.12}$$

where $v(\underline{x},t)$ is the evolution speed vector of curve $\Gamma(t)$ at $\underline{x}$ in the normal outward direction, and $\phi_0(\underline{x})$ is the initial level set function given at $t = 0$. The level set method has many advantages; for example, it can be employed to compute the topological changes of curve, based on a fixed Eulerian mesh and by means of an easily formulated higher dimensional function. Some applications, such as in fluid mechanics and materials science, can be found in the book [SET 99].

However in XFEM, the inclusion interface to model is typically static. Therefore, only the concept of level set function is applied and the zero level set curve is used to represent the interface location. A common form of function ϕ is the signed distance

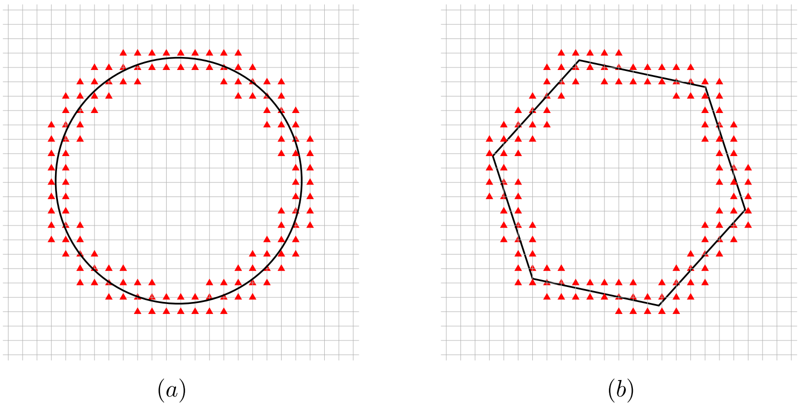

Figure 3.3: Illustration of two-dimensional inclusions with circular (a) and polygonal (b) interface. The enriched nodes are marked by red triangles ▲.

function, defined as:

$$\phi(\underline{x}) = \pm \min_{\underline{x}_\Gamma \in \Gamma} |\underline{x} - \underline{x}_\Gamma| \tag{3.13}$$

where $\underline{x}_\Gamma$ is an arbitrary point belonging to the interface Γ. The sign is normally defined to be positive (negative) if the point of interest $\underline{x}$ is outside (inside) Γ, assuming that interior and exterior regions of Γ exist. For an interface with a simple form, mathematical formulation can be easily found as shown later; for a more general interface with some given parameters, the fast marching method can be used to efficiently compute the signed distance function as introduced in [SET 96].

Figure 3.3 presents two examples of inclusion with circular and polygonal interface. For the former one, the signed distance function to the interface can be formulated as:

$$\phi(\underline{x}) = |\underline{x} - \underline{x}_c| - r_c \tag{3.14}$$

where $\underline{x}_c$ and r_c are the center and radius of the circular inclusion, respectively. Assuming the polygonal interface is composed of n segments, the level set function for the latter one can be defined as:

$$\phi(\underline{x}) = |\underline{x} - \underline{x}_{min}| \mathrm{sgn}[(\underline{x} - \underline{x}_{min}) \cdot \underline{n}_{min}] \tag{3.15}$$

where $\underline{x}_{min}$ denotes the projection of point $\underline{x}$ on the polygon, $\underline{n}_{min}$ is the outward vector at $\underline{x}_{min}$ normal to the interface, and $\mathrm{sgn}(x)$ indicates the signed function.

As introduced before, one important issue in XFEM lies in the selection of enriched nodes relative to the materials interface. To this end, the support of nodal shape functions is defined as the union of elements associated with the node j, i.e. having j as one of its vertices. If the support is crossed by the interface, then node j is enriched. The enriched nodes in the examples are marked by red triangles as shown in Fig.3.3. Finally, for the case of multiple inclusions, a distinct level set function is attributed to every distinct materials interface.

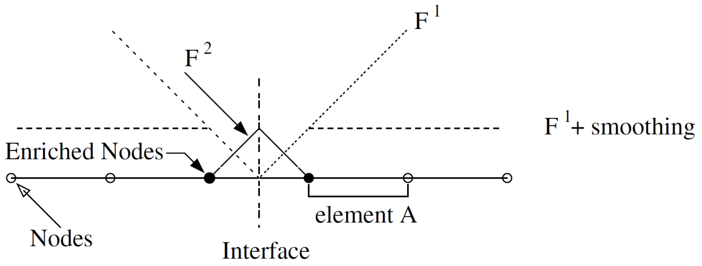

Figure 3.4: Illustration of enrichment functions. Source: [MOË 03]

3.2.3 Enrichment function

The displacement approximation in XFEM, as formulated by Eq.3.4, can be concisely summarized as:

$$\begin{aligned} \boldsymbol{u}^{\mathrm{XFEM}} &= \boldsymbol{u}^{\mathrm{FEM}} + \boldsymbol{u}^{\mathrm{enr}} \\ &= \sum_I \boldsymbol{N}_I \boldsymbol{u}_I + \sum_J \boldsymbol{N}_J \boldsymbol{a}_J F \end{aligned} \tag{3.16}$$

The enrichment function F plays a key role in XFEM. It represents the discontinuity in the additional displacement approximation $\underline{u}^{\mathrm{enr}}$, and can have different forms for different applications such as crack modeling and inclusion modeling. Anyhow, its first derivative is discontinuous across the interface.

For the inclusion modeling, it was firstly proposed in [SUK 01] to use the absolute value of the level set function as the enrichment function whose first derivative is indeed discontinuous. Assuming each node I of the mesh has been assigned the distance ϕ_I to the interface, the level set function of any arbitrary point $\underline{x}$ can be obtained by interpolation:

$$\phi(\underline{x}) = \sum_I N_I(\underline{x}) \phi_I \tag{3.17}$$

where the sum denotes a sum over all nodes; yet in practice, only the nodes of the elements intersecting the interface are considered. This first enrichment function thus reads:

$$F^1(\underline{x}) = \left| \sum_I N_I(\underline{x}) \phi_I \right| \tag{3.18}$$

A similar function was also described in [BEL 03] to calculate $\underline{u}^{\mathrm{enr}}$, expressed as:

$$\boldsymbol{u}^{\mathrm{enr}}(\underline{x}) = \sum_J \boldsymbol{N}_J(\underline{x}) \boldsymbol{a}_J \left[F^1(\underline{x}) - F^1(\underline{x}_J) \right] \tag{3.19}$$

Indeed, these two choices can give rise to the same approximation space but different conditioning number of the resulting matrices. For the function F^1, a smoothing practice is usually applied to improve the convergence. Later, in [MOË 03], another enrichment strategy was proposed and the function was shown to provide a better convergence rate which is even close to that of the optimal FEM, written as:

$$F^2(\underline{x}) = \sum_I N_I(\underline{x}) \left| \phi_I \right| - \left| \sum_I N_I(\underline{x}) \phi_I \right| \tag{3.20}$$

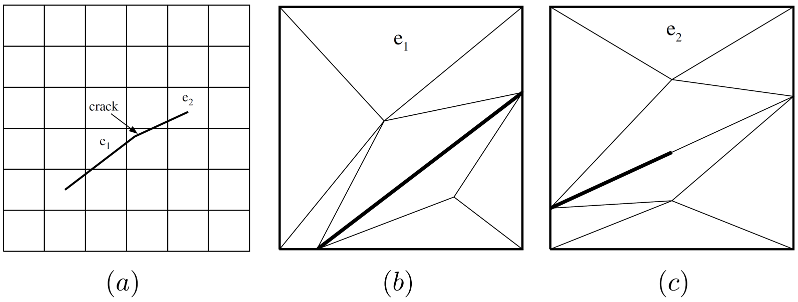

Figure 3.5: Partitioning of QUAD4 element into sub-triangles. Source: [SUK 03]

The enrichment functions introduced above are illustrated in Fig.3.4. Due to its convergence performance, the function F^2 is applied in this PhD work.

3.3 Element partition

In XFEM, the elements cut by interfaces (crack, inclusion, etc.) have to be partitioned into sub-elements. It is only for the purpose of integrating the discrete system of equations. Unlike those resulting from remeshing, the subdivided elements resulting from element partitioning are imaginary and do not add supplementary nodes or degrees of freedom on the intersecting points, which in fact reveals the main idea of XFEM. The differences between these two procedures are well analysed in [SUK 03]. In this section, the conventional partitioning methods are introduced for quadrilateral (QUAD4) element in 2D as well as hexahedral (HEXA8) element in 3D. The methods in 2D were effectively described in the works focusing on the crack modeling [SUK 03, NIS 08], but they are also valid for other cases including inclusion modeling. Besides, a *hexa-priority* partitioning method is proposed and presented for HEXA8 element.

3.3.1 Two-dimensional case

3.3.1.1 Triangle-based

In two-dimensions, we focus here on the partitioning of the QUAD4 element. Typically, it is a straightforward and easily implemented exercise to divide the cut element into triangular sub-elements. This was indeed applied in the early reports such as [MOË 99, SUK 01, SUK 03]. As shown in Fig.3.5(a), a crack intersects with a regular mesh constructed by QUAD4 elements. For the cut elements, such as e_1 and e_2 displayed in Fig.3.5(b) and (c), respectively, the centroids of the two zones on both sides of the interface are computed. The triangles are then obtained by connecting the centroid with vertices of QUAD4 or intersecting points. In this partitioning strategy, higher-order quadrature rules are usually required to ensure the accuracy of numerical integration results; for instance, we could use six-point integration rule on the triangular sub-elements.

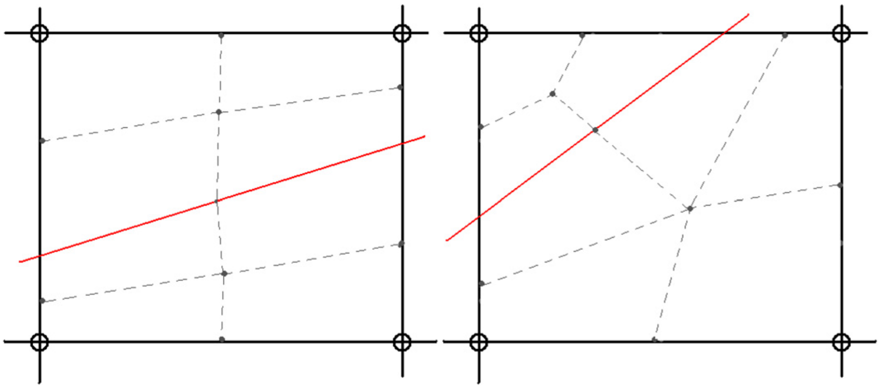

Figure 3.6: Partitioning of QUAD4 element into sub-quadrangles. Source: [NIS 08]

3.3.1.2 Quadrangle-based

In the implementation of Nistor *et al.* [NIS 08], another partitioning method based on quadrilateral sub-elements was proposed. As shown in Fig.3.6, to partition the cut QUAD4 element, the centroids are connected with the middle points of surrounding edges, leading to the subdivision into quadrangles. In this approach, the same integration rule as for the other QUAD4 elements, like the standard four Gauss points rule, is used on the sub-quadrangles within the cut element for the quadrature purpose. The key advantage is that, compared to the above partitioning by triangles using three or six-point integration rule, this partitioning strategy can produce more accurate quadrature results. For this reason, this quadrangle-based partitioning method was applied in our Fortran solver for 2D problems.

3.3.2 Three-dimensional case

3.3.2.1 Tetrahedron-based

In three-dimensions, we concentrate on the partitioning of the HEXA8 element. As an extended case from that in two-dimensions, sub-tetrahedrons are usually applied and generated during the partition procedure. For example, a schematic illustration for three cases of interface-element is given in the report [WAN 16], as shown in Fig.3.7. The HEXA8 element is divided into a tetrahedron and a heptahedron in the first case of (a), into a pentahedron and a heptahedron in the second case of (b), and into two hexahedrons in the third case of (c). They can also be named in terms of the number of vertices on the one side of cutting interface, leading to the case one-vertex, two-vertices and four-vertices, respectively. Further subdivision in each case finally gives rise to sub-tetrahedrons within which the numerical integration is carried out with classical Gauss quadrature rules. However, it is to be noticed that not all the possible cases are depicted in Fig.3.7. We describe here the two other possible cases in Fig.3.8, with the HEXA8 element being divided into a hexahedron and a heptahedron in (a) named the case three-vertices, and into two heptahedrons in (b) named the case special-four-vertices. Similarly, they end up with tetrahedrons only.

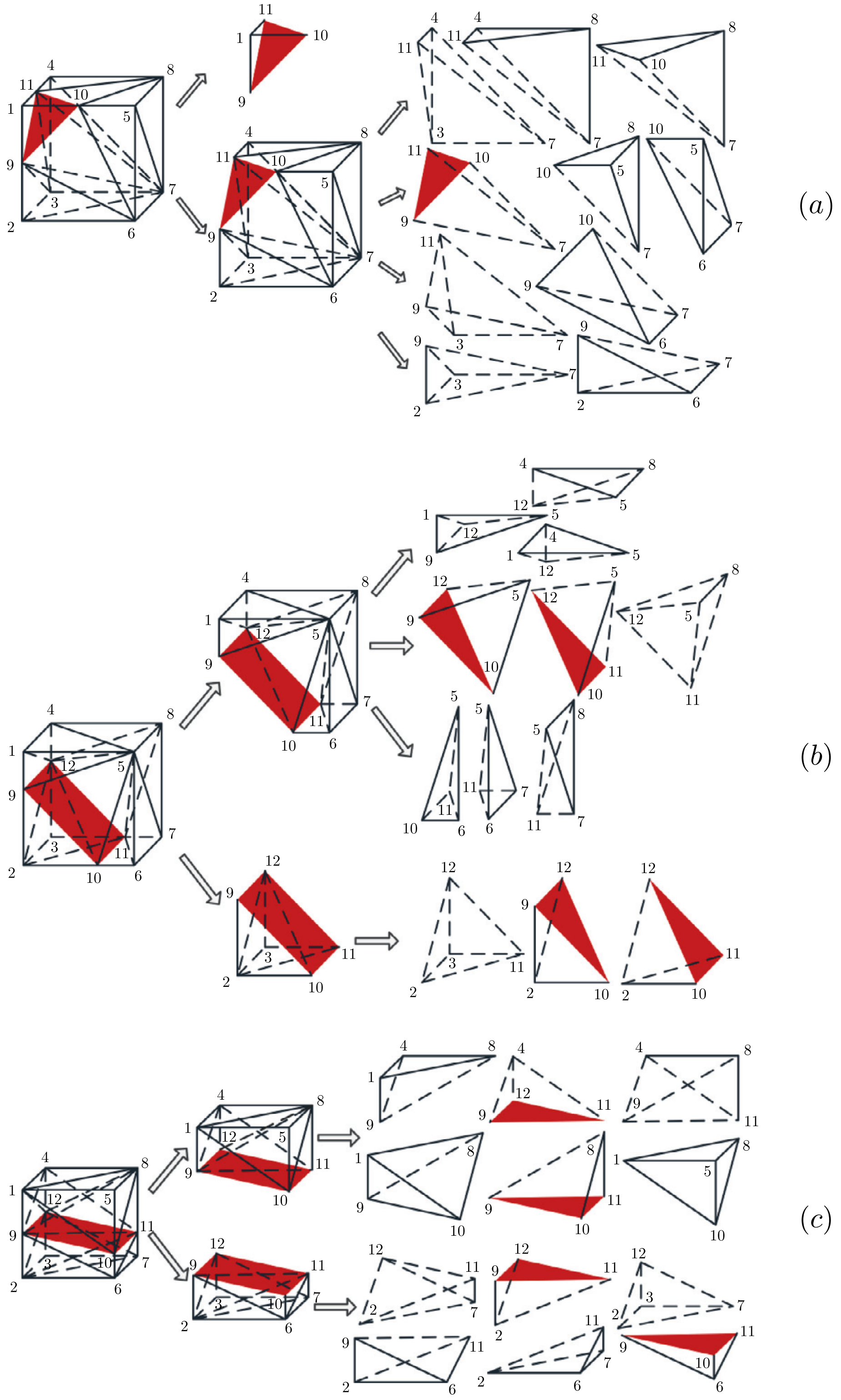

Figure 3.7: Partitioning of HEXA8 element into sub-tetrahedrons. Source: [WAN 16]

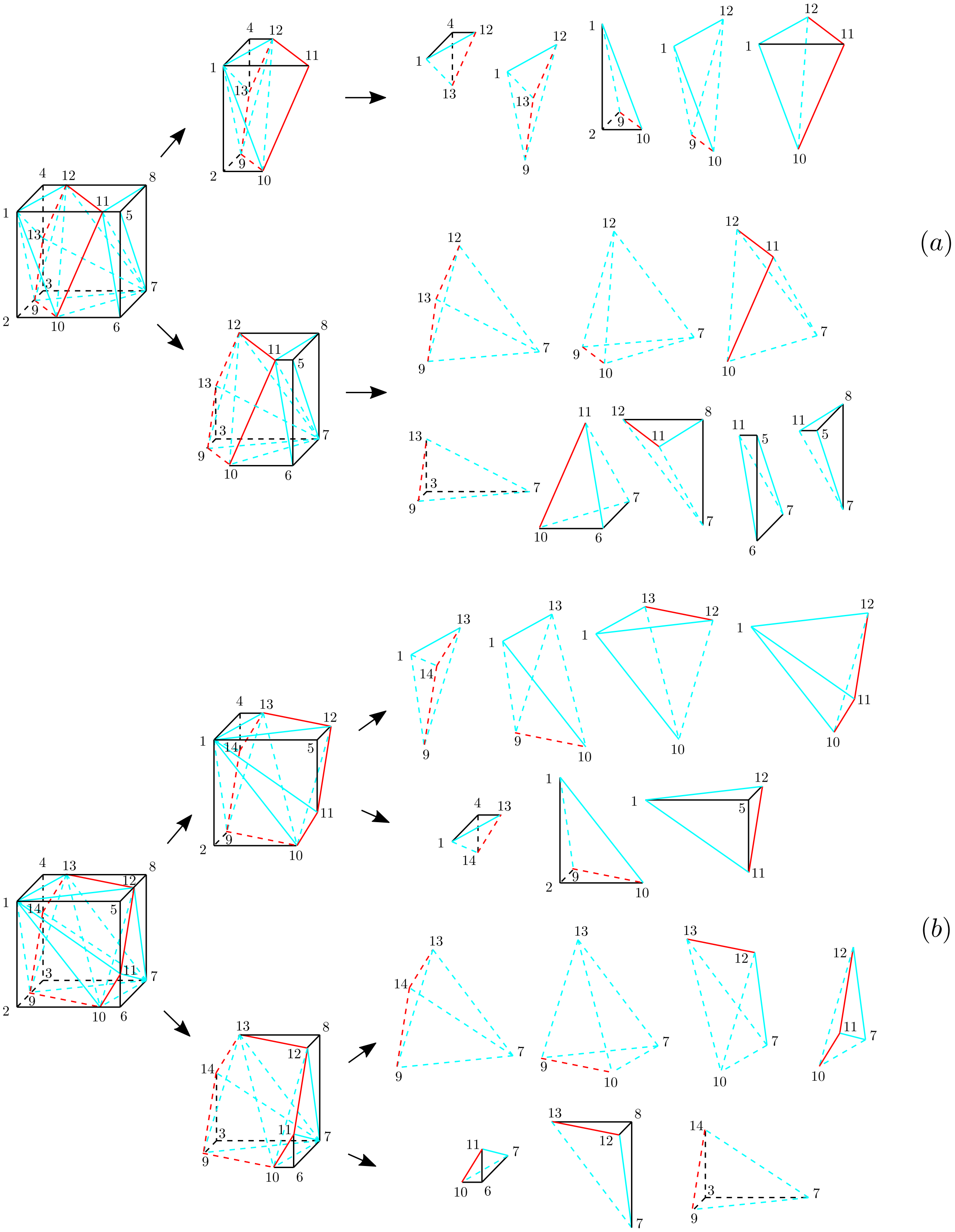

Figure 3.8: The other two cases of partitioning of HEXA8 element into sub-tetrahedrons.

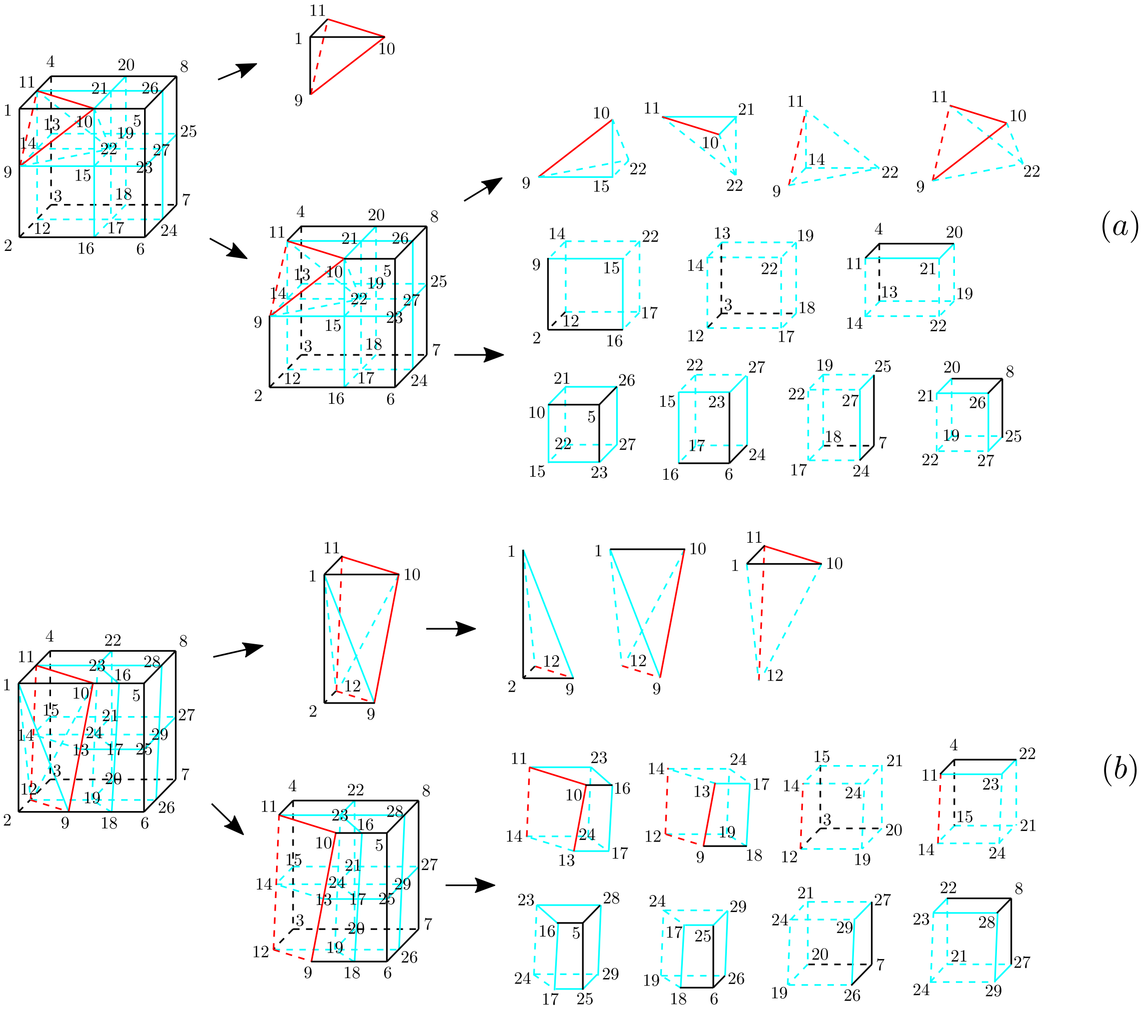

Figure 3.9: Partitioning of HEXA8 element into sub-tetrahedrons and sub-hexahedrons.

3.3.2.2 Hexahedron-priority

To improve the integration accuracy, we propose here a partitioning approach in which the subdivided elements are mixed by sub-tetrahedrons and sub-hexahedrons, and the sub-hexahedrons are expected to be as numerous as possible. All the possible cases are presented in the following.

In the one-vertex case, as shown in Fig.3.9(a), the HEXA8 element can be partitioned into 5 tetrahedrons and 7 hexahedrons in total. The sub-hexahedrons are obtained by taking middle points of edges of interest. For example, point 16 is the middle point for edge 2-6, point 24 for edge 6-7, point 23 for edge 5-6, etc. The same rule is also applied in the other cases for generating sub-hexahedrons.

In the two-vertices case, as shown in Fig.3.9(b), the proposed partitioning method can give 3 tetrahedrons and 8 hexahedrons.

In the three-vertices case, as show in Fig.3.10(a), only 4 hexahedrons are managed to

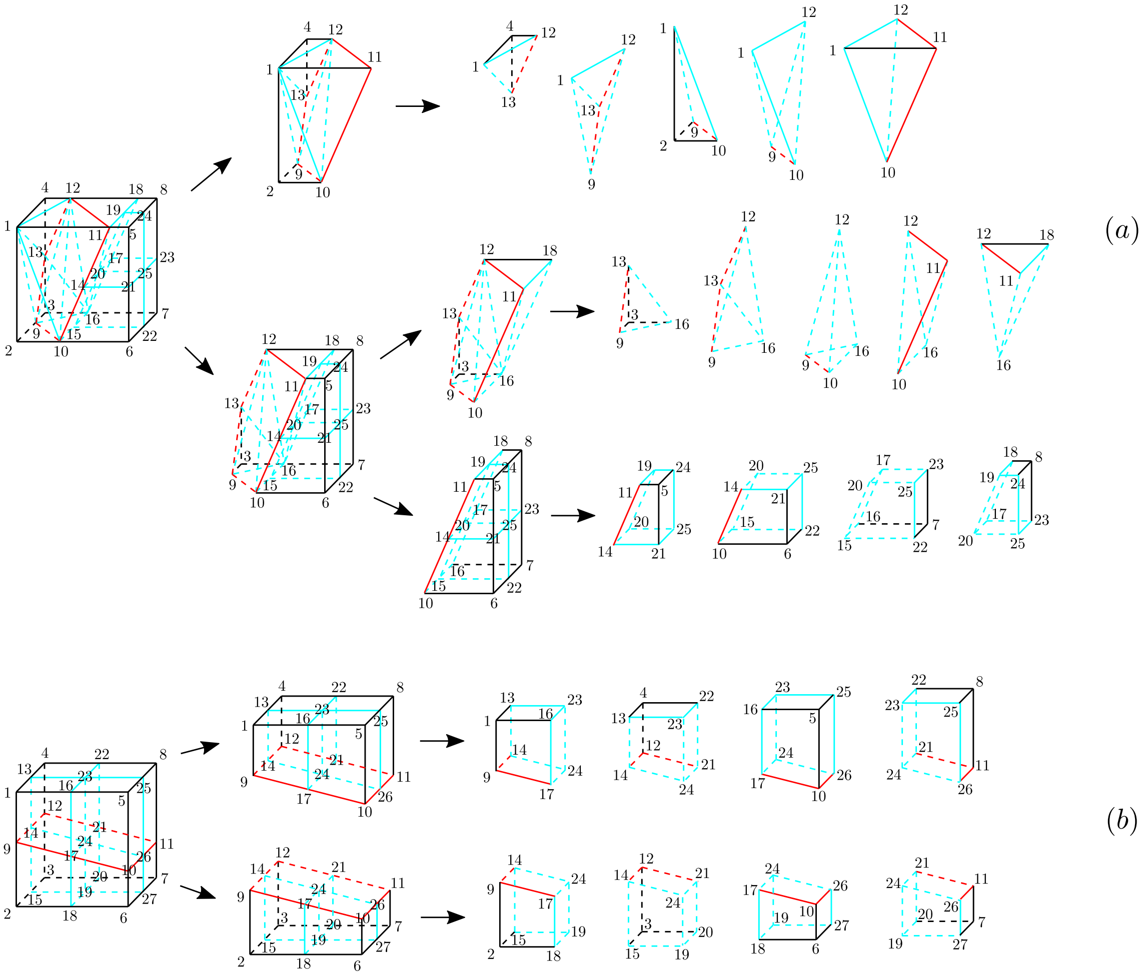

Figure 3.10: (Continued) Partitioning of HEXA8 element into sub-tetrahedrons and sub-hexahedrons.

be obtained, and the other sub-elements are 10 tetrahedrons.

In the four-vertices case, as shown in Fig.3.10(b), it is easier to partition the HEXA8 element following the rule, leading to 8 sub-hexahedrons without tetrahedrons.

In the special-four-vertices case, however, it is quite complicated to partition the HEXA8 element into sub-hexahedrons. Therefore, the case is treated in the traditional way; only sub-tetrahedrons are obtained, as depicted in Fig.3.8(b).

3.4 Numerical implementation and examples

XFEM implementation is performed based on the implementation of FEM presented in section 2.2, including similar matrices implementation, the same modified NB time integration scheme and Simo's scheme for updating internal forces of viscoelastic materials. With all the necessary introductions of XFEM in the previous sections, in this section, we

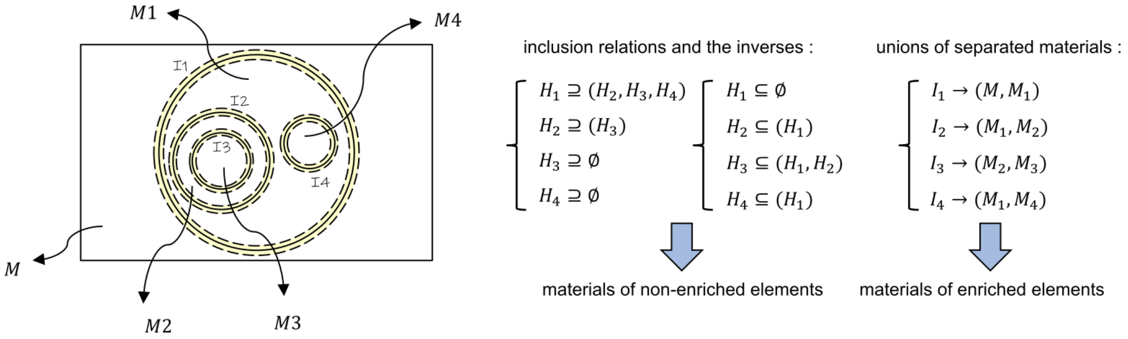

Figure 3.11: Illustration of multiple inhomogeneities implementing algorithm.

present the details of its numerical implementation and give some numerical examples.

3.4.1 Numerical implementation

In this subsection, the numerical implementation of XFEM in our Fortran solver for modeling inclusion is presented. It is mainly based on the reports of Nistor *et al.* [NIS 08] and Sukumar & Prévost [SUK 03]. Two-dimensional case is considered here for the sake of clarity.

3.4.1.1 Preprocessing

Data preparation is required prior to running the simulations for solving the discrete system.

(1) *Inhomogeneity model creation*

In Fortran language, it is more practical to apply a user-defined *derived type*, which is similar to *struct* in C/C++ or *class* in Python, for a variable containing several attributes. An inclusion model is usually characterized by several attributes, such as two extremities for a linear interface, center and radius for a circular inclusion, center, semi-major and semi-minor axes for a elliptical inclusion, etc. Therefore, a derived-type defined in a module file and a variable of this type with all necessary data are to be prepared for correctly creating an inhomogeneity model.

In addition, often more than one inclusion need to be modeled, and one inclusion could be a part of another one. To this end, an algorithm is implemented in which the inclusions and materials relations have to be figured out beforehand and stored into variables for uses later on. An example of four nested inclusions is given in Fig.3.11, along with the inclusions relations for determining materials of non-enriched elements, and with the materials relations in terms of interface for determining materials of enriched (sub-)elements. In some extreme cases, two interfaces can be so close that they cross the same one element. A multi-split solution was proposed by [BAN 19], as illustrated in Fig.3.12.

(2) *Level set values assignment*

With the inclusion model defined previously, the level set function can be numerically computed, which is actually the calculation of the signed distance from each node to the

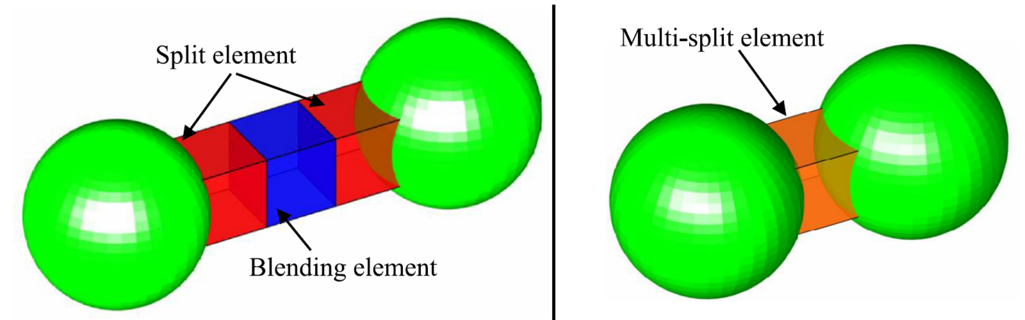

(a) 3-D representation of split element

(a) 3-D representation of multi-split element

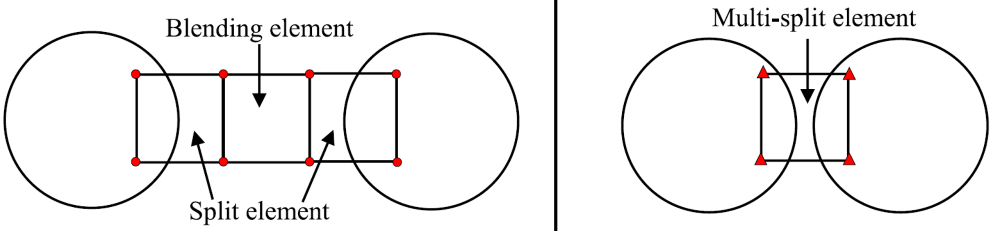

(b) 2-D representation of split element

(b) 2-D representation of multi-split element

Figure 3.12: Illustration of differences between standard XFEM (left) and multi-split XFEM (right). Source: [BAN 19]

imaginary interface. However, in practice, only the nodes of the elements cut by the interface are assigned the level set values, since the use of enrichment function F^2 allows to eliminate the effect of distanced non-enriched nodes. In addition, based on the relative position of each node and element in terms of the interface, material type (background or inhomogeneities) can also be assigned in advance to nodes and elements; these material properties are needed in the subsequent integration, in particular for updating the internal forces.

(3) *Degree of freedom mapping*

Due to the introduction of enriched displacement in XFEM, the nodal degree of freedom (*dof*) can be different from one node to another. The relation between local *dof* in terms of node and global *dof* in terms of system thus becomes more complex than that in FEM. As proposed in [NIS 08], two mapping tables *loc2glob* and *glob2loc* can be computed beforehand to facilitate the matrix assembling procedures. The *loc2glob* mapping returns the global *dof* given the node number and local *dof*, while the *glob2loc* mapping performs inversely.

(4) *Element type assignment*

Based on the level set function, three types of elements are possible: TypeC, TypeA and TypeN. TypeC corresponds to the element that is cut by the interface and whose nodes are all enriched. TypeA corresponds to the element adjacent to TypeC element, whose nodes are partly enriched. TypeN stands for the normal element without any enriched node. In the preprocessing, it is a wise practice to assign the element type to each element, which can be helpful in the later calculations.

(5) *Matrices computation and storage*

Some matrices having fixed values during the dynamic simulation can be pre-computed and stored as constants for rapid access when needed. They may include the strain-displacement matrix $\boldsymbol{B}$, the Jacobian matrix $\boldsymbol{J}$ and the mass matrix $\boldsymbol{M}$. For the sake of clarity, the displacement vector $\underline{d}$ is here defined in the other order than that in Chapter 2; for example, in two-dimensional case, it is written as $\boldsymbol{d} = [\boldsymbol{u},\boldsymbol{a}]^T$ for the global system, and $\boldsymbol{d} = [u_1, u_2, u_3, u_4, a_1, a_2, ..., b_1, b_2, ...]^T$ for a QUAD4 element.

As presented in Chapter 2, the matrix $\boldsymbol{B}$ results from the derivatives of the shape function matrix $\boldsymbol{N}$. For a QUAD4 element e, the two matrices in XFEM can be expressed as:

$$\boldsymbol{N} = [\boldsymbol{N}_1^u, \boldsymbol{N}_2^u, \boldsymbol{N}_3^u, \boldsymbol{N}_4^u, \boldsymbol{N}^a] \tag{3.21}$$

$$\boldsymbol{B} = [\boldsymbol{B}_1^u, \boldsymbol{B}_2^u, \boldsymbol{B}_3^u, \boldsymbol{B}_4^u, \boldsymbol{B}^a] \tag{3.22}$$

The sub-matrices $\boldsymbol{N}_i^u$ and $\boldsymbol{B}_i^u$ are those of FEM for standard displacement $\underline{u}$, while $\boldsymbol{N}^a$ and $\boldsymbol{B}^a$ are for additional displacement $\underline{a}$ of potential enriched nodes which can be noted as $\boldsymbol{N}^a = [\boldsymbol{N}_1^a, \boldsymbol{N}_2^a, ...]$, $\boldsymbol{B}^a = [\boldsymbol{B}_1^a, \boldsymbol{B}_2^a, ...]$. The latter is solely for enriched nodes and thus null for TypeN elements. The block matrices are $(i = 1, 2, 3, 4)$:

$$\boldsymbol{N}_i^u = \begin{bmatrix} N_i & 0 \\ 0 & N_i \end{bmatrix}; \qquad \boldsymbol{N}_i^a = \begin{bmatrix} N_i F & 0 \\ 0 & N_i F \end{bmatrix} \tag{3.23}$$

$$\boldsymbol{B}_i^u = \begin{bmatrix} \frac{\partial N_i}{\partial x} & 0 \\ 0 & \frac{\partial N_i}{\partial y} \\ \frac{\partial N_i}{\partial y} & \frac{\partial N_i}{\partial x} \end{bmatrix}; \qquad \boldsymbol{B}_i^a = \begin{bmatrix} \frac{\partial (N_i F)}{\partial x} & 0 \\ 0 & \frac{\partial (N_i F)}{\partial y} \\ \frac{\partial (N_i F)}{\partial y} & \frac{\partial (N_i F)}{\partial x} \end{bmatrix} \tag{3.24}$$

For TypeN and TypeA element, the calculation of matrix $\boldsymbol{B}$ over the (four) Gauss quadrature points are quite straightforward. However, for TypeC element (*parent* denoted as e_p), the matrix should be computed over the four points of each sub-element (*child* denoted as e_c). A coordinate converting procedure should be highlighted here. Indeed, from the local coordinates $\underline{\xi}_c$ of Gauss point of *child* element e_c, the global coordinates $\underline{x}$ of the same point can be obtained by interpolation. Then, the local coordinates $\underline{\xi}_p$ of the same Gauss point in terms of the *parent* element e_p can be derived from $\underline{x}$ by an inverse method, such as the Trust-Region solver in MKL library for solving nonlinear least squares problem with bound constraints (see *dtrnlspbc* routines in [INT 20]). Finally, the matrix $\boldsymbol{B}$ can be evaluated based on the reversed local coordinates $\underline{\xi}_p$. This is actually because the *dofs* are associated with the *parent* element and the quadrature point should also be considered in the same coordinates system.

For the Jacobian matrix $\boldsymbol{J}$, it is in fact the determinant $|\boldsymbol{J}|$ that is needed to perform numerical integration. It is usually computed along with the strain-displacement matrix. For both TypeN element and TypeA elements, the computation procedures are the same and can be easily completed. For TypeC element, however, it is to be noted that the matrix evaluation on Gauss points of sub-elements is carried out in the local coordinates of the *child* element. The vertices coordinates of *child* element instead of *parent* element should be used, and no coordinates converting procedures are required.

For the mass matrix $\boldsymbol{M}$, the same mass lumping practice as that presented in section 2.2.1.5 is carried out for the standard *dofs*. However, for the enriched *dofs*, another mass lumping technique presented in [MEN 06] is applied in our solver. It was proposed to define the diagonal coefficients associated to enriched *dofs* as:

$$m_{\text{diag}} = \frac{m}{n_{\text{nodes}}} \frac{1}{\text{mes}(\Omega_e)} \int_{\Omega_e} F^2 \text{d}\Omega \tag{3.25}$$

where Ω_e is the considered element, m is the mass, n_{nodes} is the number of element nodes, $\text{mes}(\Omega_e)$ is the measurement being length (1D), area (2D) or volume (3D), and F is the enrichment function. Indeed, $m/\text{mes}(\Omega_e)$ is equivalent to the corresponding density ρ. For the matrix assembling, the previously introduced mapping table *loc2glob* can be used here for the enriched *dofs*.

3.4.1.2 Solving

To solve the dynamic problem of wave propagation formulated by the discrete system in Eq.3.5, the modified NB scheme presented in section 2.2.2.2 is employed for explicit time integration and also spurious noise reducing. For the XFEM case, no special changes have to be made in this scheme as it is independent from the *dofs*.

In our simulations, the boundary conditions are typically displacement-based. The external forces $\underline{f}^{ext}$ are thus regarded as zero, leading to a readily reversed system given the lumped mass matrix. The boundary conditions are usually imposed in the course of time integration, and hence require to be updated in each time step. Particularly in NB scheme, each time step is divided into two sub-steps; care must be taken to impose boundary conditions within each one.

In terms of the internal forces $\underline{f}^{int}$ in XFEM, it still follows the formulations given by Eq.2.37 where the related tensors are evaluated on Gauss points of each element for numerical integration. All the elements are iterated and a final assembling procedure gives tensor $\underline{f}^{int}$. Similarly, a subroutine implementing Simo's algorithm is launched at each time step to update the internal forces. Simo's scheme can be indeed applied to TypeN and TypeA elements as done in standard FEM, since the two types of elements have the same Gauss points in terms of number and local coordinates. For TypeC element, however, the numerical integration should be performed over the Gauss points of all the subdivided elements. In particular, since updating internal forces may require a lot of computing efforts, the parallel calculation can be applied to make the best of all available CPU cores and thus accelerate the simulation; for example, properly using directives of the OpenMP (Open Multi-Processing) interface in Fortran [HER 02] can achieve this purpose.

Once $\underline{f}^{int}$ is obtained by quadrature, the discrete system can be efficiently reversed to solve the displacement vector.

3.4.1.3 Postprocessing

The solved displacement fields in each time step are written to an output file following the vtk file formats [AVI 10]. The generated vtk files can be then imported into Paraview which is an open-source software for interactive visualization, widely used by scientific researchers. In this application, a great variety of functions/tools have been implemented for postprocessing of image/volume data. In addition, a Python module was developed to read the data stored in vtk files; postprocessing can thus be carried out in a Python IDE (Integrated Development Environment) like Spyder, for analyzing and processing data with a higher freedom. See Appendix A for this module implementation.

3.4.2 Numerical examples

In this subsection, we aim to present the XFEM implementation and illustrate the advantages of XFEM over FEM, by means of some numerical examples. A two-dimensional model with plane viscoelastic P-wave propagation is first shown. The same mesh for different inclusions is used to present the convenience of XFEM; wavelengths in different media are measured and compared to analytical ones to present the accuracy of XFEM. Then a three-dimensional model with elastic S-wave propagation is shown. A plane interface separating the model into two media is applied; XFEM and FEM are both used to model the inhomogeneity. The computing efforts are compared to present the efficiency of XFEM and the proposed element-partition algorithm is tested and validated.

3.4.2.1 Two-dimensional case

Two 2D numerical models are illustrated in this subsection. The first contains only one circular inclusion, while the second has two nested inclusions.

The same square model of plane P-wave is applied, with the dimension, boundary conditions and mesh shown in Fig.3.13. The model measures 200×200 mm^2. To ensure that the inclusions can be obviously seen in the wave fields, the material parameters are adjusted such that the wavelength of P-wave is in the range of $20 \sim 40$ mm. The QUAD4 element size is accordingly chosen as 1 mm. Ten periods are simulated and ten snapshots per period are produced.

Figure 3.14 presents the two examples of inclusions; the coordinates origin is set at the lower left corner. In the first example, as show in Fig.3.14, only one circular inclusion is present and characterized by the center C at $(100, 100)$ mm and radius $r_1 = 30$ mm. In Fig.3.14(b), the second example is based on two nested inclusions; the outer one is a regular hexagon with its central part occupied by the other circular inclusion. The same center C as that of the first example is defined, and two radii are $r_1 = 30$ mm, $r_2 = 60$ mm; the radius r_2 displayed in the figure lies in an horizontal position. The two examples have the same excitation parameters, with the frequency of 100 Hz and the amplitude of 50 μm. The materials are listed in Tab.3.1.

Table 3.1: Materials of the 2D model in numerical examples.

Case	E_1 (kPa)	E_2 (kPa)	η $(Pa \cdot s)$	ρ (kg/m^3)	ν
background	0.1	0.1	0.1	1000	0.49
hexagon	0.2	0.1	0.1	1000	0.49
circle	0.3	0.1	0.1	1000	0.49

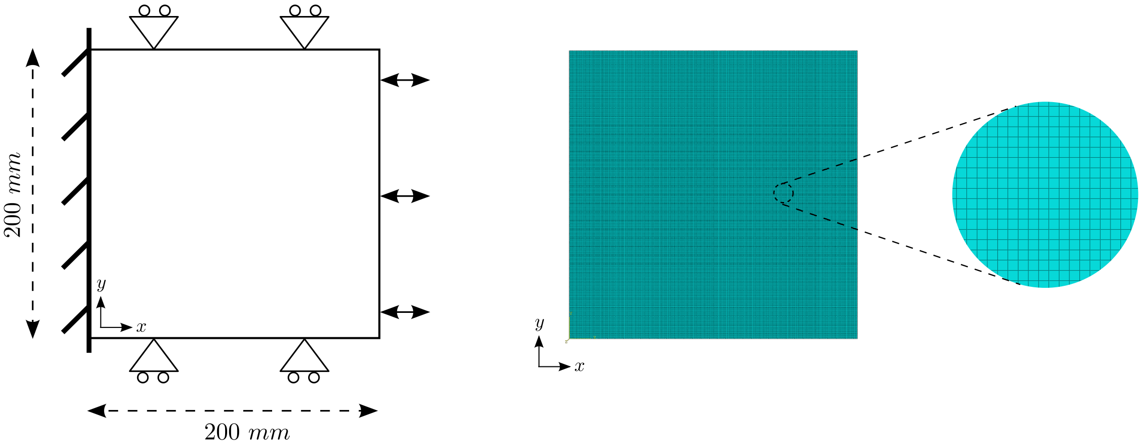

Figure 3.13: Illustration of dimension and boundary conditions (left) and mesh (right) of the 2D XFEM model in numerical examples.

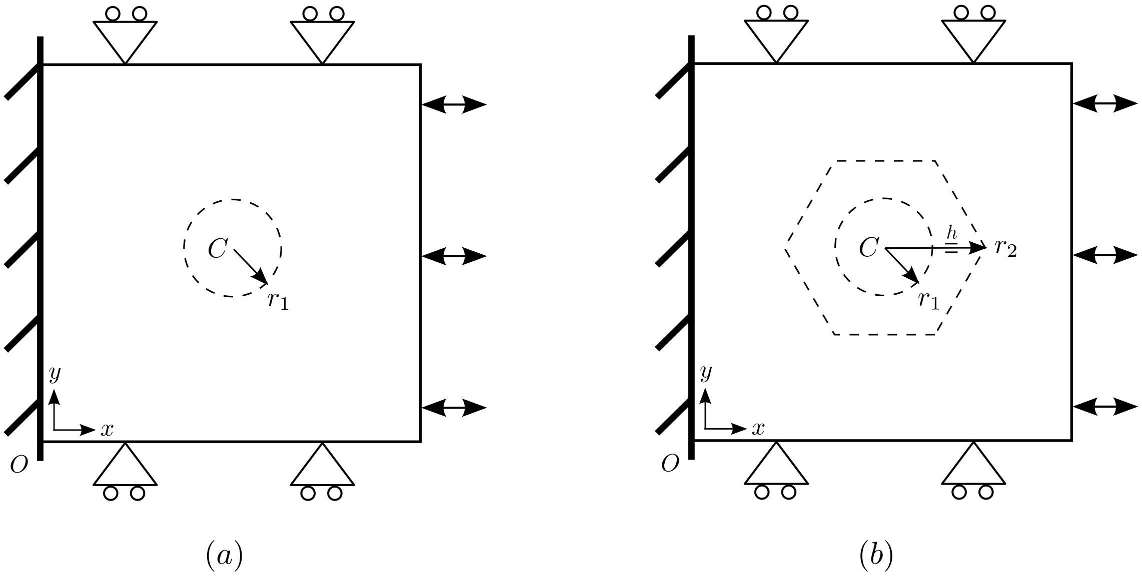

(a) (b)

Figure 3.14: Illustration of the circular inclusion (a) and the nested inclusions (b).

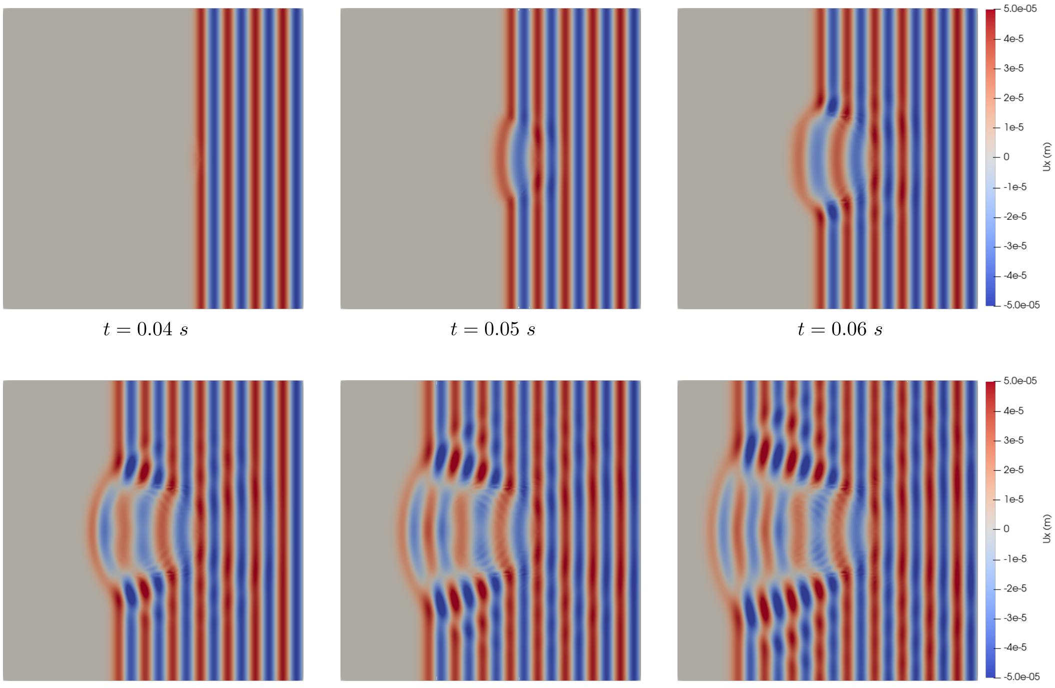

$t = 0.04\ s$ $t = 0.05\ s$ $t = 0.06\ s$

$t = 0.07\ s$ $t = 0.08\ s$ $t = 0.09\ s$

Figure 3.15: Displacement fields u_x of the circular inclusion model.

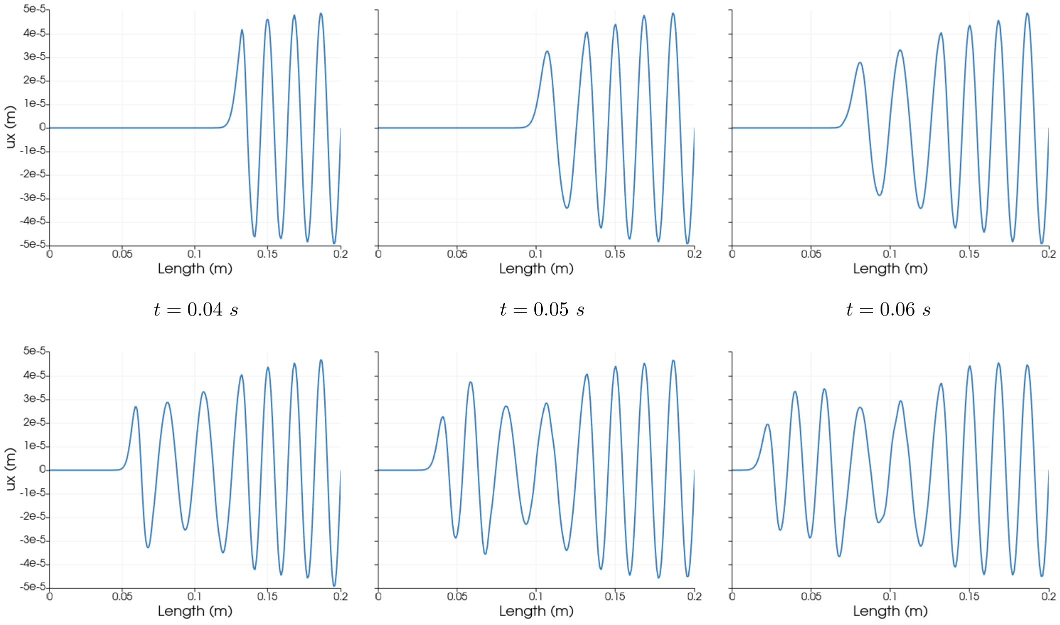

$t = 0.04\ s$ $t = 0.05\ s$ $t = 0.06\ s$

$t = 0.07\ s$ $t = 0.08\ s$ $t = 0.09\ s$

Figure 3.16: Displacements u_x along the horizontal median line of the circular inclusion model.

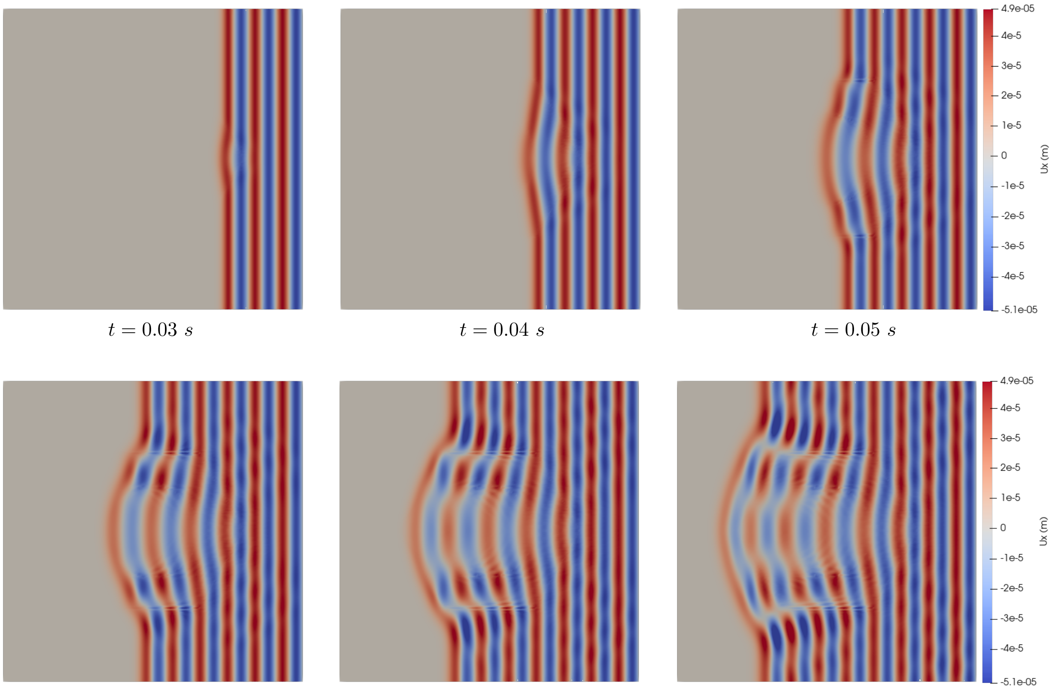

$t = 0.03\ s$ $t = 0.04\ s$ $t = 0.05\ s$

$t = 0.06\ s$ $t = 0.07\ s$ $t = 0.08\ s$

Figure 3.17: Displacement fields u_x of the nested inclusions model.

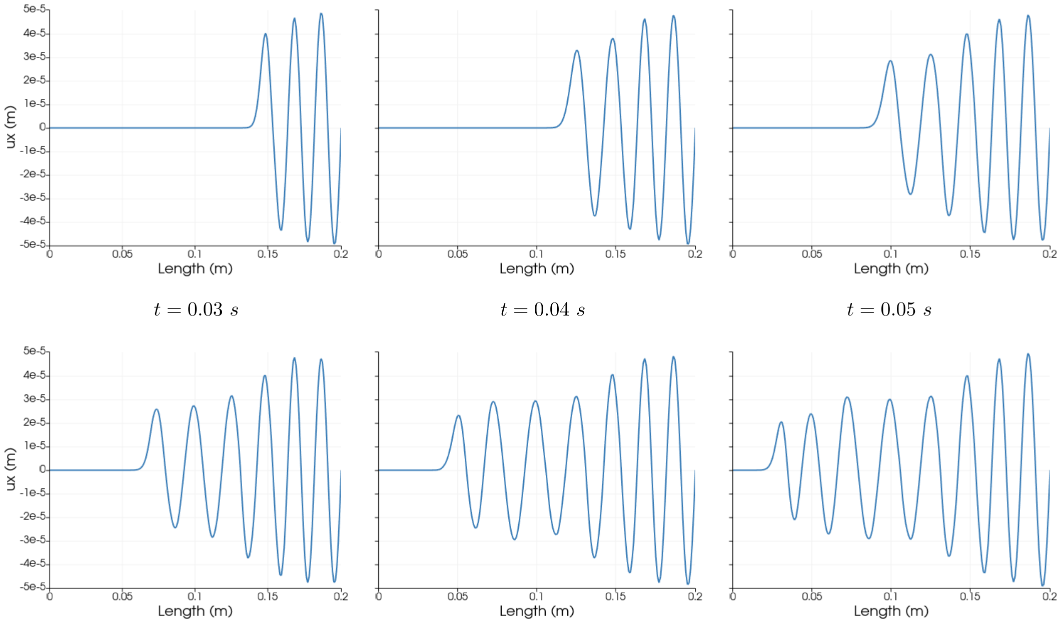

$t = 0.03\ s$ $t = 0.04\ s$ $t = 0.05\ s$

$t = 0.06\ s$ $t = 0.07\ s$ $t = 0.08\ s$

Figure 3.18: Displacements u_x along the horizontal median line of the nested inclusions model.

The numerical results of displacement fields u_x are shown in Fig.3.15 for the circular inclusion model and in Fig.3.17 for the nested inclusions model. Snapshots at the end of successive periods are displayed. The form of inclusions can be well observed in the wave fields. In addition to the reflection and refraction phenomena, it can also be found that the waves propagate faster within the stiffer medium, which corresponds to physics. Qualitatively, it shows that the XFEM implementation works well in a convenient way: one regular mesh can be indeed used to model different inclusions.

Besides, the displacements u_x along the horizontal median line at the corresponding moments are plotted, as shown in Fig.3.16 for the circular inclusion model and in Fig.3.18 for the nested inclusions model. The wavelength in stiffer medium is indeed greater. It is measured to 18.3 *mm* in background and 25.7 *mm* in circular inclusion, and the reference values, based on Eq.2.69, are 18.5 *mm* and 26.2 *mm*, respectively. Quantitatively, XFEM shows its accuracy.

3.4.2.2 Three-dimensional case

In three-dimensions, as models become more complex with more *dofs*, the advantages of XFEM over FEM can be more obvious in terms of meshing efforts and computation time. As shown in Fig.3.19, a cube model is considered in this subsection, with dimension of $100 \times 100 \times 100\ mm^3$. Transverse harmonic excitation along the x-axis is imposed on the top face and the bottom face is completely embedded. The excitation is characterized by amplitude $u_0 = 40\ \mu m$ and frequency $f = 100\ Hz$. To clearly illustrate the propagation of shear wave, purely elastic case is considered; artificial damping $\boldsymbol{C}$ (see section 2.2.1.7) is thus applied with regulated coefficients α_M and α_K. An oblique plane parallel to the z-axis, intersecting vertical edges at 30-70 *mm* points as shown in the figure, cuts the model into two parts with different materials: E for the upper part and E' for the lower part. Greatly different moduli are applied to show that, for XFEM, there is no limitation on the material difference across interface. The material parameters are summarized in Tab.3.2.

Table 3.2: Materials of the 3D model in numerical examples.

E (kPa)	E' (kPa)	ρ (kg/m^3)	ν	α_M	α_K
15	150	1000	0.49	1	1e-5

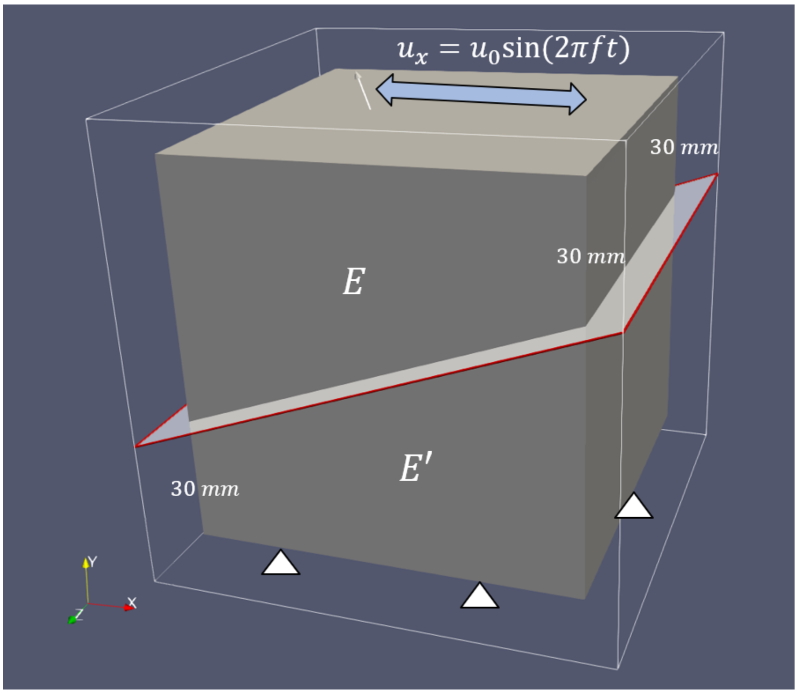

Figure 3.19: Illustration of interface plane and boundary conditions of the 3D model in numerical examples.

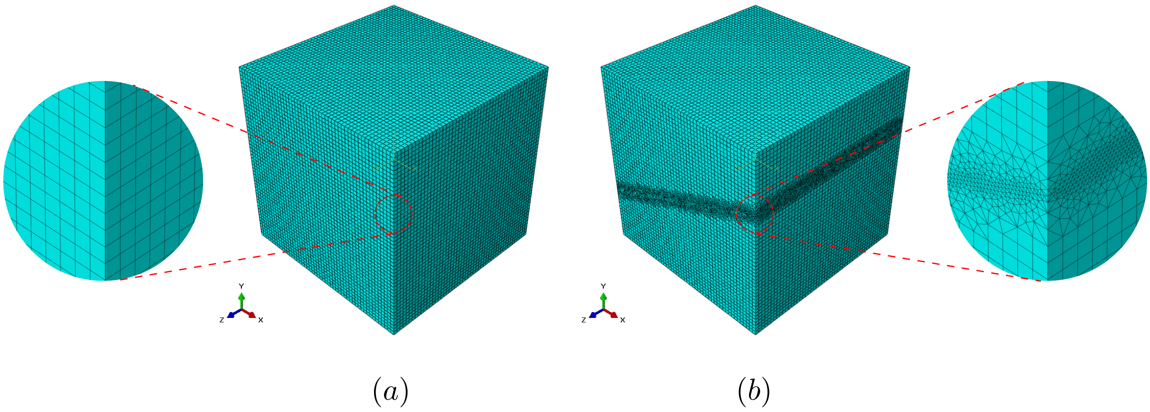

(a) (b)

Figure 3.20: Illustration of mesh of the 3D model by XFEM (a) and by FEM (b).

The model is simulated using XFEM or FEM, with different mesh as illustrated in Fig.3.20. For XFEM model, only hexahedron elements are used; the element size of 2 *mm* leads to 125 000 elements in total. For FEM model, a mixed mesh of hexahedron and tetrahedron elements is applied; the hexahedron element size of 2 *mm* and the tetrahedron element size of 0.5 $\sim$ 2 *mm* lead to 111 000 hexahedron elements and 883 073 tetrahedron elements. The choice of element size is indeed based on the shear wavelength and a convergence study. Moreover, for XFEM model, the two element partition strategies as presented in section 3.3.2 are both applied and compared.

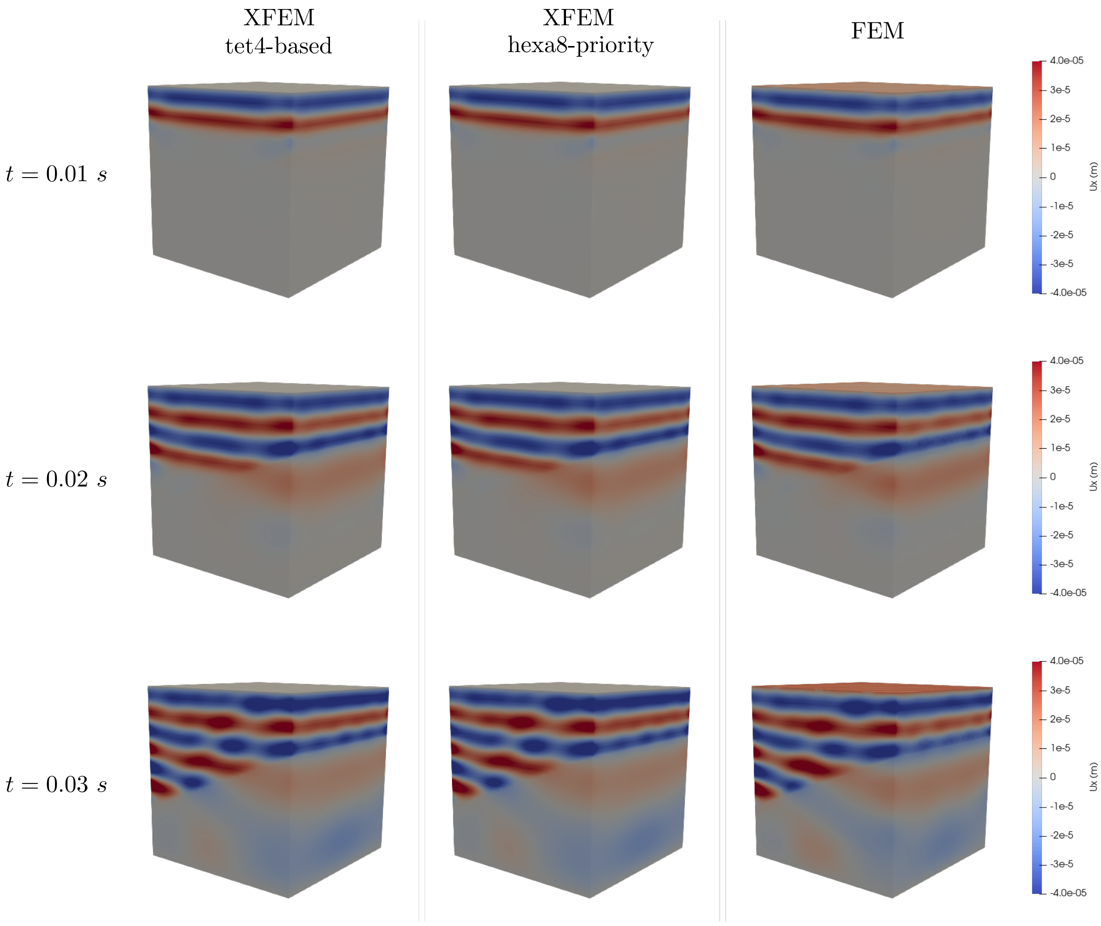

Figure 3.21: Results of the 3D model in numerical examples.

Figure 3.21 presents snapshots of displacement fields u_x at the end of three successive periods, for the tetrahedron-based XFEM model, the hexahedron-priority XFEM model and FEM model, respectively from left to right. It can be observed that the three models have a good agreement in terms of the simulation results including wave distribution and modeling of material interface. The proposed hexa8-priority partition algorithm works as well as the widely used tet4-based algorithm.

Simulations were all executed on a Linux cluster (running CentOS Linux 7.9.2009) with three CPUs *Intel(R) Xeon(R) CPU Gold 5118 @ 2.30 GHz* and *5GB RAM*. In terms of the computation time, for XFEM models, the time step set as 2.8 μs leads to CPU time of 2.5 hours, while for FEM model, the time step of 0.62 μs leads to CPU time of around 15 hours. Indeed, finer mesh in FEM due to the tetrahedron elements requires smaller time step and thus more computing efforts. This gain of time by XFEM is particularly interesting for three-dimensional models. It constitutes one of the advantages of XFEM method: efficiency.

3.5 Conclusion

In this chapter, the extended finite element method was introduced.

In terms of the bases of XFEM, we showed how to derive its basic formulations from an inclusion problem instead of a crack one, considering the future applications in MRE domain. One major concept in XFEM for defining the imaginary interface of inclusion, namely the level set method/function, was then described. Finally, different enrichment functions that represent the discontinuity across inclusion interface were introduced.

For the elements crossed by interface, an important step in the preprocessing consists in the element partitioning. By partitioning, the obtained sub-elements have the specific materials properties and numerical integration of matrices can be thus performed within the cut element. The commonly used partitioning strategies in both two-dimensional case and three-dimensional case were illustrated. In addition, a hexahedron-priority partitioning method was presented.

Finally, we introduced how the XFEM method was implemented into our numerical solver, including the preparation of inhomogeneous model and various matrices in the preprocessing, the discrete system solving and the results postprocessing. Two simple numerical examples were then given for illustration purpose. It has been clearly shown that in XFEM, a regular mesh without remeshing procedures can be used for different inclusion models. Applications in the specific field of MRE will be given in the next chapter, to further highlight the advantages of XFEM over FEM for inclusion modeling.

Chapter 4

XFEM for inclusion modeling in MRE

In this chapter, we present the feasibility of applying XFEM in MRE through some specific examples. The wave propagation through interfaces is first modeled both analytically and numerically for investigating wave conversion. A random-shape inclusion is then proposed for a pseudo-practical application in which the stiffness reconstruction is performed, and advantages of the XFEM model are revealed by comparing with the FEM model.

Contents

4.1 Introduction

In the previous chapter, XFEM formulation was introduced along with its numerical implementation. In this chapter, we aim to use this tool to investigate MRE inhomogeneous media.

Indeed, numerical simulations have been widely used in MRE to generate displacement fields for a given model with known material properties, boundary conditions and excitation sources. Such simulations modeling the wave propagation are helpful in understanding the effects of different parameters on MRE measurements [CHE 05]. In addition, simulations can also serve as a tool for evaluating novel MRE inversion methods [OLI 01, CHA 16], for assessing metric definitions [YUS 21], and even for reconstructing stiffness [DOY 00, HON 16].

Stiffness reconstruction by simulation can be generally categorized into two groups: using analytical formulations or finite element methods. A number of reconstruction methods based on analytical formulations have been proposed and commonly used [MAN 21]. Most of them assume linear viscoelasticity, local homogeneity and small-amplitude excitation, with many assuming isotropy [OLI 01, SIN 05]. Though, there have been a number of studies that have attempted to reconstruct transversely isotropic material properties [CHA 16, GUI 18, ROY 21]. Although it is easy to implement and efficient in producing simulated displacement dataset, the underlying simplifications such as exponentially attenuated plane wave and independence to boundary conditions [SIN 05] may be unrealistic in some cases. In comparison, the latter one based on FEM can describe in a more realistic way more complex wave patterns, geometries and boundary conditions. The basic principles and formulations have been given in Chapters 1 and 2. Either custom-developed codes [DOY 00, BIL 18] or commercial software [CHE 05, YUS 21] have been used to simulate 2D or 3D models subjected to different boundary conditions, and FEM-based reconstruction methods have also been used for transversely isotropic materials [MCG 20].

In FEM-based simulations, the spatial discretization by finite elements has to take into account the geometry boundaries of the whole model and potential inclusions. Usually, triangular elements in 2D [FRE 08] and tetrahedral elements in 3D [HON 17] are employed to model the curved, nonlinear inclusion interfaces. For complex interface, this could imply a burdensome task in terms of the prerequisite model partition, and the resulting finer mesh usually leads to large computational effort. In this case, the extended FEM presented in the precedent chapter can be an alternative. XFEM extends the classical FEM solution space by discontinuous enrichment function [MOË 03] so that the strain discontinuity across the inclusion interface can be reproduced with ease. The level set function defines the interface [SUK 01], making it become independent of the mesh and no longer require a mesh refinement. The model can thus dispense with the need of remeshing for a different interface. To the best of our knowledge, XFEM has not been utilized in MRE studies yet.

As discussed in section 1.1.1, two types of harmonic waves can be generated by drivers, distinguished by the polarization direction: transverse and longitudinal. In soft tissues, S-wave propagates much more slowly (1-10 m/s) than P-wave (around 1540 m/s) [GLA 12], thus allowing its detection by MRI. Besides, due to the quasi-incompressibility of soft biological tissues, the shear moduli G related to shape change and measured from S-wave can vary to a much greater extent within tissues than the bulk moduli K which is related to volume change and P-wave ($G = 10^{-2} \sim 10^{-6}K$) [SAR 95]. These features explain why S-wave propagation is investigated in MRE for stiffness reconstruction.

MRE drivers can be actuated either transversely or longitudinally depending on applications [GNA 21]. The popular transverse drivers are able to generate planar S-waves parallel to the driver/tissue interface [MUT 95], while the longitudinal ones can deliver S-waves with a cone-like hemispherical distribution and have better penetration depth and design flexibility [YIN 08]. Whatever the actuation direction is, the shear and compressional components usually coexist. It is however the former component that is really needed and can be extracted by the curl operator [SIN 05]. Note that these two components are not independent of each other, but rather connected by mode conversion existing at interfaces such as tissue boundaries and inclusion interfaces [SIN 05, GNA 21]. Due to its complexity, the wave mode conversion in MRE is often neglected, like in the numerical model [SCO 20], and has been rarely studied [LIL 21].

In this chapter, we present the applicability of XFEM in MRE by addressing two modeling problems: the wave conversion from P to S at a plane interface and a random-shape inclusion model corresponding to a pseudo-practical application. The simulations are all executed on a Linux cluster (running CentOS Linux 7.9.2009) with three CPUs *Intel(R) Xeon(R) CPU Gold 5118 @ 2.30 GHz* and *5GB RAM*. In what follows, we first introduce the postprocessing methods employed throughout this chapter, namely the curl-based algorithm for extracting the shear components [SIN 05] and the reconstruction method of AIDE [OLI 01] implemented in MREJ tool [XIA 13]. For the first model (wave conversion across a plane interface), we first introduce a theoretical work [COO 67] developed for the problem of reflection and transmission of plane waves across an oblique plane interface between viscoelastic materials and the formulations of mode conversion are given. Then, we present the numerical model by XFEM/FEM and a parametric study is carried out for comparison purpose. We then describe the second model, namely the random-shape inclusion one. The results of reconstructed stiffness are compared between the XFEM and FEM models to underline the XFEM method advantages.

4.2 S-wave extraction and stiffness reconstruction

In this section, we briefly recall two postprocessing methods to be used in the next sections, mainly for extracting shear components of displacement fields and further performing stiffness reconstruction.

As can be seen later from the theoretical formulations describing waves behavior across interface, waves are converted at a plane interface as long as the angle of incidence is not equal to zero. For example, plane P-waves propagating through a plane interface between two viscoelastic media with a given angle of incidence, in addition to the reflected and transmitted P-waves, generate reflected and transmitted S-waves. This is also valid for more general cases where incident waves and interface are not plane. It means that P-waves and S-waves generally coexist at both side of the interface.

This characteristic can also be revealed by the wave equation (Eq.1.58) that contains both the first Lamé parameter λ and the second Lamé parameter μ. The former has the same magnitude as the bulk modulus K, hence representing the compressional components. The latter is in fact the shear modulus G and hence represents the shear components. In MRE, we aim to reconstruct the shear stiffness G based on Eq.1.58. However, as there is a great difference in magnitude between λ (GPa) and μ (kPa) in soft tissues due to quasi-incompressibility, G cannot be properly recovered directly from the equation. To this end, several strategies were usually considered, such as ignoring the term containing λ due to the divergence-free relation of displacement $\nabla \cdot \boldsymbol{u} \approx 0$ (i.e. $\partial_i u_i \approx 0$) resulting from the quasi-incompressibility property [OLI 01], and applying the curl operator to the wave equation [SIN 05]. The latter one is based on the Helmholtz theorem stating that any sufficiently smooth vector field can be decomposed into an irrotational (curl-free) vector field and a solenoidal (divergence-free) vector field. For the displacement field $\underline{u}$, the curl-free part represents the compressional/longitudinal components $\underline{u}_L$ and the divergence-free part represents the shear/transverse components $\underline{u}_T$. The wave equation thus becomes a Helmohltz-type equation in terms of a new field of curl-applied displacement $\boldsymbol{q} = \nabla \times \boldsymbol{u}$ where any contributions from $\underline{u}_L$ are removed, leading to the remaining $\underline{u}_T$ for reconstructing shear stiffness.

To reconstruct the stiffness, several algorithms have been developed in MRE including direct and iterative methods. As the name suggests, direct methods aim at retrieving stiffness by directly solving the wave equation, or the simplified Helmholtz equation (Eq.1.24). Compared to iterative methods that are hard to implement and computationally expensive, direct methods have the advantages of being straightforward and fast despite the sensitivity to noise due to the multiple derivatives. The most frequently used direct methods may include local frequency estimation (LFE) and algebraic inversion of the differential equation (AIDE). The AIDE method, proposed by Oliphant *et al.* [OLI 01], consists in inverting a system of differential equations of mechanical motions, similar to Eq.1.24. Moreover, a least-square polynomial fitting by Savitzky-Golay filter is used to compute the spatial derivatives and a regularization technique is applied to prevent division by zero. These two direct methods can be accessed, for example, through the *MREJ* tool, which is a Java plugin implemented in ImageJ software [XIA 13]. It should be mentioned that the original sources in MREJ would lead to normalized stiffness maps. Sources were thus adjusted to produce maps of real shear moduli.

In this chapter, the simulated displacement fields are postprocessed by applying the curl operator to filter out the compressional components $\underline{u}_L$. The obtained fields representing shear components $\underline{u}_T$ are then imported into the MREJ tool to reconstruct shear modulus (real part G') by the implemented AIDE algorithm, which means that the displacement field $\underline{u}$ in Eq.1.24 is actually regarded as the curl-based alternative $\underline{q}$.

4.3 Wave mode conversion at plane interface

The characteristics of mechanical waves have been studied for a long time, while the problems of reflection and refraction at boundaries or interfaces were just resolved some decades ago. In the following, we will (1) concisely present an analytical model with the formulations developed in the work of Cooper [COO 67] which, in a relatively general way, models the reflection and transmission of plane waves across an oblique plane interface between two viscoelastic media; and (2) present a two-dimensional model with a specially designed linear interface to investigate wave conversion with our numerical tool; and finally (3) compare the two models through a parametric study.

Meanwhile, some errors in the formulas in [COO 67] were found and corrected. Proof and numerical implementation are provided in Appendix B and C, respectively.

4.3.1 Analytical model

As done in [COO 67], the subscripts l,m,n are taken to indicate different cases. l is used to denote incident wave type as P-wave ($l=1$) or S-wave ($l=2$). m refers to the side of the interface, i.e. $m=1$ means the incident side and $m=2$ means the transmitted side. n is used to denote the resulting wave type, as P-wave ($n=1$) or S-wave ($n=2$). For instance, ζ_{lmn} expressed as ζ_{121} would describe the angle of a refracted ($m=2$) P-wave ($n=1$) arising from an incident P-wave ($l=1$); similarly, k_{mn} expressed as k_{12} defines the wave number of a reflected ($m=1$) S-wave ($n=2$).

4.3.1.1 Plane wave representation

Here we focus on the plane wave. It can be indeed described by the Navier equations that have been formulated in section 1.2.1.5, for example, the Eq.1.58 representing the elastic waves with small amplitude and harmonic motion, propagating within a homogeneous, isotropic, linearly viscoelastic medium. This equation is widely used in the literature [OLI 01, SIN 05, FOV 18a, PAR 06, PAR 10].

Across an interface, it can be demonstrated that the reflected and transmitted waves are in the same plane as the incident wave [ROY 99]. Thus, we only consider the two-dimensional motions in the $x-y$ plane with displacements $\boldsymbol{u}=(u,v,0)$ and coordinates $\boldsymbol{x}=(x,y,0)$. As shown in [CHR 12], the solution to Eq.1.58 can be expressed conventionally in exponential form, e.g. in the x-direction:

$$u = u_0 \exp[i(kx-\omega t)] \tag{4.1}$$

where u_0 is the amplitude and k is the wavenumber.

Wavenumber can be calculated using its definition, with the subscripts defined above applied, as:

$$k_{mn} = \frac{\omega}{S_{mn}} \tag{4.2a}$$

$$S_{m1}^2 = \frac{\lambda_m + 2\mu_m}{\rho_m} \tag{4.2b}$$

$$S_{m2}^2 = \frac{\mu_m}{\rho_m} \tag{4.2c}$$

It can also be regarded as complex-valued and reads:

$$k_{mn} = \frac{\omega}{C_{mn}} (1 - i \tan \Omega_{mn}) \tag{4.3}$$

where

$$\tan 2\Omega_{mn} = \frac{\mathrm{Im} S_{mn}^2}{\mathrm{Re} S_{mn}^2} \tag{4.4a}$$

$$C_{mn} = |S_{mn}| \sec \Omega_{mn} \tag{4.4b}$$

Unlike [COO 67], we reverse the signs of $\tan \Omega_{mn}$ and $\tan 2\Omega_{mn}$, which corresponds to the conventional use. Indeed, it can be proved that original signs will lead to improper results as shown in Appendix B.

4.3.1.2 Reflection and refraction coefficients R_{lmn}

Following the notations in [COO 67], we use θ_l and ζ_{lmn} to indicate incident angle and reflected/refracted angle, respectively. The angle θ_l is real while ζ_{lmn} is generally complex. Besides, R_{lmn} is used to denote the ratio between reflected/refracted amplitude and incident amplitude.

As presented in [COO 67], after introducing some potential functions for displacement components, applying the boundary conditions at the interface and combining the complex Snell's law, a system of linear equations can be obtained for each wave type ($l = 1$ or 2):

$$\boldsymbol{A}_l \boldsymbol{R}_l = \boldsymbol{B}_l, \qquad l = 1 \text{ or } 2 \tag{4.5}$$

where

$$\boldsymbol{A}_l = \begin{bmatrix} \sin \zeta_{l11} & \cos \zeta_{l12} & -\sin \zeta_{l21} & \cos \zeta_{l22} \\ \cos \zeta_{l11} & -\sin \zeta_{l12} & \cos \zeta_{l21} & \sin \zeta_{l22} \\ -\rho_1 S_{11} \cos 2\zeta_{l12} & \rho_1 S_{12} \sin 2\zeta_{l12} & \rho_2 S_{21} \cos 2\zeta_{l22} & \rho_2 S_{22} \sin 2\zeta_{l22} \\ (\rho_1 S_{12}^2 / S_{11}) \sin 2\zeta_{l11} & \rho_1 S_{12} \cos 2\zeta_{l12} & (\rho_2 S_{22}^2 / S_{21}) \sin 2\zeta_{l21} & -\rho_2 S_{22} \cos 2\zeta_{l22} \end{bmatrix} \tag{4.6}$$

$$\boldsymbol{B}_1 = \begin{Bmatrix} -\sin \theta_1 \\ \cos \theta_1 \\ \rho_1 S_{11} \cos 2\zeta_{112} \\ (\rho_1 S_{12}^2 / S_{11}) \sin 2\theta_1 \end{Bmatrix}, \quad \boldsymbol{B}_2 = \begin{Bmatrix} \cos \theta_2 \\ \sin \theta_2 \\ \rho_1 S_{12} \sin 2\theta_2 \\ -\rho_1 S_{12} \cos 2\theta_2 \end{Bmatrix}, \quad \boldsymbol{R}_l = \begin{Bmatrix} R_{l11} \\ R_{l12} \\ R_{l21} \\ R_{l22} \end{Bmatrix} \tag{4.7}$$

The expressions above include some corrections compared to the expressions in [COO 67], namely $\boldsymbol{A}_l(3,1)$ corrected from $-\rho_1 S_{11}\cos\zeta_{l12}$, $\boldsymbol{B}_1(4)$ from $\rho_1 S_{12}^2 \sin 2\theta_1$ and $\boldsymbol{B}_2(3)$ from $-\rho_1 S_{12}\sin 2\theta_2$.

4.3.1.3 Reflection and refraction angles θ_{lmn}

Solving the precedent system of equations requires the knowledge of complex angle ζ_{lmn}. To this end, the angle is represented by:

$$\zeta_{lmn} = \alpha_{lmn} + i\beta_{lmn} \tag{4.8}$$

It can be proven that β_{lmn} satisfies:

$$\sinh^2\beta_{lmn} = \frac{1}{2}\left\{\Gamma_{lmn}^2 - 1 + \left[\left(1-\Gamma_{lmn}^2\right)^2 + 4\Gamma_{lmn}^2 \sin^2\Delta_{lmn}\right]^{\frac{1}{2}}\right\} \tag{4.9}$$

where

$$\Gamma_{lmn} = \gamma_{lmn}\cos\Omega_{mn}/\cos\Omega_{1l} \tag{4.10}$$

$$\gamma_{lmn} = C_{mn}\sin\theta_l / C_{1l} \tag{4.11}$$

$$\Delta_{lmn} = \Omega_{1l} - \Omega_{mn} \tag{4.12}$$

With some derivations in terms of wavenumber, the real reflection or refraction angle θ_{lmn} can be determined by the formula:

$$\sin\theta_{lmn} = \xi_{lmn}\gamma_{lmn} \tag{4.13}$$

where

$$\xi_{lmn} = \left(1 + \sinh^2\beta_{lmn}\sec^2\Omega_{mn}\right)^{-\frac{1}{2}} \tag{4.14}$$

Finally, the real part of complex angle can be calculated by:

$$\alpha_{lmn} = \theta_{lmn} + \phi_{lmn} \tag{4.15}$$

where

$$\tan\phi_{lmn} = \tan\Omega_{mn}\tanh\beta_{lmn} \tag{4.16}$$

It should be noted that the sign of β_{lmn} is determined by:

$$\mathrm{sign}(\beta_{lmn}) = -\mathrm{sign}(\xi_{lmn}^2\tan\Omega_{mn} - \tan\Omega_{1l}) \tag{4.17}$$

4.3.2 Numerical model

In this section, we present a P-S conversion model. It is two-dimensional under plane strain hypothesis since a model with plane interfaces and plane waves can be reduced from 3D to 2D.

To numerically study wave conversion from plane P-waves to plane S-waves at an oblique interface between two different viscoelastic materials, we could have taken a two-dimensional finite model divided into two parts directly by an oblique linear interface. However, such a simple, intuitive model can cause some undesired reflections at boundaries which pollute the S-waves generated at the interface, leading to a more complex interpretation of results. To this end, we designed a model with a piecewise linear interface, as illustrated in Fig.4.1.

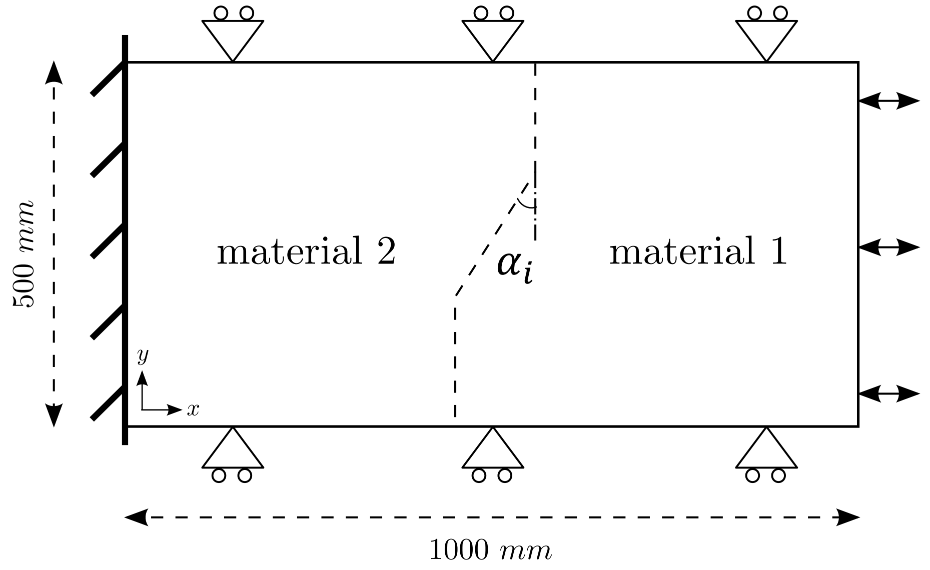

Figure 4.1: P-S conversion model.

The rectangular P-S conversion model dimension is 1000×500 mm^2. The P-waves are generated from the right edge and propagate to the left. The left edge is totally embedded. Symmetric boundary conditions (SBC) are applied along the top and bottom edges to make the incident P-waves plane. The three linear segments in dashed lines represent the interface separating the materials with material 1 on the right side and material 2 on the left side. The inner oblique segment, characterized by the angle of incidence α_i of incident P-waves, serves as the targeted linear interface across which S-waves will be generated from P-wave conversion and studied. The upper and lower vertical segments, across which only plane P-waves are present, protect the inner transmitted waves from being polluted by reflections at boundaries. In this manner, the measurements within the zones following the inner segment will be relatively representative of S-waves arising only from P-wave conversion at the interface, and comparable to theoretical predictions.

4.3.3 Comparison by a parametric study

With the above P-S conversion model, we conducted a parametric study. The transmitted S-waves were measured in terms of the angle of refraction α_t and the amplitude A_t. The influence of the angle of incidence α_i (10 to 80 degrees), the Young's modulus E_1 (10 to 80 *kPa*) of material 2, the excitation frequency f (25 to 100 *Hz*) and the excitation amplitude A_i (50 to 200 *µm*) on α_t and A_t was evaluated. The default parameters of the model are listed in Tab.4.1.

This parametric study was performed in two ways for interface modeling: by XFEM and by FEM. A case of $\alpha_i = 40$ degrees is illustrated in Fig.4.2. A regular mesh with 125000 quadrilateral elements with size of 2 *mm* was used in XFEM, while in FEM mesh, 123878 quadrilateral elements with size of 2 *mm* and 14754 triangular elements with a minimum size of 0.5 *mm* were mixed to match the material interface. A mesh convergence study was performed for determining the mesh size.

The simulations were all launched for 10 harmonic periods considering the speed of incident P-wave, while the measurements of α_t and A_t for each study were performed at different times around the fifth period when fields near the oblique interface became stable, depending on the speed of transmitted S-waves. Finally, the numerical results were compared with predictions given by the analytical model of Cooper [COO 67].

Figure 4.3 illustrates the numerical results of the displacements and extracted S-waves of the P-S conversion model with the default parameters, all captured at the moment of 4.5 periods. Recall by Figs.4.3(a) and (b) presenting the displacement fields along x-axis and y-axis, respectively, that the incident wave was a P-wave propagating from right to left and impacting the oblique interface. In Figs.4.3(c) and (d) presenting the extracted S-waves from the displacements of model by XFEM and FEM, respectively, the inner oblique segment of the interface can be distinctly observed. Due to the existence of the angle between oblique and vertical segments, undesired waves are generated from the two corners. Moreover, the spurious oscillations are produced before the shock front following the wave conversion. The measurements of the angle of refraction α_t and amplitude A_t of the transmitted S-waves, on the left side, are hence performed several periods later when the displacement fields next to the oblique interface become stable. In terms of α_t, the nodes respecting $\underline{u}_T \approx \underline{0}$, corresponding to the wavefront as illustrated by the dashed line in Fig.4.3(c), are chosen to determine the tilted angle and calculate α_t by the difference with α_i. In terms of A_t, since the S-waves propagate with great attenuation, the maximum displacement picked from the zone just following the upper part of the oblique interface, as indicated by the arrow in Fig.4.3(c), is considered as a good estimate of the wave amplitude A_t.

Table 4.1: Default parameters of the P-S conversion model.

	E_1 (kPa)	E_2 (kPa)	η $(Pa \cdot s)$	G' (kPa)	ρ (kg/m^3)	ν	f (Hz)	A_i (μm)	α_i $(degree)$
material 1	6	10	16	3.7	1000	0.49	-	-	-
material 2	20	10	16	8.4	1000	0.49	-	-	-
incident P-waves	-	-	-	-	-	-	100	150	40

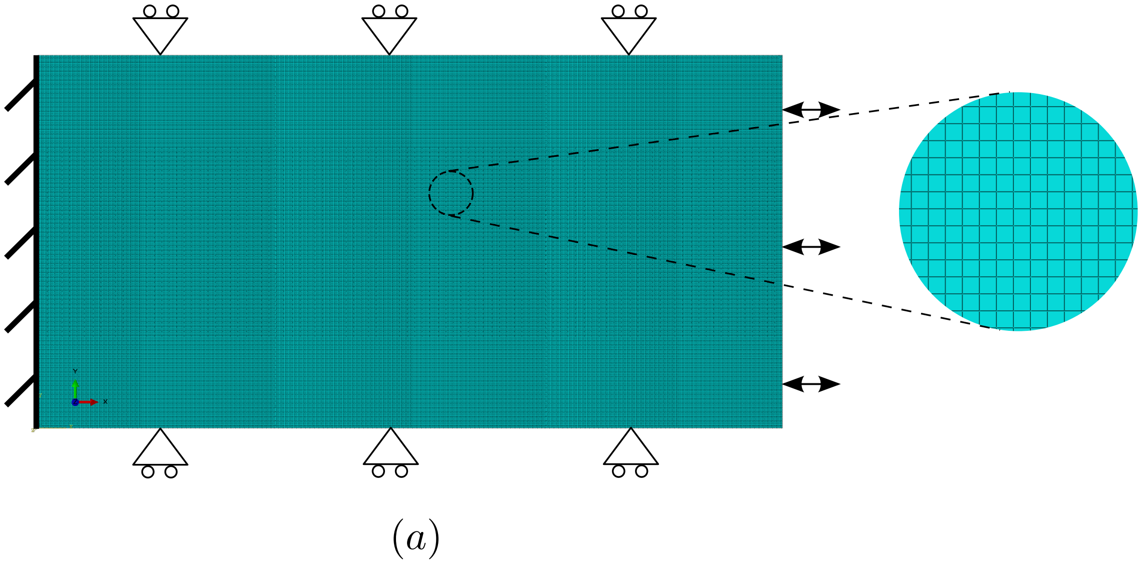

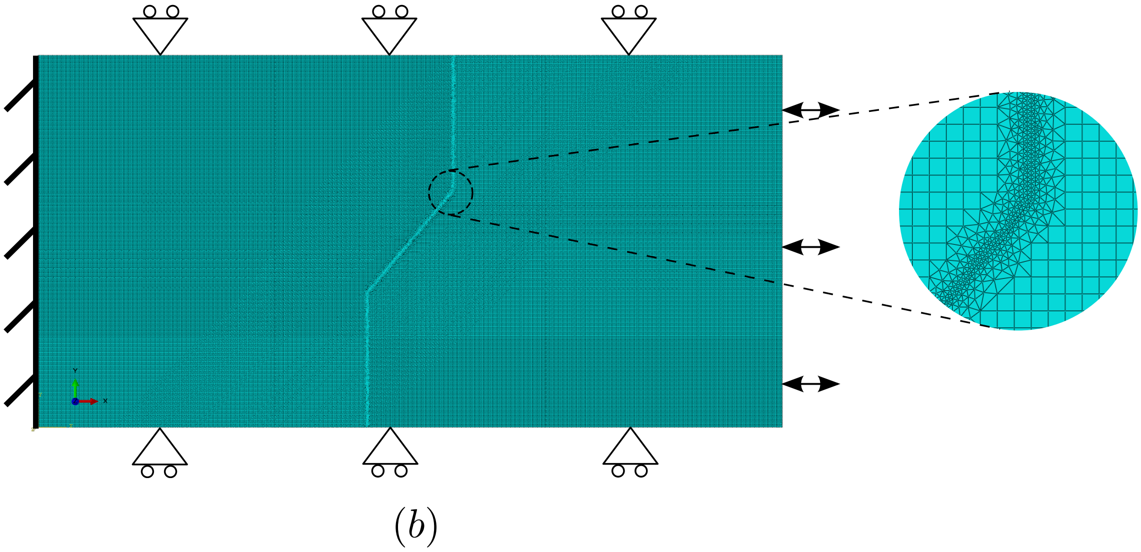

Figure 4.2: Illustration of mesh of the P-S conversion model by XFEM (a) and FEM (b).

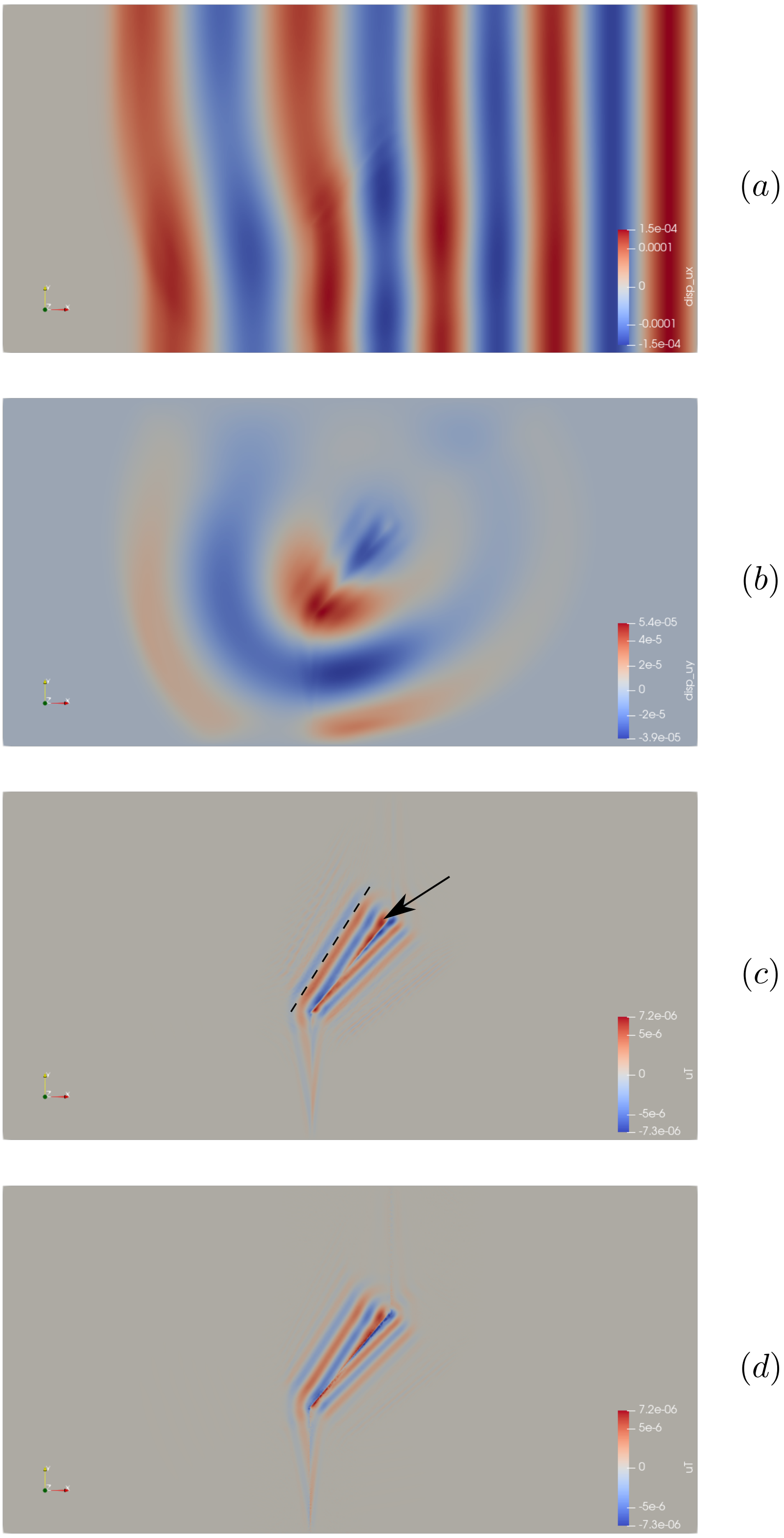

Figure 4.3: Illustration of displacement fields along x-axis (a) and y-axis (b), and extracted S-waves by XFEM (c) and FEM (d) of the P-S conversion model.

Figure 4.4 presents the results of the parametric study. α_t and A_t are generally in accordance between the theoretical model, the XFEM model and the FEM model, for various values of the angle of incidence α_i, the modulus E_1 of material 2, the frequency f and the amplitude A_i of excitation.

For different angles of incidence α_i, as shown in the first column of Fig.4.4, the three models predict that the angle α_t increases with α_i, while the amplitude A_t reaches a maximum at around 60 degrees and then decreases as α_i tends to 90 degrees. However, we observe a discrepancy between the numerical models and the theoretical one, as neither FEM nor XFEM predict the sharp increase of A_t above $\alpha_i = 40$ degrees.

For different moduli E_1 of material 2 varying from 10 to 80 *kPa*, we can derive the more commonly-used complex modulus using Eqs.1.92 and 1.93. Thus, the second column of Fig.4.4 also represents the influence of the storage modulus G' of material 2 from 5.04 *kPa* to 28.53 *kPa*, or the effect of the stiffness ratio of material 2 to material 1 varying from 1.35 to 7.57. As can be seen, both α_t and A_t increase with E_1 (or G', or the stiffness ratio). Although the numerical results by XFEM model and FEM model present the same increasing tendency, the numerical models seem to underestimate A_t for E_1 greater than 40 *kPa*.

For different excitation frequencies f, as shown in the third column of Fig.4.4, both α_t and A_t decrease as the excitation frequency increases. In terms of α_t, all the three models are in good agreement. Finally, for different excitation amplitudes A_i, the angle α_t remains constant and the amplitude A_t increases linearly with A_i. Particularly, the XFEM model is in better agreement with the theoretical model, in comparison with the FEM model.

4.3.4 Discussion

A comparison between a theoretical model on the one hand, and FEM and XFEM models on the other hand is performed in the academic case of a plane P-wave impacting an oblique plane interface, to evaluate the potential of FEM and XFEM to correctly predict wave conversion at interfaces. Analytical solutions exist for this case and are considered here as the reference. Good agreement has been shown between the three models, except for some specific cases addressed in the following.

First, numerical errors have been dramatically reduced at the beginning of the simulations, due to the application of the modified-NB time integration scheme. The presence of material interface, however, results in the amplification of these noises. Figure 4.5 compares the case of $\alpha_i = 60$ degrees with normal mesh size (2 *mm*) to another one with finer mesh (1 *mm*), both captured at the moment of 4.5 periods. The finer mesh leads to smoother displacement fields, while the coarser mesh yields spurious oscillations that extend much further from the interface. The measurements in the parametric study are conducted several ($2 \sim 3$) periods later when the shock front has progressed far away ($\sim$ 300 *mm*) from the region of interest, implying that the results are not likely to be impacted by these noises. However, for other studies requiring the focus on the entire domain, such as the second model with a random-shape inclusion, these numerical oscillations might be an issue and have effects on the reconstruction precision.

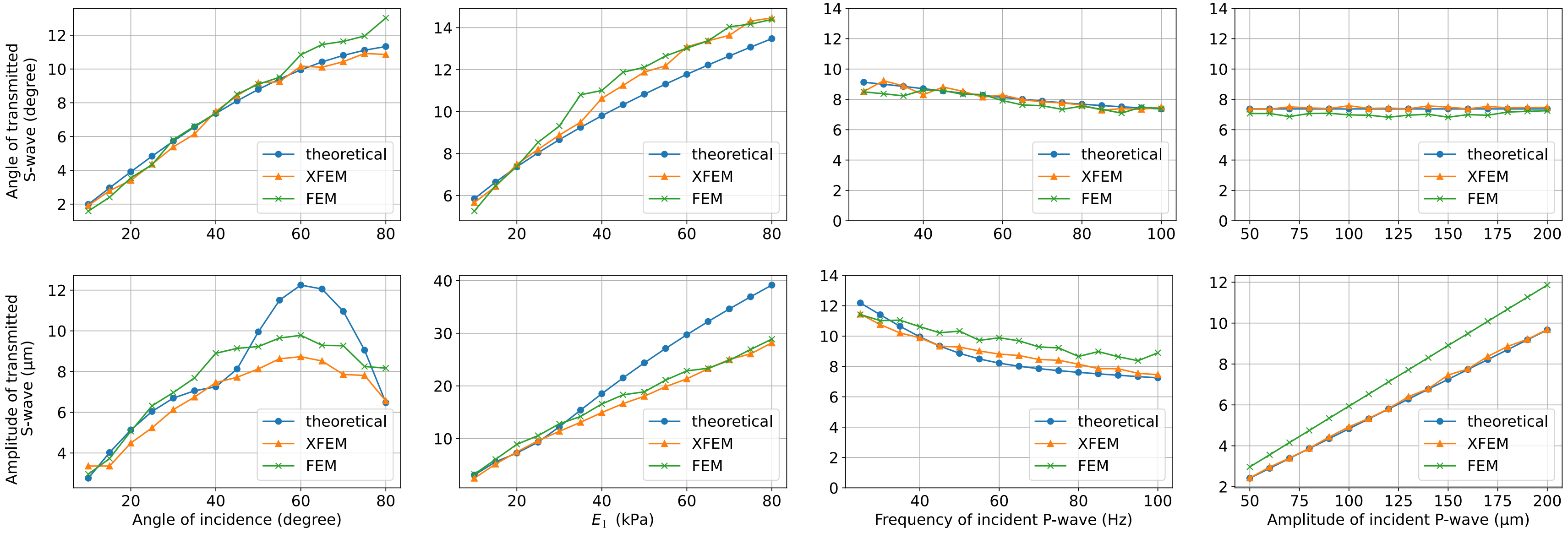

Figure 4.4: Results of the parametric study based on P-S conversion model.

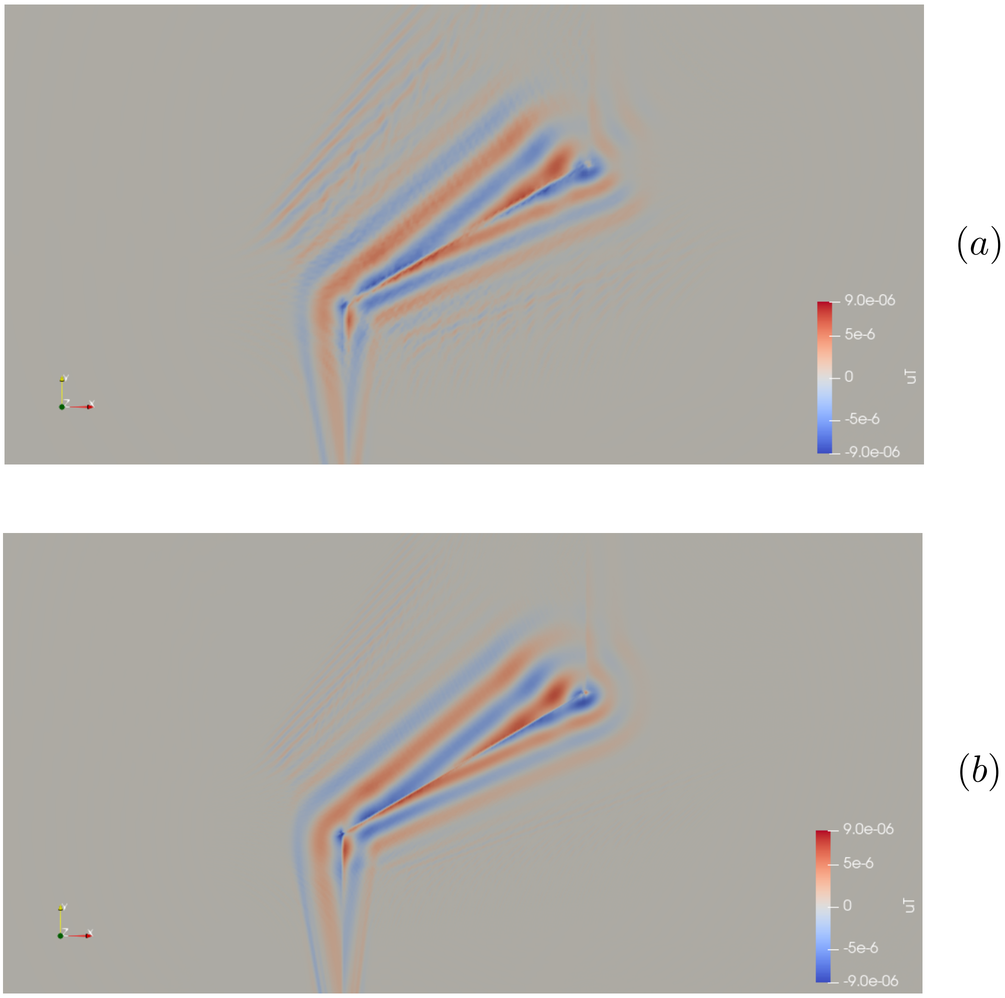

Figure 4.5: Illustration of converted S-waves by the P-S conversion XFEM model with the angle of incidence $\alpha_i = 60$ degrees and element size of 2 *mm* (a) or 1 *mm* (b). A central zoom is taken for illustration purpose.

Then, from the parametric study results in Fig.4.4, the conclusion can be drawn that the XFEM model has similar performance to the FEM model in modeling wave mode conversion at plane interface. For different excitation frequencies and amplitudes, XFEM can produce better results than FEM with respect to the analytical predictions. However, for different angles of incidence and moduli E_1 (or G', or the stiffness ratio of material 2 to 1), an offset between the numerical and analytical results is observed. Indeed, the analytical model assumes an infinite plane interface which is hard to model in reality. The interface with finite length, however, implies two extremities such as the two corners formed by the oblique segment and the vertical segments in the P-S conversion model. These two extremities can degrade the wave fields, making the theoretically plane transmitted and reflected waves become no longer plane. Greater angle of incidence and larger value of E_1 (which also means greater wavelength) will further amplify these effects.

Moreover, as reported in [COO 67], the interface waves, i.e. $\theta_{lmn} = \pi/2$, can exist when the parameter γ_{lmn} in Eq.4.11 satisfies $\gamma_{lmn} \geq 1$. It can be demonstrated that $\gamma_{121} \geq 1$ for angle of incidence greater than 50 degrees. This indicates that an interface wave exists, though hard to observe, on the transmission side (material 2) for the large angles, which can probably have an influence on the measurements.

4.4 Random-shape inclusion

4.4.1 Inclusion modeling by XFEM and FEM

To further investigate XFEM performances in a more practical application, we develop a two-dimensional square model containing a random-shape inclusion, as shown in Fig.4.6(a). The model has dimension of 150×150 mm^2. The inclusion is characterized by two vertical/horizontal segments and four circular arcs with radius $r_1 = 15$ *mm*, $r_2 = 10$ *mm*, $r_3 = 8$ *mm* and $r_4 = 6$ *mm*, and the first arc is centered at $(x_{c1}, y_{c1}) = (100, 100)$ *mm*. In addition to this *aligned* inclusion, a *tilted* inclusion is also considered by rotating the *aligned* one in the counter clockwise direction around the point $(100, 80)$ *mm* by 30 degrees, as presented in Fig.4.6(b). In terms of boundary conditions, the right edge is longitudinally actuated, the left and top edges are embedded, and the bottom edge is free of restrictions. The other parameters of materials and excitation are summarized in Tab.4.2.

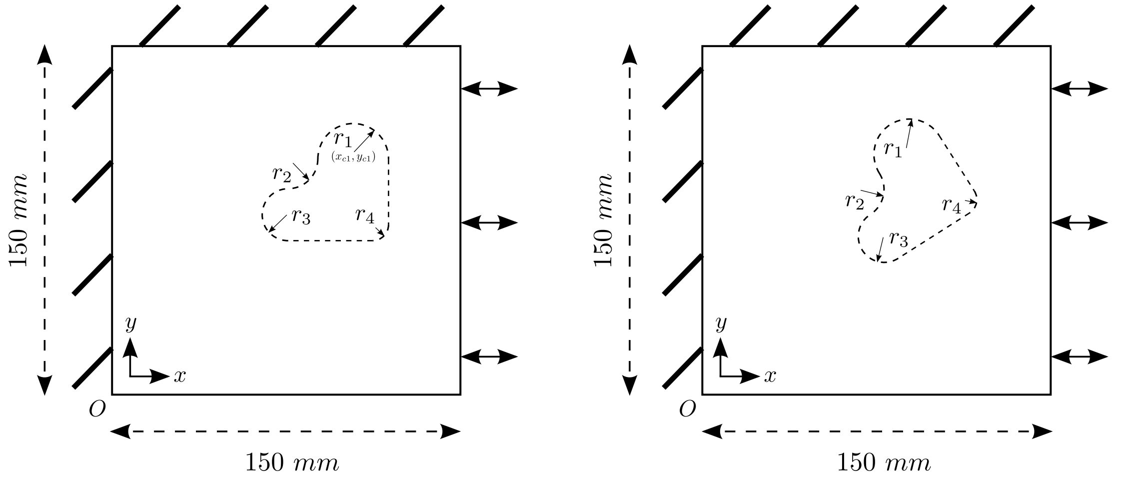

(a) (b)

Figure 4.6: Random-shape inclusion model. The random-shape inclusion is represented by dashed lines. (a) *aligned* inclusion and (b) *tilted* inclusion.

As with the P-S conversion model, the above inclusion model is also studied in two ways for the interface modeling: by XFEM and by FEM. Figure 4.7 presents the mesh difference between XFEM and FEM. As can be seen, in FEM triangular elements are still needed around the material boundaries to match the mesh with the interface, while in

Table 4.2: Parameters of the random-shape inclusion model.

	E_1 (kPa)	E_2 (kPa)	η $(Pa \cdot s)$	G' (kPa)	ρ (kg/m^3)	ν	f (Hz)	A_i (μm)
background	3.3	6	6.5	1.6	1000	0.49	-	-
inclusion	10.5	2	4	3.88	1000	0.49	-	-
incident P-waves	-	-	-	-	-	-	84	100

XFEM a regular mesh with only quadrilateral elements is sufficient. Concretely, 90000 quadrilateral elements with size of 0.5 *mm* are employed in XFEM for modeling the *aligned* and *tilted* inclusion shown in Figs.4.7(a) and (c), respectively. In FEM, 87311 quadrilateral elements with size of 0.5 *mm* and 17142 triangular elements with a minimum size of 0.2 *mm* are used for the *aligned* inclusion illustrated in Fig.4.7(b), and 87188 quadrilateral elements with size of 0.5 *mm* and 17688 triangular elements with a minimum size of 0.2 *mm* are used for the *tilted* inclusion illustrated in Fig.4.7(d). The mesh size has been determined by a mesh convergence study.

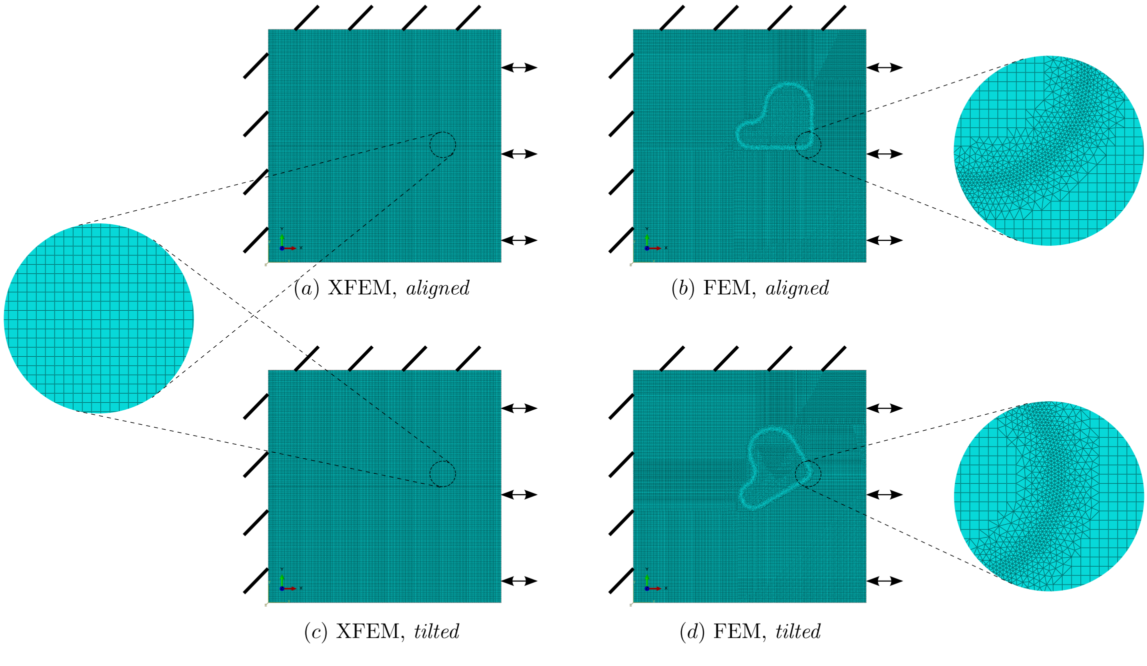
(*a*) XFEM, *aligned*
(*b*) FEM, *aligned*
(*c*) XFEM, *tilted*
(*d*) FEM, *tilted*

Figure 4.7: Illustration of mesh of the random-shape inclusion model by XFEM and FEM.

The simulations by XFEM and FEM are both launched for 100 harmonic periods at the end of which the model is observed to reach a steady state. The displacement fields, sampled at 8 snapshots evenly distributed over one period, are postprocessed by applying the curl operator to extract the shear components $\underline{u}_T$. The results are then imported into the MREJ tool for reconstructing shear modulus G' by the AIDE algorithm.

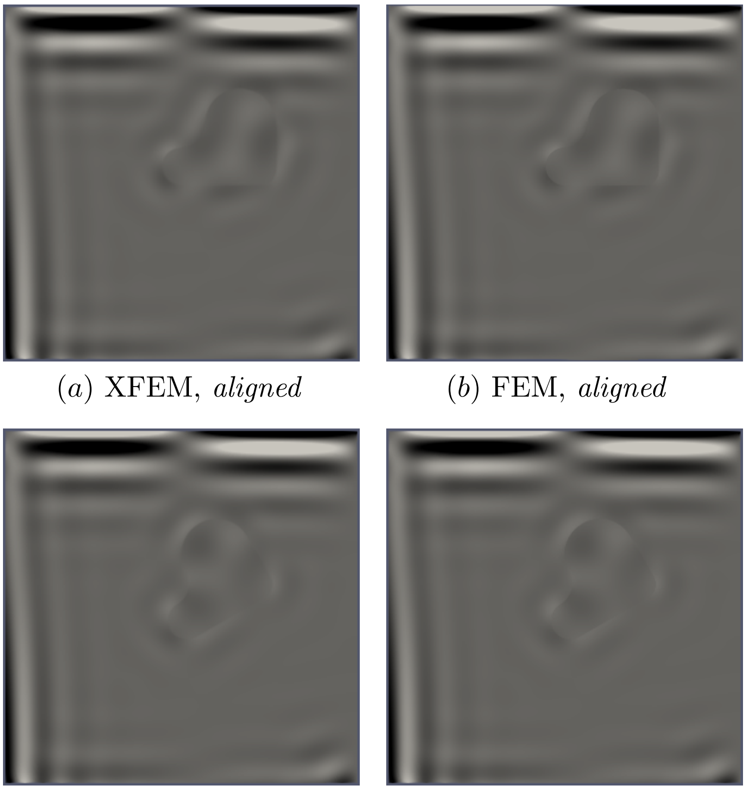

(a) XFEM, *aligned* (b) FEM, *aligned*

(c) XFEM, *tilted* (d) FEM, *tilted*

Figure 4.8: Illustration of the first snapshot during a period in steady state of curl-applied displacement $\underline{u}_T$ of the random-shape inclusion model.

4.4.2 Comparison between XFEM and FEM

Figure 4.8 illustrates, for the random-shape inclusion modeled by XFEM and FEM, the extracted shear components with curl operator applied to the simulated displacement fields. For both models, only one snapshot is shown, which is indeed the first one of the last simulated period (100th). Reflected S-waves from the top and left embedded boundaries can be observed by their great amplitude. The inclusion can also be easily located due to the phase difference between the waves at the two sides of interface. Qualitatively, the two models provide very similar results.

Figures 4.9(a) and (b) present the stiffness reconstruction results for the *aligned* inclusion modeled by XFEM and FEM, respectively. For each model, the shear modulus G' is measured within two zones. Zone 1, represented as a circle at the top left, is used for estimating G' of the background. This area is chosen for the relatively large amplitude of the shear waves due to reflections at the boundaries. Zone 2 is used for estimating G' in the inclusion. In terms of the computation time, it takes about 19.2 hours of CPU time (6.4 hours of real time) for the XFEM model, and 22.0 hours of CPU time (7.3 hours of real time) for the FEM model.

Figures 4.9(c) and (d) present the stiffness reconstruction results for the *tilted* inclu-

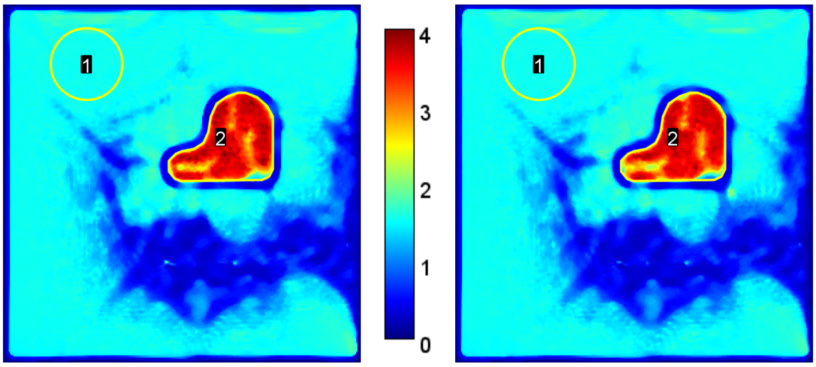

(a) XFEM, *aligned* (b) FEM, *aligned*

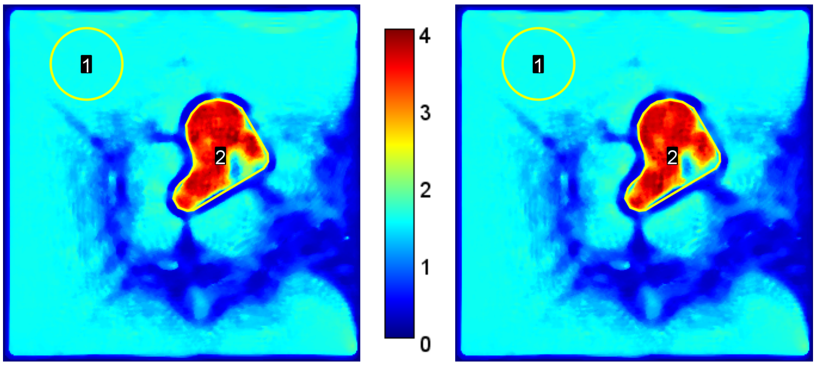

(c) XFEM, *tilted* (d) FEM, *tilted*

Figure 4.9: Results of shear modulus G' reconstruction from the curl-applied displacement $\underline{u}_T$ of the random-shape inclusion model.

sion modeled by XFEM and FEM, respectively. In terms of the computation time, it takes about 19.5 hours of CPU time (6.5 hours of real time) for the XFEM model, and 21.6 hours of CPU time (7.2 hours of real time) for the FEM model.

All the stiffness estimates are summarized in Tab.4.3. Quantitatively, both XFEM and FEM have yielded stiffness estimates close to the ground truth values which are 1.60 *kPa* for the background and 3.88 *kPa* for the inclusion. We can also observe that the *tilted* inclusion model yields larger variance within the inclusion, the estimated modulus being more inhomogeneous than that of the *aligned* inclusion model.

4.4.3 Discussion

Although XFEM has been developed for two decades and successfully used in modeling different inhomogeneities such as cracks, holes and inclusions, the application to the domain of MRE is not yet introduced in the literature. The second model in this chapter containing a random-shape inclusion is intended to illustrate the convenience of XFEM in inclusion modeling, namely the advantage of being remeshing-free. The stiffness estimation from the simulated wave fields further helps in investigating the accuracy of XFEM,

Table 4.3: Stiffness estimates of the random-shape inclusion model.

	XFEM				FEM				“True”
	Mean	SD	SD/Mean %	Error %	Mean	SD	SD/Mean %	Error %	
Aligned inclusion									
background	1.599	0.033	2.06	0.06	1.600	0.027	1.69	0	1.60
inclusion	3.450	0.503	14.58	11.08	3.384	0.576	17.02	12.78	3.88
Tilted inclusion									
background	1.597	0.016	1	0.19	1.597	0.015	0.94	0.19	1.60
inclusion	3.191	0.794	24.88	17.76	3.162	0.806	25.49	18.51	3.88

[*] The mean, standard deviation (SD), the ratio of standard deviation to the mean (as x%), and the error of the mean with respect to “True” (as x%) in each region are presented for both the XFEM and FEM methods. The “True” values indicate the known ground truth values in the simulations. All the units except those of percentages are in *kPa*.

and shows that XFEM is totally likely to be integrated and applied in MRE studies. In terms of the computation time, 2 to 3 hours of CPU time are gained by XFEM with respect to FEM, revealing the efficiency of XFEM in this rather simple case. We can imagine that the gain would be even more interesting when it comes to complex geometries of inclusions, such as the irregular ones of real tissues in three-dimensions.

The mesh in the XFEM model is composed of only quadrilateral elements (QUAD4), considering the accuracy and the model shape. However, in addition to QUAD4, the triangular elements (TRI3) are also compatible with XFEM in case of complex outer boundaries.

The mesh in the FEM model is mixed with QUAD4 and TRI3. QUAD4 are used as the main elements due to the high accuracy and TRI3 are used for modeling the interface due to the flexibility. Indeed, using TRI3 for the entire mesh is also feasible in spite of the potential degradation of simulated results quality.

For the stiffness estimation results, the boundary regions including the model boundaries and the material interfaces are not well reconstructed. This comes from the limits of AIDE method and is probably due to the inherent homogeneity assumption as reported in [OLI 01]. For the background, the regions with obvious converted S-waves are well reconstructed with G' being around the ground truth value of 1.60 *kPa*, such as those close to the left, top and bottom edges of model, and those close to the interface of inclusion. The other regions are poorly reconstructed by AIDE due to the absence of S-waves.

From the results summarized in Tab.4.3, it can be found that XFEM and FEM yield similar stiffness estimates, and that XFEM performs even better than FEM in the inclusion region. This performance can be more evident by comparing Fig.4.9(a) with (b) where the inclusion stiffness by XFEM is more homogeneous near the interface than that by FEM. However, it has to be highlighted that by the AIDE reconstruction algorithm, the stiffness estimates of inclusion here are not quite satisfying, with the ratio of standard deviation to the mean between 14.58 % and 25.49 % and the error of the mean with respect to the ground truth varying from 11.08 % to 18.51 %. Using other methods such as inhomogeneous direct ones assuming stiffness inhomogeneity and iterative ones independent from data quality could possibly produce better estimates [FOV 18b].

XFEM would be particularly powerful compared to FEM for more complex geometries than those proposed in this chapter. Multiple inclusions could for instance be modeled by several level-set functions, without any limitation in stiffness ratio. However, if interfaces are too close, i.e. two interfaces cross the same element, the mesh should be locally refined, or a recent algorithm of multi-split XFEM could be implemented [BAN 19].

4.5 Conclusion

In this chapter, XFEM has been proposed to model inclusions in MRE simulations. A two-dimensional model containing piecewise linear interfaces was developed to study the plane wave conversion from P-waves to S-waves at a plane oblique interface. Results from numerical simulations by XFEM/FEM and theoretical predictions revealed the P-S conversion rules, and also suggested that it is hard to perfectly reproduce the analytical model due to the infinite plane assumption and the undesired perturbations. The other model containing a random-shape inclusion was developed to investigate XFEM in a pseudo-practical application. By conducting the stiffness reconstruction and comparing the results of XFEM model with those of FEM model, it was demonstrated that with respect to FEM, XFEM can have similar and even better performance. XFEM can also be time-saving with the same computation device. Due to its convenience, accuracy and efficiency, XFEM can be a better choice and a promising tool for inclusion modeling in MRE.

Chapter 5

Steady state in MRE

The low acquisition frequency of MRI induces that phase snapshots are sampled on different cycles to image wave propagation into a soft tissue for MRE purposes. The associated assumption is that the tissue has reached steady state under the harmonic mechanical excitation, for correct recording by MRI. In this chapter, we investigate steady state and propose a metric to quantify it in numerical models based on XFEM, to provide practical guidelines for MRE.

Contents

5.1 Introduction

In MRE, a mechanical steady state is usually required for the investigated tissue and assumed before proceeding to stiffness reconstruction. This requirement is indeed necessary since continuously changing fields from one snapshot to another would lead to different wave inversion results. A common practice to establish the steady state is to apply a number of trigger pulses of driver [MUT 95], typically lasting for a few seconds, and then the system displacement field is supposed in steady state. However, this default agreement is based on human experience and can be biased from one person, one experiment to another. A quantitative metric could be useful for practical applications.

In this chapter, a steady-state metric is proposed to quantitatively measure the steady state of a homogeneous/inhomogeneous medium subjected to a harmonic mechanical excitation, and numerical models based on XFEM/FEM are used to investigate this metric. The rest of this chapter is organized as follows. First, the steady-state metric definition is given, and two square models, designed for studying this metric and its threshold separating the steady state from the transient state, are investigated. Then, this metric is applied to four breast models, based on different technical options to perform breast MRE [BOH 18], and a parametric study is performed using XFEM to evaluate the influence of different MRE configurations on steady state.

For the sake of clarity, in the following, a solid in steady state is called *stable*, the capacity of reaching steady state is called *stability*, and the process of reaching steady state is called *being stabilized*. The simulations are all executed for 200 harmonic periods, and on a Linux cluster (running CentOS Linux 7.9.2009) with three CPUs *Intel(R) Xeon(R) CPU Gold 5118 @ 2.30 GHz* and *5GB RAM*.

5.2 Steady-state metric and threshold

In MRE, displacement fields used for stiffness reconstruction are required to be in steady state, which means that the fields at a time t_k within an excitation period T_i become unchanged with respect to the same time t_k within the preceding period T_{i-1}. This requirement is logical since unstable fields for reconstruction would produce unstable stiffness, as will be shown later. However, in MRE studies, it is typically assumed to reach the steady state after a certain number of periods and to the best of our knowledge, this has never been quantitatively discussed. In this context, we propose here a quantitative metric for measuring the steady state in MRE, and two simple models for investigating the metric threshold.

5.2.1 Metric definition

In MRE, several (usually four or eight) snapshots of signal phases or displacement fields are evenly taken during one period and for each selected two-dimensional slice. Consider, for a certain slice, $u_x^j(T_i)$ and $u_y^j(T_i)$ as the displacement u_x and u_y, respectively, of the element/pixel j in the first snapshot of period T_i, and N as the total number of elements/pixels, u_0 as the amplitude of excitation. We could thus define a normalized metric in terms of mean differences of displacement fields:

$$\Delta_{sqrt}(T_i) = \frac{1}{Nu_0} \sum_{j=1}^{N} \sqrt{\left[u_x^j(T_{i+1}) - u_x^j(T_i)\right]^2 + \left[u_y^j(T_{i+1}) - u_y^j(T_i)\right]^2} \tag{5.1}$$

Associated with a threshold δ, this metric allows to evaluate whether the system in period T_i has reached steady state, namely if $\Delta_{sqrt}(T_i) \leq \delta$. Once this has been checked, waves displacement fields can be further postprocessed to produce shear modulus maps.

5.2.2 Material and methods for threshold determination

To investigate which threshold δ is appropriate and what is the influence of an inclusion on steady state, we have designed two square models; one homogeneous, and the other inhomogeneous with a random-shape inclusion, as illustrated in Fig.5.1. They are both two-dimensional and in plane strain, share the same length and height ($H = L = 150$ *mm*). For the inhomogeneous model, the *tilted* inclusion is the same as that in Chapter 4, obtained by rotating an *aligned* one in the counter clockwise direction by 30 degrees. The *aligned* one is characterized by two vertical/horizontal segments, four circular arcs with radius $r_1 = 15$ *mm*, $r_2 = 10$ *mm*, $r_3 = 8$ *mm* and $r_4 = 6$ *mm*, and the first arc centered at $(x_{c1}, y_{c1}) = (100, 100)$ *mm*; the coordinate origin is imposed at the lower left point and the rotation center is located at $(x_{c1}, y_{c1} - r_2)$ *mm*. In terms of boundary conditions, they are chosen to mimic one of the possible breast MRE configurations [BOH 18]: the left and top edges are embedded, the right edge is harmonically actuated to generate P-waves and the bottom edge is kept free. The parameters of materials and excitation are the same as those in Chapter 4, as summarized in Tab.5.1.

For the homogeneous model, FEM is sufficient for simulating wave propagation. For the inhomogeneous model, both FEM and XFEM are applied to model the inclusion, aiming at comparing these two methods and illustrating the advantages of XFEM over classical FEM. Figure 5.2 presents the two models meshes. As can be seen, a regular mesh with only quadrilateral elements (QUAD4) is used in the homogeneous model by FEM and the inhomogeneous model by XFEM, while in the inhomogeneous model by FEM, triangular elements (TRI3) are also needed, in addition to QUAD4, around the material boundaries to match the mesh with the interface. By a mesh convergence study, the element size of QUAD4 is set to 0.5 mm, leading to 90000 elements in the regular mesh, as illustrated in Fig.5.2(a). For the inhomogeneous FEM model, 87188 QUAD4 elements with size of 0.5 mm and 17688 TRI3 elements with a minimum size of 0.2 mm are employed.

The steady-state metric Δ_{sqrt} is calculated for each period except the last one, and three regions named “ALL”, “BAC” and “INC” representing the whole model, the background and the inclusion, respectively, are considered. Indeed, to investigate the threshold of Δ_{sqrt} in terms of steady state, stiffness reconstruction is also performed and the obtained shear

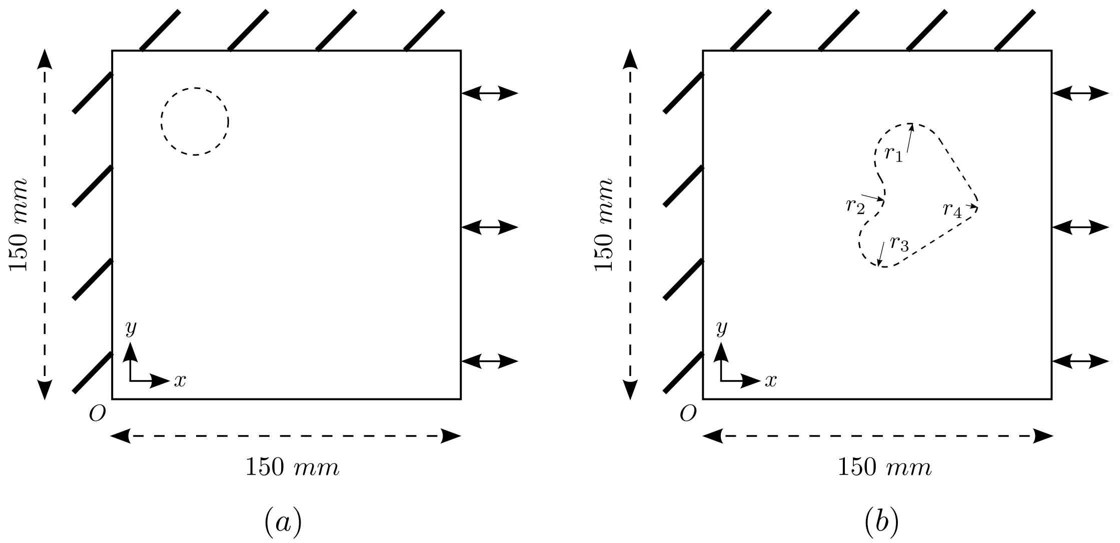

Figure 5.1: Homogeneous (a) and inhomogeneous (b) model. The dashed lines in (a) and (b) represent the “BAC” and “INC” region, respectively.

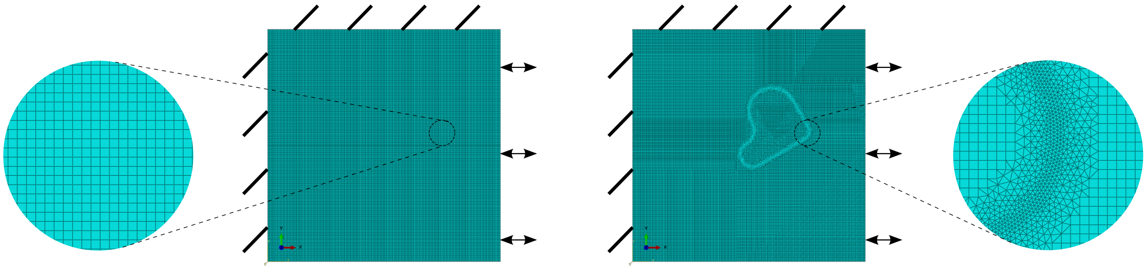
(a) homogeneous FEM model and inhomogeneous XFEM model
(b) inhomogeneous FEM model

Figure 5.2: Illustration of the regular mesh for both homogeneous FEM model and inhomogeneous XFEM model (a), and the mixed mesh for inhomogeneous FEM model (b).

Table 5.1: Parameters of the two square models in Fig.5.1.

	E_1 (kPa)	E_2 (kPa)	η $(Pa\cdot s)$	G' (kPa)	ρ (kg/m^3)	ν	f (Hz)	A_i (μm)
background	3.3	6	6.5	1.6	1000	0.49	-	-
inclusion	10.5	2	4	3.88	1000	0.49	-	-
incident P-waves	-	-	-	-	-	-	84	100

moduli G' are averaged in the “BAC” and “INC” regions, leading to an estimated value of each region. In particular, “BAC” is characterized by a circular region with center at $(35,125)$ mm and radius of 15 mm, as illustrated in Fig.5.1(a). This region is chosen since reflections at boundaries can lead to relatively large amplitude of shear waves and thus better quality of stiffness estimation.

5.2.3 Results

Figure 5.3 presents the results of the steady-state metric Δ_{sqrt} and normalized reconstructed shear modulus G', in the “ALL”, “BAC” and “INC” regions, over the simulated 200 periods, for the homogeneous and inhomogeneous square models. Here, normalization means division by the ground truth which is 1.6 *kPa* for “BAC” and 3.88 *kPa* for “INC”. In general, the convergence to a steady state for both the metric and modulus is observed long before the end of simulation. To further investigate the convergence to steady state by means of the shear modulus G', we also calculated its mean values and standard deviation over each set of 5-periods. The normalized results are presented in Fig.5.4 where the standard deviation is represented by the error bar. An ideal steady state can be represented and visualized as a horizontal plateau in the figure with the error bar reduced to zero.

For the homogeneous model, on the one hand, the reconstructed shear modulus G' of the background region “BAC” has converged to a plateau as shown in Fig.5.3(a). Specifically, as shown in Fig.5.4(a), it enters a stabilized state around the 15th period, and quickly reaches a steady state which can be characterized by a final normalized stiffness estimate of “BAC” region with an average value of about 1.0025 and standard deviation of about 0.001. On the other hand, as can be seen from Fig.5.3(a), the metric Δ_{sqrt} measured in regions “ALL” and “BAC” presents different variances but the same converged value. The metric averaged in “ALL” region exhibits a lower variance than that in the “BAC” region, while they present basically the same convergence rate and both are not stabilized until around the 50th period.

For the inhomogeneous model, XFEM and FEM led to almost the same results by comparing Fig.5.3(b) to (c), respectively, in terms of either the metric or the stiffness. The measurements over the two regions “ALL” and “BAC” are basically identical with those from the homogeneous model. Moreover, as can be observed in Fig.5.3(b) and (c), different from modulus G' of “BAC” region, the reconstructed stiffness of “INC” region cannot be easily stabilized. Quantitatively, as shown in Fig.5.4(b) and (c), although the mean G' in the two regions “ALL” and “INC” has entered a stabilized zone around the 15th period, the averaged stiffness of “INC” region continues to fluctuate with greater standard deviation than that from “BAC” region. From the 60th period, a plateau characterized by much less fluctuations and deviation could be observed, leading to a final normalized stiffness estimate of “INC” region with mean value of about 0.822 and standard deviation of about 0.001. The model could be considered in a steady state.

Overall, at the 60th period, either the metric or the stiffness in different regions have converged to a plateau and a steady state could thus be assumed; the investigated threshold can be established based on this observation. Indeed, all the metrics of different regions are calculated to around 0.01 at the 60th period. Therefore, $\delta = 0.01$ is chosen as the threshold of the steady-state metric Δ_{sqrt}; the first period T_0 satisfying $\Delta_{sqrt}(T_0) \leq 0.01$ can represent the beginning of system steady state and the stiffness reconstruction can be safely performed from this time T_0.

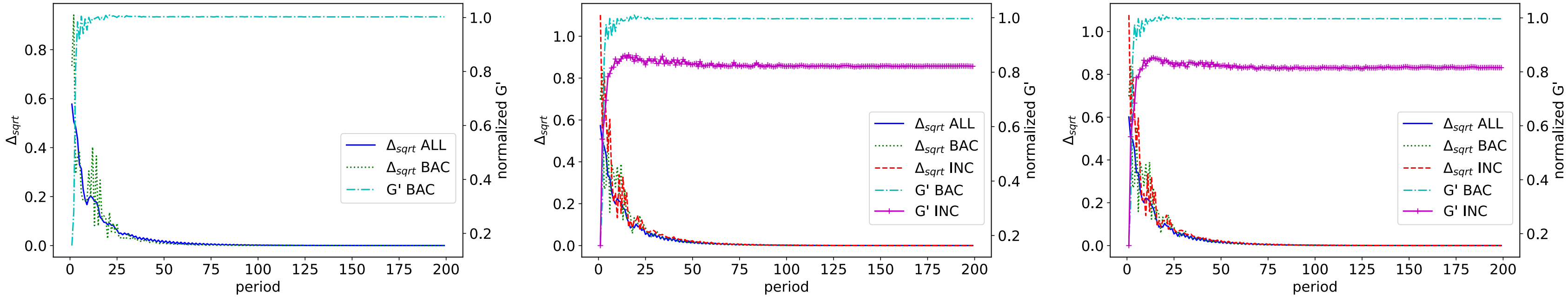

(a) (b) (c)

Figure 5.3: Results of the steady-state metric Δ_{sqrt} and normalized reconstructed shear modulus G' averaged in different regions over time, for the homogeneous model (a), the inhomogeneous model by XFEM (b) and by FEM (c).

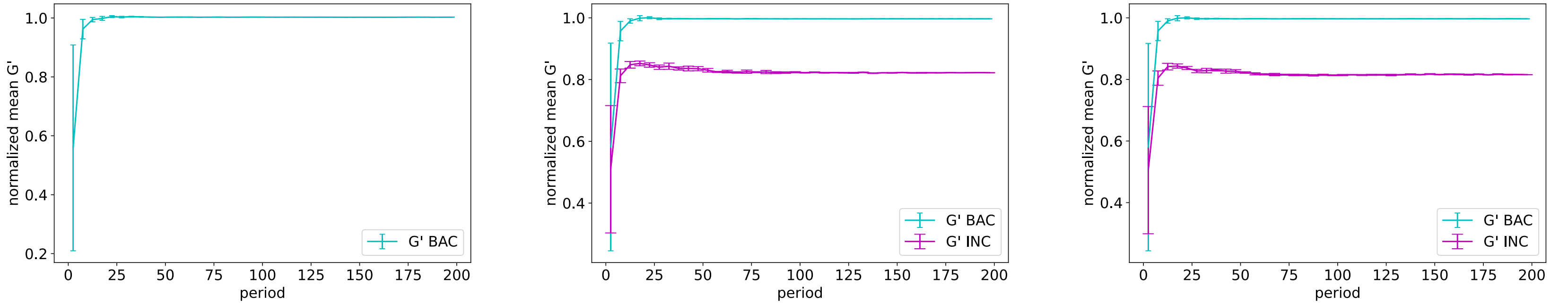

(a) (b) (c)

Figure 5.4: Results of the mean value and standard deviation (represented by the error bar) of normalized reconstructed shear modulus G' over each set of 5-periods, for the homogeneous model (a), the inhomogeneous model by XFEM (b) and by FEM (c).

5.2.4 Discussion

Traditionally, it is assumed that after dozens of periods of excitation or several seconds, the whole system under MRE investigation can be stabilized. As revealed in Fig.5.3, the designed models indeed reach a plateau representing a steady state, in terms of either the metric or the stiffness, long before the end of our 200 periods simulation (2.38 seconds in real time). This traditional practice can be considered reasonable in most cases. However, some models can be difficultly or never stabilized, such as the breast model C shown later. In this case, a quantitative metric can be useful for determining the right time to image the displacements for stiffness reconstruction.

The metric in different regions presents different variances, especially at the beginning of wave propagation. “ALL” region has the least variance probably because it represents the whole system and contains all the varying nodes; the averaging procedure has attenuated the population variance. Nevertheless, different regions have basically the same convergence rate and finally lie on the same level/plateau. The steady-state investigation by the metric can thus be directly performed over the whole system, i.e. the “ALL” region.

The metric has experienced a rapid convergence from the beginning of simulations, which indeed corresponds to a transient state. Passing the value of around 0.1, it enters into another state with quite slow convergence rate, representing the beginning of a steady state. The final decision of the metric threshold as 0.01 is based on the investigation of reconstructed G' over “INC” region. This is indeed a compromise between accuracy and efficiency. Smaller values such as 0.005 and even 0.001 leading to later period T_0 could also be applied, but would not result in a significantly more accurate modulus reconstruction.

The normalized reconstructed shear modulus has converged to about 1.0025 for “BAC” region and about 0.822 for “INC” region. Considering the underlying assumption of local homogeneity of the employed AIDE reconstruction algorithm, the model stiffness is indeed well recovered.

Finally, it is found that the introduction of inclusion in inhomogeneous square model has almost no influence on the metric and stiffness measurements in “ALL” and “BAC” regions, in comparison with those in homogeneous square model. The presence of inclusion is thus not much related to the system stability, as confirmed later in the parametric study of breast model.

5.3 Application to breast models

To further investigate the utility of the defined metric in a pseudo-practical application with the threshold determined from the preceding study, we build four breast models based on the review of breast MRE by Bohte *et al.* [BOH 18], and study the influences of several factors on the solid steady state. [BOH 18] schematically illustrates six potential breast MRE setups, as shown in Fig.5.5. As the last two configurations (E, F) would be equivalent to (A, B), respectively, in our 2D model, we take the first four (A, B, C, D) as the bases of our numerical models. All models are in two-dimensions and the same

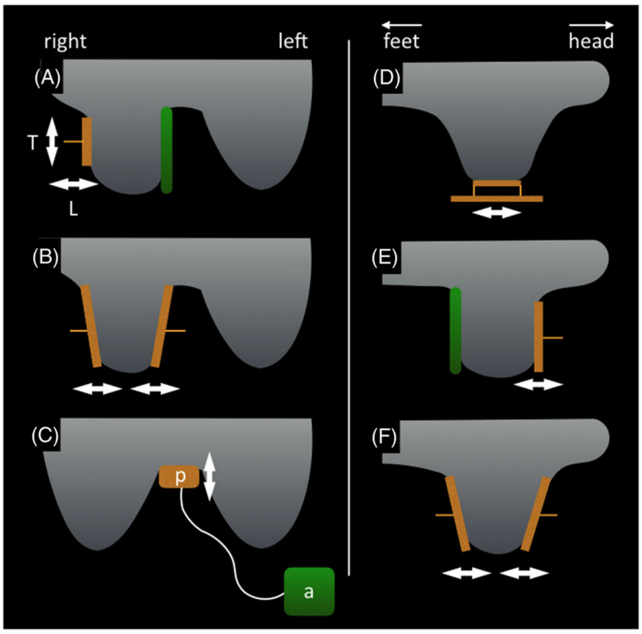

Figure 5.5: Schematic illustrations of MRE setups for breast tissues. Source: [BOH 18]

inclusion shape as in the previous inhomogeneous square model is applied. Besides, based on the first model A, a parametric study is performed to investigate the effect of inclusion size and position, driver size, wave polarization and frequency on model steady state. The default parameters are summarized in Tab.4.2, and all the following simulations use XFEM to model inclusions.

5.3.1 Breast MRE setups

The four models, each with a different configuration of boundary conditions, are illustrated in Fig.5.6; the sequence numbers correspond to those in Fig.5.5. For model A, the top and right edges are embedded and harmonic P-waves are generated from the left edge. For model B, the top edge is embedded, the left and right edges are longitudinally actuated. For model C, only the top edge is longitudinally actuated and no constraints are imposed on other edges. Finally, for model D, the top edge is embedded and the bottom edge is transversely actuated.

In terms of the model size, since they are not given in [BOH 18] and the breast can be quite different from one person to another, we chose to construct the models based on the breast volumes reported in [MCG 11]. The out-of-plane thickness is assumed to be 20 cm, and the corresponding volume would be around 1300 cm^3. The models dimensions are presented in Fig.5.6.

In terms of the inclusion, the same random shape as in the previous inhomogeneous square model is applied, while the size and position are adjusted to the breast models whose size is smaller than the square model. Besides, for the sake of comparison, the same inclusion size and position are applied for all the four breast models. In detail, the

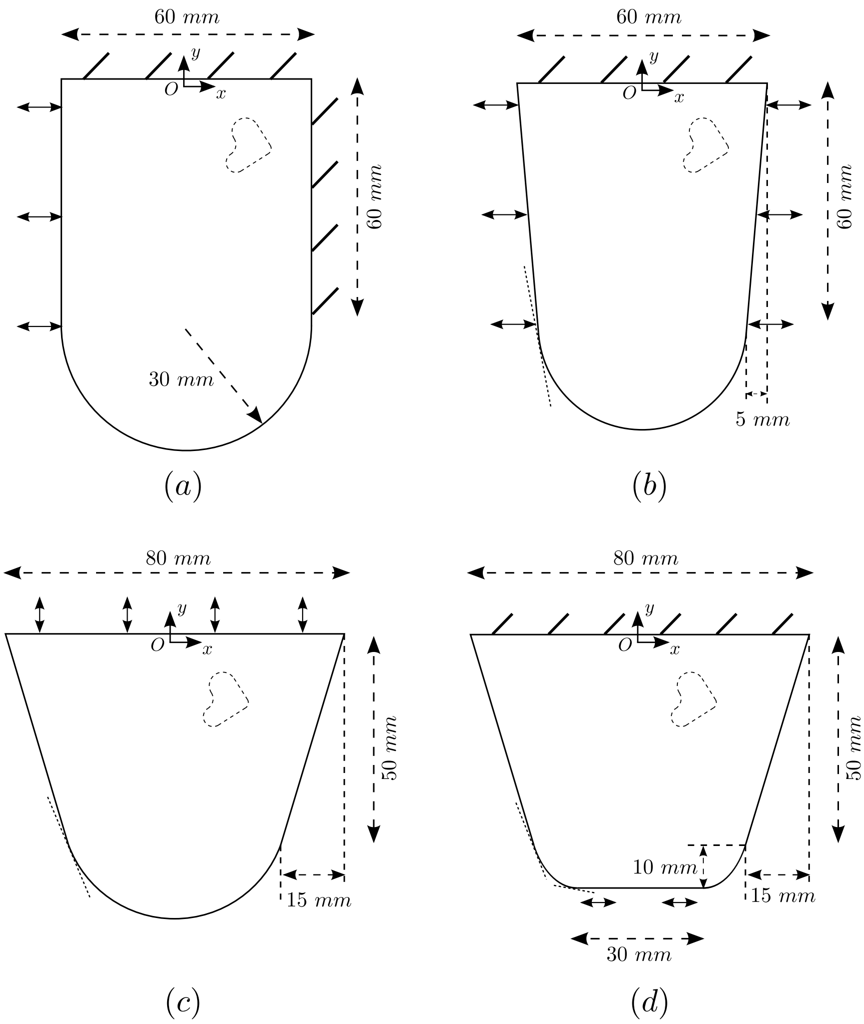

Figure 5.6: Illustration of the boundary conditions and dimensions of the four breast models with sequence numbers corresponding to those in Fig.5.5.

size is reduced to a quarter, leading to the imaginary *aligned* inclusion characterized by four circular arcs with radius $r_1 = 3.75$ *mm*, $r_2 = 2.5$ *mm*, $r_3 = 2$ *mm* and $r_4 = 1.5$ *mm*, and the first arc centered at $(x_{c1}, y_{c1}) = (15, -15)$ *mm*; the middle point of the top edge is imposed as the origin. The *tilted* inclusion is obtained by rotating the *aligned* one in the counter clockwise direction around the point $(x_{c1}, y_{c1} - r_2)$ by 30 degrees.

In terms of the mesh of the XFEM models, models are first partitioned into such two parts that the upper part only contains linear edges, and the lower part contains curved boundaries. Only QUAD4 elements are used in the upper region, while the lower region is meshed by QUAD4 and TRI3 elements, as shown by mesh of the model C in Fig.5.7. The element size is around 0.5 *mm* considering the wavelength. Specifically, 21091 QUAD4 elements and 174 TRI3 elements are used for model A, 17824 QUAD4 elements and 149 TRI3 elements for model B, 17857 QUAD4 elements and 130 TRI3 elements for model C, and 16274 QUAD4 elements and 66 TRI3 elements for model D.

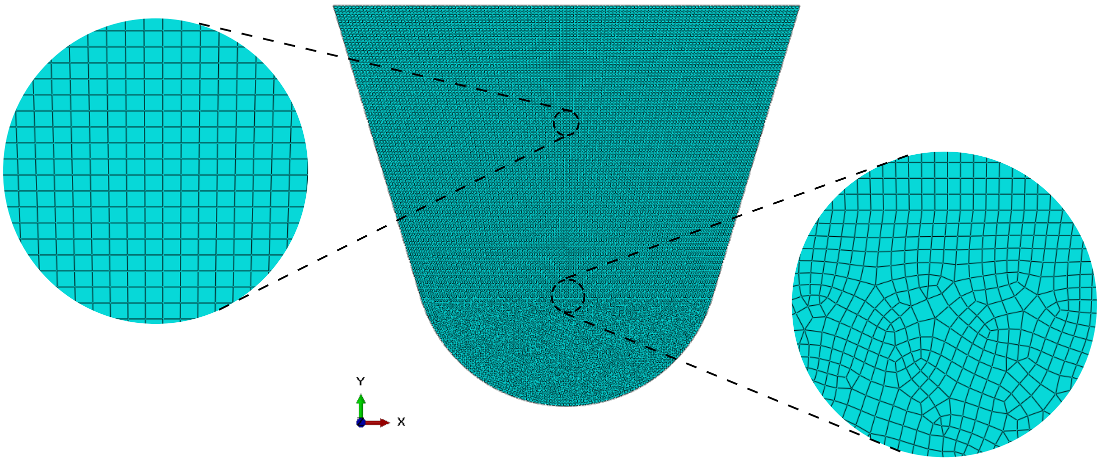

Figure 5.7: Illustration of the breast mesh based on the model C in Fig.5.6.

5.3.2 Parametric study

Based on model A, a parametric study to investigate the effect of inclusion and driver on the system steady state is performed. For the inclusion, we study its size by zoom factors of 0.7, 1.0, 1.2 or 1.5 with the first arc center of *aligned* inclusion unchanged, and its position by the first arc center of *aligned* inclusion at $(-15,-15)$ mm, $(0,-15)$ mm, $(15,-15)$ mm, $(-15,-30)$ mm, $(0,-30)$ mm, $(15,-30)$ mm, $(-15,-45)$ mm, $(0,-45)$ mm or $(15,-45)$ mm. Different configurations in terms of inclusion size and position are illustrated in Fig.5.8. For the driver, we investigate its length of 15 mm, 20 mm, 30 mm or 60 mm, its direction (generating P-waves or S-waves) and its frequency of 28 Hz, 56 Hz, 84 Hz or 100 Hz. Those frequencies and the corresponding measured tissue moduli were indeed reported in [BOH 18]. The derived viscoelastic parameters of SLS model are summarized in Tab.5.2.

Table 5.2: Excitation frequencies and the corresponding SLS model parameters for breast tissues, based on [BOH 18].

f (Hz)	E_1^{bac} (kPa)	E_2^{bac} (kPa)	η^{bac} $(Pa\cdot s)$	E_1^{inc} (kPa)	E_2^{inc} (kPa)	η^{inc} $(Pa\cdot s)$	G'_{bac} (kPa)	G'_{inc} (kPa)
28	0.95	4	2.6	1.4	4	6.6	0.34	0.57
56	2.1	6	4	5.6	3	5	0.81	2.14
84	3.3	6	6.5	10.5	2	4	1.60	3.88
100	3.47	7	8.8	14.84	3	2.1	2.07	5.14

* f, frequency; E_1, E_2 and η, parameters of the SLS model; G', shear storage modulus. The subscript or superscript “bac” denotes background (FGT) and “inc” denotes inclusion (tumor).

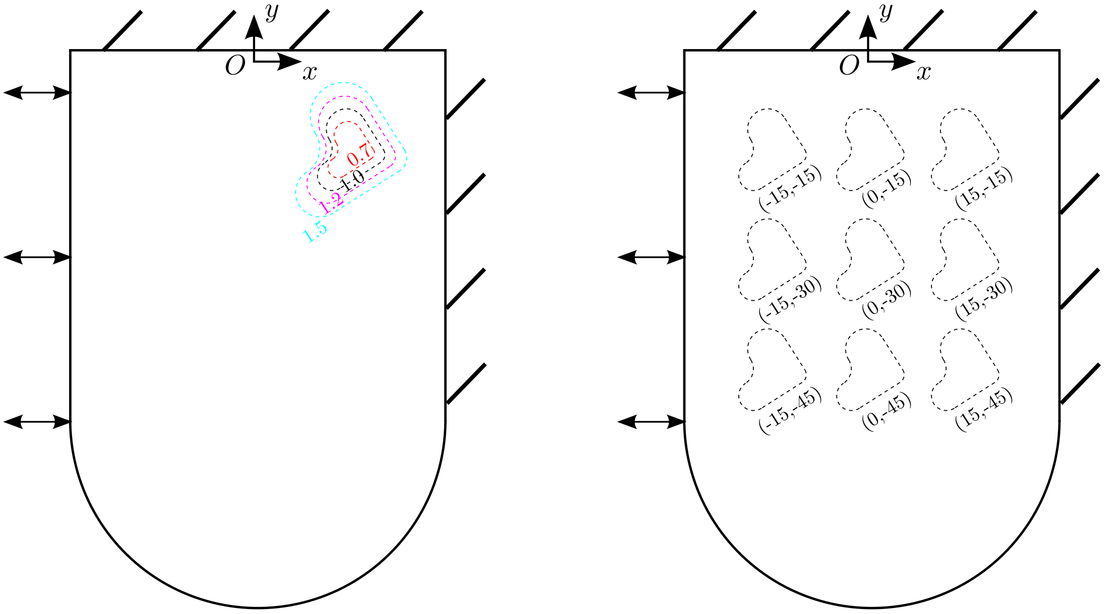

(a) inclusion size (b) inclusion position

Figure 5.8: Illustration of inclusion sizes (a) and positions (b) based on the model A.

5.3.3 Results

Figure 5.9 presents the metric evolution over time for the four breast models and Fig.5.10 presents the results of stability analysis. The bar height in the bar charts represents, for each corresponding simulation, the first period T_0 satisfying $\Delta_{sqrt}(T_0) \leq \delta$ with the previously recommended threshold $\delta = 0.01$. For the sake of clarity, only the two regions “ALL” and “INC” are considered for T_0 investigation, representing the entire breast model and the inclusion region, respectively.

Figure 5.10(a) illustrates the stability differences among the four breast models. Model B exhibits the best stability, while model C is not stabilized until the 160 periods with great fluctuations as shown in Fig.5.9(c). Besides, both “BAC” and “INC” regions of models A, B and D could reach steady state before the 20th period, and “INC” region is in general characterized by a better stability than “ALL” region.

Figure 5.10(b) presents the results of the parametric study, based on model A, that investigates the influence of inclusion size, inclusion position, driver size, wave polarization and wave frequency on system stability. It can be observed that, in general, “INC” region is still more easily stabilized than “ALL” region. The inclusion size and position hardly affect the system stability, while the driver plays a more important role. Specifically, the smaller the driver and the higher the wave frequency, the better stability the system can have. Moreover, driver generating transverse waves results in a better system stability than that with compressional waves.

Finally, based on the above investigation of model stability by T_0, we perform the stiffness reconstruction and illustrate the $\underline{q}$ fields and G' fields for the four breast models,

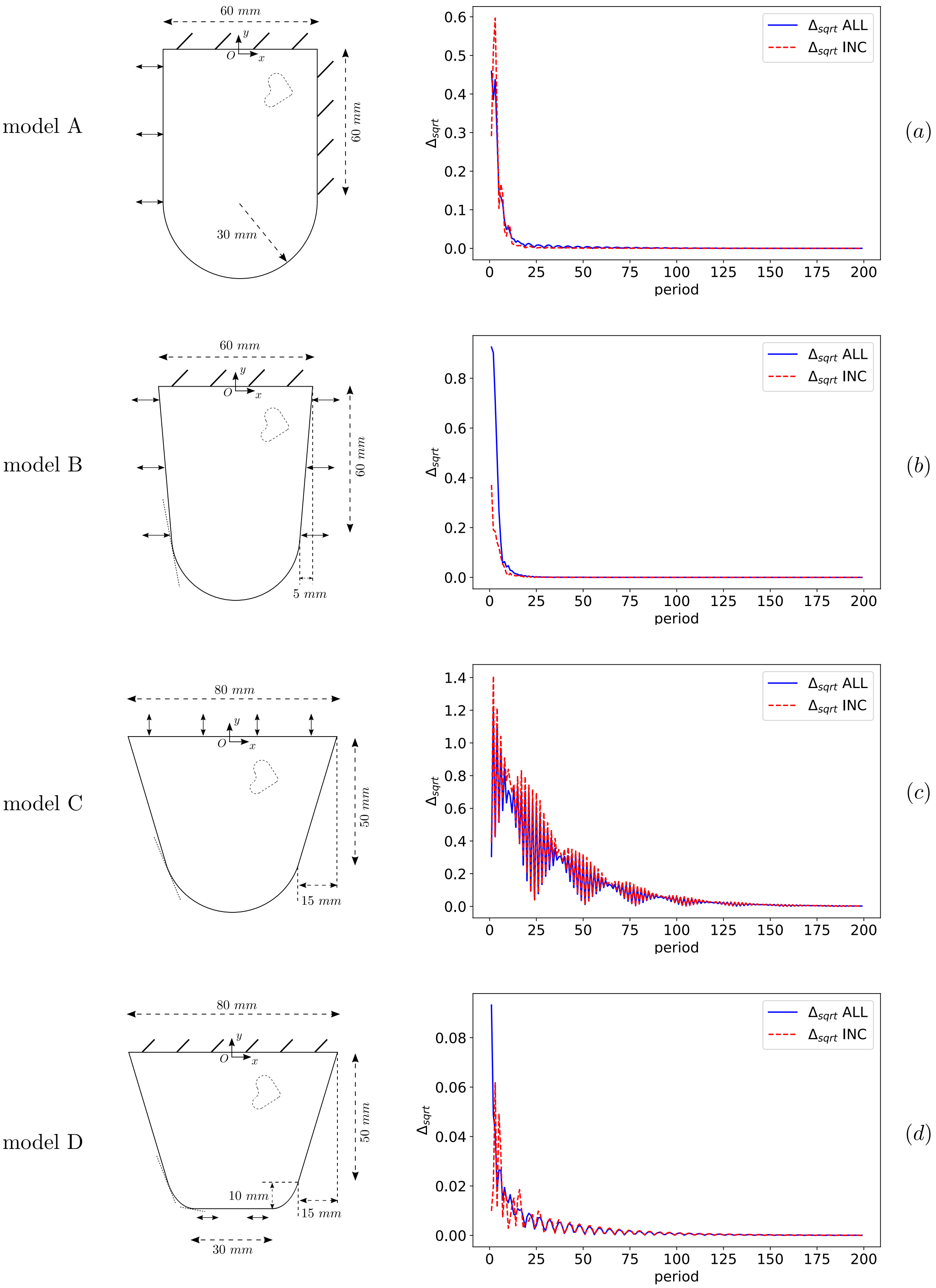

Figure 5.9: Evolution of the steady-state metric over time for the four breast models.

as shown in the first and second column, respectively, of Fig.5.11. The 160th period when all the models have reached steady state is chosen for the reconstruction. In particular, the first column presents the first snapshots of the 160th period for each model. The inclusion regions are selected in the G' fields and used for performing the measurements, leading to the estimates of 2.505 ± 0.792 *kPa* for model A, 3.778 ± 0.611 *kPa* for model B, 1.517 ± 0.849 *kPa* for model C and 0.324 ± 0.106 *kPa* for model D. For reference, the ground truth value of inclusion stiffness is 3.88 *kPa*. It should be emphasized that configuration D is particularly poor to investigate a deep inclusion, as the one present in the model.

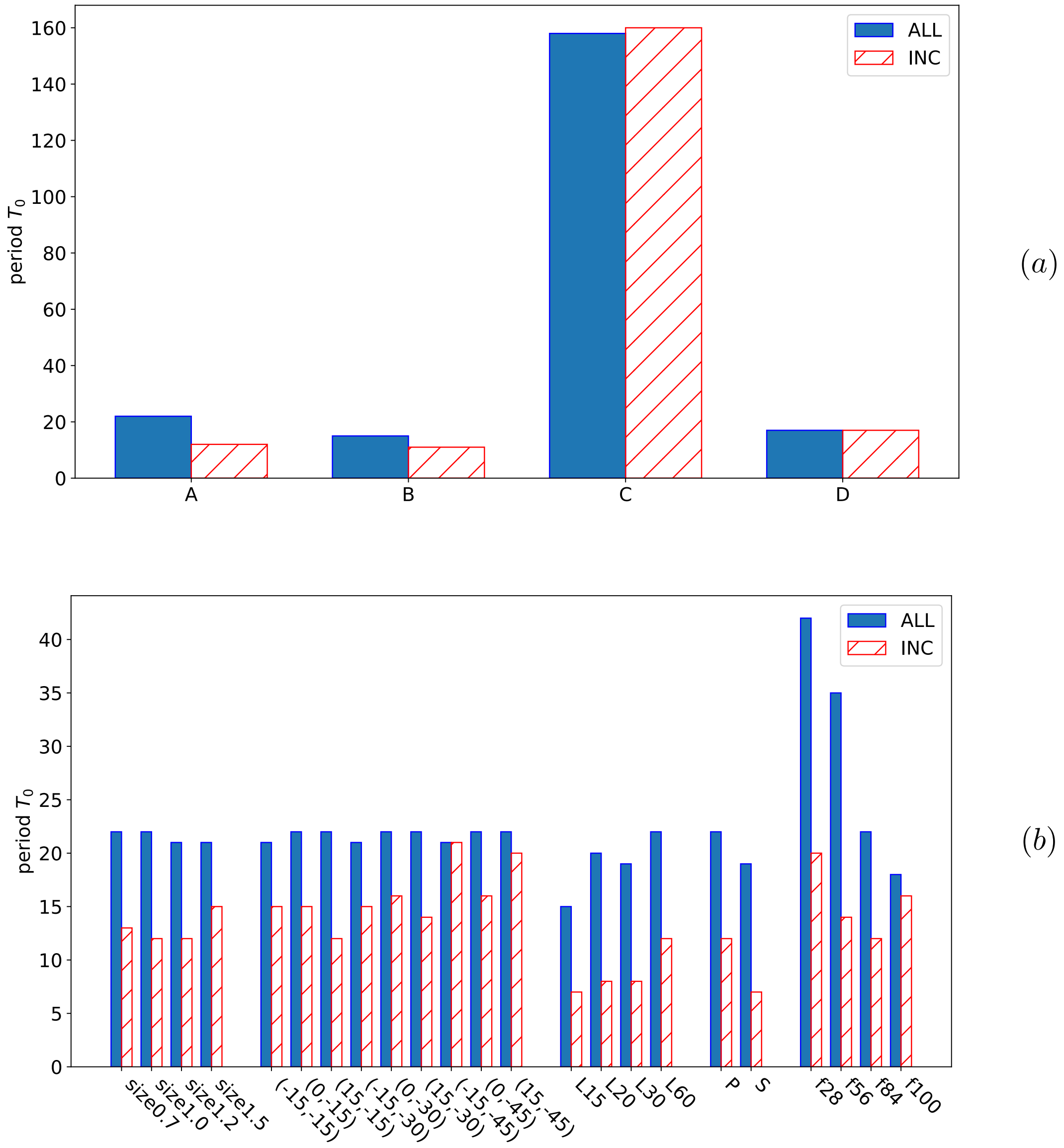

Figure 5.10: Results of the stability analysis of the four breast models (a), and the parametric study (b) presenting the influence of inclusion and driver on system stability.

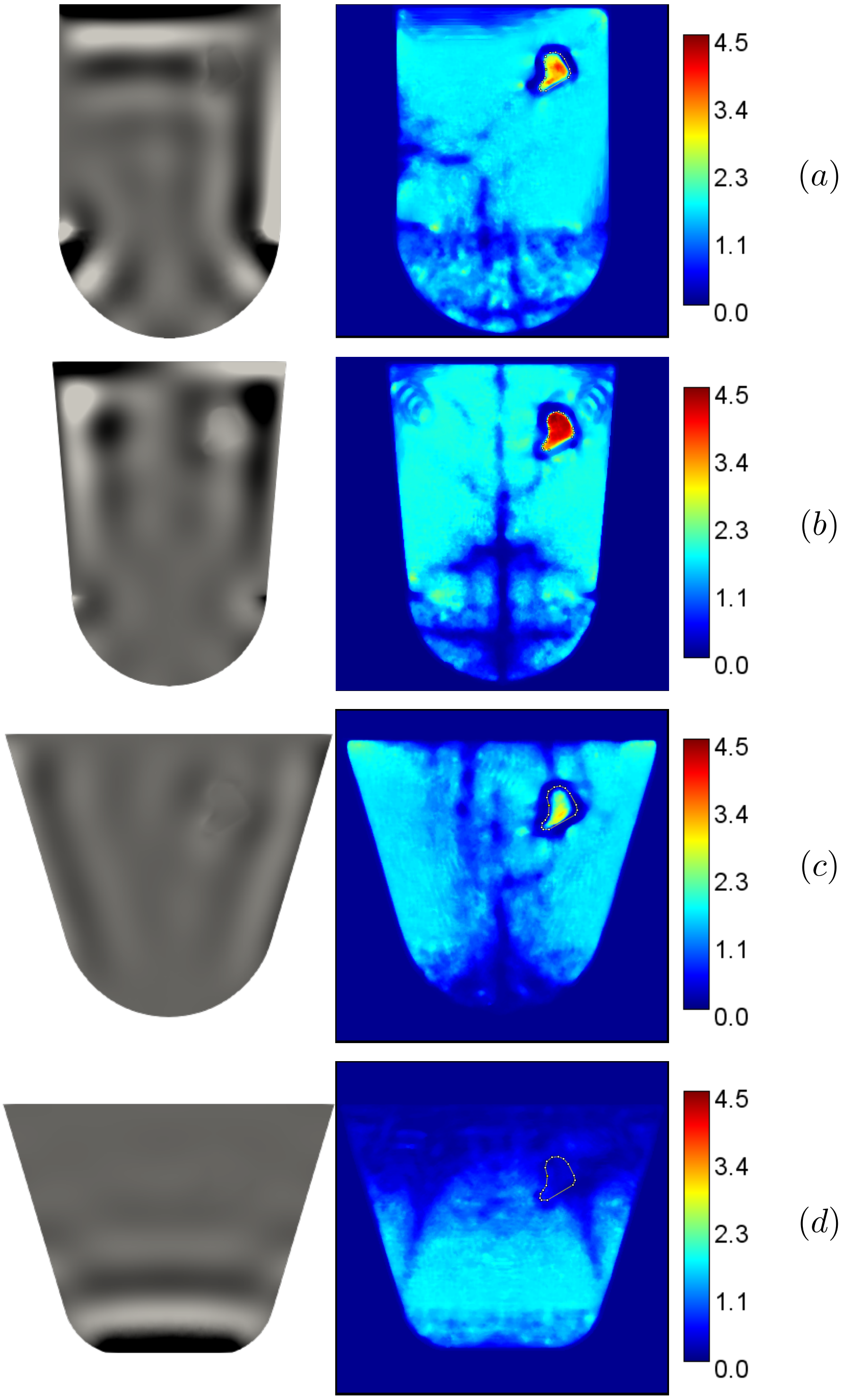

Figure 5.11: Illustration of the curl-applied displacement fields $\underline{q}$ (first column) and the corresponding reconstruction of shear modulus G' (second column) for the four breast models. The selected regions in the second column represent inclusions and are used for stiffness estimates.

5.3.4 Discussion

The application of our proposed metric and recommended threshold to four 2D breast models has shown their stability differences. Both model A and B present a good stability and also result in a rather accurate stiffness reconstruction. Model C has the worst stability, probably due to the lack of constraints associated with boundary conditions. Besides, a poor stiffness reconstruction shown in Fig.5.11(c) can be observed, with the stiffness estimate of 1.517 ± 0.849 *kPa* far from the ground truth of 3.88 *kPa*; the inclusion is indeed flattened due to the fluctuation of inclusion position, as revealed in Fig.5.9(c). Model D, though easily stabilized, does not perform well in stiffness reconstruction. This can be explained by the differences between transverse and longitudinal drivers. The transverse driver of model D generates shear waves which decay rapidly and have limited penetration depth, while the longitudinal driver of other models generates compressional waves which are not easily attenuated and can be converted into shear waves at the boundary and materials interface.

Results of the parametric study provide some guides for designing a MRE system; for example, a smaller driver with higher frequency and transverse polarization can result in an increased stability. In addition, it is interesting to observe that to some extent, inclusion size and position hardly affect the system steady state.

From Fig.5.10, it is found that "INC" region has a better stability than "ALL" region. In fact, some other localized regions have been tested and they are all found to become stable earlier than "ALL" region. This fact is quite reasonable and logical since "ALL" region, which is composed of many partial regions, can hardly be stabilized unless all the subzones become stabilized. For this reason, considering "ALL" region for steady-state investigation is a safe choice.

In the parametric study, the same mesh of breast model A is used even for investigating different inclusion sizes and positions. Adjusting the level-set function for describing different material interfaces is sufficient, which shows the convenience of XFEM especially for the case of parametric simulations.

When investigating the metric threshold, both XFEM and FEM are applied for inclusion modeling in the inhomogeneous square model. Comparison of results of either the calculated metric or the reconstructed stiffness shows that these two methods lead to almost the same displacement fields, illustrating the accuracy of XFEM.

In addition, the above simulations take about 41.2 hours of CPU time (14.4 hours of real time) for the XFEM model, and about 44 hours of CPU time (15.4 hours of real time) for the FEM model. This is a slight decrease but added to the other advantages, it shows the interest of XFEM compared to FEM.

5.4 Conclusion

In this chapter, a quantitative metric Δ_{sqrt} for measuring the steady state of a region or a system was proposed. By the designed 2D square models, investigations on the metric threshold were performed. The value of 0.01 is recommended as a compromise between accuracy and efficiency. Calculating this metric over the whole regions of interest can be regarded as a safe choice. In addition, four breast models were built in two-dimensions and the proposed metric was applied for investigating the system stability. A parametric study based on one breast model was conducted and the results have provided guidelines for MRE driver design. The numerical method of XFEM was employed throughout this chapter for inclusion modeling. In comparison with the classical FEM model, once again, we have successfully illustrated the advantages of XFEM: convenience, accuracy and efficiency.

Conclusions and prospects

Conclusions

In this thesis, we modeled the MRE experiment from the numerical aspect, and have especially addressed the tissue inhomogeneity and MRE excitation issues.

A homemade FE solver, which is dynamic and explicit, was first developed from scratch. It is capable of modeling the propagation of small-amplitude mechanical wave in a linear, isotropic, locally homogeneous and viscoelastic medium. Using this solver, we studied a homogeneous viscoelastic model with symmetry boundary conditions, and illustrated the propagation of plane longitudinal wave and plane transverse wave. Comparison of the FEM results to the analytical results confirmed the validation of our numerical model. Based on the plane shear wave model, a parametric study was also performed and the effect of different parameters on the wave damping was illustrated; the dimensionless quantity of relative viscosity was demonstrated to be capable of describing the wave damping.

To further investigate the tissue inhomogeneity in MRE simulations, the XFEM method was proposed and its formulations were implemented in the solver. In addition, a new strategy of 3D partition for hexahedral element was presented. By comparing the results from a XFEM model and a FEM model, either in 2D or 3D, we could find out the coherence, and also showed the advantages of XFEM, namely its convenience, accuracy and efficiency.

Based on the XFEM implementation, we performed two studies to investigate the applicability of XFEM in MRE. In the first study, the problem of plane wave conversion across a plane oblique inhomogeneity interface was addressed. A XFEM model and a FEM model were thus proposed for numerical simulations and an analytical model based on a previous work was also used. By a parametric study, the effect of different factors on the wave conversion has been revealed. In addition, the comparison of the three models also showed the better accuracy of XFEM model than FEM model. In the second study, a pseudo-practical application was proposed. Indeed, a random-shape inclusion was modeled by both XFEM and FEM, and a reconstruction method was applied to investigate the specific values of shear modulus. It was shown that both models have produced similar stiffness results. XFEM can be even more accurate than FEM with respect to the ground truth values, while using the same mesh for different inclusions and taking shorter CPU time. These further highlighted the advantages of XFEM over FEM. To the best of our knowledge, this was the first time that XFEM has been used for inclusion modeling in MRE studies.

Finally, a metric was proposed to measure the steady state of model/phantom in MRE studies. Numerical analyses suggested that the value 0.01 is a good estimate of the threshold which separates the steady state from the transient state. Using this steady-state metric, we further investigated a breast model with different excitation setups and a parametric study was performed by XFEM. The effect of different factors on system stability was illustrated, such as the inclusion, the driver type and the excitation frequency.

Prospects

A few points can be expected to be addressed in future work.

- Experimental validation

  The XFEM/FEM model developed in this thesis has been validated by comparison with analytical models. It is expected to validate the numerical implementation by an experimental model of either an *in vitro* phantom or an *in vivo* soft tissue/organ. For example, a cylindrical phantom made of agar gelatin actuated along the axial direction can be imagined, and a 2D axisymmetric numerical model can be easily built for comparison. Boundary conditions are particularly to be well prepared and controlled. In addition to homogeneous models, inhomogeneous models, which could contain inclusions for instance, are also expected in order to validate the XFEM implementation.

- Mode conversion simulation

  In Chapter 4, we applied a two-dimensional model with a finite piecewise linear interface for investigating the P-S conversion. A more realistic model in three-dimensions, containing better designed interface might produce results closer to the analytical predictions. In addition, other theories using different methods and assumptions for the wave behaviors at interface are also available, such as that applied decomposition and superposition of wave components [LOC 62] and that applied generalized Snell's law [BOR 09]. They could be further studied to compare with the results in this work.

- Three-dimensional XFEM

  The work presented here investigated XFEM by a two-dimensional inclusion model. Three-dimensional inclusions can also be modeled by XFEM. For its implementation, the definition of 3D interface can be a challenge. The applicability of 3D XFEM in MRE is expected to be studied in future work.

- Multi-scale simulation

  In the context of MRE simulations, XFEM can be expected to get more attention and application, since (1) the mesh is no longer required to match the geometry of any complex, arbitrary inclusion, (2) there are no known limits on the material property (non-linearity, anisotropy, etc.), excitation frequency and problem scale. It can be applied not only for modeling inclusions at macroscale [SUK 01] but also for solving microstructures [MOË 03], by appropriate level set function and right-sized element. In MRE studies, in addition to macroscopic structures such as certain tissues and organs, microscopic structures also require numerical modeling, such as vessels and aggregates. It would be thus interesting to model multi-scale structures by XFEM and figure out the law of behaviors from the simulations. For example, an adaptive XFEM was recently proposed which can be applied for solving the multiscale problems [WAN 16].

- Stiffness reconstruction

  The stiffness reconstruction has been a research topic in the MRE field for a long time. Many inverse methods were developed over the past two decades, as stated in Chapter 1. In particular, the methods based on artificial neural network (ANN) have been recently proposed [MUR 18, HE 19, SOL 18, MUR 20, SCO 20]. A few popular ANN models were applied, and the most promising one may be the convolutional neural network (CNN), which is especially suitable for processing images and has been widely used in medical imaging field [SOL 18, MUR 20, SCO 20]. The most recent work based on the CNN model for stiffness estimation in inhomogeneous media used a coupled harmonic oscillators (CHO) model to accelerate the generation of training data [SCO 20]. However, it was highlighted that the CHO model does not consider the full Navier equations of motion and neglect longitudinal waves and wave conversions across interface. It was thus suggested that a more realistic model, like the FEM model, should be expected.

  However, training a neural network generally requires numerous samples with different features. Using FEM can indeed model the wave propagation in a more realistic way, but it can be more time-consuming, especially when considering the requirement of sample amount. In addition, different features of the generated samples mean that inclusions with different configurations should be modeled. Using FEM, this can be a burdensome task in terms of model partition and remeshing.

  In this context, the proposed XFEM model can be a good alternative to the FEM model. By XFEM, we can readily model different inclusions just by regulating the level set function, while using the same mesh. In addition to the same, even better accuracy with respect to the FEM model, we can also accelerate the computation thanks to less elements in the mesh. Therefore, in future work, it is expected to apply the XFEM model in MRE simulations to generate displacement samples, which can then be used to train a neural network for reconstructing stiffness in a simultaneous way.

Appendix A

This appendix consists in presenting a Python module for reading data stored in vtk file.

```python
# -*- coding: utf-8 -*-
"""
Created on Tue Sep 22 08:19:49 2020

@author: qdu
objective : read data from vtk file
"""

import numpy as np
import vtk
from vtk.util.numpy_support import vtk_to_numpy

# points coordinates
def vtk_points_reader(FileName):
    # vtk reader initialization
    reader = vtk.vtkUnstructuredGridReader()
    reader.SetFileName(FileName)
    reader.ReadAllVectorsOn()
    reader.ReadAllScalarsOn()
    reader.Update()

    data = reader.GetOutput()
    npoints = data.GetNumberOfPoints()

    points = vtk_to_numpy(data.GetPoints().GetData())
    return points, npoints

# connectivity matrix
def vtk_cells_reader(FileName):
    # vtk reader initialization
    reader = vtk.vtkUnstructuredGridReader()
    reader.SetFileName(FileName)
```

```
    reader.ReadAllVectorsOn()
    reader.ReadAllScalarsOn()
    reader.Update()

    data = reader.GetOutput()
    ncells = data.GetNumberOfCells()

    tmp = vtk_to_numpy(data.GetCells().GetData())
    cells = []
    cnt = 0
    for i in range(ncells):
        npoint = tmp[cnt]
        cells.append(np.array(tmp[cnt+1:cnt+npoint+1]))
        cnt += npoint+1
    cells = np.reshape(vtk_to_numpy(data.GetCells().GetData()), (ncells,-1))
    cells = cells[:, 1:]
    return cells, ncells

# PointData
def vtk_pdata_reader(FileName, DataName):
    # vtk reader initialization
    reader = vtk.vtkUnstructuredGridReader()
    reader.SetFileName(FileName)
    reader.ReadAllVectorsOn()
    reader.ReadAllScalarsOn()
    reader.Update()

    data = reader.GetOutput()

    pdata = vtk_to_numpy(data.GetPointData().GetArray(DataName))
    return pdata

# CellData
def vtk_cdata_reader(FileName, DataName):
    # vtk reader initialization
    reader = vtk.vtkUnstructuredGridReader()
    reader.SetFileName(FileName)
    reader.ReadAllVectorsOn()
    reader.ReadAllScalarsOn()
    reader.Update()

    data = reader.GetOutput()

```

```
    cdata = vtk_to_numpy(data.GetCellData().GetArray(DataName))
    return cdata

# FieldData
def vtk_fdata_reader(FileName, DataName):
    # vtk reader initialization
    reader = vtk.vtkUnstructuredGridReader()
    reader.SetFileName(FileName)
    reader.Update()

    data = reader.GetOutput()

    fdata = []
    for dn in DataName:
        fdata.append(vtk_to_numpy(data.GetFieldData().GetArray(dn)))
    return fdata
```

Appendix B

Introduction

This appendix aims at pointing out some formulation errors in [COO 67] and giving the proof. In the following, equations from [COO 67] with the same sequence number are first listed with the corrected ones given and highlighted alongside. Then, the corrections are demonstrated.

Equations

Equation of motion:

$$\mu\Delta\underline{u}+(\lambda+\mu)\underline{\nabla}(\underline{\nabla}\cdot\underline{u})+\rho\omega^2\underline{u}=\underline{0} \tag{A.1}$$

Constitutive equation:

$$\tau_{ij}=\lambda\delta_{ij}\underline{\nabla}\cdot\underline{u}+\mu(\partial u_i/\partial x_j+\partial u_j/\partial x_i) \tag{A.2}$$

Displacement components by eight potential functions Φ_{lmn}:

$$\begin{aligned} u_{lm} &= \partial\Phi_{lm1}/\partial x+\partial\Phi_{lm2}/\partial y \\ v_{lm} &= \partial\Phi_{lm1}/\partial y-\partial\Phi_{lm2}/\partial x \end{aligned} \tag{A.3}$$

Helmholtz equation:

$$\Delta\Phi_{lmn}+k_{mn}^2\Phi_{lmn}=0, \quad l,m,n=1,2 \tag{A.4}$$

where

$$k_{mn}\equiv\omega/S_{mn}; \quad S_{m1}^2=(\lambda_m+2\mu_m)/\rho_m; \quad S_{m2}^2=\mu_m/\rho_m \tag{A.5}$$

Complex wave number:

$$\begin{aligned} k_{mn} &= (\omega/C_{mn})(1+i\tan\Omega_{mn}) \\ &= (\omega/C_{mn})(1-i\tan\Omega_{mn}) \end{aligned} \tag{A.6}$$

where

$$\begin{aligned} \tan 2\Omega_{mn} &\equiv -\mathrm{Im}S_{mn}^2/\mathrm{Re}S_{mn}^2, \quad 0\leq\Omega_{mn}<\pi/2 \\ &\equiv \mathrm{Im}S_{mn}^2/\mathrm{Re}S_{mn}^2, \quad 0\leq\Omega_{mn}<\pi/2 \\ C_{mn} &\equiv |S_{mn}|\sec\Omega_{mn} \end{aligned} \tag{A.7}$$

Combining Eqs. A.2, A.3 and A.4:

$$\begin{aligned}\sigma_{xlm} &= 2\mu_m(\partial^2\Phi_{lm1}/\partial x^2 + \partial^2\Phi_{lm2}/\partial x\partial y) - \lambda_m k_{m1}^2 \Phi_{lm1}\\ \sigma_{ylm} &= 2\mu_m(\partial^2\Phi_{lm1}/\partial y^2 - \partial^2\Phi_{lm2}/\partial x\partial y) - \lambda_m k_{m1}^2 \Phi_{lm1}\\ \tau_{lm} &= \mu_m(2\partial^2\Phi_{lm1}/\partial x\partial y + \partial^2\Phi_{lm2}/\partial y^2 - \partial^2\Phi_{lm2}/\partial x^2)\end{aligned} \tag{A.8}$$

Boundary conditions at interface $y = 0$:

$$\begin{aligned}u_{l1}(x,0) &= u_{l2}(x,0), \qquad & v_{l1}(x,0) &= v_{l2}(x,0)\\ \sigma_{yl1}(x,0) &= \sigma_{yl2}(x,0), \qquad & \tau_{l1}(x,0) &= \tau_{l2}(x,0)\end{aligned} \tag{A.9}$$

Total potential functions:

$$\Phi_{l1n} = \delta_{ln}\Psi_l + \psi_{l1n}; \quad \Phi_{l2n} = \psi_{l2n} \tag{A.10}$$

Potential functions:

$$\begin{aligned}\Psi_l &= (I_l S_{l1}/\omega)\exp\{ik_{1l}(\boldsymbol{r}_l \cdot \boldsymbol{x})\}\\ &= (I_l S_{1l}/\omega)\exp\{ik_{1l}(\boldsymbol{r}_l \cdot \boldsymbol{x})\}\\ \psi_{lmn} &= (I_l R_{lmn} S_{mn}/\omega)\exp\{ik_{mn}(\boldsymbol{r}_{lmn} \cdot \boldsymbol{x})\}\end{aligned} \tag{A.11}$$

where

$$\begin{aligned}\boldsymbol{r}_l &\equiv \boldsymbol{i}\sin\theta_l - \boldsymbol{j}\cos\theta_l, \qquad & \boldsymbol{x} &\equiv \boldsymbol{i}x + \boldsymbol{j}y,\\ \boldsymbol{r}_{lmn} &\equiv \boldsymbol{i}\sin\zeta_{lmn} + \boldsymbol{j}\varepsilon_m\cos\zeta_{lmn}, \qquad & \varepsilon_m &\equiv (-1)^{m+1}\end{aligned} \tag{A.12}$$

Combing Eqs. A.3, A.8, A.10, A.11 and A.12:

$$\begin{aligned}\begin{Bmatrix} u_{lm} \\ v_{lm} \\ \sigma_{xlm} \\ \sigma_{ylm} \\ \tau_{lm} \end{Bmatrix} = &\begin{bmatrix} ik_{m1}\sin\zeta_{lm1} & ik_{m2}\varepsilon_m\cos\zeta_{lm2} \\ \varepsilon_m ik_{m1}\cos\zeta_{lm1} & -ik_{m2}\sin\zeta_{lm2} \\ -k_{m1}^2(\lambda_m + 2\mu_m\sin^2\zeta_{lm1}) & -\mu_m k_{m2}^2\varepsilon_m\sin 2\zeta_{lm2} \\ -k_{m1}^2(\lambda_m + 2\mu_m\cos^2\zeta_{lm1}) & \mu_m k_{m2}^2\varepsilon_m\sin 2\zeta_{lm2} \\ -\varepsilon_m\mu_m k_{m1}^2\sin 2\zeta_{lm1} & -\mu_m k_{m2}^2\cos 2\zeta_{lm2} \end{bmatrix} \begin{Bmatrix} \psi_{lm1} \\ \psi_{lm2} \end{Bmatrix}\\ &+ \delta_{m1}\Psi_l \begin{Bmatrix} i(\delta_{l1}k_{11}\sin\theta_1 - \delta_{l2}k_{12}\cos\theta_2) \\ -i(\delta_{l1}k_{11}\cos\theta_1 + \delta_{l2}k_{12}\sin\theta_2) \\ -\delta_{l1}k_{11}^2(\lambda_1 + 2\mu_1\sin^2\theta_1) + \delta_{l2}\mu_1 k_{12}^2\sin 2\theta_2 \\ -\delta_{l1}k_{11}^2(\lambda_1 + 2\mu_1\cos^2\theta_1) - \delta_{l2}\mu_1 k_{12}^2\sin 2\theta_2 \\ \delta_{l1}\mu_1 k_{11}^2\sin 2\theta_1 - \delta_{l2}\mu_1 k_{12}^2\cos 2\theta_2 \end{Bmatrix}\end{aligned} \tag{A.13}$$

Complex Snell's law:

$$\sin\zeta_{lmn} = S_{mn}\sin\theta_l / S_{1l} \tag{A.14}$$

The linear set of equations for coefficients:

$$\boldsymbol{A}_l\boldsymbol{R}_l = \boldsymbol{B}_l, \quad l = 1,2 \tag{A.15}$$

$$\boldsymbol{A}_l = \begin{bmatrix} \sin\zeta_{l11} & \cos\zeta_{l12} & -\sin\zeta_{l21} & \cos\zeta_{l22} \\ \cos\zeta_{l11} & -\sin\zeta_{l12} & \cos\zeta_{l21} & \sin\zeta_{l22} \\ -\rho_1 S_{11}\cos\zeta_{l12} & \rho_1 S_{12}\sin 2\zeta_{l12} & \rho_2 S_{21}\cos 2\zeta_{l22} & \rho_2 S_{22}\sin 2\zeta_{l22} \\ (\rho_1 S_{12}^2/S_{11})\sin 2\zeta_{l11} & \rho_1 S_{12}\cos 2\zeta_{l12} & (\rho_2 S_{22}^2/S_{21})\sin 2\zeta_{l21} & -\rho_2 S_{22}\cos 2\zeta_{l22} \end{bmatrix}$$
$$= \begin{bmatrix} \sin\zeta_{l11} & \cos\zeta_{l12} & -\sin\zeta_{l21} & \cos\zeta_{l22} \\ \cos\zeta_{l11} & -\sin\zeta_{l12} & \cos\zeta_{l21} & \sin\zeta_{l22} \\ -\rho_1 S_{11}\cos 2\zeta_{l12} & \rho_1 S_{12}\sin 2\zeta_{l12} & \rho_2 S_{21}\cos 2\zeta_{l22} & \rho_2 S_{22}\sin 2\zeta_{l22} \\ (\rho_1 S_{12}^2/S_{11})\sin 2\zeta_{l11} & \rho_1 S_{12}\cos 2\zeta_{l12} & (\rho_2 S_{22}^2/S_{21})\sin 2\zeta_{l21} & -\rho_2 S_{22}\cos 2\zeta_{l22} \end{bmatrix} \tag{A.16}$$

$$\boldsymbol{B}_1 = \begin{Bmatrix} -\sin\theta_1 \\ \cos\theta_1 \\ \rho_1 S_{11}\cos 2\zeta_{112} \\ \rho_1 S_{12}^2 \sin 2\theta_1 \end{Bmatrix}, \quad \boldsymbol{B}_2 = \begin{Bmatrix} \cos\theta_2 \\ \sin\theta_2 \\ -\rho_1 S_{12}\sin 2\theta_2 \\ -\rho_1 S_{12}\cos 2\theta_2 \end{Bmatrix}, \quad \boldsymbol{R}_l = \begin{Bmatrix} R_{l11} \\ R_{l12} \\ R_{l21} \\ R_{l22} \end{Bmatrix}$$
$$= \begin{Bmatrix} -\sin\theta_1 \\ \cos\theta_1 \\ \rho_1 S_{11}\cos 2\zeta_{112} \\ (\rho_1 S_{12}^2/S_{11}) \sin 2\theta_1 \end{Bmatrix} \quad = \begin{Bmatrix} \cos\theta_2 \\ \sin\theta_2 \\ +\rho_1 S_{12}\sin 2\theta_2 \\ -\rho_1 S_{12}\cos 2\theta_2 \end{Bmatrix} \tag{A.17}$$

Proofs

Eqs. A.6 and A.7

For Eqs. A.6 and A.7, it's hard to find the original source from which the expression in Cooper's paper comes. However, it can be shown by numeric implementation that the sign taken will give rise to improper and unreasonable results. We give here a simple explanation for our corrections.

For the sake of simplicity, we use a complex modulus noted by E^* instead of $\lambda(\omega)$ or $\mu(\omega)$. Generally, the complex dynamic modulus of viscoelastic material can be expressed by $E^* = E' + iE''$ where E' is called storage modulus representing stored energy and E'' is loss modulus representing dissipated energy. The ratio of loss modulus and storage modulus is defined as $\tan\delta$ where δ is actually the phase lag between stress and strain in viscoelastic material. Thus, we have $\tan\delta = E''/E'$.

Using Euler's formula, E^* can be alternatively expressed by $E^* = |E^*|e^{i\delta}$. Similar to Eq. A.5, we have $S^2 = E^*/\rho = |E^*|e^{i\delta}/\rho$. Thus, $S = \sqrt{|E^*|e^{i\delta}/\rho} = \sqrt{|E^*|/\rho}\, e^{i\frac{\delta}{2}}$ and the complex wave number reads:

$$\begin{aligned} k = \frac{\omega}{S} &= \frac{\omega}{\sqrt{|E^*|/\rho}} e^{-i\frac{\delta}{2}} \\ &= \frac{\omega}{\sqrt{|E^*|/\rho}} (\cos\frac{\delta}{2} - i\sin\frac{\delta}{2}) \\ &= \frac{\omega}{\sqrt{|E^*|/\rho}\sec\frac{\delta}{2}} (1 - i\tan\frac{\delta}{2}) \\ &= \frac{\omega}{C} (1 - i\tan\frac{\delta}{2}) \end{aligned} \tag{A.18}$$

where $\frac{\delta}{2}$ correspond to Ω_{mn} in Eq. A.6 and C correspond to C_{mn} in Eq. A.7.

Note that the corrections made are just flipping the sign from plus to minus and from minus to plus. It's thus possible that these two versions are equivalent. We demonstrate here that with the condition $0 \le \frac{\delta}{2} < \pi/2$, they are no more the same.

Generally, storage and loss modulus are all non-negative, namely $E' \ge 0$ and $E'' \ge 0$. Assuming hereby $\arctan(E''/E') = \theta$ where $0 \le \theta < \pi/2$. Our corrected formulas work as:

$$\begin{cases} k = \frac{\omega}{C}(1 - i\tan\frac{\delta}{2}) \\ \tan\delta = E''/E', 0 \le \frac{\delta}{2} < \pi/2 \end{cases} \Rightarrow \begin{cases} \delta = \theta \\ \tan\frac{\delta}{2} = \tan\frac{\theta}{2} \\ k = \frac{\omega}{C}(1 - i\tan\frac{\theta}{2}) \end{cases} \tag{A.19}$$

And the original formulas work as:

$$\begin{cases} k = \frac{\omega}{C}(1 + i\tan\frac{\delta}{2}) \\ \tan\delta = -E''/E', 0 \le \frac{\delta}{2} < \pi/2 \end{cases} \Rightarrow \begin{cases} \delta = \pi - \theta \\ \tan\frac{\delta}{2} = \frac{1}{\tan\frac{\theta}{2}} \\ k = \frac{\omega}{C}(1 + i\frac{1}{\tan\frac{\theta}{2}}) \end{cases} \tag{A.20}$$

Eq. A.8

Equation A.2 can be alternatively expressed using the strain ε_{ij} as $\sigma_{ij} = \lambda\varepsilon_{kk}\delta_{ij} + 2\mu\varepsilon_{ij}$ where $\varepsilon_{ij} = \frac{1}{2}(u_{i,j} + u_{j,i})$. Combining with Eqs. A.3 and A.4, we have the three stress components in Eq. A.8:

$$\begin{aligned} \sigma_{xlm} &= \lambda_m(\varepsilon_{xx} + \varepsilon_{yy}) + 2\mu_m\varepsilon_{xx} \\ &= \lambda_m(\frac{\partial u_{lm}}{\partial x} + \frac{\partial v_{lm}}{\partial y}) + 2\mu_m\frac{\partial u_{lm}}{\partial x} \\ &= \lambda_m(\frac{\partial^2\Phi_{lm1}}{\partial x^2} + \frac{\partial^2\Phi_{lm2}}{\partial x\partial y} + \frac{\partial^2\Phi_{lm1}}{\partial y^2} - \frac{\partial^2\Phi_{lm2}}{\partial x\partial y}) + 2\mu_m(\frac{\partial^2\Phi_{lm1}}{\partial x^2} + \frac{\partial^2\Phi_{lm2}}{\partial x\partial y}) \\ &= 2\mu_m(\frac{\partial^2\Phi_{lm1}}{\partial x^2} + \frac{\partial^2\Phi_{lm2}}{\partial x\partial y}) - \lambda_m k_{m1}^2\Phi_{lm1} \end{aligned} \tag{A.21}$$

$$\begin{aligned}
\sigma_{ylm} &= \lambda_m(\varepsilon_{xx}+\varepsilon_{yy})+2\mu_m\varepsilon_{yy} \\
&= \lambda_m(\frac{\partial u_{lm}}{\partial x}+\frac{\partial v_{lm}}{\partial y})+2\mu_m\frac{\partial v_{lm}}{\partial y} \\
&= \lambda_m(\frac{\partial^2\Phi_{lm1}}{\partial x^2}+\frac{\partial^2\Phi_{lm2}}{\partial x\partial y}+\frac{\partial^2\Phi_{lm1}}{\partial y^2}-\frac{\partial^2\Phi_{lm2}}{\partial x\partial y})+2\mu_m(\frac{\partial^2\Phi_{lm1}}{\partial y^2}-\frac{\partial^2\Phi_{lm2}}{\partial x\partial y}) \\
&= 2\mu_m(\frac{\partial^2\Phi_{lm1}}{\partial y^2}-\frac{\partial^2\Phi_{lm2}}{\partial x\partial y})-\lambda_m k_{m1}^2\Phi_{lm1}
\end{aligned} \tag{A.22}$$

$$\begin{aligned}
\tau_{lm} = 2\mu_m\varepsilon_{xy} &= \mu_m(\frac{\partial u_{lm}}{\partial y}+\frac{\partial v_{lm}}{\partial x}) \\
&= \mu_m(\frac{\partial^2\Phi_{lm1}}{\partial x\partial y}+\frac{\partial^2\Phi_{lm2}}{\partial y^2}+\frac{\partial^2\Phi_{lm1}}{\partial x\partial y}-\frac{\partial^2\Phi_{lm2}}{\partial x^2}) \\
&= \mu_m(2\frac{\partial^2\Phi_{lm1}}{\partial x\partial y}+\frac{\partial^2\Phi_{lm2}}{\partial y^2}-\frac{\partial^2\Phi_{lm2}}{\partial x^2})
\end{aligned} \tag{A.23}$$

Eq. A.11

S_{mn} is referred to as complex wave speed. The subscript m represents the medium, i.e. $m = 1$ implies incident side and $m = 2$ implies the other side. The subscript n is used to denote dilatational and shear waves, respectively. Therefore, in Eq. A.11, it ought to be S_{1l} instead of S_{l1} to represent the incident wave Φ_l.

Eq. A.13

- u_{lm}

  From Eq. A.3, $u_{lm} = \partial\Phi_{lm1}/\partial x + \partial\Phi_{lm2}/\partial y$. Using Eqs. A.10, A.11 and A.12 and discussing different cases in terms of m, we have:

  when $m = 1$

$$\begin{aligned}
u_{l1} &= \frac{\partial\Phi_{l11}}{\partial x}+\frac{\partial\Phi_{l12}}{\partial y} \\
&= \frac{\partial(\delta_{l1}\Psi_l+\psi_{l11})}{\partial x}+\frac{\partial(\delta_{l2}\Psi_l+\psi_{l12})}{\partial y}
\end{aligned} \tag{A.24}$$

  when $m = 2$

$$\begin{aligned}
u_{l2} &= \frac{\partial\Phi_{l21}}{\partial x}+\frac{\partial\Phi_{l22}}{\partial y} \\
&= \frac{\partial\psi_{l21}}{\partial x}+\frac{\partial\psi_{l22}}{\partial y}
\end{aligned} \tag{A.25}$$

It is concluded that:

$$\begin{aligned}
u_{lm} &= \frac{\partial \psi_{lm1}}{\partial x} + \frac{\partial \psi_{lm2}}{\partial y} + \delta_{m1}(\delta_{l1}\frac{\partial \Psi_l}{\partial x} + \delta_{l2}\frac{\partial \Psi_l}{\partial y}) \\
&= ik_{m1}\sin\zeta_{lm1}\psi_{lm1} + ik_{m2}\varepsilon_m\cos\zeta_{lm2}\psi_{lm2} \\
&\quad + \delta_{m1}\Psi_l\, i\,(\delta_{l1}k_{1l}\sin\theta_l - \delta_{l2}k_{1l}\cos\theta_l) \\
&= ik_{m1}\sin\zeta_{lm1}\psi_{lm1} + ik_{m2}\varepsilon_m\cos\zeta_{lm2}\psi_{lm2} \\
&\quad + \delta_{m1}\Psi_l\, i\,(\delta_{l1}k_{11}\sin\theta_1 - \delta_{l2}k_{12}\cos\theta_2) \\
&= \begin{bmatrix} ik_{m1}\sin\zeta_{lm1} & ik_{m2}\varepsilon_m\cos\zeta_{lm2} \end{bmatrix} \begin{Bmatrix} \psi_{lm1} \\ \psi_{lm2} \end{Bmatrix} \\
&\quad + \delta_{m1}\Psi_l \left[i(\delta_{l1}k_{11}\sin\theta_1 - \delta_{l2}k_{12}\cos\theta_2) \right]
\end{aligned} \tag{A.26}$$

- v_{lm}

From Eq. A.3, $v_{lm} = \partial\Phi_{lm1}/\partial y - \partial\Phi_{lm2}/\partial x$. Using Eqs. A.10, A.11 and A.12 and discussing different cases in terms of m, we have:

when $m = 1$

$$\begin{aligned}
v_{l1} &= \frac{\partial \Phi_{l11}}{\partial y} - \frac{\partial \Phi_{l12}}{\partial x} \\
&= \frac{\partial(\delta_{l1}\Psi_l + \psi_{l11})}{\partial y} - \frac{\partial(\delta_{l2}\Psi_l + \psi_{l12})}{\partial x}
\end{aligned} \tag{A.27}$$

when $m = 2$

$$\begin{aligned}
v_{l2} &= \frac{\partial \Phi_{l21}}{\partial y} - \frac{\partial \Phi_{l22}}{\partial x} \\
&= \frac{\partial \psi_{l21}}{\partial y} - \frac{\partial \psi_{l22}}{\partial x}
\end{aligned} \tag{A.28}$$

It is concluded that:

$$\begin{aligned}
v_{lm} &= \frac{\partial \psi_{lm1}}{\partial y} - \frac{\partial \psi_{lm2}}{\partial x} + \delta_{m1}(\delta_{l1}\frac{\partial \Psi_l}{\partial y} - \delta_{l2}\frac{\partial \Psi_l}{\partial x}) \\
&= ik_{m1}\varepsilon_m\cos\zeta_{lm1}\psi_{lm1} - ik_{m2}\sin\zeta_{lm2}\psi_{lm2} \\
&\quad + \delta_{m1}\Psi_l\, i\,(-\delta_{l1}k_{1l}\cos\theta_l - \delta_{l2}k_{1l}\sin\theta_l) \\
&= ik_{m1}\varepsilon_m\cos\zeta_{lm1}\psi_{lm1} - ik_{m2}\sin\zeta_{lm2}\psi_{lm2} \\
&\quad + \delta_{m1}\Psi_l\, i\,(-\delta_{l1}k_{11}\cos\theta_1 - \delta_{l2}k_{12}\sin\theta_2) \\
&= \begin{bmatrix} ik_{m1}\varepsilon_m\cos\zeta_{lm1} & -ik_{m2}\sin\zeta_{lm2} \end{bmatrix} \begin{Bmatrix} \psi_{lm1} \\ \psi_{lm2} \end{Bmatrix} \\
&\quad + \delta_{m1}\Psi_l \left[-i(\delta_{l1}k_{11}\cos\theta_1 + \delta_{l2}k_{12}\sin\theta_2) \right]
\end{aligned} \tag{A.29}$$

- σ_{xlm}

From Eq. A.8, $\sigma_{xlm} = 2\mu_m(\partial^2\Phi_{lm1}/\partial x^2 + \partial^2\Phi_{lm2}/\partial x\partial y) - \lambda_m k_{m1}^2\Phi_{lm1}$. Using Eqs. A.10, A.11 and A.12 and discussing different cases in terms of m, we have:

when $m = 1$

$$\begin{aligned}\sigma_{xl1} &= 2\mu_1(\frac{\partial^2\Phi_{l11}}{\partial x^2} + \frac{\partial^2\Phi_{l12}}{\partial x\partial y}) - \lambda_1 k_{11}^2 \Phi_{l11} \\ &= 2\mu_1[\frac{\partial^2(\delta_{l1}\Psi_l + \psi_{l11})}{\partial x^2} + \frac{\partial^2(\delta_{l2}\Psi_l + \psi_{l12})}{\partial x\partial y}] - \lambda_1 k_{11}^2(\delta_{l1}\Psi_l + \psi_{l11})\end{aligned} \tag{A.30}$$

when $m = 2$

$$\begin{aligned}\sigma_{xl2} &= 2\mu_2(\frac{\partial^2\Phi_{l21}}{\partial x^2} + \frac{\partial^2\Phi_{l22}}{\partial x\partial y}) - \lambda_2 k_{21}^2 \Phi_{l21} \\ &= 2\mu_2(\frac{\partial^2\psi_{l21}}{\partial x^2} + \frac{\partial^2\psi_{l22}}{\partial x\partial y}) - \lambda_2 k_{21}^2 \psi_{l21}\end{aligned} \tag{A.31}$$

It is concluded that:

$$\begin{aligned}\sigma_{xlm} &= 2\mu_m(\frac{\partial^2\psi_{lm1}}{\partial x^2} + \frac{\partial^2\psi_{lm2}}{\partial x\partial y}) - \lambda_m k_{m1}^2 \psi_{lm1} \\ &\quad + \delta_{m1}[2\mu_1(\delta_{l1}\frac{\partial^2\Psi_l}{\partial x^2} + \delta_{l2}\frac{\partial^2\Psi_l}{\partial x\partial y}) - \lambda_1 k_{11}^2 \delta_{l1}\Psi_l] \\ &= 2\mu_m(-k_{m1}^2 \sin^2\zeta_{lm1}\psi_{lm1} - k_{m2}^2 \sin\zeta_{lm2}\varepsilon_m \cos\zeta_{lm2}\psi_{lm2}) - \lambda_m k_{m1}^2 \psi_{lm1} \\ &\quad + \delta_{m1}[2\mu_1(-\delta_{l1}k_{1l}^2 \sin^2\theta_l \Psi_l + \delta_{l2}k_{1l}^2 \sin\theta_l \cos\theta_l \Psi_l) - \lambda_1 k_{11}^2 \delta_{l1}\Psi_l] \\ &= -k_{m1}^2(\lambda_m + 2\mu_m \sin^2\zeta_{lm1})\psi_{lm1} - \mu_m k_{m2}^2 \varepsilon_m \sin 2\zeta_{lm2}\psi_{lm2} \\ &\quad + \delta_{m1}\Psi_l[-\delta_{l1}(\lambda_1 k_{11}^2 + 2\mu_1 k_{1l}^2 \sin^2\theta_l) + \delta_{l2}\mu_1 k_{1l}^2 \sin 2\theta_l] \\ &= -k_{m1}^2(\lambda_m + 2\mu_m \sin^2\zeta_{lm1})\psi_{lm1} - \mu_m k_{m2}^2 \varepsilon_m \sin 2\zeta_{lm2}\psi_{lm2} \\ &\quad + \delta_{m1}\Psi_l[-\delta_{l1}k_{11}^2(\lambda_1 + 2\mu_1 \sin^2\theta_1) + \delta_{l2}\mu_1 k_{12}^2 \sin 2\theta_2] \\ &= \begin{bmatrix} -k_{m1}^2(\lambda_m + 2\mu_m \sin^2\zeta_{lm1}) & -\mu_m k_{m2}^2 \varepsilon_m \sin 2\zeta_{lm2} \end{bmatrix} \begin{Bmatrix} \psi_{lm1} \\ \psi_{lm2} \end{Bmatrix} \\ &\quad + \delta_{m1}\Psi_l \left[-\delta_{l1}k_{11}^2(\lambda_1 + 2\mu_1 \sin^2\theta_1) + \delta_{l2}\mu_1 k_{12}^2 \sin 2\theta_2\right]\end{aligned} \tag{A.32}$$

- σ_{ylm}

From Eq. A.8, $\sigma_{ylm} = 2\mu_m(\partial^2\Phi_{lm1}/\partial y^2 - \partial^2\Phi_{lm2}/\partial x\partial y) - \lambda_m k_{m1}^2 \Phi_{lm1}$. Using Eqs. A.10, A.11 and A.12 and discussing different cases in terms of m, we have:

when $m = 1$

$$\begin{aligned}\sigma_{yl1} &= 2\mu_1(\frac{\partial^2\Phi_{l11}}{\partial y^2} - \frac{\partial^2\Phi_{l12}}{\partial x\partial y}) - \lambda_1 k_{11}^2 \Phi_{l11} \\ &= 2\mu_1[\frac{\partial^2(\delta_{l1}\Psi_l + \psi_{l11})}{\partial y^2} - \frac{\partial^2(\delta_{l2}\Psi_l + \psi_{l12})}{\partial x\partial y}] - \lambda_1 k_{11}^2(\delta_{l1}\Psi_l + \psi_{l11})\end{aligned} \tag{A.33}$$

when $m = 2$

$$\begin{aligned}\sigma_{yl2} &= 2\mu_2(\frac{\partial^2\Phi_{l21}}{\partial y^2} - \frac{\partial^2\Phi_{l22}}{\partial x\partial y}) - \lambda_2 k_{21}^2 \Phi_{l21} \\ &= 2\mu_2(\frac{\partial^2\psi_{l21}}{\partial y^2} - \frac{\partial^2\psi_{l22}}{\partial x\partial y}) - \lambda_2 k_{21}^2 \psi_{l21}\end{aligned} \tag{A.34}$$

It is concluded that:

$$\begin{aligned}\sigma_{ylm} = {} & 2\mu_m(\frac{\partial^2\psi_{lm1}}{\partial y^2} - \frac{\partial^2\psi_{lm2}}{\partial x\partial y}) - \lambda_m k_{m1}^2 \psi_{lm1} \\ & + \delta_{m1}[2\mu_1(\delta_{l1}\frac{\partial^2\Psi_l}{\partial y^2} - \delta_{l2}\frac{\partial^2\Psi_l}{\partial x\partial y}) - \lambda_1 k_{11}^2 \delta_{l1}\Psi_l] \\ = {} & 2\mu_m(-k_{m1}^2\varepsilon_m^2\cos^2\zeta_{lm1}\psi_{lm1} + k_{m2}^2\sin\zeta_{lm2}\varepsilon_m\cos\zeta_{lm2}\psi_{lm2}) - \lambda_m k_{m1}^2\psi_{lm1} \\ & + \delta_{m1}[2\mu_1(-\delta_{l1}k_{1l}^2\cos^2\theta_l\Psi_l - \delta_{l2}k_{1l}^2\sin\theta_l\cos\theta_l\Psi_l) - \lambda_1 k_{11}^2\delta_{l1}\Psi_l] \\ = {} & -k_{m1}^2(\lambda_m + 2\mu_m\cos^2\zeta_{lm1})\psi_{lm1} + \mu_m k_{m2}^2\varepsilon_m\sin 2\zeta_{lm2}\psi_{lm2} \\ & + \delta_{m1}\Psi_l[-\delta_{l1}(\lambda_1 k_{11}^2 + 2\mu_1 k_{1l}^2\cos^2\theta_l) - \delta_{l2}\mu_1 k_{1l}^2\sin 2\theta_l] \\ = {} & -k_{m1}^2(\lambda_m + 2\mu_m\cos^2\zeta_{lm1})\psi_{lm1} + \mu_m k_{m2}^2\varepsilon_m\sin 2\zeta_{lm2}\psi_{lm2} \\ & + \delta_{m1}\Psi_l[-\delta_{l1}k_{11}^2(\lambda_1 + 2\mu_1\cos^2\theta_1) - \delta_{l2}\mu_1 k_{12}^2\sin 2\theta_2] \\ = {} & \left[-k_{m1}^2(\lambda_m + 2\mu_m\cos^2\zeta_{lm1}) \quad \mu_m k_{m2}^2\varepsilon_m\sin 2\zeta_{lm2}\right]\begin{Bmatrix}\psi_{lm1} \\ \psi_{lm2}\end{Bmatrix} \\ & + \delta_{m1}\Psi_l\left[-\delta_{l1}k_{11}^2(\lambda_1 + 2\mu_1\cos^2\theta_1) - \delta_{l2}\mu_1 k_{12}^2\sin 2\theta_2\right]\end{aligned} \tag{A.35}$$

- τ_{lm}

From Eq. A.8, $\tau_{lm} = \mu_m(2\partial^2\Phi_{lm1}/\partial x\partial y + \partial^2\Phi_{lm2}/\partial y^2 - \partial^2\Phi_{lm2}/\partial x^2)$. Using Eqs. A.10, A.11 and A.12 and discussing different cases in terms of m, we have:

when $m = 1$

$$\begin{aligned}\tau_{l1} &= \mu_1(2\frac{\partial^2\Phi_{l11}}{\partial x\partial y} + \frac{\partial^2\Phi_{l12}}{\partial y^2} - \frac{\partial^2\Phi_{l12}}{\partial x^2}) \\ &= \mu_1[2\frac{\partial^2(\delta_{l1}\Psi_l + \psi_{l11})}{\partial x\partial y} + \frac{\partial^2(\delta_{l2}\Psi_l + \psi_{l12})}{\partial y^2} - \frac{\partial^2(\delta_{l2}\Psi_l + \psi_{l12})}{\partial x^2}]\end{aligned} \tag{A.36}$$

when $m = 2$

$$\begin{aligned}\tau_{l2} &= \mu_2(2\frac{\partial^2\Phi_{l21}}{\partial x\partial y} + \frac{\partial^2\Phi_{l22}}{\partial y^2} - \frac{\partial^2\Phi_{l22}}{\partial x^2}) \\ &= \mu_2(2\frac{\partial^2\psi_{l21}}{\partial x\partial y} + \frac{\partial^2\psi_{l22}}{\partial y^2} - \frac{\partial^2\psi_{l22}}{\partial x^2})\end{aligned} \tag{A.37}$$

It is concluded that:

$$\begin{aligned}
\tau_{lm} &= \mu_m\left(2\frac{\partial^2\psi_{lm1}}{\partial x\partial y}+\frac{\partial^2\psi_{lm2}}{\partial y^2}-\frac{\partial^2\psi_{lm2}}{\partial x^2}\right)\\
&\quad+\delta_{m1}\mu_1\left(2\delta_{l1}\frac{\partial^2\Psi_l}{\partial x\partial y}+\delta_{l2}\frac{\partial^2\Psi_l}{\partial y^2}-\delta_{l2}\frac{\partial^2\Psi_l}{\partial x^2}\right)\\
&=\mu_m(-2k_{m1}^2\sin\zeta_{lm1}\varepsilon_m\cos\zeta_{lm1}\psi_{lm1}-k_{m2}^2\varepsilon_m^2\cos^2\zeta_{lm2}\psi_{lm2}+k_{m2}^2\sin^2\zeta_{lm2}\psi_{lm2})\\
&\quad+\delta_{m1}\mu_1(2\delta_{l1}k_{1l}^2\sin\theta_l\cos\theta_l\Psi_l-\delta_{l2}k_{1l}^2\cos^2\theta_l\Psi_l+\delta_{l2}k_{1l}^2\sin^2\theta_l\Psi_l)\\
&=-\mu_m k_{m1}^2\varepsilon_m\sin 2\zeta_{lm1}\psi_{lm1}-\mu_m k_{m2}^2\cos 2\zeta_{lm2}\psi_{lm2}\\
&\quad+\delta_{m1}\Psi_l(\delta_{l1}\mu_1k_{1l}^2\sin 2\theta_l-\delta_{l2}\mu_1k_{1l}^2\cos 2\theta_l)\\
&=-\mu_m k_{m1}^2\varepsilon_m\sin 2\zeta_{lm1}\psi_{lm1}-\mu_m k_{m2}^2\cos 2\zeta_{lm2}\psi_{lm2}\\
&\quad+\delta_{m1}\Psi_l(\delta_{l1}\mu_1k_{11}^2\sin 2\theta_1-\delta_{l2}\mu_1k_{12}^2\cos 2\theta_2)\\
&=\left[-\mu_m k_{m1}^2\varepsilon_m\sin 2\zeta_{lm1}\quad -\mu_m k_{m2}^2\cos 2\zeta_{lm2}\right]\begin{Bmatrix}\psi_{lm1}\\ \psi_{lm2}\end{Bmatrix}\\
&\quad+\delta_{m1}\Psi_l\left[\delta_{l1}\mu_1k_{11}^2\sin 2\theta_1-\delta_{l2}\mu_1k_{12}^2\cos 2\theta_2\right]
\end{aligned} \tag{A.38}$$

Eq. A.14

Since the relation $\exp\{ik_{1l}(\boldsymbol{r}_l\cdot\boldsymbol{x})\}=\exp\{ik_{mn}(\boldsymbol{r}_{lmn}\cdot\boldsymbol{x})\}$ should be satisfied on $y=0$, we have the following equations:

$$\begin{aligned}
k_{mn}\sin\zeta_{lmn} &= k_{1l}\sin\theta_l\\
\frac{\omega}{S_{mn}}\sin\zeta_{lmn} &= \frac{\omega}{S_{1l}}\sin\theta_l
\end{aligned} \tag{A.39}$$

which results in the complex Snell's law:

$$\sin\zeta_{lmn}=\frac{S_{mn}}{S_{1l}}\sin\theta_l \tag{A.40}$$

Eqs. A.15, A.16 and A.17

In the following demonstrations, we assume all the equal exponents being noted as *Exp*.

- First row

  Using Eq. A.26 and potential functions defined in Eq. A.11, we can write $u_{lm}(x,0)$ for different cases of m:

  when $m=1$

$$\begin{aligned}
u_{l1}(x,0) &= ik_{11}\sin\zeta_{l11}I_lR_{l11}\frac{S_{11}}{\omega}Exp+ik_{12}(-1)^2\cos\zeta_{l12}I_lR_{l12}\frac{S_{12}}{\omega}Exp\\
&\quad+i(\delta_{l1}k_{11}\sin\theta_1-\delta_{l2}k_{12}\cos\theta_2)I_l\frac{S_{1l}}{\omega}Exp
\end{aligned} \tag{A.41}$$

when $m = 2$

$$u_{l2}(x,0) = ik_{21}\sin\zeta_{l21}I_lR_{l21}\frac{S_{21}}{\omega}Exp + ik_{22}(-1)^3\cos\zeta_{l22}I_lR_{l22}\frac{S_{22}}{\omega}Exp \tag{A.42}$$

Considering the definition of wave number k_{mn} in Eq. A.5, the boundary condition $u_{l1}(x,0) = u_{l2}(x,0)$ leads to:

$$\begin{gathered}\sin\zeta_{l11}R_{l11} + \cos\zeta_{l12}R_{l12} + (\delta_{l1}\sin\theta_1 - \delta_{l2}\cos\theta_2) = \sin\zeta_{l21}R_{l21} - \cos\zeta_{l22}R_{l22} \\ \sin\zeta_{l11}R_{l11} + \cos\zeta_{l12}R_{l12} - \sin\zeta_{l21}R_{l21} + \cos\zeta_{l22}R_{l22} = -\delta_{l1}\sin\theta_1 + \delta_{l2}\cos\theta_2\end{gathered} \tag{A.43}$$

Thus the first rows of $\boldsymbol{A}_l$, $\boldsymbol{B}_1$ and $\boldsymbol{B}_2$ read:

$$\begin{aligned}\boldsymbol{A}_l(1,:) &= \begin{bmatrix}\sin\zeta_{l11} & \cos\zeta_{l12} & -\sin\zeta_{l21} & \cos\zeta_{l22}\end{bmatrix} \\ \boldsymbol{B}_1(1,:) &= \begin{bmatrix}-\sin\theta_1\end{bmatrix} \\ \boldsymbol{B}_2(1,:) &= \begin{bmatrix}\cos\theta_2\end{bmatrix}\end{aligned} \tag{A.44}$$

- Second row

  Using Eq. A.29 and potential functions defined in Eq. A.11, we can write $v_{lm}(x,0)$ for different cases of m:

  when $m = 1$

$$\begin{aligned}v_{l1}(x,0) = {} & ik_{11}(-1)^2\cos\zeta_{l11}I_lR_{l11}\frac{S_{11}}{\omega}Exp - ik_{12}\sin\zeta_{l12}I_lR_{l12}\frac{S_{12}}{\omega}Exp \\ & - i(\delta_{l1}k_{11}\cos\theta_1 + \delta_{l2}k_{12}\sin\theta_2)I_l\frac{S_{1l}}{\omega}Exp\end{aligned} \tag{A.45}$$

when $m = 2$

$$v_{l2}(x,0) = ik_{21}(-1)^3\cos\zeta_{l21}I_lR_{l21}\frac{S_{21}}{\omega}Exp - ik_{22}\sin\zeta_{l22}I_lR_{l22}\frac{S_{22}}{\omega}Exp \tag{A.46}$$

Considering the definition of wave number k_{mn} in Eq. A.5, the boundary condition $v_{l1}(x,0) = v_{l2}(x,0)$ leads to:

$$\begin{gathered}\cos\zeta_{l11}R_{l11} - \sin\zeta_{l12}R_{l12} - (\delta_{l1}\cos\theta_1 + \delta_{l2}\sin\theta_2) = -\cos\zeta_{l21}R_{l21} - \sin\zeta_{l22}R_{l22} \\ \cos\zeta_{l11}R_{l11} - \sin\zeta_{l12}R_{l12} + \cos\zeta_{l21}R_{l21} + \sin\zeta_{l22}R_{l22} = \delta_{l1}\cos\theta_1 + \delta_{l2}\sin\theta_2\end{gathered} \tag{A.47}$$

Thus the second rows of $\boldsymbol{A}_l$, $\boldsymbol{B}_1$ and $\boldsymbol{B}_2$ read:

$$\begin{aligned}\boldsymbol{A}_l(2,:) &= \begin{bmatrix}\cos\zeta_{l11} & -\sin\zeta_{l12} & \cos\zeta_{l21} & \sin\zeta_{l22}\end{bmatrix} \\ \boldsymbol{B}_1(2,:) &= \begin{bmatrix}\cos\theta_1\end{bmatrix} \\ \boldsymbol{B}_2(2,:) &= \begin{bmatrix}\sin\theta_2\end{bmatrix}\end{aligned} \tag{A.48}$$

- Third row

  Using Eq. A.35 and potential functions defined in Eq. A.11, we can write $\sigma_{ylm}(x,0)$ for different cases of m:

  when $m = 1$

$$\sigma_{yl1}(x,0) = -k_{11}^2(\lambda_1 + 2\mu_1\cos^2\zeta_{l11})I_lR_{l11}\frac{S_{11}}{\omega}Exp + \mu_1k_{12}^2(-1)^2\sin 2\zeta_{l12}I_lR_{l12}\frac{S_{12}}{\omega}Exp$$
$$+[-\delta_{l1}k_{11}^2(\lambda_1 + 2\mu_1\cos^2\theta_1) - \delta_{l2}\mu_1k_{12}^2\sin 2\theta_2]I_l\frac{S_{1l}}{\omega}Exp \tag{A.49}$$

  when $m = 2$

$$\sigma_{yl2}(x,0) = -k_{21}^2(\lambda_2 + 2\mu_2\cos^2\zeta_{l21})I_lR_{l21}\frac{S_{21}}{\omega}Exp + \mu_2k_{22}^2(-1)^3\sin 2\zeta_{l22}I_lR_{l22}\frac{S_{22}}{\omega}Exp \tag{A.50}$$

  Considering the definition of wave number k_{mn} in Eq. A.5, the boundary condition $\sigma_{yl1}(x,0) = \sigma_{yl2}(x,0)$ leads to:

$$\begin{gathered}
-k_{11}(\lambda_1 + 2\mu_1\cos^2\zeta_{l11})R_{l11} + \mu_1k_{12}\sin 2\zeta_{l12}R_{l12} - [\delta_{l1}k_{11}(\lambda_1 + 2\mu_1\cos^2\theta_1) + \delta_{l2}\mu_1k_{12}\sin 2\theta_2] \\
= -k_{21}(\lambda_2 + 2\mu_2\cos^2\zeta_{l21})R_{l21} - \mu_2k_{22}\sin 2\zeta_{l22}R_{l22} \\
-\frac{1}{S_{11}}(\lambda_1 + 2\mu_1\cos^2\zeta_{l11})R_{l11} + \mu_1\frac{1}{S_{12}}\sin 2\zeta_{l12}R_{l12} + \frac{1}{S_{21}}(\lambda_2 + 2\mu_2\cos^2\zeta_{l21})R_{l21} + \mu_2\frac{1}{S_{22}}\sin 2\zeta_{l22}R_{l22} \\
= \delta_{l1}\frac{1}{S_{11}}(\lambda_1 + 2\mu_1\cos^2\theta_1) + \delta_{l2}\mu_1\frac{1}{S_{12}}\sin 2\theta_2
\end{gathered} \tag{A.51}$$

  For the factors of R_{l11}, R_{l12}, R_{l21}, R_{l22}, δ_{l1} and δ_{l2}, we have the following derivations considering the definition of wave speed S_{mn} in Eq. A.5 and Snell's law:

  - R_{l11}

$$\begin{aligned}
-\frac{1}{S_{11}}(\lambda_1 + 2\mu_1\cos^2\zeta_{l11}) &= -\frac{1}{S_{11}}(\lambda_1 + 2\mu_1 - 2\mu_1\sin^2\zeta_{l11}) \\
&= -\frac{1}{S_{11}}(\rho_1S_{11}^2 - 2\rho_1S_{12}^2\frac{S_{11}^2}{S_{12}^2}\sin^2\zeta_{l12}) \\
&= -\frac{1}{S_{11}}\rho_1S_{11}^2(1 - 2\sin^2\zeta_{l12}) \\
&= -\rho_1S_{11}\cos 2\zeta_{l12}
\end{aligned} \tag{A.52}$$

  - R_{l12}

$$\begin{aligned}
\mu_1\frac{1}{S_{12}}\sin 2\zeta_{l12} &= \rho_1S_{12}^2\frac{1}{S_{12}}\sin 2\zeta_{l12} \\
&= \rho_1S_{12}\sin 2\zeta_{l12}
\end{aligned} \tag{A.53}$$

- R_{l21}

$$\begin{aligned}\frac{1}{S_{21}}(\lambda_2+2\mu_2\cos^2\zeta_{l21}) &= \frac{1}{S_{21}}(\lambda_2+2\mu_2-2\mu_2\sin^2\zeta_{l21})\\ &= \frac{1}{S_{21}}(\rho_2S_{21}^2-2\rho_2S_{22}^2\frac{S_{21}^2}{S_{22}^2}\sin^2\zeta_{l22})\\ &= \frac{1}{S_{21}}\rho_2S_{21}^2(1-2\sin^2\zeta_{l22})\\ &= \rho_2S_{21}\cos 2\zeta_{l22}\end{aligned} \tag{A.54}$$

- R_{l22}

$$\begin{aligned}\mu_2\frac{1}{S_{22}}\sin 2\zeta_{l22} &= \rho_2S_{22}^2\frac{1}{S_{22}}\sin 2\zeta_{l22}\\ &= \rho_2S_{22}\sin 2\zeta_{l22}\end{aligned} \tag{A.55}$$

- δ_{l1}

$$\begin{aligned}\frac{1}{S_{11}}(\lambda_1+2\mu_1\cos^2\theta_1) &= \frac{1}{S_{11}}(\lambda_1+2\mu_1-2\mu_1\sin^2\theta_1)\\ &= \frac{1}{S_{11}}(\rho_1S_{11}^2-2\rho_1S_{12}^2\frac{S_{11}^2}{S_{12}^2}\sin^2\zeta_{112})\\ &= \frac{1}{S_{11}}\rho_1S_{11}^2(1-2\sin^2\zeta_{112})\\ &= \rho_1S_{11}\cos 2\zeta_{112}\end{aligned} \tag{A.56}$$

- δ_{l2}

$$\begin{aligned}\mu_1\frac{1}{S_{12}}\sin 2\theta_2 &= \rho_1S_{12}^2\frac{1}{S_{12}}\sin 2\theta_2\\ &= \rho_1S_{12}\sin 2\theta_2\end{aligned} \tag{A.57}$$

Thus the third rows of $\boldsymbol{A}_l$, $\boldsymbol{B}_1$ and $\boldsymbol{B}_2$ read:

$$\begin{aligned}&\boldsymbol{A}_l(3,:) = \left[-\rho_1S_{11}\cos 2\zeta_{l12} \quad \rho_1S_{12}\sin 2\zeta_{l12} \quad \rho_2S_{21}\cos 2\zeta_{l22} \quad \rho_2S_{22}\sin 2\zeta_{l22}\right]\\ &\boldsymbol{B}_1(3,:) = \left[\rho_1S_{11}\cos 2\zeta_{112}\right]\\ &\boldsymbol{B}_2(3,:) = \left[\rho_1S_{12}\sin 2\theta_2\right]\end{aligned} \tag{A.58}$$

- Fourth row

  Using Eq. A.38 and potential functions defined in Eq. A.11, we can write $\tau_{lm}(x,0)$ for different cases of m:

  when $m=1$

$$\begin{aligned}\tau_{l1}(x,0) = &-(-1)^2\mu_1k_{11}^2\sin 2\zeta_{l11}I_lR_{l11}\frac{S_{11}}{\omega}Exp-\mu_1k_{12}^2\cos 2\zeta_{l12}I_lR_{l12}\frac{S_{12}}{\omega}Exp\\ &+(\delta_{l1}\mu_1k_{11}^2\sin 2\theta_1-\delta_{l2}\mu_1k_{12}^2\cos 2\theta_2)I_l\frac{S_{1l}}{\omega}Exp\end{aligned} \tag{A.59}$$

when $m = 2$

$$\tau_{l2}(x,0) = -(-1)^3 \mu_2 k_{21}^2 \sin 2\zeta_{l21} I_l R_{l21} \frac{S_{21}}{\omega} Exp - \mu_2 k_{22}^2 \cos 2\zeta_{l22} I_l R_{l22} \frac{S_{22}}{\omega} Exp \tag{A.60}$$

Considering the definition of wave number k_{mn} in Eq. A.5, the boundary condition $\tau_{l1}(x,0) = \tau_{l2}(x,0)$ leads to:

$$\begin{aligned}
-\mu_1 k_{11} \sin 2\zeta_{l11} R_{l11} - \mu_1 k_{12} \cos 2\zeta_{l12} R_{l12} + (\delta_{l1} \mu_1 k_{11} \sin 2\theta_1 - \delta_{l2} \mu_1 k_{12} \cos 2\theta_2) \\
= \mu_2 k_{21} \sin 2\zeta_{l21} R_{l21} - \mu_2 k_{22} \cos 2\zeta_{l22} R_{l22} \\
\mu_1 \frac{1}{S_{11}} \sin 2\zeta_{l11} R_{l11} + \mu_1 \frac{1}{S_{12}} \cos 2\zeta_{l12} R_{l12} + \mu_2 \frac{1}{S_{21}} \sin 2\zeta_{l21} R_{l21} - \mu_2 \frac{1}{S_{22}} \cos 2\zeta_{l22} R_{l22} \\
= \delta_{l1} \mu_1 \frac{1}{S_{11}} \sin 2\theta_1 - \delta_{l2} \mu_1 \frac{1}{S_{12}} \cos 2\theta_2
\end{aligned} \tag{A.61}$$

For the factors of R_{l11}, R_{l12}, R_{l21}, R_{l22}, δ_{l1} and δ_{l2}, we have the following derivations considering the definition of wave speed S_{mn} in Eq. A.5 and Snell's law:

- R_{l11}

$$\mu_1 \frac{1}{S_{11}} \sin 2\zeta_{l11} = \frac{\rho_1 S_{12}^2}{S_{11}} \sin 2\zeta_{l11} \tag{A.62}$$

- R_{l12}

$$\begin{aligned}
\mu_1 \frac{1}{S_{12}} \cos 2\zeta_{l12} &= \frac{\rho_1 S_{12}^2}{S_{12}} \cos 2\zeta_{l12} \\
&= \rho_1 S_{12} \cos 2\zeta_{l12}
\end{aligned} \tag{A.63}$$

- R_{l21}

$$\mu_2 \frac{1}{S_{21}} \sin 2\zeta_{l21} = \frac{\rho_2 S_{22}^2}{S_{21}} \sin 2\zeta_{l21} \tag{A.64}$$

- R_{l22}

$$\begin{aligned}
-\mu_2 \frac{1}{S_{22}} \cos 2\zeta_{l22} &= -\frac{\rho_2 S_{22}^2}{S_{22}} \cos 2\zeta_{l22} \\
&= -\rho_2 S_{22} \cos 2\zeta_{l22}
\end{aligned} \tag{A.65}$$

- δ_{l1}

$$\mu_1 \frac{1}{S_{11}} \sin 2\theta_1 = \frac{\rho_1 S_{12}^2}{S_{11}} \sin 2\theta_1 \tag{A.66}$$

- δ_{l2}

$$\begin{aligned}
-\mu_1 \frac{1}{S_{12}} \cos 2\theta_2 &= -\frac{\rho_1 S_{12}^2}{S_{12}} \cos 2\theta_2 \\
&= -\rho_1 S_{12} \cos 2\theta_2
\end{aligned} \tag{A.67}$$

Thus the fourth rows of $\boldsymbol{A}_l$, $\boldsymbol{B}_1$ and $\boldsymbol{B}_2$ read:

$$\begin{aligned}
&\boldsymbol{A}_l(4,:) = \left[(\rho_1 S_{12}^2/S_{11})\sin 2\zeta_{l11} \quad \rho_1 S_{12}\cos 2\zeta_{l12} \quad (\rho_2 S_{22}^2/S_{21})\sin 2\zeta_{l21} \quad -\rho_2 S_{22}\cos 2\zeta_{l22}\right]\\
&\boldsymbol{B}_1(4,:) = \left[(\rho_1 S_{12}^2/S_{11})\sin 2\theta_1\right]\\
&\boldsymbol{B}_2(4,:) = \left[-\rho_1 S_{12}\cos 2\theta_2\right]
\end{aligned} \tag{A.68}$$

Appendix C

This appendix consists in presenting the numerical implementation of the wave reflection and transmission formulations that have been originally given in [COO 67] and corrected in Appendix B. It is completed by a Python script. Based on the functions defined in the codes, the theoretical values of the parametric study in section 4.3.3 can be computed.

```python
# -*- coding: utf-8 -*-
"""
Created on Fri Jul  2 17:05:52 2021
@author: qdu
objective : calculate reflection & refraction angle & coefficients
            in function of inputs
paper : 'Reflection and Transmission of Oblique Plane Waves at a Plane
         Interface between Viscoelastic Media' by H. F. Cooper Jr, 1967
characteristics : small amplitude time harmonic plane waves in homogeneous
                  and isotropic linearly viscoelastic materials
notation :
    l = 0 : incident P-wave
    l = 1 : incident S-wave
    m = 0 : y > 0 zone (incident side)
    m = 1 : y < 0 zone
    n = 0 : reflected/refracted P-wave
    n = 1 : reflected/refracted S-wave
"""
import numpy as np
from numpy import sin
from numpy import cos
from numpy import tan
from numpy import tanh
from numpy import arcsin
from numpy import arctan
from numpy import arcsinh

def E_complex(E1, E2, eta, omega):
    """ complex Young modulus of one-branch GM model """
```

```
    tau = eta / E2
    Ed = E1 + (tau*omega)**2 / (1 + (tau*omega)**2) * E2
    El = tau*omega / (1 + (tau*omega)**2) * E2
    return complex(Ed, El)

def angle_coef(thetaI, E1, E2, eta, rho=[1000,1000], nu=[0.49,0.49], f=100):
    """
    thetaI (rad): array of angle of incidence (length 2 with subscript l);
    E1 (kPa), E2 (kPa), eta (Pa*s): viscoelastic SLS model parameters
                                    (array of length 2 with subscript m);
    rho (kg/m³): array of density (length 2 with subscript m);
    nu: array of Poisson's ratio (length 2 with subscript m);
    f (Hz): excitation frequency
    """

    # angular frequency
    omega = 2*np.pi*f

    # complex Young's modulus
    E = np.zeros(2, dtype=complex)
    for m in range(2):
        E[m] = E_complex(E1[m], E2[m], eta[m], omega)

    # complex Lame parameters
    lamb = np.zeros(2, dtype=complex)
    mu = np.zeros(2, dtype=complex)
    for m in range(2):
        lamb[m] = E[m] * nu[m] / (1+nu[m]) / (1-2*nu[m])
        mu[m] = E[m] / 2 / (1+nu[m])

    # Smn²
    # Sm0² = (lamb_m + 2*mu_m) / rho_m
    # Sm1² = mu_m / rho_m
    S_sq = np.zeros((2,2), dtype=complex)
    for m in range(2):
        S_sq[m,0] = (lamb[m] + 2*mu[m]) / rho[m]
        S_sq[m,1] = mu[m] / rho[m]

    # Omega_mn
    # tan(2*Omega_mn) = + Im(Smn²) / Re(Smn²)
    # => modified from minus to plus, requiring that in other equations,
    # Omega[m,n] should be modified to -Omega[m,n]
    # 0 <= Omega_mn < pi/2
```

```
    Omega = np.zeros((2,2))
    for m in range(2):
        for n in range(2):
            tmp = + S_sq[m,n].imag / S_sq[m,n].real     # plus instead of minus
            if tmp < 0:
                Omega[m,n] = (arctan(tmp) + np.pi) / 2
            else:
                Omega[m,n] = arctan(tmp) / 2

            if Omega[m,n] < 0 or Omega[m,n] >= np.pi/2:
                print("error : Omega -> ", Omega[m,n])

    # Cmn = |Smn| * sec(Omega_mn)
    C = np.zeros((2,2))
    for m in range(2):
        for n in range(2):
            C[m,n] = abs(np.sqrt(S_sq[m,n])) / cos(Omega[m,n])

    # gamma_lmn = Cmn * sin(theta_l) / C_0l
    gamma = np.zeros((2,2,2))
    for l in range(2):
        for m in range(2):
            for n in range(2):
                gamma[l,m,n] = C[m,n] * sin(thetaI[l]) / C[0,l]

    # Gamma_lmn = gamma_lmn * cos(Omega_mn) / cos(Omega_0l)
    Gamma = np.zeros((2,2,2))
    for l in range(2):
        for m in range(2):
            for n in range(2):
                Gamma[l,m,n] = gamma[l,m,n] * cos(Omega[m,n]) / cos(Omega[0,l])

    # Delta_lmn = Omega_0l - Omega_mn
    Delta = np.zeros((2,2,2))
    for l in range(2):
        for m in range(2):
            for n in range(2):
                Delta[l,m,n] = -Omega[0,l] - -Omega[m,n]

    # sinh²(beta_lmn) = 0.5 * { Gamma_lmn² - 1 + [(1-Gamma_lmn²)² +
    # 4*Gamma_lmn²*sin²(Delta_lmn)]^0.5 }
    sinh_sq_beta = np.zeros((2,2,2))
    for l in range(2):
```

```
        for m in range(2):
            for n in range(2):
                sinh_sq_beta[l,m,n] = 0.5 * ( Gamma[l,m,n]**2 - 1
                                                 + ( (1-Gamma[l,m,n]**2)**2 +
                                                        4*Gamma[l,m,n]**2 *
                                                        sin(Delta[l,m,n])**2
                                                   )**0.5
                                            )

    # xi_lmn = (1 + sinh²(beta_lmn) * sec²(Omega_mn))^(-0.5)
    xi = np.zeros((2,2,2))
    for l in range(2):
        for m in range(2):
            for n in range(2):
                xi[l,m,n] = (1 + sinh_sq_beta[l,m,n] / cos(Omega[m,n])**2 )**(-0.5)

    # real angle theta
    # sin(theta_lmn) = xi_lmn * gamma_lmn
    theta = np.zeros((2,2,2))
    for l in range(2):
        for m in range(2):
            for n in range(2):
                theta[l,m,n] = arcsin(xi[l,m,n] * gamma[l,m,n])

    # complex angle zeta
    # zeta_lmn = alpha_lmn + i beta_lmn
    # beta_lmn :
    beta = np.zeros((2,2,2))
    for l in range(2):
        for m in range(2):
            for n in range(2):
                sgn = - np.sign(xi[l,m,n]**2 * tan(-Omega[m,n]) - tan(-Omega[0,1]))
                beta[l,m,n] = sgn * arcsinh(abs(np.sqrt(sinh_sq_beta[l,m,n])))
    # alpha_lmn & zeta_lmn :
    alpha = np.zeros((2,2,2))
    zeta = np.zeros((2,2,2), dtype=complex)
    for l in range(2):
        for m in range(2):
            for n in range(2):
                alpha[l,m,n] = theta[l,m,n] + arctan(tan(-Omega[m,n]) * tanh(beta[l,m,n]))
                zeta[l,m,n] = complex(alpha[l,m,n], beta[l,m,n])

    # S_mn
```

```
    S = np.zeros((2,2), dtype=complex)
    for m in range(2):
        for n in range(2):
            S[m,n] = np.sqrt(S_sq[m,n])

    # solve coefficients R_lmn
    # A_l * R_l = B_l
    # R_l = {R_l00, R_l01, R_l10, R_l11}
    A = np.zeros((2,4,4), dtype=complex)
    B = np.zeros((2,4,1), dtype=complex)
    R = np.zeros((2,4,1), dtype=complex)
    for l in range(2):
        A[l,0,:] = np.array([sin(zeta[l,0,0]), cos(zeta[l,0,1]),
                            -sin(zeta[l,1,0]), cos(zeta[l,1,1])])
        A[l,1,:] = np.array([cos(zeta[l,0,0]), -sin(zeta[l,0,1]),
                             cos(zeta[l,1,0]), sin(zeta[l,1,1])])
        A[l,2,:] = np.array([-rho[0]*S[0,0]*cos(2*zeta[l,0,1]),
                             rho[0]*S[0,1]*sin(2*zeta[l,0,1]),
                             rho[1]*S[1,0]*cos(2*zeta[l,1,1]),
                             rho[1]*S[1,1]*sin(2*zeta[l,1,1])])
        A[l,3,:] = np.array([rho[0]*S_sq[0,1]/S[0,0]*sin(2*zeta[l,0,0]),
                             rho[0]*S[0,1]*cos(2*zeta[l,0,1]),
                             rho[1]*S_sq[1,1]/S[1,0]*sin(2*zeta[l,1,0]),
                             -rho[1]*S[1,1]*cos(2*zeta[l,1,1])])
    B[0,:,0] = np.array([-sin(thetaI[0]), cos(thetaI[0]),
                         rho[0]*S[0,0]*cos(2*zeta[0,0,1]),
                         rho[0]*S_sq[0,1]/S[0,0]*sin(2*thetaI[0])])
    B[1,:,0] = np.array([cos(thetaI[1]), sin(thetaI[1]),
                         +rho[0]*S[0,1]*sin(2*thetaI[1]),
                         -rho[0]*S[0,1]*cos(2*thetaI[1])])

    R[0,:,0] = np.linalg.solve(A[0,:,:], B[0,:,0])
    R[1,:,0] = np.linalg.solve(A[1,:,:], B[1,:,0])

    return theta, R

if __name__ == '__main__':

    # amplitude of incident P-wave (μm)
    A_i = 150

    # angle of incidence of P-wave (degree)
    alpha_i = 40
```

```

    thetaI = (alpha_i*np.pi/180, 0)
    E1 = (6e3, 20e3)
    E2 = (10e3, 10e3)
    eta = (16, 16)
    rho = [1000, 1000]
    nu = [0.49, 0.49]
    f = 100

    theta, R = angle_coef(thetaI, E1, E2, eta, rho, nu, f)
    theta_degree = theta * 180/np.pi
    R_abs = abs(R)
    Amps = A_i * R_abs

    print('theta (degree):')
    print(theta_degree)
    print('')
    print('R:')
    print(R_abs)
    print('')
    print('Amplitude (µm):')
    print(Amps)
```

Bibliography

[ASK 15] Askes H., Rodríguez-Ferran A., Hetherington J.
The effects of element shape on the critical time step in explicit time integrators for elasto-dynamics. *International Journal for Numerical Methods in Engineering*, vol. 101, n^{o} 11, 2015, p. 809–824, Wiley Online Library.

[AVI 10] Avila L. S., Barre S., Blue R., Geveci B., Henderson A., Hoffman W. A., King B., Law C. C., Martin K. M., Schroeder W. J.
The VTK user's guide. Kitware Clifton Park, 2010.

[AZA 00] Azar F. S., Metaxas D. N., Schnall M. D.
A finite element model of the breast for predicting mechanical deformations during biopsy procedures. *Proceedings IEEE Workshop on Mathematical Methods in Biomedical Image Analysis. MMBIA-2000 (Cat. No. PR00737)* IEEE, 2000, p. 38–45.

[AZA 01] Azar F. S., Metaxas D. N., Schnall M. D.
A deformable finite element model of the breast for predicting mechanical deformations under external perturbations. *Academic Radiology*, vol. 8, n^{o} 10, 2001, p. 965–975, Elsevier.

[BAN 19] Bansal M., Singh I., Mishra B., Bordas S.
A parallel and efficient multi-split XFEM for 3-D analysis of heterogeneous materials. *Computer Methods in Applied Mechanics and Engineering*, vol. 347, 2019, p. 365–401, Elsevier.

[BAT 06] Bathe K.-J.
Finite element procedures. Klaus-Jurgen Bathe, 2006.

[BEL 99] Belytschko T., Black T.
Elastic crack growth in finite elements with minimal remeshing. *International journal for numerical methods in engineering*, vol. 45, n^{o} 5, 1999, p. 601–620, Wiley Online Library.

[BEL 03] Belytschko T., Parimi C., Moës N., Sukumar N., Usui S.
Structured extended finite element methods for solids defined by implicit surfaces. *International journal for numerical methods in engineering*, vol. 56, n^{o} 4, 2003, p. 609–635, Wiley Online Library.

[BER 04] BERCOFF J., TANTER M., FINK M.
Supersonic shear imaging: a new technique for soft tissue elasticity mapping. *IEEE transactions on ultrasonics, ferroelectrics, and frequency control*, vol. 51, n° 4, 2004, p. 396–409, IEEE.

[BIL 18] BILASSE M., CHATELIN S., ALTMEYER G., MAROUF A., VAPPOU J., CHARPENTIER I.
A 2D finite element model for shear wave propagation in biological soft tissues: Application to magnetic resonance elastography. *International journal for numerical methods in biomedical engineering*, vol. 34, n° 8, 2018, Page e3102, Wiley Online Library.

[BOH 18] BOHTE A., NELISSEN J., RUNGE J., HOLUB O., LAMBERT S., DE GRAAF L., KOLKMAN S., VAN DER MEIJ S., STOKER J., STRIJKERS G. et al.
Breast magnetic resonance elastography: a review of clinical work and future perspectives. *NMR in Biomedicine*, vol. 31, n° 10, 2018, Page e3932, Wiley Online Library.

[BOR 09] BORCHERDT R. D.
Viscoelastic waves in layered media. Cambridge University Press, 2009.

[CAR 07] CARCIONE J. M.
Wave fields in real media: Wave propagation in anisotropic, anelastic, porous and electromagnetic media. Elsevier, 2007.

[CAT 99] CATHELINE S., WU F., FINK M.
A solution to diffraction biases in sonoelasticity: the acoustic impulse technique. *The Journal of the Acoustical Society of America*, vol. 105, n° 5, 1999, p. 2941–2950, Acoustical Society of America.

[CHA 16] CHATELIN S., CHARPENTIER I., CORBIN N., MEYLHEUC L., VAPPOU J.
An automatic differentiation-based gradient method for inversion of the shear wave equation in magnetic resonance elastography: specific application in fibrous soft tissues. *Physics in Medicine & Biology*, vol. 61, n° 13, 2016, Page 5000, IOP Publishing.

[CHE 05] CHEN Q., RINGLEB S. I., MANDUCA A., EHMAN R. L., AN K.-N.
A finite element model for analyzing shear wave propagation observed in magnetic resonance elastography. *Journal of Biomechanics*, vol. 38, n° 11, 2005, p. 2198–2203, Elsevier.

[CHE 06] CHEN Q., RINGLEB S. I., MANDUCA A., EHMAN R. L., AN K.-N.
Differential effects of pre-tension on shear wave propagation in elastic media with different boundary conditions as measured by magnetic resonance elastography and finite element modeling. *Journal of biomechanics*, vol. 39, n° 8, 2006, p. 1428–1434, Elsevier.

[CHR 12] CHRISTENSEN R.
Theory of viscoelasticity: an introduction. Elsevier, 2012.

[COO 67] Cooper Jr H. F.
Reflection and transmission of oblique plane waves at a plane interface between viscoelastic media. *The Journal of the Acoustical Society of America*, vol. 42, n° 5, 1967, p. 1064–1069, Acoustical Society of America.

[DOL 00] Dolbow J., Moës N., Belytschko T.
Discontinuous enrichment in finite elements with a partition of unity method. *Finite elements in analysis and design*, vol. 36, n° 3-4, 2000, p. 235–260, Elsevier.

[DOY 00] Doyley M., Meaney P., Bamber J.
Evaluation of an iterative reconstruction method for quantitative elastography. *Physics in Medicine & Biology*, vol. 45, n° 6, 2000, Page 1521, IOP Publishing.

[DOY 12] Doyley M. M.
Model-based elastography: a survey of approaches to the inverse elasticity problem. *Physics in Medicine & Biology*, vol. 57, n° 3, 2012, Page R35, IOP Publishing.

[ESK 08] Eskandari H., Salcudean S. E., Rohling R., Ohayon J.
Viscoelastic characterization of soft tissue from dynamic finite element models. *Physics in Medicine & Biology*, vol. 53, n° 22, 2008, Page 6569, IOP Publishing.

[FAT 03] Fatemi M., Manduca A., Greenleaf J. F.
Imaging elastic properties of biological tissues by low-frequency harmonic vibration. *Proceedings of the IEEE*, vol. 91, n° 10, 2003, p. 1503–1519, IEEE.

[FOV 18a] Fovargue D., Kozerke S., Sinkus R., Nordsletten D.
Robust MR elastography stiffness quantification using a localized divergence free finite element reconstruction. *Medical image analysis*, vol. 44, 2018, p. 126–142, Elsevier.

[FOV 18b] Fovargue D., Nordsletten D., Sinkus R.
Stiffness reconstruction methods for MR elastography. *NMR in Biomedicine*, vol. 31, n° 10, 2018, Page e3935, Wiley Online Library.

[FRE 08] Frehner M., Schmalholz S. M., Saenger E. H., Steeb H.
Comparison of finite difference and finite element methods for simulating two-dimensional scattering of elastic waves. *Physics of the earth and planetary interiors*, vol. 171, n° 1-4, 2008, p. 112–121, Elsevier.

[FUN 03] Fung T.
Numerical dissipation in time-step integration algorithms for structural dynamic analysis. *Progress in Structural Engineering and Materials*, vol. 5, n° 3, 2003, p. 167–180, Wiley Online Library.

[GIN 09] Giner E., Sukumar N., Tarancón J., Fuenmayor F.
An Abaqus implementation of the extended finite element method. *Engineering fracture mechanics*, vol. 76, n° 3, 2009, p. 347–368, Elsevier.

[GLA 12] Glaser K. J., Manduca A., Ehman R. L.
Review of MR elastography applications and recent developments. *Journal of Magnetic Resonance Imaging*, vol. 36, n^o 4, 2012, p. 757–774, Wiley Online Library.

[GNA 21] Gnanago J.-L., Capsal J.-F., Gerges T., Lombard P., Semet V., Cottinet P.-J., Cabrera M., Lambert S. A.
Actuators for MRE: New Perspectives With Flexible Electroactive Materials. *Frontiers in Physics*, , 2021, Page 580, Frontiers.

[GRI 95] Griffiths D., Mustoe G. G.
Selective reduced integration of four-node plane element in closed form. *Journal of engineering mechanics*, vol. 121, n^o 6, 1995, p. 725–729, American Society of Civil Engineers.

[GRI 06] Grimm R. C., Lake D. S., Manduca A., Ehman R. L.
MRE/Wave. *Rochester (MN): Mayo Clinic*, , 2006, Available from Focus Areas in EhmanLab (http://mayoresearch.mayo.edu/ehman_lab).

[GUI 18] Guidetti M., Royston T. J.
Analytical solution for converging elliptic shear wave in a bounded transverse isotropic viscoelastic material with nonhomogeneous outer boundary. *The Journal of the Acoustical Society of America*, vol. 144, n^o 4, 2018, p. 2312–2323, Acoustical Society of America.

[HAO 19] Hao Q., Greenhalgh S.
The generalized standard-linear-solid model and the corresponding viscoacoustic wave equations revisited. *Geophysical Journal International*, vol. 219, n^o 3, 2019, p. 1939–1947, Oxford University Press.

[HE 19] He L., Li H., Dudley J. A., Maloney T. C., Brady S. L., Somasundaram E., Trout A. T., Dillman J. R.
Machine learning prediction of liver stiffness using clinical and T2-weighted MRI radiomic data. *American Journal of Roentgenology*, vol. 213, n^o 3, 2019, p. 592–601, Am Roentgen Ray Soc.

[HEN 10] Hennings B., Lammering R.
Modelling of wave propagation using spectral finite elements. *PAMM*, vol. 10, n^o 1, 2010, p. 7–10, Wiley Online Library.

[HER 02] Hermanns M.
Parallel programming in Fortran 95 using OpenMP. *Technique Report, Universidad Politecnica De Madrid*, , 2002.

[HIR 17] Hirsch S., Braun J., Sack I.
Magnetic resonance elastography: physical background and medical applications. John Wiley & Sons, 2017.

[HON 16] HONARVAR M., ROHLING R., SALCUDEAN S.
A comparison of direct and iterative finite element inversion techniques in dynamic elastography. *Physics in Medicine & Biology*, vol. 61, n° 8, 2016, Page 3026, IOP Publishing.

[HON 17] HONARVAR M., SAHEBJAVAHER R. S., ROHLING R., SALCUDEAN S. E.
A comparison of finite element-based inversion algorithms, local frequency estimation, and direct inversion approach used in MRE. *IEEE transactions on medical imaging*, vol. 36, n° 8, 2017, p. 1686–1698, IEEE.

[HUG 12] HUGHES T. J.
The finite element method: linear static and dynamic finite element analysis. Courier Corporation, 2012.

[INT 20] INTEL
Intel Math Kernel Library Developer Reference. , 2020.

[JAF 21] JAFARI A., BROUMAND P., VAHAB M., KHALILI N.
An eXtended Finite Element Method Implementation in COMSOL Multiphysics: Solid Mechanics. *arXiv preprint arXiv:2109.03153*, , 2021.

[JOH 01] JOHNSON G. R., BEISSEL S. R.
Damping algorithms and effects for explicit dynamics computations. *International journal of impact engineering*, vol. 25, n° 9, 2001, p. 911–925, Elsevier.

[JUN 13] JUNG J., JEONG C., TACIROGLU E.
Identification of a scatterer embedded in elastic heterogeneous media using dynamic XFEM. *Computer Methods in Applied Mechanics and Engineering*, vol. 259, 2013, p. 50–63, Elsevier.

[KAL 96] KALLEL F., BERTRAND M.
Tissue elasticity reconstruction using linear perturbation method. *IEEE Transactions on Medical Imaging*, vol. 15, n° 3, 1996, p. 299–313, IEEE.

[KAL 97] KALISKE M., ROTHERT H.
Formulation and implementation of three-dimensional viscoelasticity at small and finite strains. *Computational Mechanics*, vol. 19, n° 3, 1997, p. 228–239, Springer.

[KLA 07] KLATT D., HAMHABER U., ASBACH P., BRAUN J., SACK I.
Noninvasive assessment of the rheological behavior of human organs using multifrequency MR elastography: a study of brain and liver viscoelasticity. *Physics in Medicine & Biology*, vol. 52, n° 24, 2007, Page 7281, IOP Publishing.

[KRU 08] KRUSE S. A., ROSE G. H., GLASER K. J., MANDUCA A., FELMLEE J. P., JACK JR C. R., EHMAN R. L.
Magnetic resonance elastography of the brain. *Neuroimage*, vol. 39, n° 1, 2008, p. 231–237, Elsevier.

[LAK 98] LAKES R. S.
Viscoelastic solids, vol. 9. CRC press, 1998.

[LAN 86] LANDAU L. D., KOSEVICH A., PITAEVSKII L. P., LIFSHITZ E. M.
Theory of elasticity. Butterworth, 1986.

[LER 90] LERNER R. M., HUANG S., PARKER K. J.
"Sonoelasticity" images derived from ultrasound signals in mechanically vibrated tissues. *Ultrasound in medicine & biology*, vol. 16, n^{o} 3, 1990, p. 231–239, Elsevier.

[LI 10] LI B. N., CHUI C. K., ONG S. H., WASHIO T., NUMANO T., CHANG S., VENKATESH S., KOBAYASHI E.
Soft tissue discrimination using magnetic resonance elastography with a new elastic level set model. *International Workshop on Machine Learning in Medical Imaging* Springer, 2010, p. 76–83.

[LIL 21] LILAJ L., HERTHUM H., MEYER T., SHAHRYARI M., BERTALAN G., CAIAZZO A., BRAUN J., FISCHER T., HIRSCH S., SACK I.
Inversion-recovery MR elastography of the human brain for improved stiffness quantification near fluid–solid boundaries. *Magnetic Resonance in Medicine*, , 2021, Wiley Online Library.

[LIN 02] LING X., CHERUKURI H. P.
Stability analysis of an explicit finite element scheme for plane wave motions in elastic solids. *Computational Mechanics*, vol. 29, n^{o} 4, 2002, p. 430–440, Springer.

[LIU 13] LIU Z., OSWALD J., BELYTSCHKO T.
XFEM modeling of ultrasonic wave propagation in polymer matrix particulate/fibrous composites. *Wave motion*, vol. 50, n^{o} 3, 2013, p. 389–401, Elsevier.

[LOC 62] LOCKETT F.
The reflection and refraction of waves at an interface between viscoelastic materials. *Journal of the Mechanics and Physics of Solids*, vol. 10, n^{o} 1, 1962, p. 53–64, Elsevier.

[MAH 13] MAHEO L., GROLLEAU V., RIO G.
Numerical damping of spurious oscillations: a comparison between the bulk viscosity method and the explicit dissipative Tchamwa–Wielgosz scheme. *Computational Mechanics*, vol. 51, n^{o} 1, 2013, p. 109–128, Springer.

[MAH 20] MAHARJAN S., NUMANO T., HABE T., ITO D., UEKI T., IGARASHI K., MAENO T.
Directional Filter, Local Frequency Estimate and Algebraic Inversion of Differential Equation of Psoas Major Magnetic Resonance Elastography. *Open Journal of Medical Imaging*, vol. 10, n^{o} 1, 2020, p. 1–16, Scientific Research Publishing.

[MAI 02] MAI J. J., INSANA M. F.
Strain imaging of internal deformation. *Ultrasound in medicine & biology*, vol. 28, n° 11-12, 2002, p. 1475–1484, Elsevier.

[MAN 96] MANDUCA A., MUTHUPILLAI R., ROSSMAN P. J., GREENLEAF J. F., EHMAN R. L.
Local wavelength estimation for magnetic resonance elastography. *Proceedings of 3rd IEEE International Conference on Image Processing*, vol. 3 IEEE, 1996, p. 527–530.

[MAN 01] MANDUCA A., OLIPHANT T. E., DRESNER M. A., MAHOWALD J., KRUSE S. A., AMROMIN E., FELMLEE J. P., GREENLEAF J. F., EHMAN R. L.
Magnetic resonance elastography: non-invasive mapping of tissue elasticity. *Medical image analysis*, vol. 5, n° 4, 2001, p. 237–254, Elsevier.

[MAN 03] MANDUCA A., LAKE D. S., KRUSE S. A., EHMAN R. L.
Spatio-temporal directional filtering for improved inversion of MR elastography images. *Medical image analysis*, vol. 7, n° 4, 2003, p. 465–473, Elsevier.

[MAN 21] MANDUCA A., BAYLY P. J., EHMAN R. L., KOLIPAKA A., ROYSTON T. J., SACK I., SINKUS R., VAN BEERS B. E.
MR elastography: Principles, guidelines, and terminology. *Magnetic Resonance in Medicine*, vol. 85, n° 5, 2021, p. 2377–2390, Wiley Online Library.

[MAR 63] MARQUARDT D. W.
An algorithm for least-squares estimation of nonlinear parameters. *Journal of the society for Industrial and Applied Mathematics*, vol. 11, n° 2, 1963, p. 431–441, SIAM.

[MAR 10] MARIAPPAN Y. K., GLASER K. J., EHMAN R. L.
Magnetic resonance elastography: a review. *Clinical anatomy*, vol. 23, n° 5, 2010, p. 497–511, Wiley Online Library.

[MCG 11] MCGHEE D. E., STEELE J. R.
Breast volume and bra size. *International Journal of Clothing Science and Technology*, , 2011, Emerald Group Publishing Limited.

[MCG 20] MCGARRY M. D., VAN HOUTEN E., GUERTLER C., OKAMOTO R. J., SMITH D. R., SOWINSKI D. R., JOHNSON C. L., BAYLY P., WEAVER J., PAULSEN K. D.
A heterogenous, time harmonic, nearly incompressible transverse isotropic finite element brain simulation platform for MR elastography. *Physics in Medicine & Biology*, , 2020, IOP Publishing.

[MEL 96] MELENK J. M., BABUŠKA I.
The partition of unity finite element method: basic theory and applications. *Research Report/Seminar für Angewandte Mathematik*, vol. 1996 Eidgenössische Technische Hochschule, Seminar für Angewandte Mathematik, 1996.

[MEN 06] MENOUILLARD T., RETHORE J., COMBESCURE A., BUNG H.
Efficient explicit time stepping for the eXtended Finite Element Method (X-FEM). *International Journal for Numerical Methods in Engineering*, vol. 68, n° 9, 2006, p. 911–939, Wiley Online Library.

[MIG 03] MIGA M. I.
A new approach to elastography using mutual information and finite elements. *Physics in medicine & biology*, vol. 48, n° 4, 2003, Page 467, IOP Publishing.

[MIR 15] MIRBAGHERI Y., NAHVI H., PARVIZIAN J., DÜSTER A.
Reducing spurious oscillations in discontinuous wave propagation simulation using high-order finite elements. *Computers & Mathematics with Applications*, vol. 70, n° 7, 2015, p. 1640–1658, Elsevier.

[MOË 99] MOËS N., DOLBOW J., BELYTSCHKO T.
A finite element method for crack growth without remeshing. *International journal for numerical methods in engineering*, vol. 46, n° 1, 1999, p. 131–150, Wiley Online Library.

[MOË 03] MOËS N., CLOIREC M., CARTRAUD P., REMACLE J.-F.
A computational approach to handle complex microstructure geometries. *Computer methods in applied mechanics and engineering*, vol. 192, n° 28-30, 2003, p. 3163–3177, Elsevier.

[MUR 18] MURPHY M. C., MANDUCA A., TRZASKO J. D., GLASER K. J., HUSTON III J., EHMAN R. L.
Artificial neural networks for stiffness estimation in magnetic resonance elastography. *Magnetic resonance in medicine*, vol. 80, n° 1, 2018, p. 351–360, Wiley Online Library.

[MUR 20] MURPHY M. C., COGSWELL P. M., TRZASKO J. D., MANDUCA A., SENJEM M. L., MEYER F. B., EHMAN R. L., HUSTON III J.
Identification of normal pressure hydrocephalus by disease-specific patterns of brain stiffness and damping ratio. *Investigative radiology*, vol. 55, n° 4, 2020, p. 200–208, LWW.

[MUT 95] MUTHUPILLAI R., LOMAS D., ROSSMAN P., GREENLEAF J. F., MANDUCA A., EHMAN R. L.
Magnetic resonance elastography by direct visualization of propagating acoustic strain waves. *science*, vol. 269, n° 5232, 1995, p. 1854–1857, American Association for the Advancement of Science.

[NIS 08] NISTOR I., PANTALÉ O., CAPERAA S.
Numerical implementation of the extended finite element method for dynamic crack analysis. *Advances in Engineering Software*, vol. 39, n° 7, 2008, p. 573–587, Elsevier.

[NOH 13] NOH G., BATHE K.-J.
An explicit time integration scheme for the analysis of wave propagations. *Computers & structures*, vol. 129, 2013, p. 178–193, Elsevier.

[OBE 03] OBERAI A. A., GOKHALE N. H., FEIJÓO G. R.
Solution of inverse problems in elasticity imaging using the adjoint method. *Inverse problems*, vol. 19, n° 2, 2003, Page 297, IOP Publishing.

[OBE 04] OBERAI A. A., GOKHALE N. H., DOYLEY M. M., BAMBER J. C.
Evaluation of the adjoint equation based algorithm for elasticity imaging. *Physics in Medicine & Biology*, vol. 49, n° 13, 2004, Page 2955, IOP Publishing.

[OLI 01] OLIPHANT T. E., MANDUCA A., EHMAN R. L., GREENLEAF J. F.
Complex-valued stiffness reconstruction for magnetic resonance elastography by algebraic inversion of the differential equation. *Magnetic Resonance in Medicine: An Official Journal of the International Society for Magnetic Resonance in Medicine*, vol. 45, n° 2, 2001, p. 299–310, Wiley Online Library.

[OPH 91] OPHIR J., CESPEDES I., PONNEKANTI H., YAZDI Y., LI X.
Elastography: a quantitative method for imaging the elasticity of biological tissues. *Ultrasonic imaging*, vol. 13, n° 2, 1991, p. 111–134, Elsevier.

[OSH 88] OSHER S., SETHIAN J. A.
Fronts propagating with curvature-dependent speed: algorithms based on Hamilton-Jacobi formulations. *Journal of computational physics*, vol. 79, n° 1, 1988, p. 12–49, Elsevier.

[PAR 06] PARK E., MANIATTY A. M.
Shear modulus reconstruction in dynamic elastography: time harmonic case. *Physics in Medicine & Biology*, vol. 51, n° 15, 2006, Page 3697, IOP Publishing.

[PAR 10] PARKER K. J., DOYLEY M. M., RUBENS D. J.
Imaging the elastic properties of tissue: the 20 year perspective. *Physics in medicine & biology*, vol. 56, n° 1, 2010, Page R1, IOP Publishing.

[PAT 84] PATERA A. T.
A spectral element method for fluid dynamics: laminar flow in a channel expansion. *Journal of computational Physics*, vol. 54, n° 3, 1984, p. 468–488, Elsevier.

[RAB 38] RABI I. I., ZACHARIAS J. R., MILLMAN S., KUSCH P.
A new method of measuring nuclear magnetic moment. *Physical review*, vol. 53, n° 4, 1938, Page 318, APS.

[ROY 99] ROYER D., DIEULESAINT E.
Elastic waves in solids I: Free and guided propagation. Springer Science & Business Media, 1999.

[ROY 11] ROYSTON T. J., DAI Z., CHAUNSALI R., LIU Y., PENG Y., MAGIN R. L.
Estimating material viscoelastic properties based on surface wave measurements: A comparison of techniques and modeling assumptions. *The Journal of the Acoustical Society of America*, vol. 130, n° 6, 2011, p. 4126–4138, Acoustical Society of America.

[ROY 21] ROYSTON T. J.
Analytical solution based on spatial distortion for a time-harmonic Green's function in a transverse isotropic viscoelastic solid. *The Journal of the Acoustical Society of America*, vol. 149, n° 4, 2021, p. 2283–2291, Acoustical Society of America.

[SAD 09] SADD M. H.
Elasticity: theory, applications, and numerics. Academic Press, 2009.

[SAN 03] SANDRIN L., FOURQUET B., HASQUENOPH J.-M., YON S., FOURNIER C., MAL F., CHRISTIDIS C., ZIOL M., POULET B., KAZEMI F. et al.
Transient elastography: a new noninvasive method for assessment of hepatic fibrosis. *Ultrasound in medicine & biology*, vol. 29, n° 12, 2003, p. 1705–1713, Elsevier.

[SAR 95] SARVAZYAN A., SKOVORODA A., EMELIANOV S., FOWLKES J., PIPE J., ADLER R., BUXTON R., CARSON P.
Biophysical bases of elasticity imaging. *Acoustical imaging*, p. 223–240 Springer, 1995.

[SAR 98] SARVAZYAN A.
Mechanical imaging:: A new technology for medical diagnostics. *International journal of medical informatics*, vol. 49, n° 2, 1998, p. 195–216, Elsevier.

[SAR 11] SARVAZYAN A., J HALL T., W URBAN M., FATEMI M., R AGLYAMOV S., S GARRA B.
An overview of elastography-an emerging branch of medical imaging. *Current Medical Imaging*, vol. 7, n° 4, 2011, p. 255–282, Bentham Science Publishers.

[SCO 20] SCOTT J. M., ARANI A., MANDUCA A., MCGEE K. P., TRZASKO J. D., HUSTON III J., EHMAN R. L., MURPHY M. C.
Artificial neural networks for magnetic resonance elastography stiffness estimation in inhomogeneous materials. *Medical Image Analysis*, vol. 63, 2020, Page 101710, Elsevier.

[SET 96] SETHIAN J. A.
A fast marching level set method for monotonically advancing fronts. *Proceedings of the National Academy of Sciences*, vol. 93, n° 4, 1996, p. 1591–1595, National Acad Sciences.

[SET 99] SETHIAN J. A.
Level set methods and fast marching methods: evolving interfaces in computational

geometry, fluid mechanics, computer vision, and materials science, vol. 3. Cambridge university press, 1999.

[SIM 87] SIMO J. C.
On a fully three-dimensional finite-strain viscoelastic damage model: formulation and computational aspects. *Computer methods in applied mechanics and engineering*, vol. 60, n° 2, 1987, p. 153–173, Elsevier.

[SIM 06] SIMO J. C., HUGHES T. J.
Computational inelasticity, vol. 7. Springer Science & Business Media, 2006.

[SIM 14] SIMULIA) D. D. S.
. « Abaqus Theory Manual Version 6.11 », 2014.

[SIN 05] SINKUS R., TANTER M., XYDEAS T., CATHELINE S., BERCOFF J., FINK M.
Viscoelastic shear properties of in vivo breast lesions measured by MR elastography. *Magnetic resonance imaging*, vol. 23, n° 2, 2005, p. 159–165, Elsevier.

[SOL 18] SOLAMEN L., SHI Y., AMOH J.
Dual Objective Approach Using A Convolutional Neural Network for Magnetic Resonance Elastography. *arXiv preprint arXiv:1812.00441*, , 2018.

[SUK 01] SUKUMAR N., CHOPP D. L., MOËS N., BELYTSCHKO T.
Modeling holes and inclusions by level sets in the extended finite-element method. *Computer methods in applied mechanics and engineering*, vol. 190, n° 46-47, 2001, p. 6183–6200, Elsevier.

[SUK 03] SUKUMAR N., PRÉVOST J.-H.
Modeling quasi-static crack growth with the extended finite element method Part I: Computer implementation. *International journal of solids and structures*, vol. 40, n° 26, 2003, p. 7513–7537, Elsevier.

[TSE 09] TSE Z., JANSSEN H., HAMED A., RISTIC M., YOUNG I., LAMPERTH M.
Magnetic resonance elastography hardware design: a survey. *Proceedings of the Institution of Mechanical Engineers, Part H: Journal of Engineering in Medicine*, vol. 223, n° 4, 2009, p. 497–514, SAGE Publications Sage UK: London, England.

[VAN 99] VAN HOUTEN E. E., PAULSEN K. D., MIGA M. I., KENNEDY F. E., WEAVER J. B.
An overlapping subzone technique for MR-based elastic property reconstruction. *Magnetic Resonance in Medicine: An Official Journal of the International Society for Magnetic Resonance in Medicine*, vol. 42, n° 4, 1999, p. 779–786, Wiley Online Library.

[VAN 01] VAN HOUTEN E. E., MIGA M. I., WEAVER J. B., KENNEDY F. E., PAULSEN K. D.
Three-dimensional subzone-based reconstruction algorithm for MR elastography.

Magnetic Resonance in Medicine: An Official Journal of the International Society for Magnetic Resonance in Medicine, vol. 45, n° 5, 2001, p. 827–837, Wiley Online Library.

[VAN 17] VAN PAMEL A., SHA G., ROKHLIN S. I., LOWE M. J.
Finite-element modelling of elastic wave propagation and scattering within heterogeneous media. *Proceedings of the Royal Society A: Mathematical, Physical and Engineering Sciences*, vol. 473, n° 2197, 2017, The Royal Society Publishing.

[VEN 14] VENKATESH S. K., EHMAN R. L.
Magnetic resonance elastography. Springer, 2014.

[VLA 03] VLAARDINGERBROEK M. T., BOER J. A.
Magnetic resonance imaging: theory and practice. Springer Science & Business Media, 2003.

[VON 50] VONNEUMANN J., RICHTMYER R. D.
A method for the numerical calculation of hydrodynamic shocks. *Journal of applied physics*, vol. 21, n° 3, 1950, p. 232–237, American Institute of Physics.

[VON 52] VON GIERKE H. E., OESTREICHER H. L., FRANKE E. K., PARRACK H. O., VON WITTERN W. W.
Physics of vibrations in living tissues. *Journal of applied physiology*, vol. 4, n° 12, 1952, p. 886–900, American Physiological Society Bethesda, MD.

[WAN 16] WANG Z., YU T., BUI T. Q., TRINH N. A., LUONG N. T. H., DUC N. D., DOAN D. H.
Numerical modeling of 3-D inclusions and voids by a novel adaptive XFEM. *Advances in Engineering Software*, vol. 102, 2016, p. 105–122, Elsevier.

[WIL 82] WILSON L., ROBINSON D.
Ultrasonic measurement of small displacements and deformations of tissue. *Ultrasonic imaging*, vol. 4, n° 1, 1982, p. 71–82, Elsevier.

[WOO 77] WOOD J. G.
Nature's teachings: human invention anticipated by nature. Daldy, Isbister, 1877.

[WU 05] WU B., BAO H., OU J., TIAN S.
Stability and accuracy analysis of the central difference method for real-time substructure testing. *Earthquake engineering & structural dynamics*, vol. 34, n° 7, 2005, p. 705–718, Wiley Online Library.

[XIA 13] XIANG K., ZHU X. L., WANG C. X., LI B. N.
MREJ: MRE elasticity reconstruction on ImageJ. *Computers in biology and medicine*, vol. 43, n° 7, 2013, p. 847–852, Elsevier.

[XU 07] XU L., LIN Y., XI Z., SHEN H., GAO P.
Magnetic resonance elastography of the human brain: a preliminary study. *Acta radiologica*, vol. 48, nº 1, 2007, p. 112–115, Taylor & Francis.

[XU 17] XU C., YU Z.
Numerical simulation of elastic wave propagation in functionally graded cylinders using time-domain spectral finite element method. *Advances in Mechanical Engineering*, vol. 9, nº 11, 2017, Page 1687814017734457, SAGE Publications Sage UK: London, England.

[YAS 13] YASAR T. K., ROYSTON T. J., MAGIN R. L.
Wideband MR elastography for viscoelasticity model identification. *Magnetic resonance in medicine*, vol. 70, nº 2, 2013, p. 479–489, Wiley Online Library.

[YIN 08] YIN M., ROUVIÈRE O., GLASER K. J., EHMAN R. L.
Diffraction-biased shear wave fields generated with longitudinal magnetic resonance elastography drivers. *Magnetic resonance imaging*, vol. 26, nº 6, 2008, p. 770–780, Elsevier.

[YUS 21] YUSHCHENKO M., SARRACANIE M., AMANN M., SINKUS R., WUERFEL J., SALAMEH N.
Elastography validity criteria definition using numerical simulations and MR acquisitions on a low-cost structured phantom. *Frontiers in Physics*, vol. 9, 2021, Page 620331.

[ZER 88] ZERHOUNI E. A., PARISH D. M., ROGERS W. J., YANG A., SHAPIRO E. P.
Human heart: tagging with MR imaging–a method for noninvasive assessment of myocardial motion. *Radiology*, vol. 169, nº 1, 1988, p. 59–63.

[ZIE 00] ZIENKIEWICZ O. C., TAYLOR R. L.
The finite element method: solid mechanics, vol. 2. Butterworth-heinemann, 2000.

[ZIE 05] ZIENKIEWICZ O. C., TAYLOR R. L., ZHU J. Z.
The finite element method: its basis and fundamentals. Elsevier, 2005.

FOLIO ADMINISTRATIF

THESE DE L'UNIVERSITE DE LYON OPEREE AU SEIN DE L'INSA LYON

NOM : DU DATE de SOUTENANCE : 05/07/2022

Prénoms : Quanshangze

TITRE : Numerical modeling of MR elastography experiment : excitation and tissue inhomogeneity

NATURE : Doctorat Numéro d'ordre : 2022LYSEI055

Ecole doctorale : ED 162 MEGA

Spécialité : Biomécanique

RESUME : The diagnosis of various pathologies, including some cancers, has long been based on palpation, since a tumor is significantly stiffer than healthy tissue. More advanced and quantitative methods have been developed over the last decades, especially the Magnetic Resonance Elastography (MRE). This method uses magnetic resonance imaging (MRI) on mechanically stressed tissue to estimate the mechanical properties of soft tissue. The reconstruction of the elasticity modulus of the tissue in MRE is often based on a model with simple behavior laws of the imaged tissue (linear elasticity, isotropy, homogeneity), which could be extended to more complex cases thanks to modeling by the Finite Element Method (FEM) in particular. FEM has been used in MRE to simulate the propagation of mechanical waves in a tissue, to better understand the effects of different parameters on MRE measurements, to reconstruct stiffness, to evaluate novel MRE inversion methods, etc. However, in inhomogeneous cases with complex interfaces, FEM modeling can be particularly costly as it requires an explicit mesh of these interfaces.

In this work, we explored, using an explicit dynamic FE solver developed in this thesis, the behavior of mechanical waves propagating in a linear, isotropic, viscoelastic and inhomogeneous medium, in order to better control the parameters of a MRE experiment. In the solver, the eXtended Finite Element Method (XFEM) has been implemented; this formulation of FEM originates from fracture mechanics and has been widely used over the last two decades to model discontinuities such as cracks and inclusions.

Using the developed numerical tool, we studied the behavior of waves in the vicinity of an interface (oblique or complex), in particular the phenomena of wave reflection and wave conversion. It has been shown that the use of the XFEM method significantly reduces the computation time while ensuring an equivalent accuracy, in terms of displacement fields and reconstructed stiffness. Furthermore, we have addressed, by simulation, the criterion of establishing the steady state of the waves which must be reached to ensure correct recording by MRI. Today, this criterion is still empirical and can influence the quality of MRE data. We have thus proposed a metric to quantify the achievement of the steady state of wave propagation in a tissue with or without inclusion. Finally, these methods were implemented on a practical case of breast MRE. Based on breast models, we evaluated the influence of experimental parameters (size and position of the inclusion, polarization of the excitation, boundary conditions, etc.) on the achievement of steady state.

MOTS-CLÉS : Magnetic resonance elastography, extended finite element method, inhomogeneity interface, wave conversion, steady-state metric

Laboratoire (s) de recherche : Laboratoire de Mécanique des Contacts et des Structures
UMR CNRS 5259 - INSA de Lyon
20 Avenue Albert Einstein
69621 Villeurbanne Cedex FRANCE

Directeur de thèse : Monsieur Professeur Nahiène HAMILA

Président de jury :

Composition du jury : Jean-Luc GENNISSON
Christian GEINDREAU
Aline BEL-BRUNON
Patrick ROZYCKI
Nahiène HAMILA
Simon Auguste LAMBERT